NASA-CR-203932

ERCI/HSV-TR95-02

IN 34-CR

Final Report

p. 192

SRM Internal Flow Tests and Computational Fluid Dynamic Analysis

Volume III
Titan, ASRM, and Subscale Motor Analyses

November, 1995

Prepared for:
George C. Marshall Space Flight Center
National Aeronautics and Space Administration
Marshall Space Flight Center, AL 35812

Contract NAS8-39095

Prepared by:
ERC, Incorporated
555 Sparkman Drive, Suite 1622
Huntsville, AL 35816

Table of Contents

Volume II

Volume III

Volume IV

PREFACE

This report was prepared by the Huntsville Operation of ERC, Incorporated for the Aerophysics Division of the Science and Engineering Directorate, George C. Marshall Space Flight Center, National Aeronautics and Space Administration. This effort was performed under Contract NAS8-39095 with David L. Bacchus serving as the Contracting Officer's Technical Representative. The deformed propellant grain geometries for the various load conditions were contributed by Victor I. Richard, ED24.

The CFD analysis was performed and this report was prepared by R. Harold Whitesides and Richard A. Dill. Computer results data were evaluated and presented with the support of Lori A. Sisk.

Computational Fluid Dynamics Analysis of the Aft Slot Region in the Titan IV Solid Rocket Motor Upgrade (SRMU)

August, 1991

Prepared for:
George C. Marshall Space Flight Center
National Aeronautics and Space Administration

Contract NAS8-39095

Prepared by:
ERC, Incorporated
Huntsville Operation
555 Sparkman Drive, Suite 846
Huntsville, AL 35816

(b) Subsequently, a deformed grain geometry was computed including the effects of cure shrinkage, 1-g axial acceleration, and internal motor pressure distributions obtained from Step 3(a).

4 (a) A final CFD model, configuration 4, was developed by using the deformed grain geometry resulting from Step 3(b). The resulting internal motor pressure distributions were provided to NASA stress analysts for further investigation.

The results from each of the four CFD analyses performed are presented herein.

CFD Modeling Description

The CFD analysis was performed assuming an axi-symmetric flow field using the Navier Stokes equations with turbulence accounted for through a k-e model. The FLUENT/BFC code was used to compute the flow fields for all geometric configurations considered.

In order to get an overall perspective of the problem under investigation, Figure 1 is provided to illustrate the location of the various important regions of the Titan IV SRMU including the motor aft slot. The portion of the motor for which the CFD analysis was performed is highlighted in the figure. Figure 2 shows an enlarged view of the portion of the motor that was investigated. The undeformed motor configuration illustrated in Figure 2 is the nominal propellant grain configuration of the motor obtained from propellant design drawings. As shown in the figure, a portion of both the center and aft segments was analyzed along with the aft slot. A 100 inch portion of the center propellant grain segment upstream of the slot and a 178 inch portion of the aft propellant grain segment downstream of the slot were analyzed. The only difference between the analyzed undeformed configuration and the actual Titan IV motor slot is that the corners toward the bottom of the slot on the stress relief grooves are rounded in the actual motor. This detail was not added to the analysis due to the lack of information on the exact geometry of the stress relief grooves and the negligible effect this detail has on the CFD analysis.

Figure 3 shows an enlargement of the slot region for the undeformed motor aft slot, configuration 1. The slot geometry in this figure can be compared with the deformed grain configurations. This is possible because the deformed grain configurations of the motor utilized the same propellant grain geometry except in the region of the slot. The radius of the center propellant grain at the inlet remained constant for all configurations analyzed. Only the slope of the center propellant grain changed due to the deformation of the upstream corner of the slot. Similarly, the radius of the aft propellant grain remained constant for all configurations analyzed from the propellant grain slope change location to the exit (See Figure 2). The slope of the aft propellant grain did change from the slope change location

Introduction

A computational fluid dynamics (CFD) analysis has been performed on the aft slot region of the Titan IV Solid Rocket Motor Upgrade (SRMU). This analysis was performed in conjunction with MSFC structural modeling of the propellant grain to determine if the flow field induced stresses would adversely alter the propellant geometry to the extent of causing motor failure. The results of the coupled CFD/stress analysis have shown that there is a continual increase of flow field resistance at the aft slot due to the aft segment propellant grain being progressively moved radially toward the centerline of the motor port. This "bootstrapping" effect between grain radial movement and internal flow resistance is conducive to causing a rapid motor failure.

Analysis Procedure

The iterative process between flow field analysis and structural modeling required the development of CFD models for several geometric configurations of the SRMU propellant grain. The general procedure was as follows:

1 (a) A CFD model was developed based on design drawings of the SRMU grain at zero burn time and will be referred to as configuration 1. This analysis was needed to provide a parametric comparison case for the smallest possible slot width. The resulting grain pressure distributions were provided to NASA stress analysts for use in assessing the effects of motor pressure on grain deformations.

(b) Concurrently, a stress analysis was performed by NASA, MSFC to predict the grain deformations created by the combined effects of cure shrinkage and 1-g axial acceleration on the center and aft propellant segments.

2 (a) A second CFD model, referred to as configuration 2, was developed utilizing the grain geometry resulting from step 1(b). The resulting propellant grain pressure distributions were provided to NASA stress analysts for additional structural modeling.

(b) Concurrently, a deformed grain geometry was produced including the effects of cure shrinkage, 1-g axial acceleration, and motor pressure. The internal pressure distributions were those generated from Step 1(a) for the "per drawing" grain configuration.

3 (a) A third CFD model was developed utilizing the grain geometry resulting from Step 2(b). This configuration will be referenced as configuration 3. The completed analytical results for this configuration were provided to NASA stress analysts for further analysis.

1. The boundary condition types for the CFD solution are shown graphically in Figure 4. A velocity boundary condition was utilized at the port inlet upstream of the aft slot. A Culick velocity profile was used at the port inlet. The mass flow rate, static pressure and static temperature were known at the inlet from the ballistic solution. These values were used to determine the average port velocity. The Culick velocity profile was then generated by the equation shown below.

$$U = \frac{\pi}{2} U_{avg} \cos\left[\frac{\pi}{2}\left(\frac{r}{r_o}\right)^2\right]$$

U_{avg}: average port velocity
r: radial distance
r_o: port radius

Table 1. ASRM Motor Aft Slot Problem Thermochemical Properties

Inlet Static Pressure, psia	860.2
Specific Heat Ratio	1.128
Viscosity, lbm/ft-s	6.399e-5
Thermal Conductivity, BTU/sec-ft-°R	6.8608e-5
Molecular Weight	28.04
Gas Constant, ft-lbf/lbm-°R	52.406
Stagnation Temperature, °R	6345

The static pressure was used as the reference pressure at the port inlet. The total temperature used at the inlet was the chamber temperature taken from the ballistic run. A velocity boundary condition was used at all the propellant grain surfaces. These surfaces are shown in Figure 4. Table 2 summarizes the propellant grain boundary conditions associated with the boundaries displayed in Figure 4.

Table 2. Summary of the Propellant Grain Boundary Conditions

Injection Velocity, Region 2	$V_x = 0.0138$ m/s	$v_y = -3.4842$ m/s
Injection Velocity, Region 3	$v_x = 3.4533$ m/s	$v_y = 0.0247$ m/s
Injection Velocity, Region 4	$v_x = 0.0439$ m/s	$v_y = -4.0233$ m/s

These velocity boundary conditions were computed by knowing the mass flow rate along the propellant boundaries from the ASRM ballistic run and also deriving average pressures on the propellant surfaces from the ASRM ballistic run. The only other boundaries which have not been discussed are the port exit boundary and the inhibited walls in the slot. A non-slip wall boundary condition was used for the inhibited walls

ASRM Coupled Structural/Fluid Dynamic Stress Analysis

A team was formed to perform an interactive CFD/Propellant Structural analysis to determine the deformed grain geometry in the vicinity of the aft and forward field joint slots. ED32 will coordinate the CFD analysis to be performed by ERCI and the structural analysis to be performed by Sverdrup Technologies. ED24 will oversee the structural analysis. The aft field joint will be analyzed first at a propellant temperature of 90 °F which should result in the maximum propellant deflection. The analyses will be started with a deformed grain geometry which includes the effect of cure and thermal shrinkage, 1g vertical storage, 0.6, flight acceleration, and 1-D pressure loads.

Work on the coupled mechanical/fluid dynamic stress analysis of the ASRM propellant grain began during the latter part of September, 1992. The purpose of this analysis is to examine the propellant grain in the vicinity of the field joints and determine the stresses generated on the propellant grain induced by the flow field during motor burning. The analysis will also examine the coupling between the propellant deformations and the motor flow field to determine if the propellant structure is stable during motor burn. The flow field in the aft slot region has been determined to be the most stressing case from previous analyses and only this field joint will be examined at this time.

This analysis will be performed in steps as an iterative process. The 2 main steps in the coupled analytical process can be outlined in the following way.

1. ERCI will provide Sverdrup with a pressure distribution on the center and aft propellant grain segments. This will be derived from the Aerojet CDR ballistic runs, and adjusted to a 90°F firing temperature. Sverdrup will perform a linear stress analysis on the propellant grain. This stress analysis will include the following sources of stress on the propellant grain: propellant curing, thermal cool down, vertical storage, lift-off acceleration, and fluid dynamic induced pressure. This stress analysis process will produce a deformed geometry grain which will be taken by ERCI and used to produce a computational grid for the CFD code. The CFD code will produce a new pressure distribution on the propellant grain.

2. The new pressure distribution produced by the last stage of step 1 will be used by Sverdrup to generate a new deformed propellant grain due to the previously mentioned sources of stress. The new deformed propellant grain geometry will be used by ERCI to produce a new CFD generated pressure distribution on the propellant grain. This step 2 of the process will be performed several times until the propellant grain deformation ceases to change between iterations.

The boundary conditions used in the CFD run were derived from an Aerojet ballistic prediction. The thermophysical properties of the ASRM propellant are shown in Table

Figure 62. Normalized Kinetic Energy

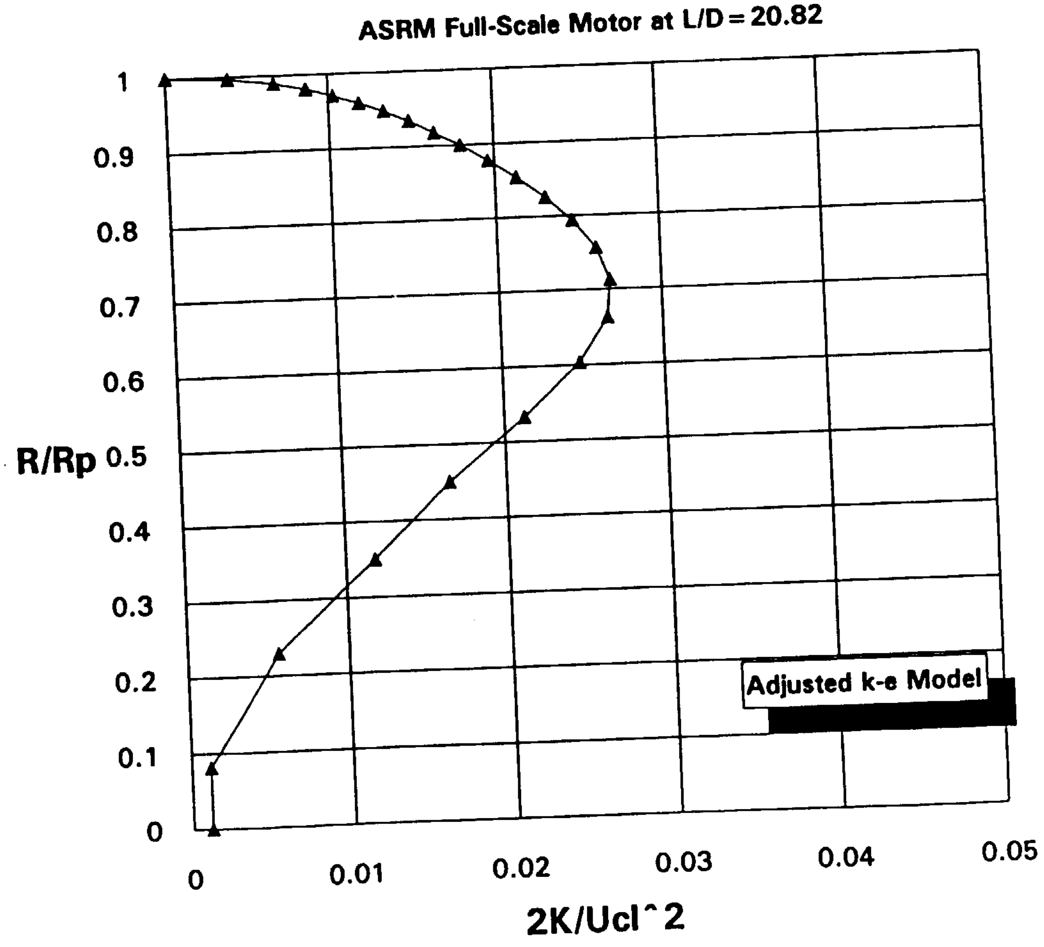

Figure 61. Normalized Kinetic Energy

ASRM Full-Scale Motor at L/D = 16.63

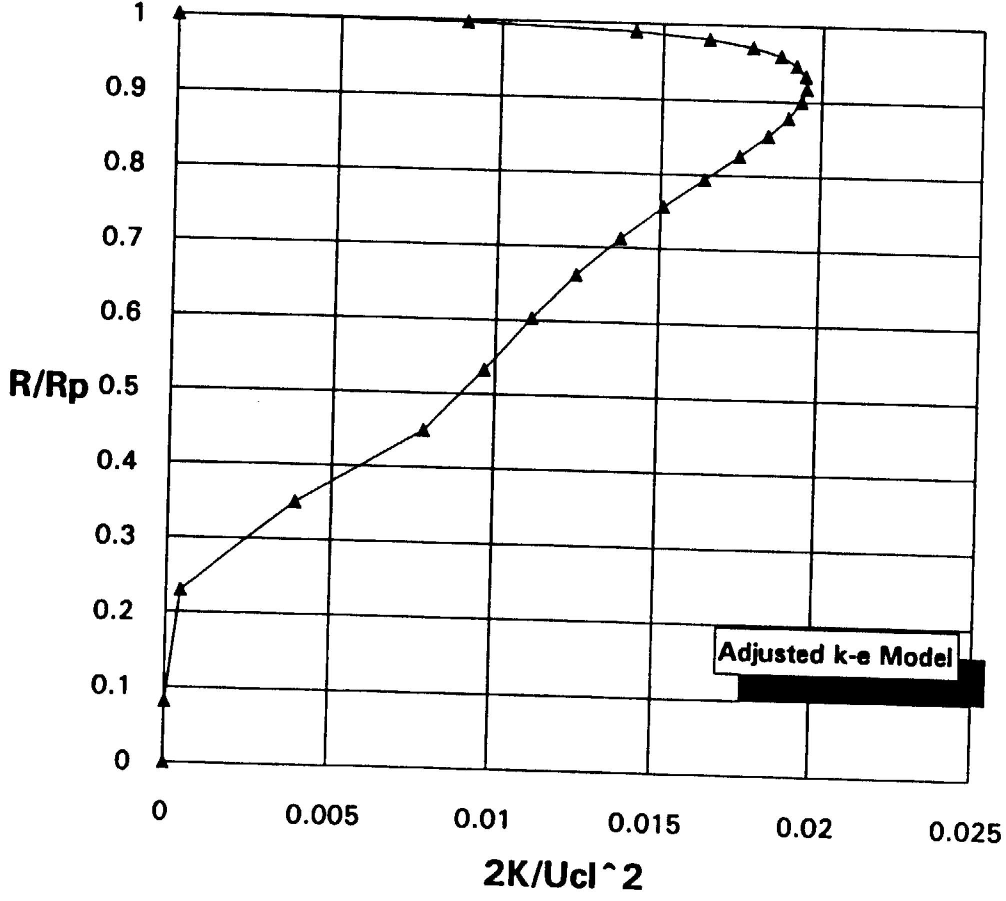

Figure 60. Normalized Kinetic Energy

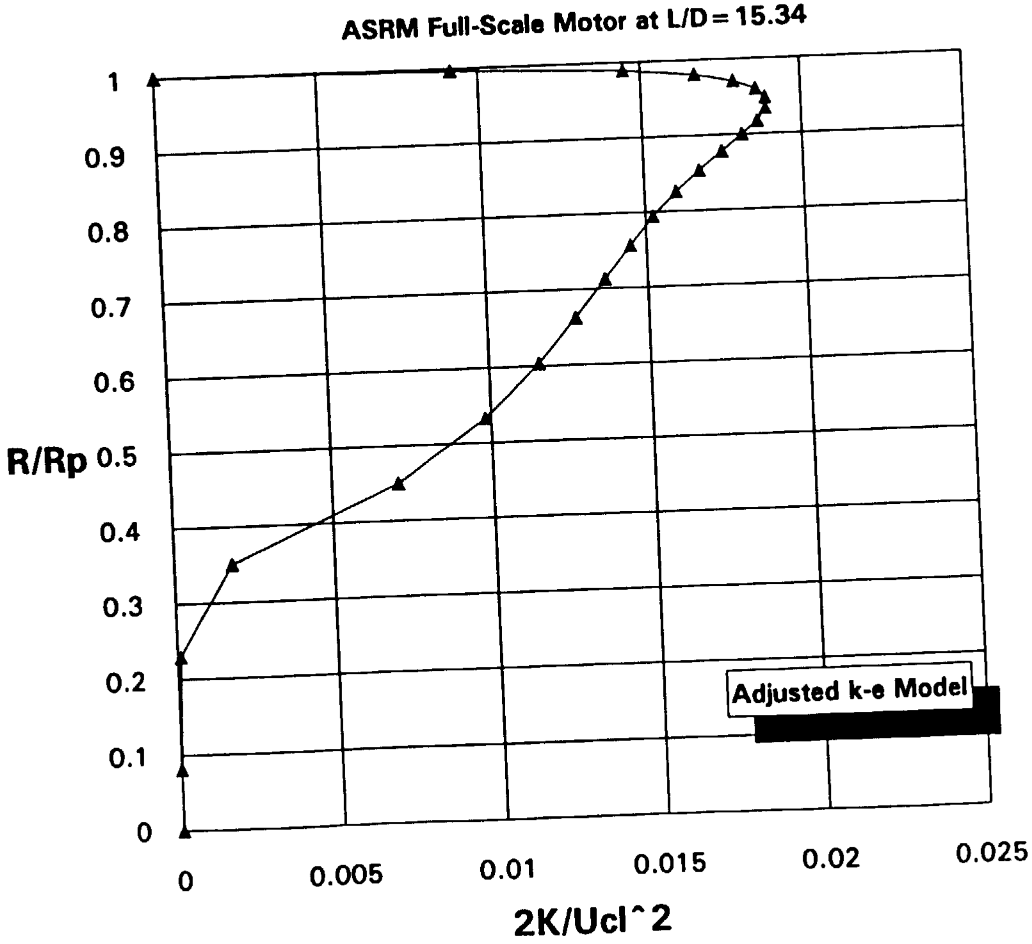

Figure 59. Normalized Kinetic Energy

ASRM Full-Scale Motor at L/D=14.6

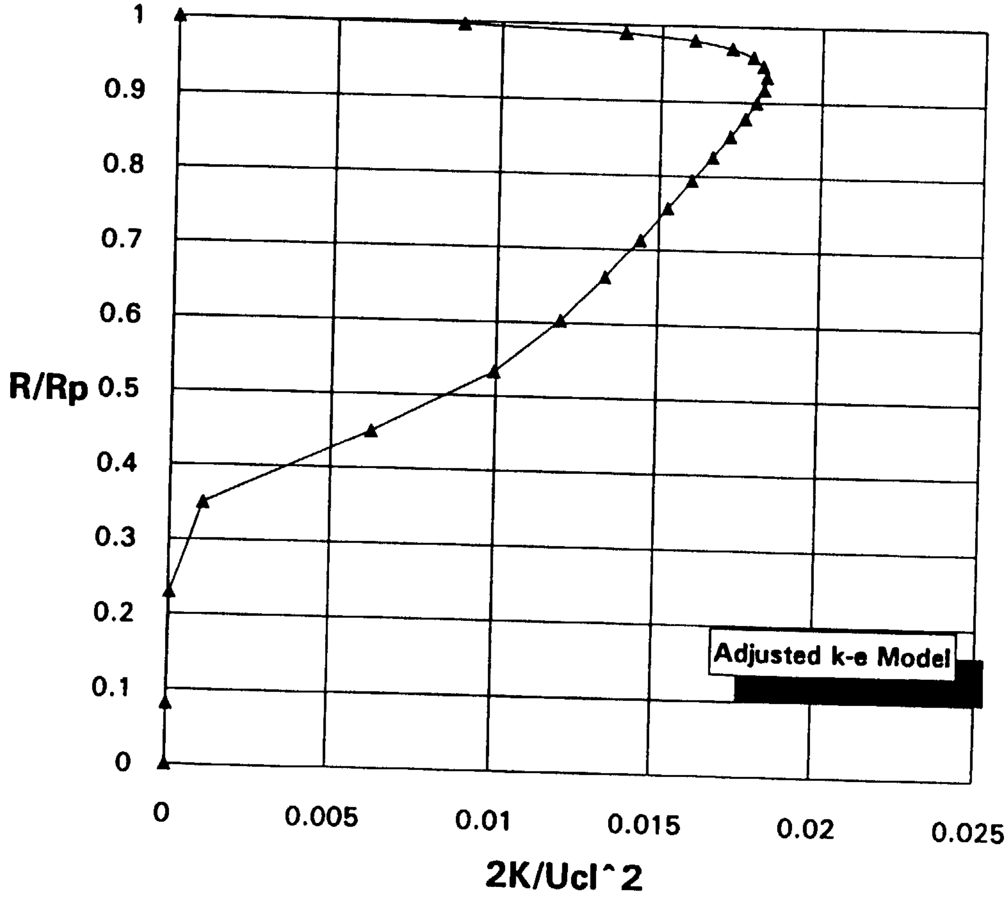

Figure 58. Normalized Kinetic Energy

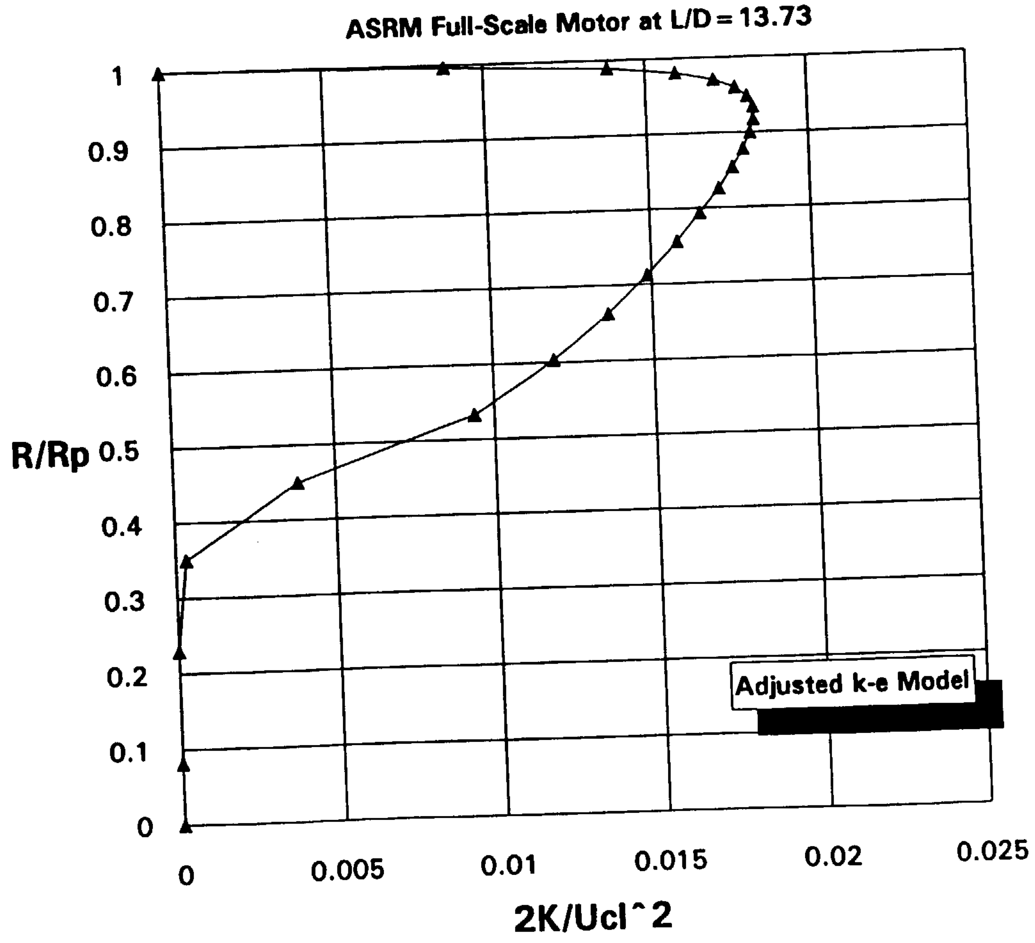

Figure 57. Normalized Kinetic Energy

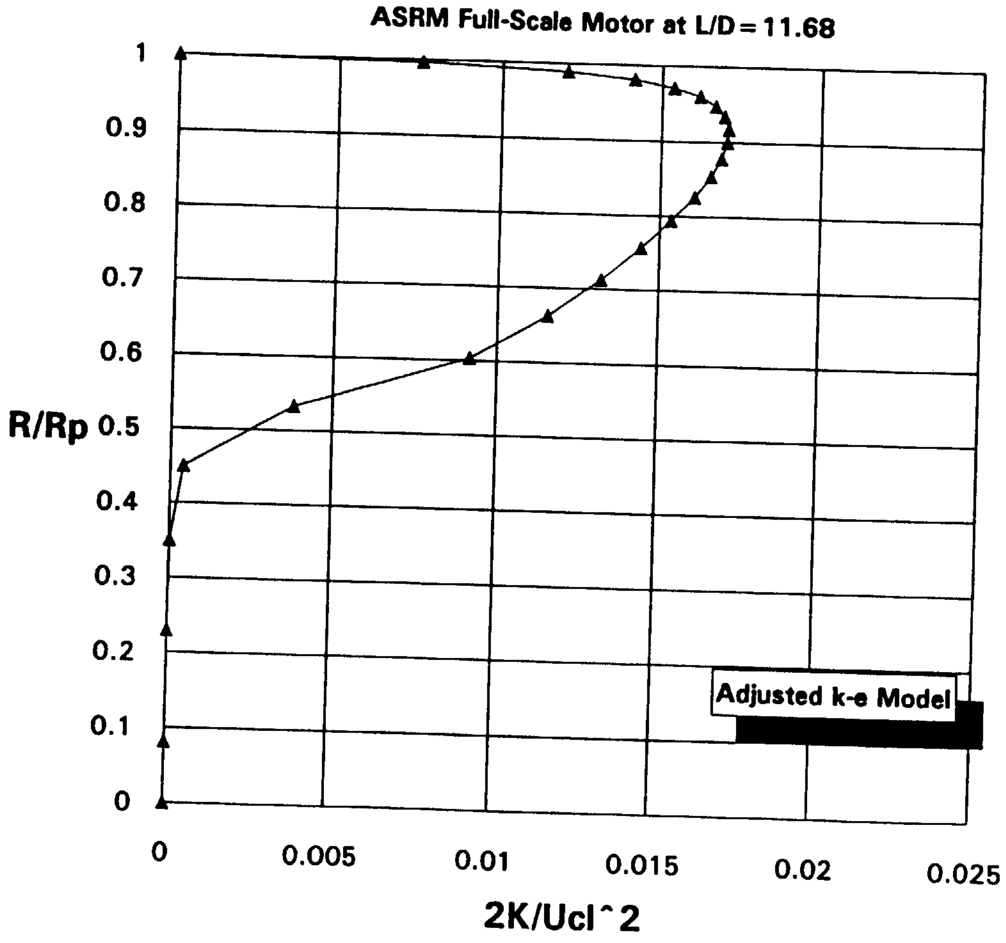

Figure 56. Normalized Kinetic Energy

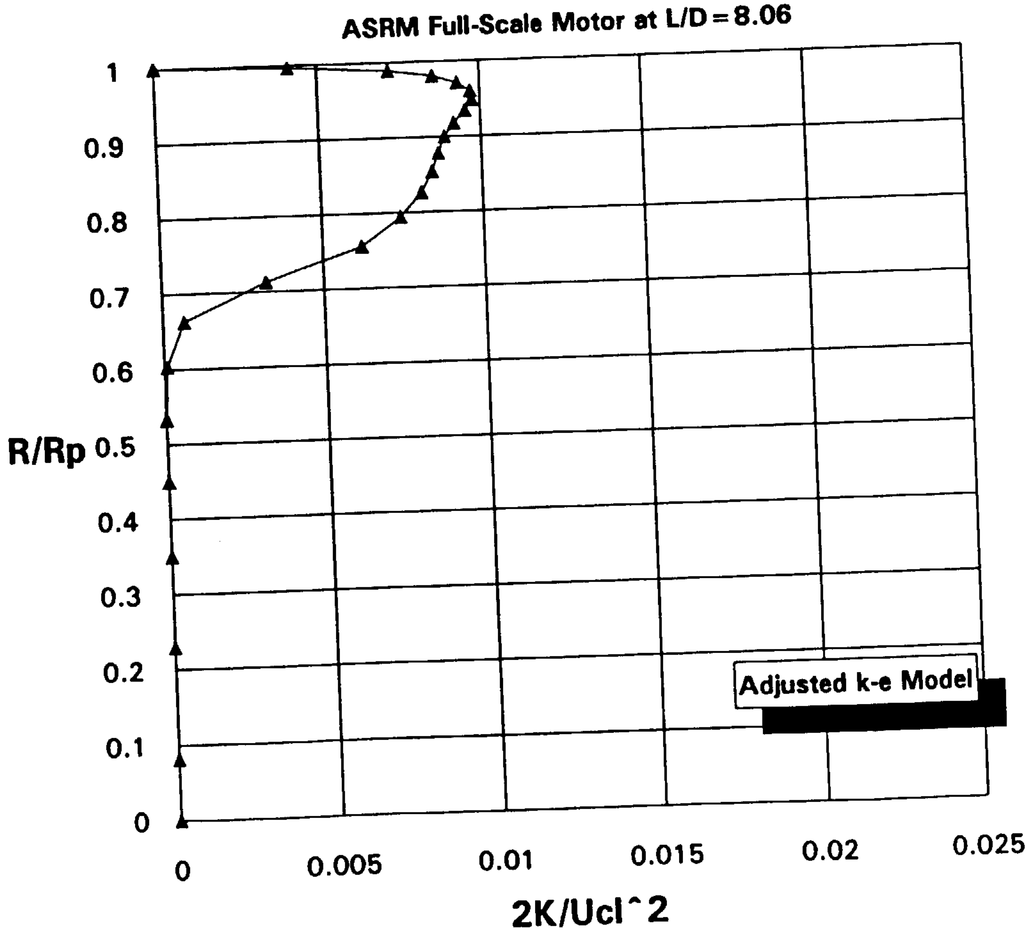

Figure 55. Normalized Kinetic Energy

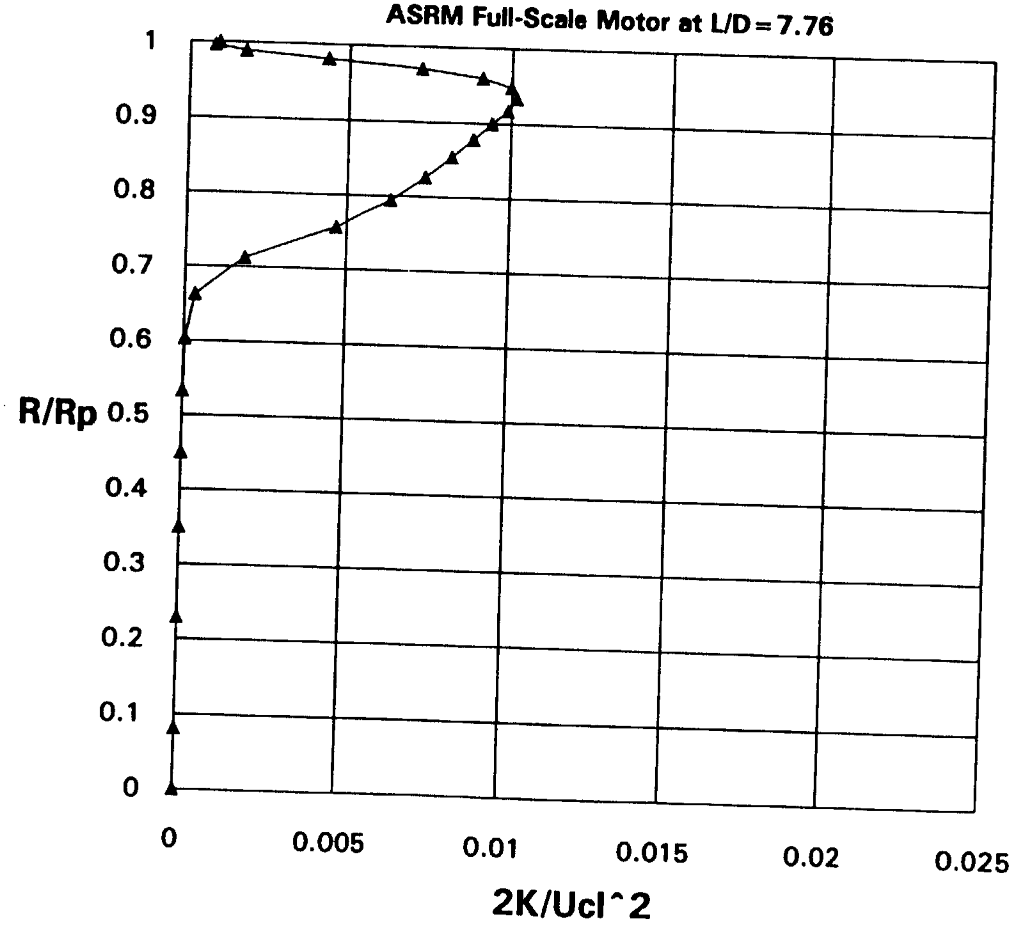

Figure 54. Normalized Kinetic Energy

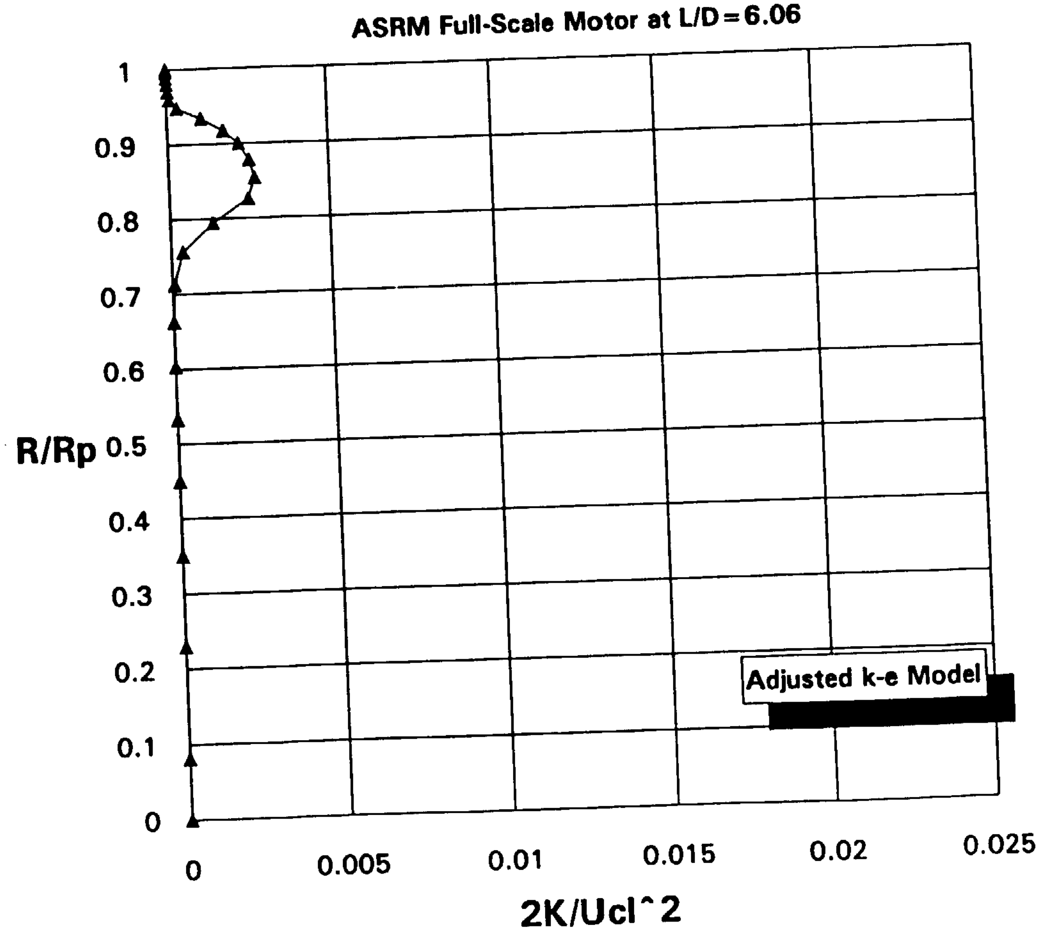

Figure 53. Normalized Kinetic Energy

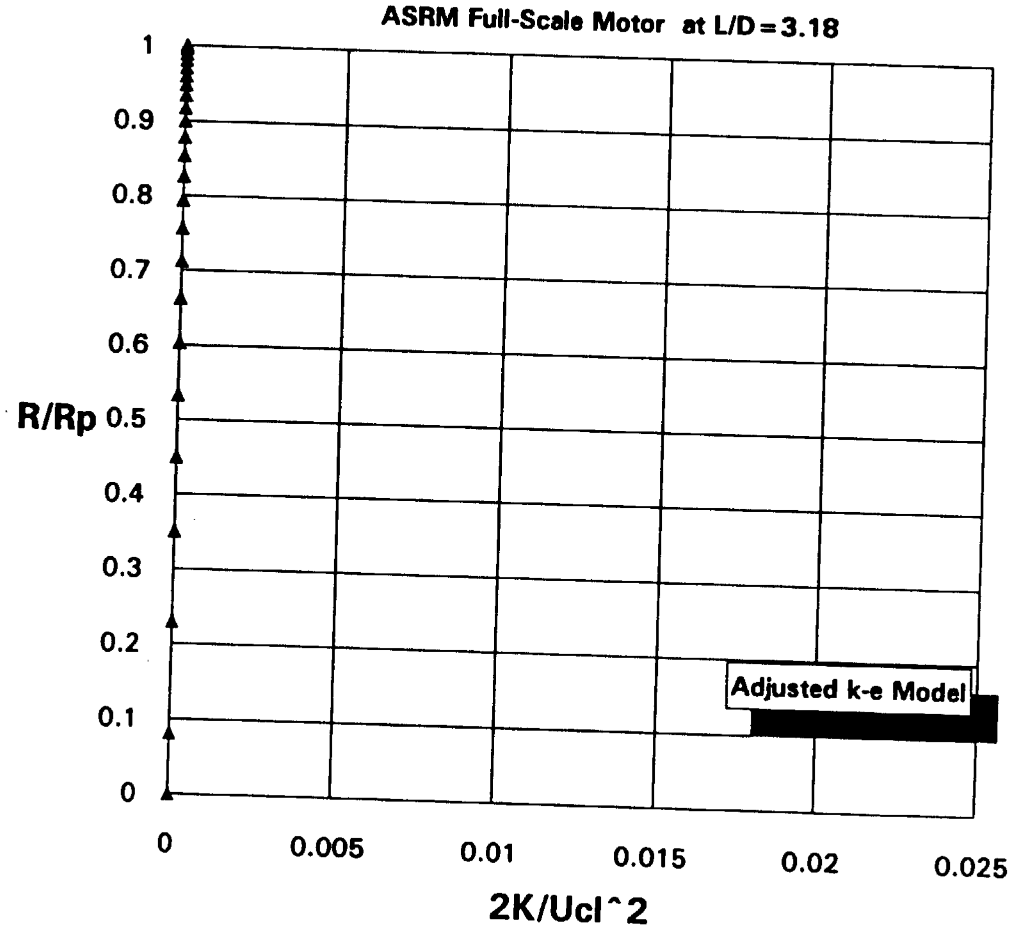

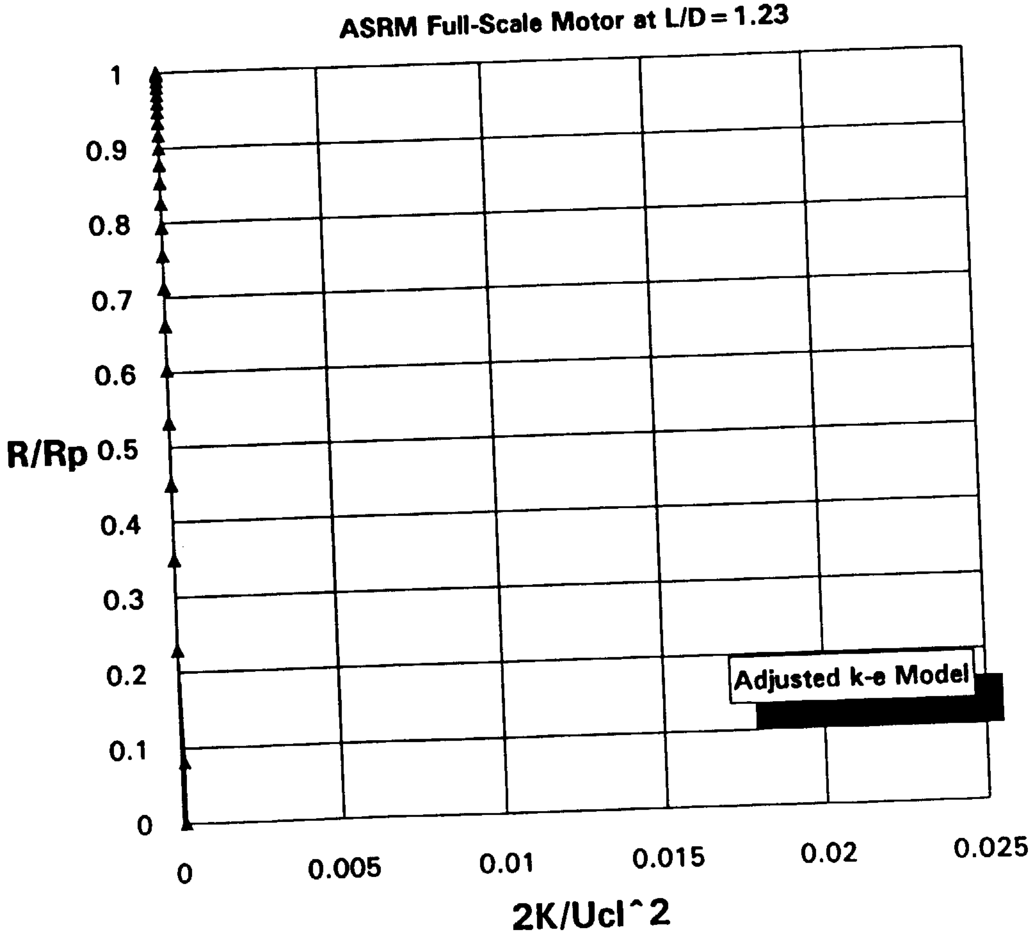

Figure 52. Normalized Kinetic Energy

Figure 51. Normalized Kinetic Energy

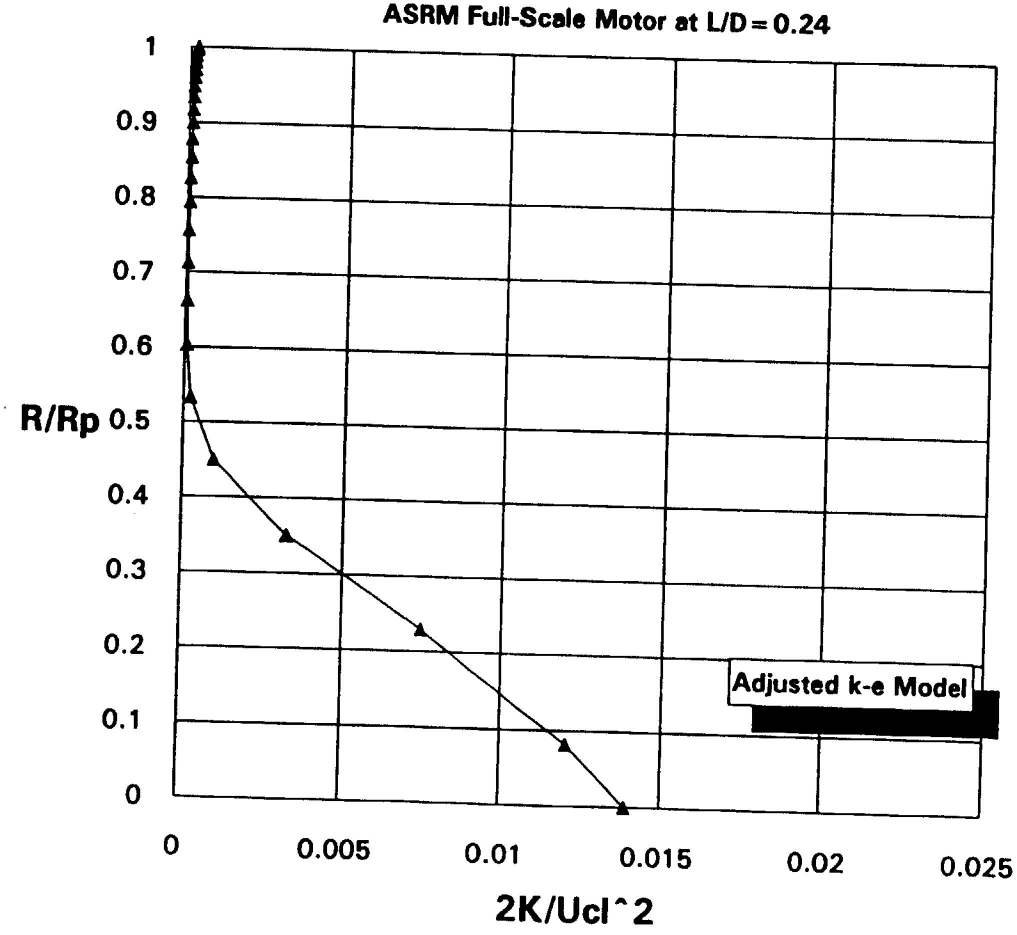

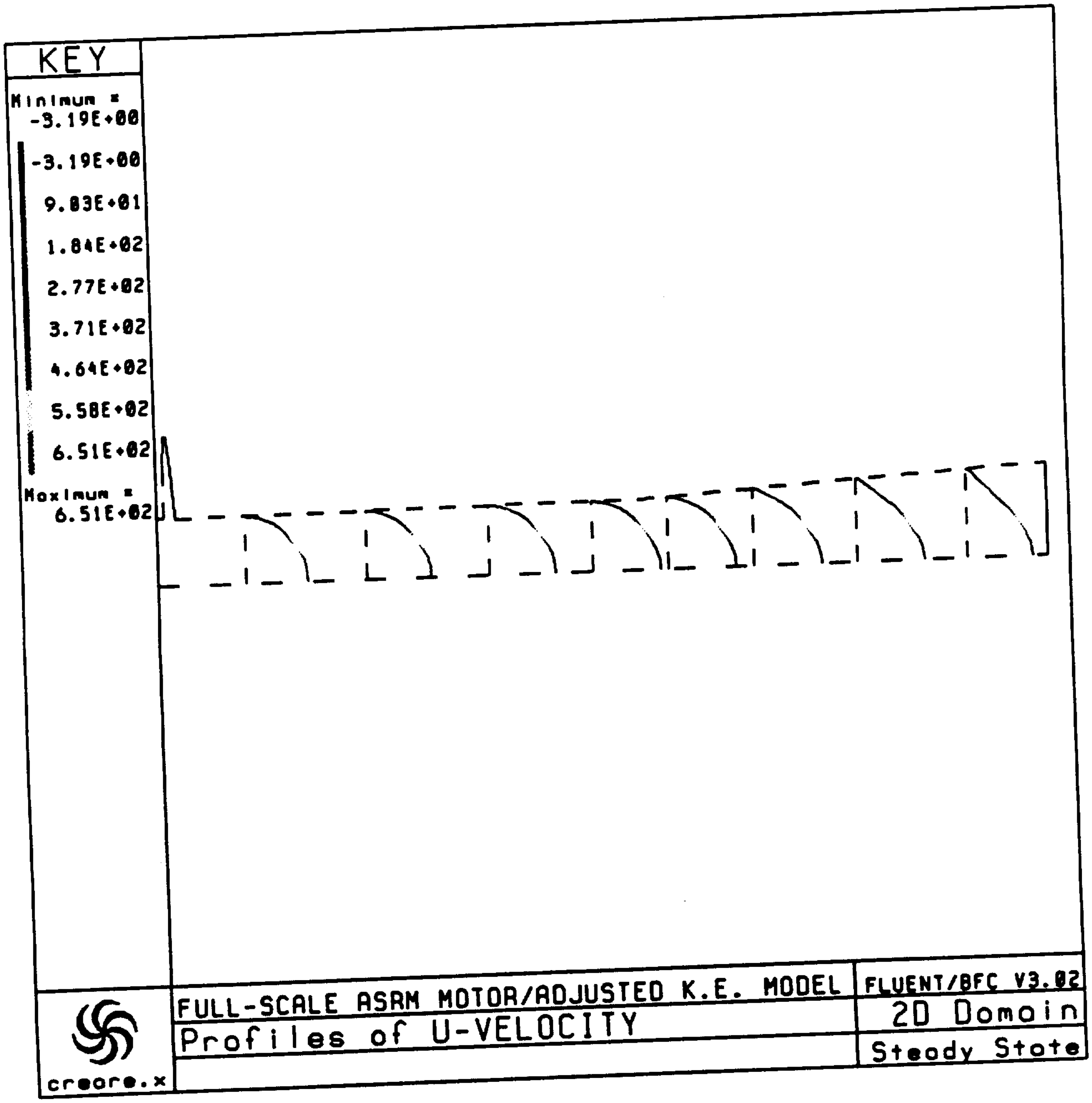

Figure 50. U-Velocity Profiles in the Aft Section of the Motor, AKE Model

Figure 49. ASRM Full-Scale Motor Velocity Profiles

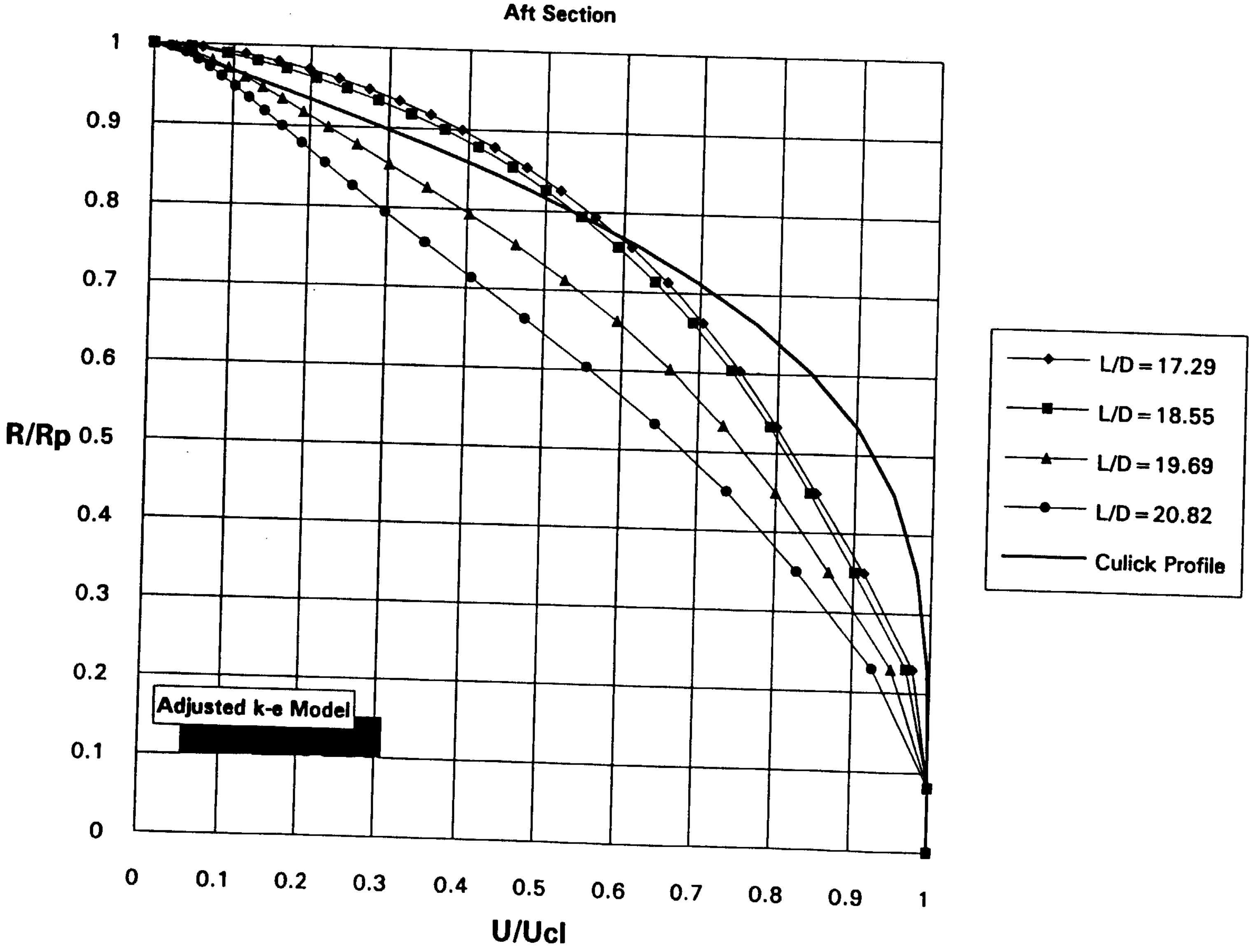

ERCI 08/13/92

Figure 48. ASRM Full-Scale Motor Velocity Profiles

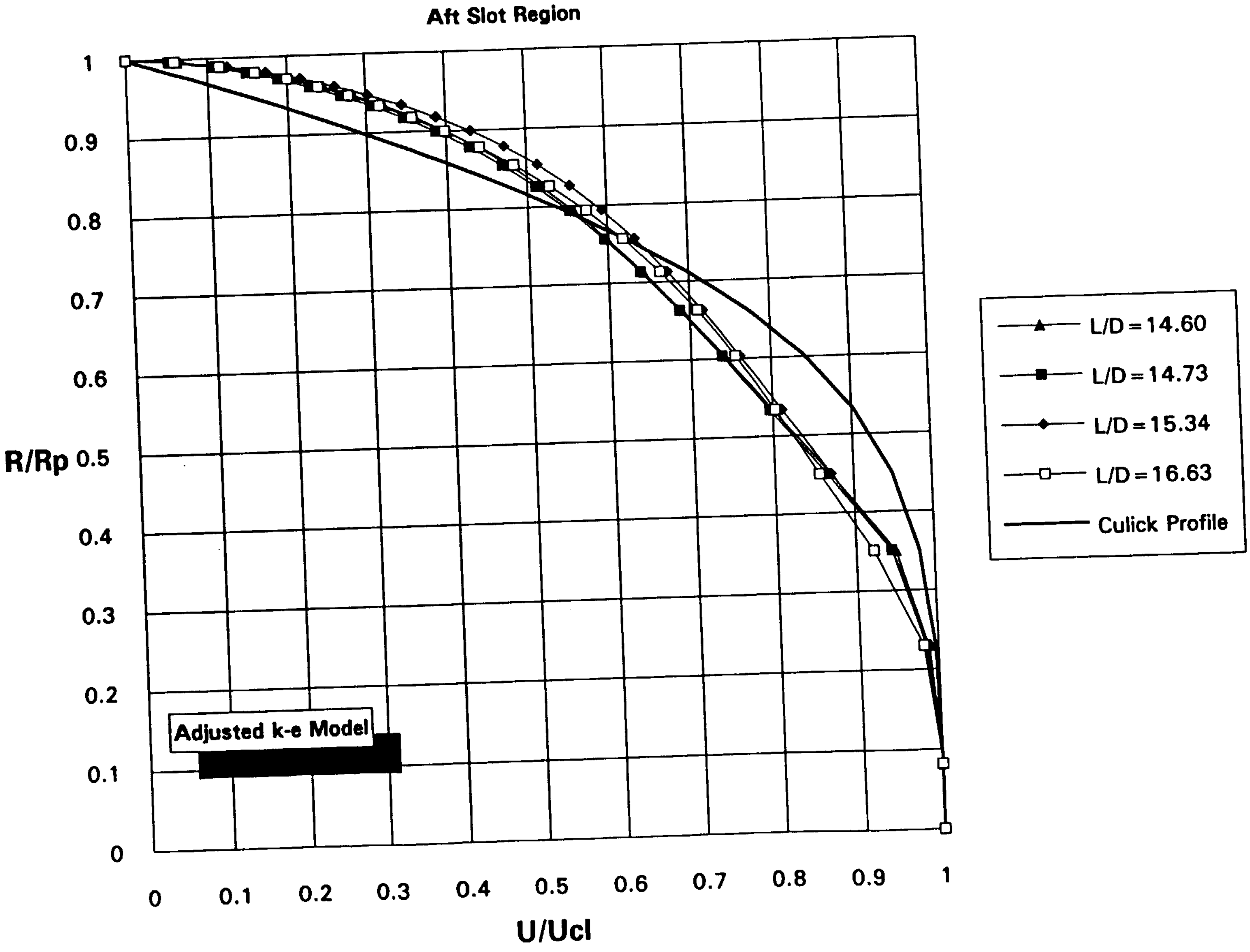

ERCI 08/13/92

Figure 47. ASRM Full-Scale Motor Velocity Profiles

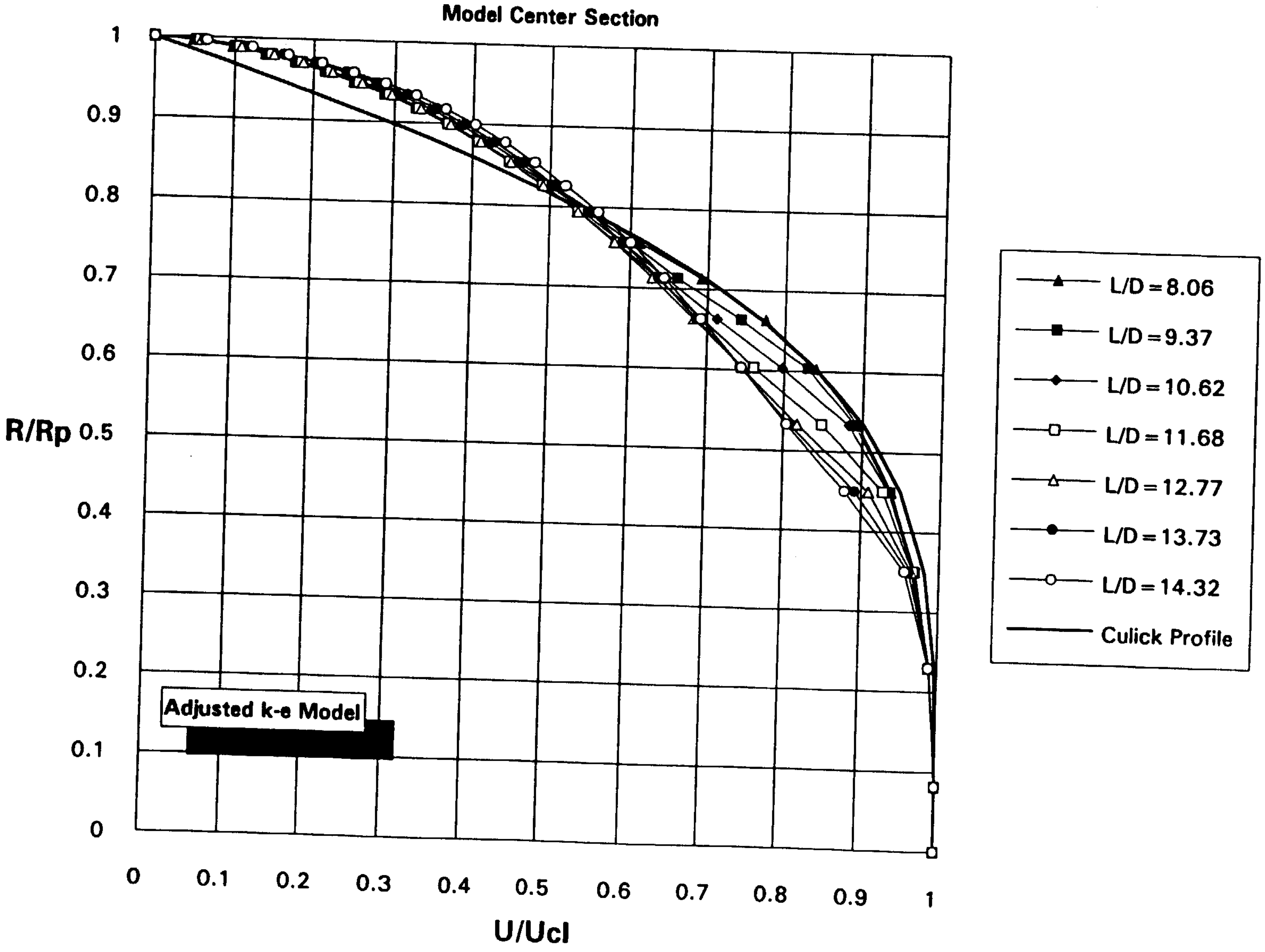

ERCI 08/13/92

Figure 46. ASRM Full-Scale Motor Velocity Profiles

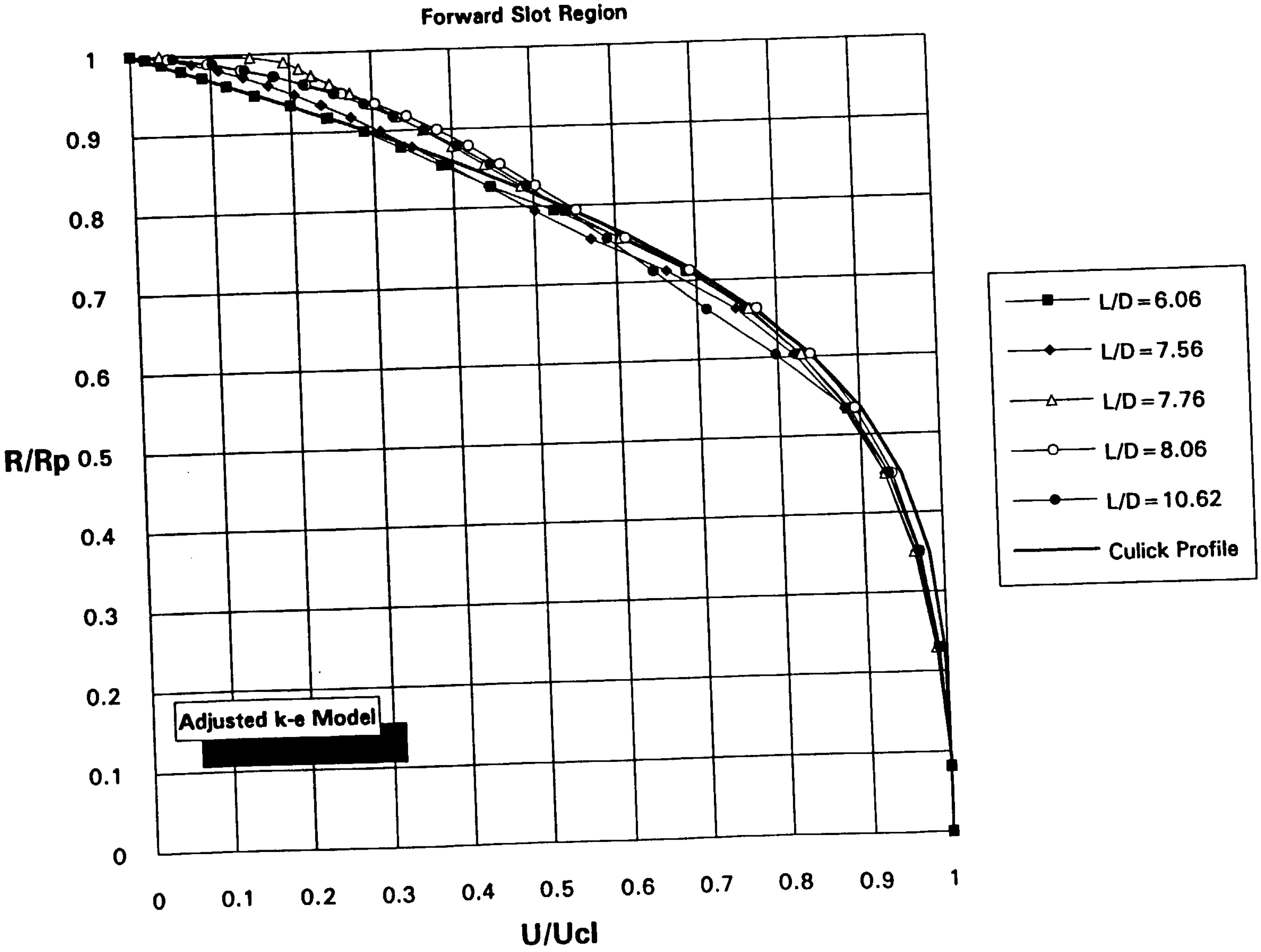

ERCI 08/13/92

Figure 45. ASRM Full-Scale Motor Velocity Profiles

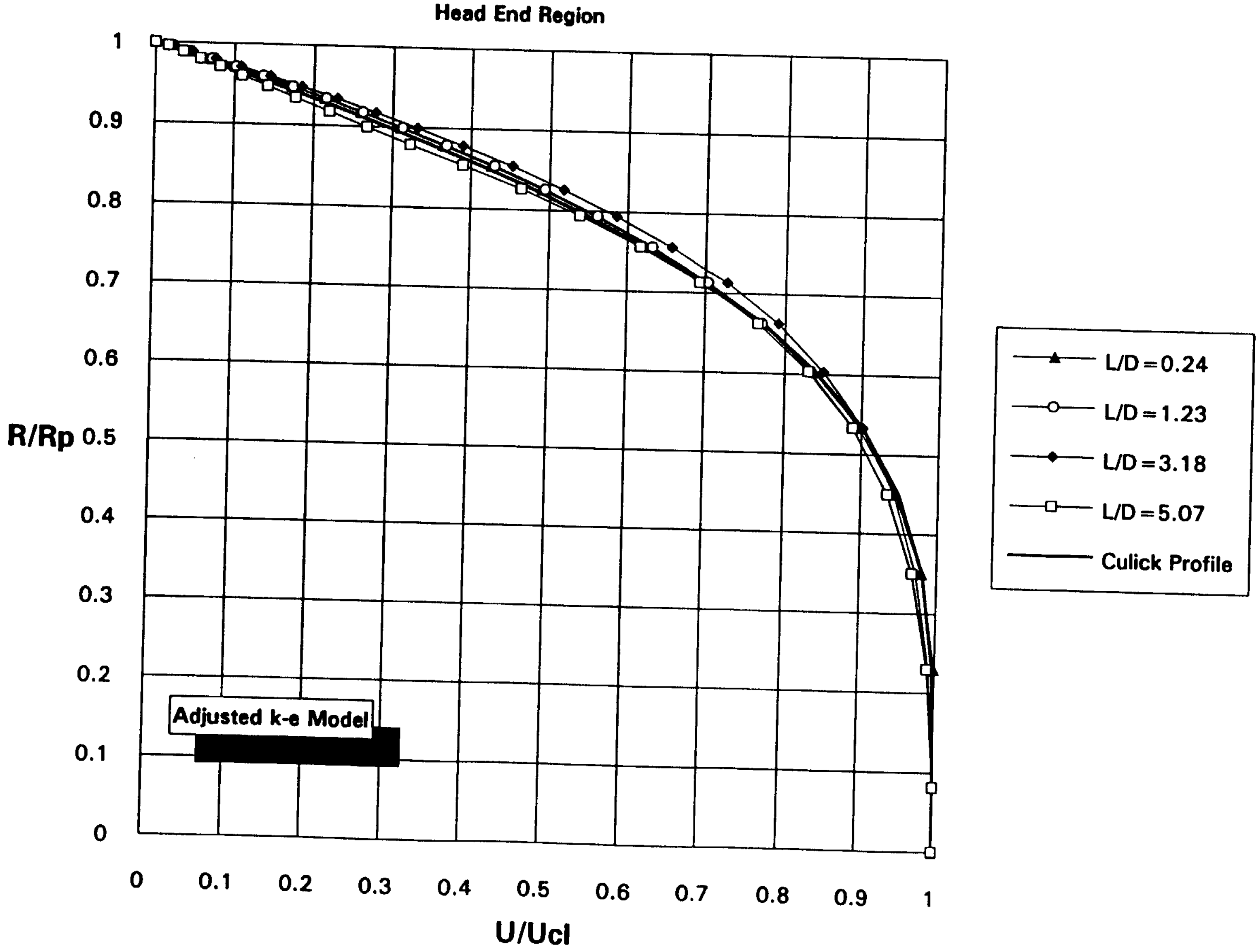

ERCI 08/13/92

Figure 44. ASRM Full-Scale Motor Velocity Profiles

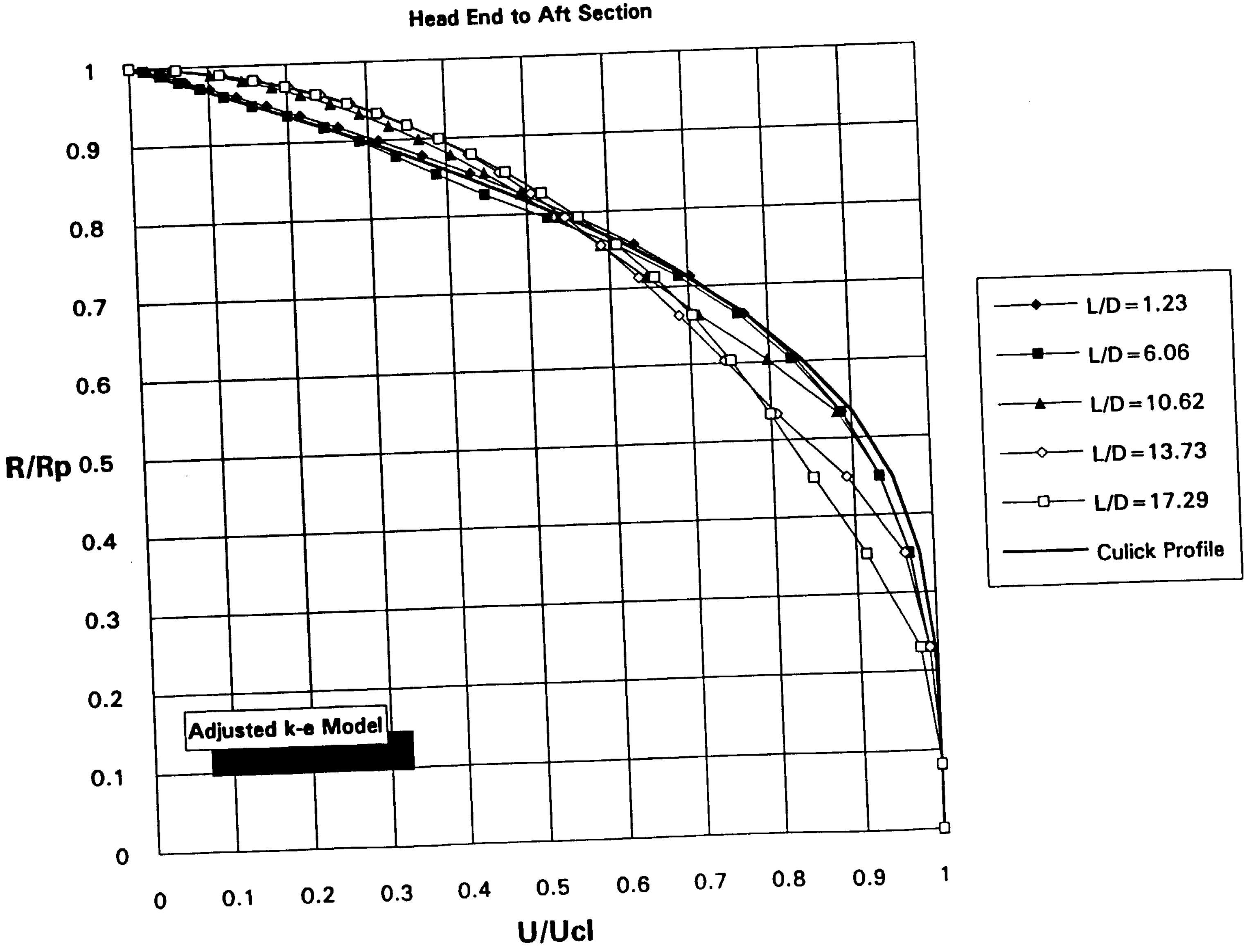

ERCI 08/13/92

Figure 43. Normalized Kinetic Energy

ASRM Full-Scale Motor at L/D=20.82

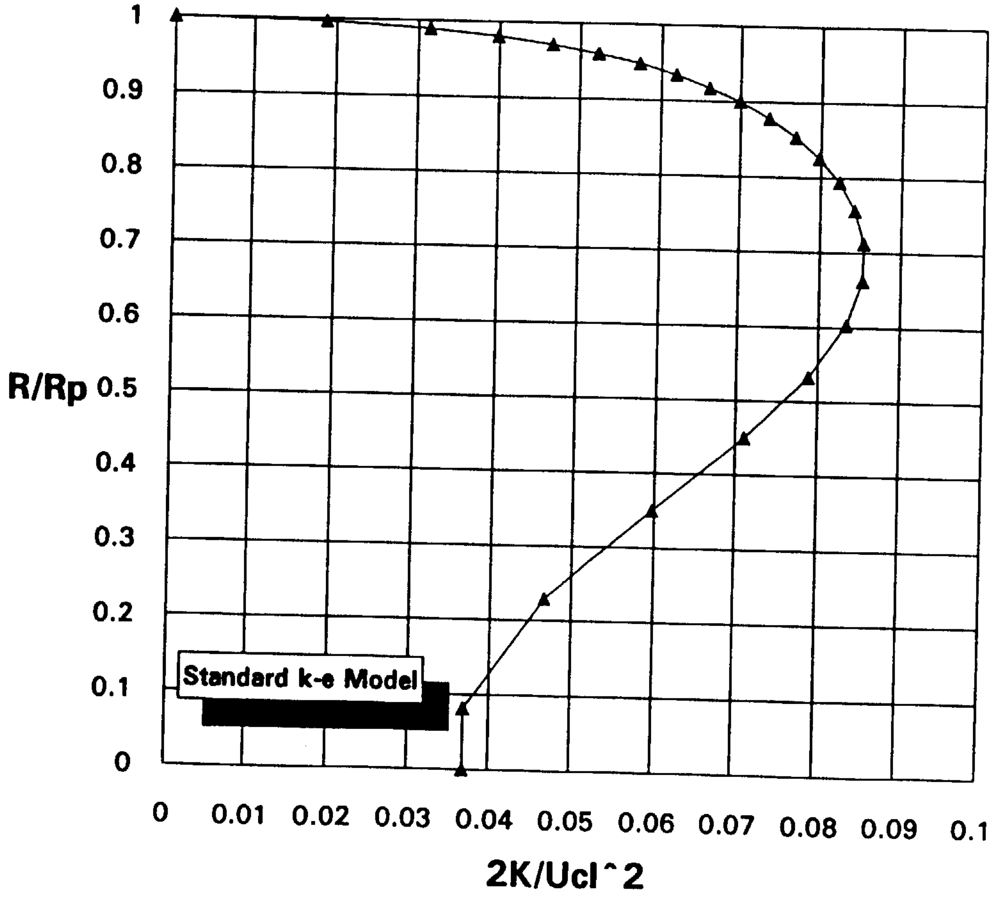

Figure 42. Normalized Kinetic Energy

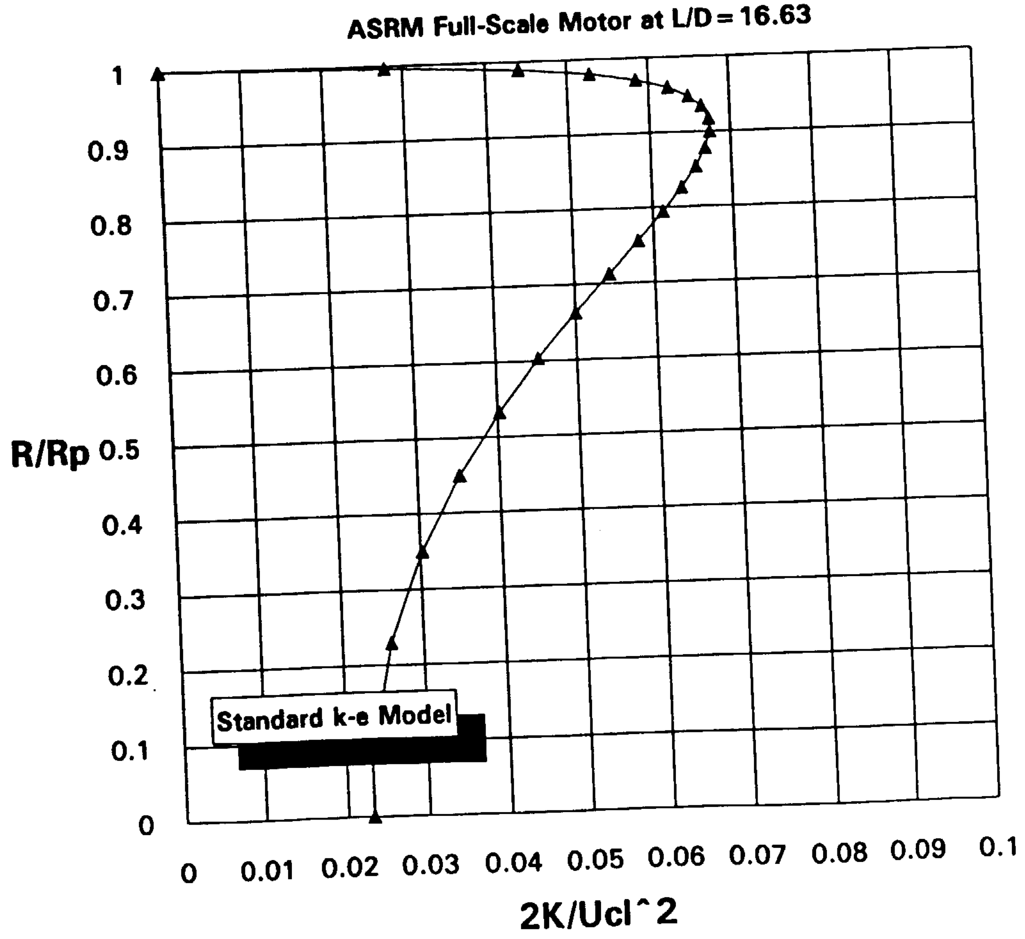

Figure 41. Normalized Kinetic Energy

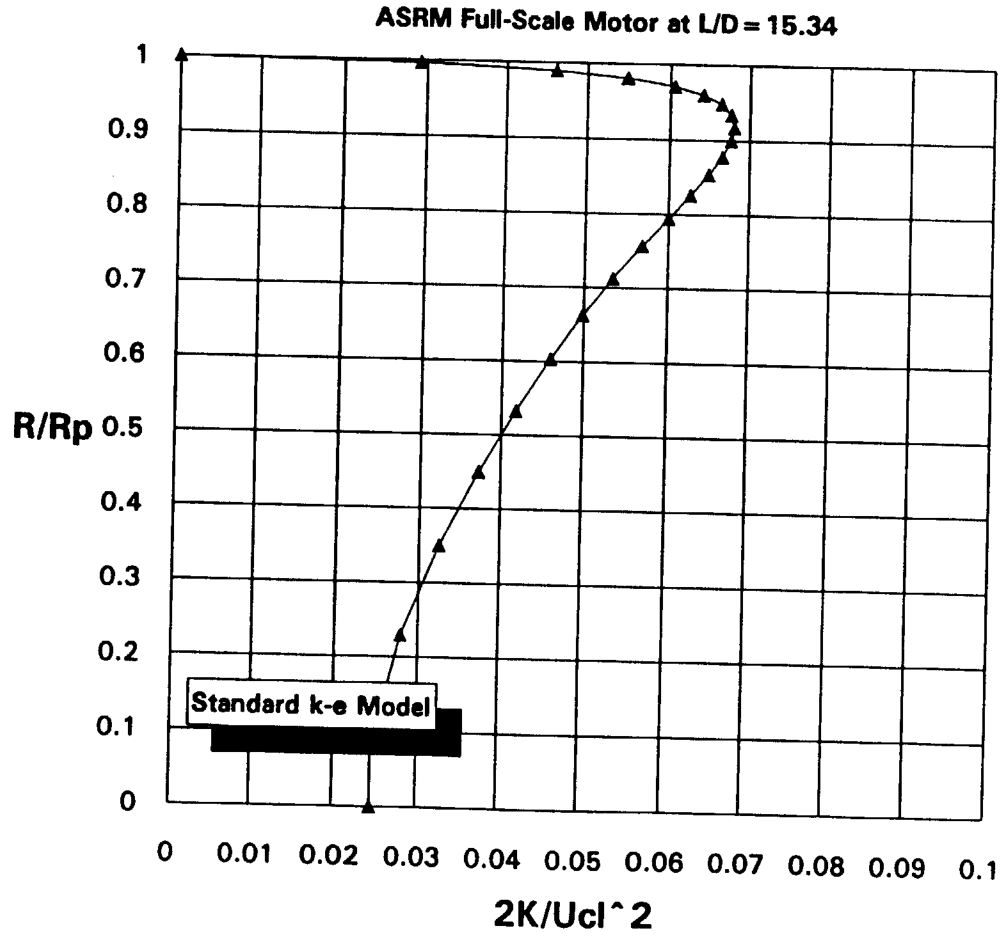

Figure 40. Normalized Kinetic Energy

ASRM Full-Scale Motor at L/D = 14.6

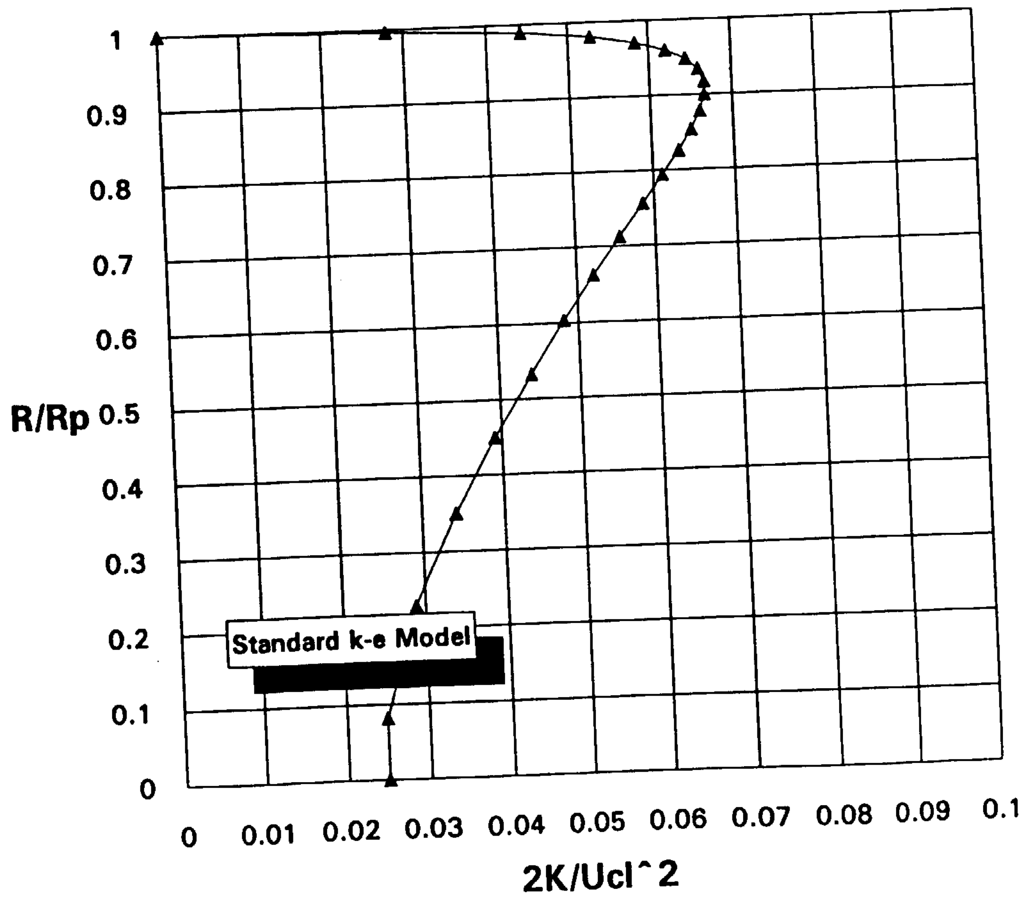

Figure 39. Normalized Kinetic Energy

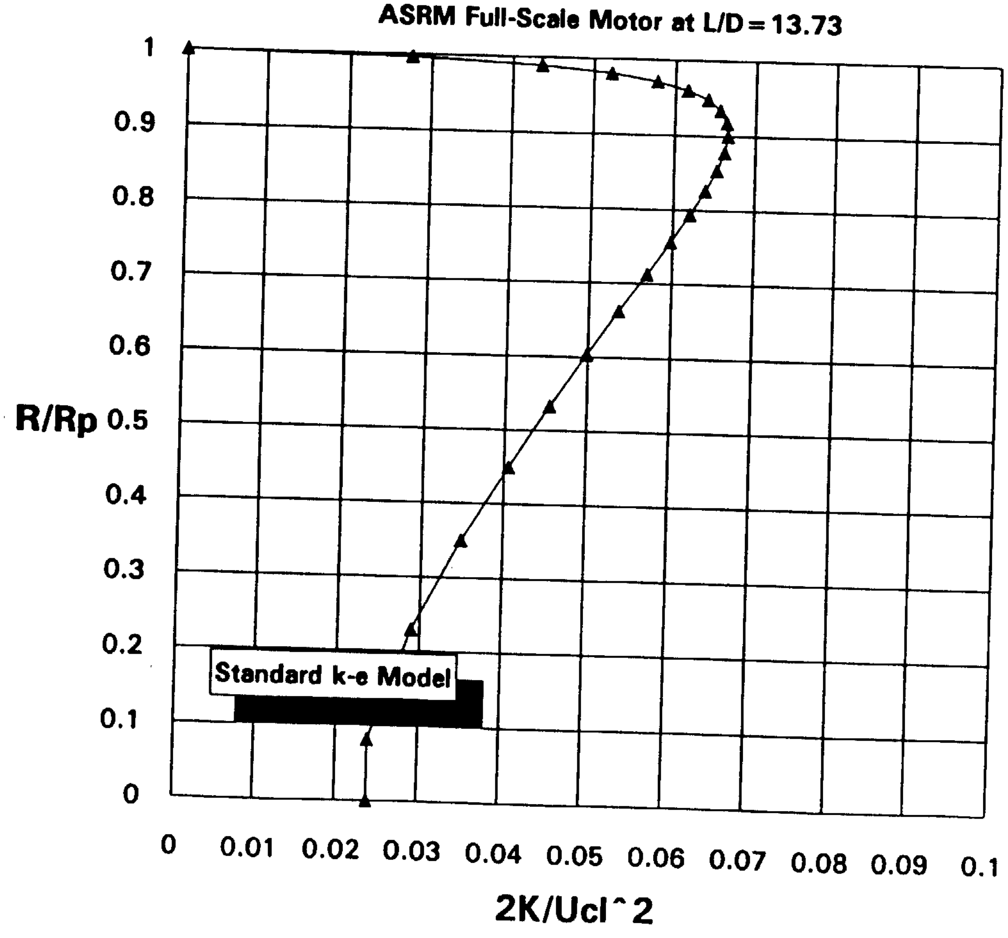

Figure 38. Normalized Kinetic Energy

ASRM Full-Scale Motor at L/D = 11.68

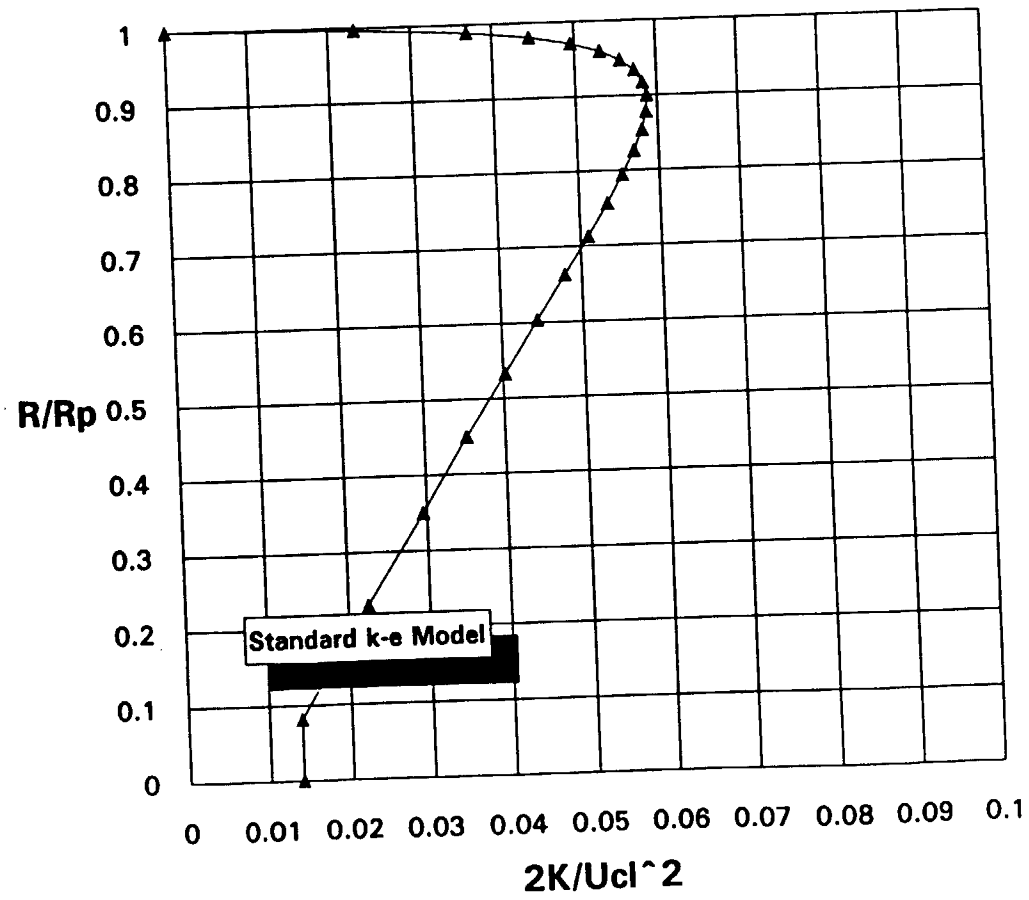

Figure 37. Normalized Kinetic Energy

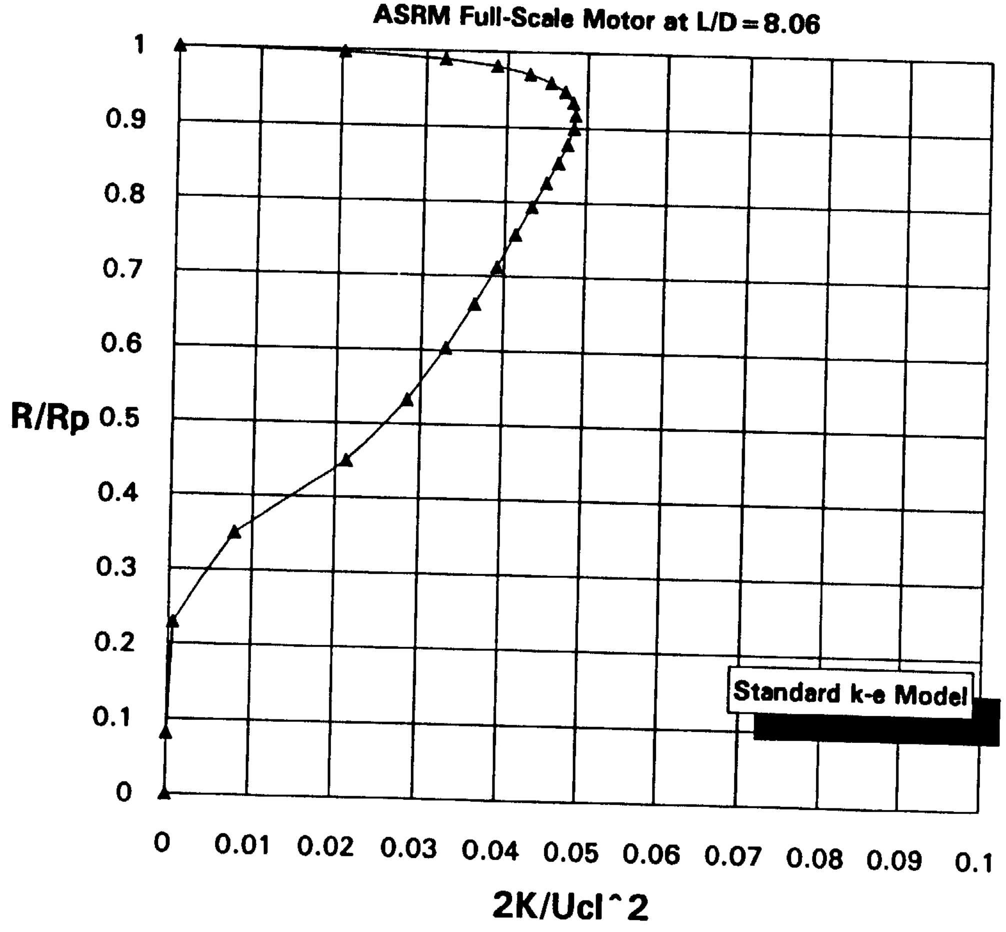

Figure 36. Normalized Kinetic Energy

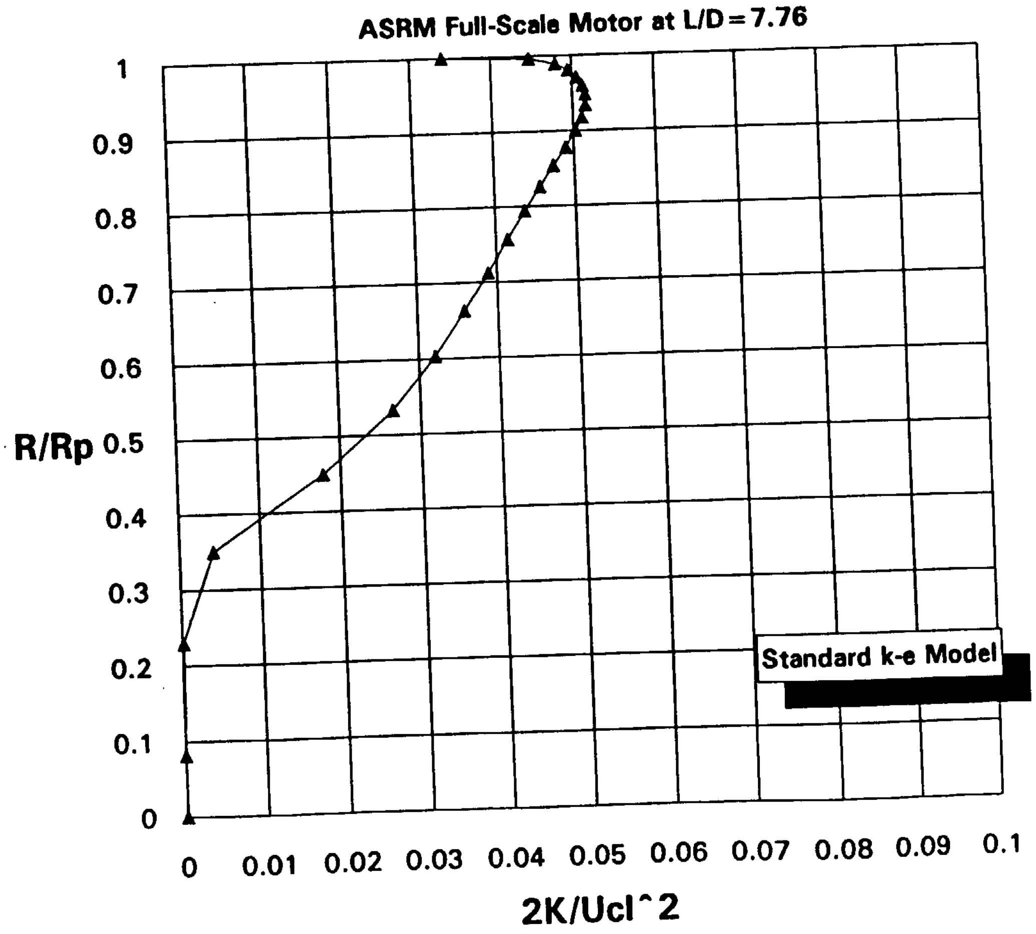

Figure 35. Normalized Kinetic Energy

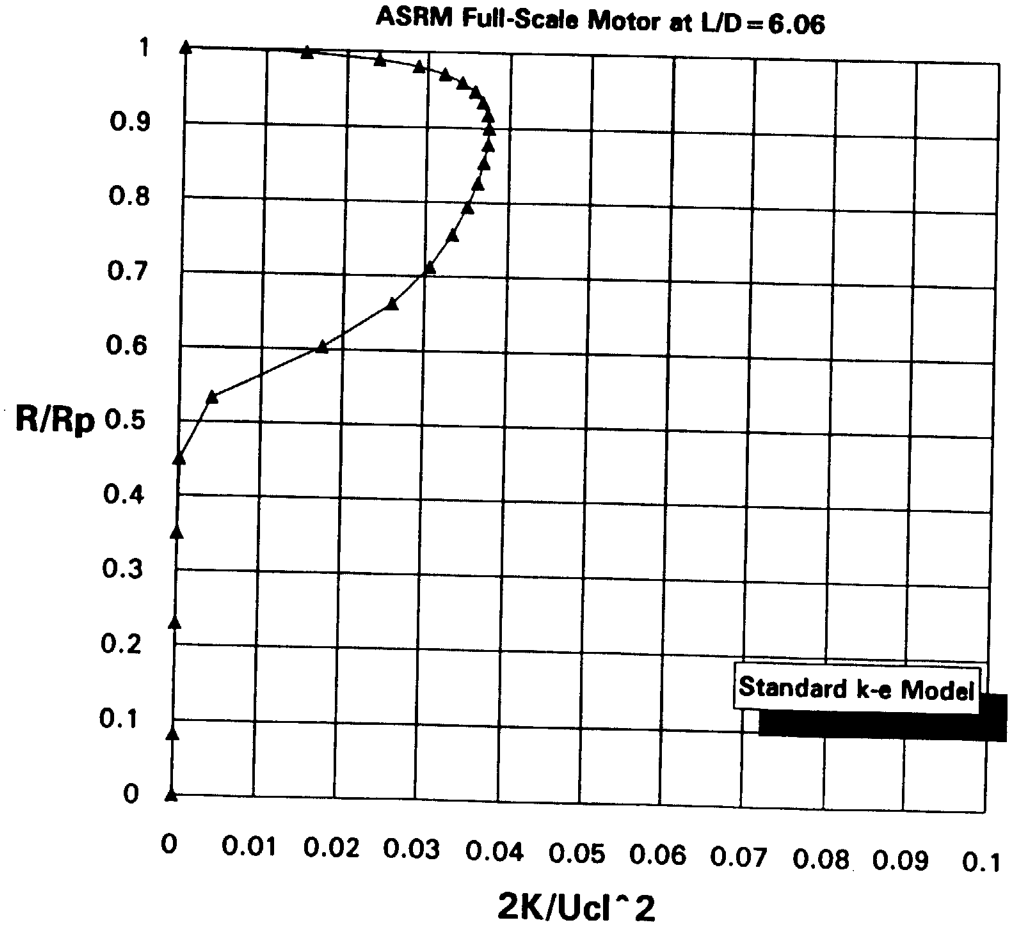

Figure 34. Normalized Kinetic Energy

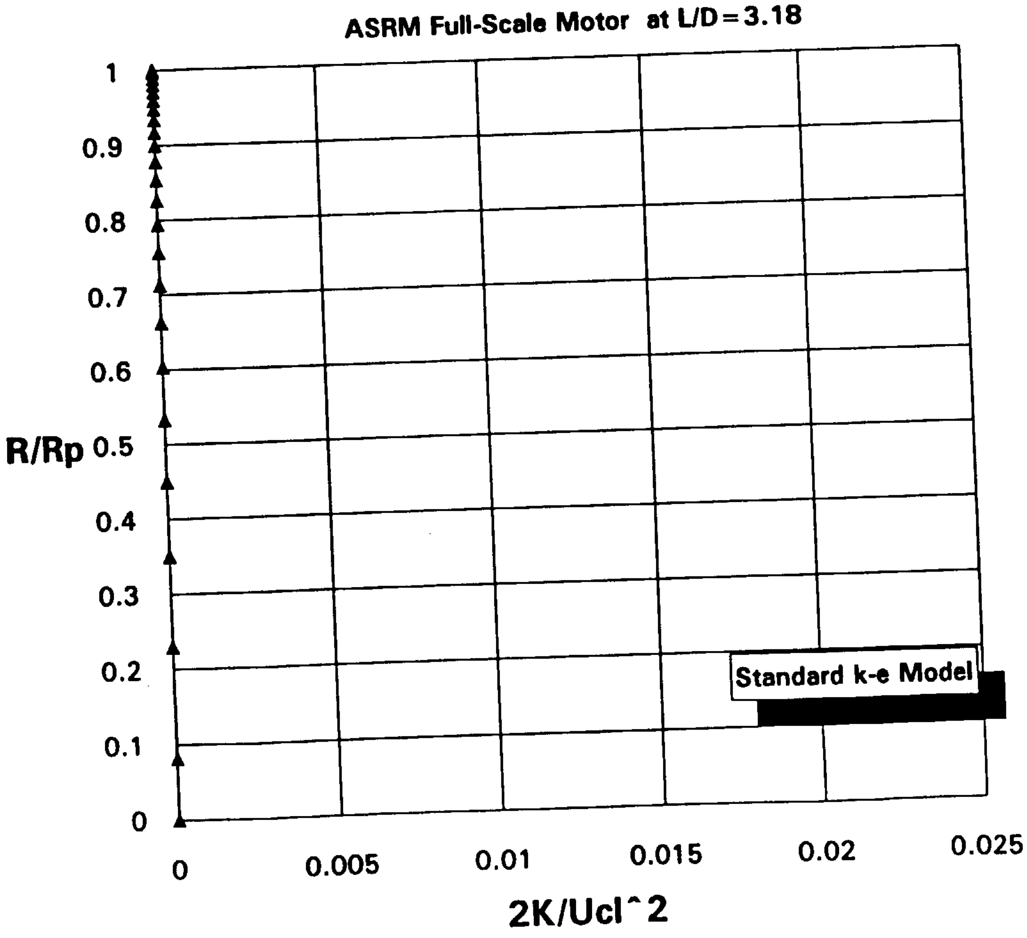

Figure 33. Normalized Kinetic Energy

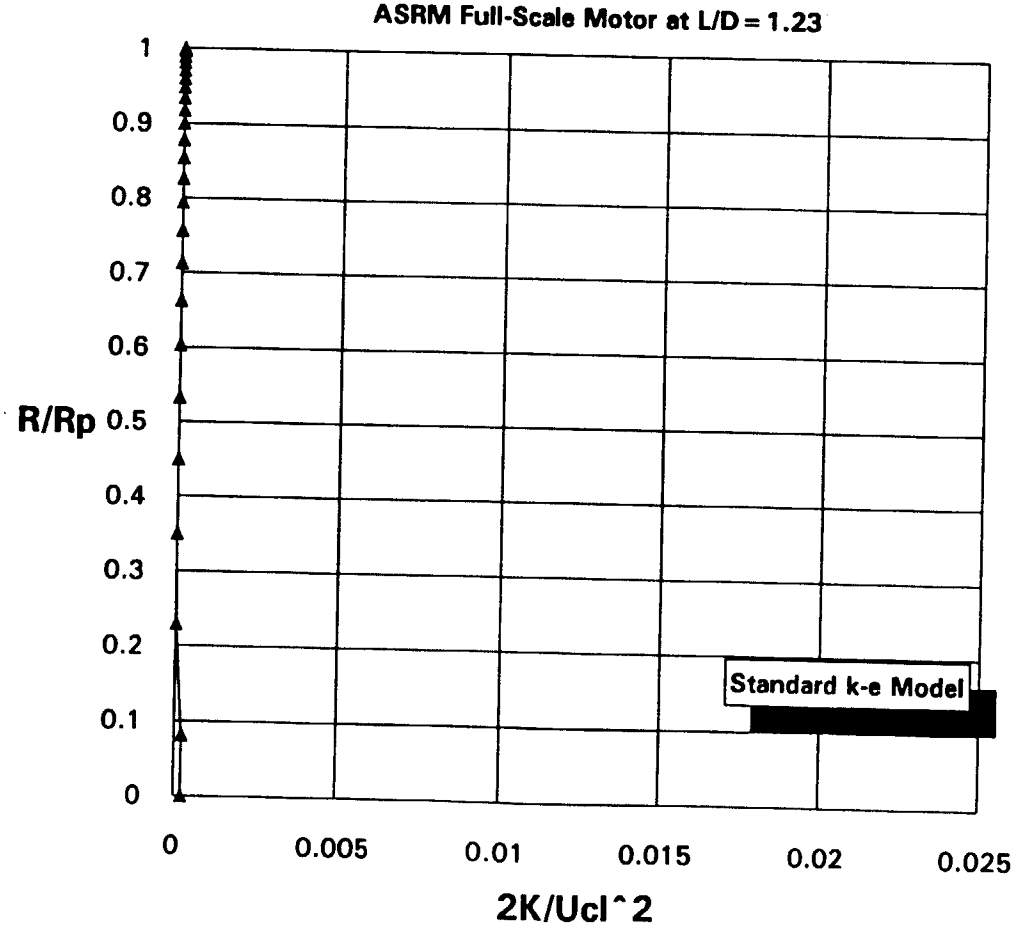

Figure 32. Normalized Kinetic Energy

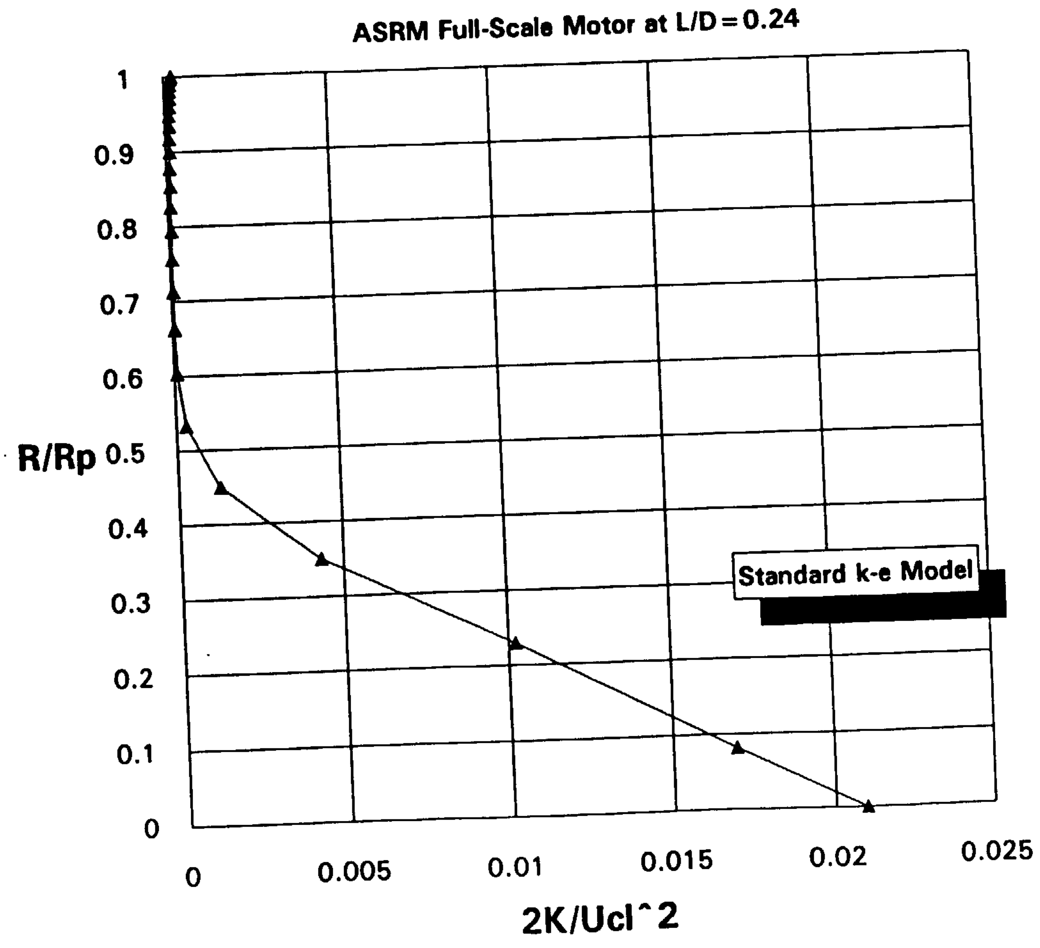

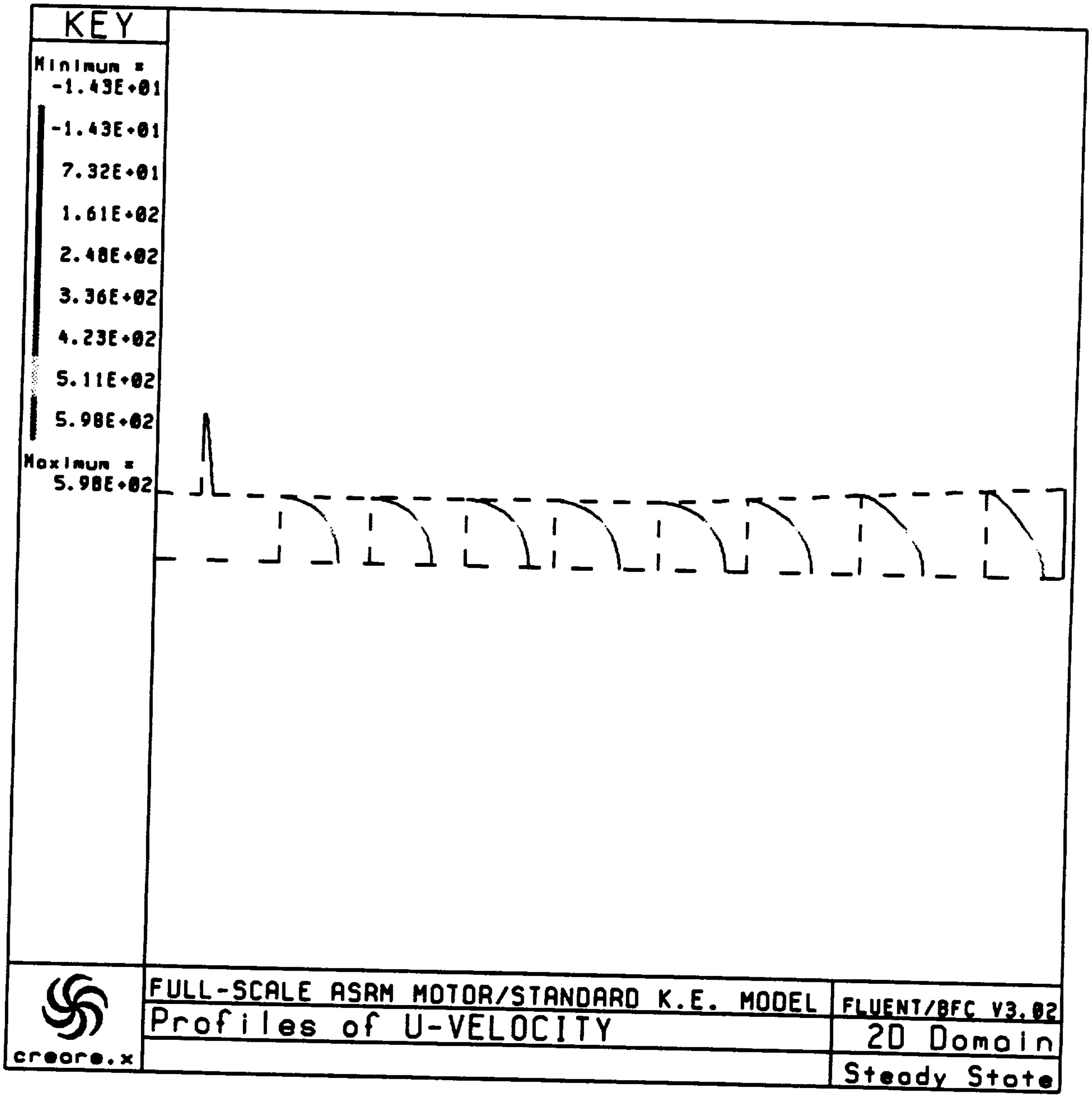

Figure 31. U-Velocity Profiles in the Aft Section of the Motor, SKE Model

Figure 30. ASRM Full-Scale Motor Velocity Profiles

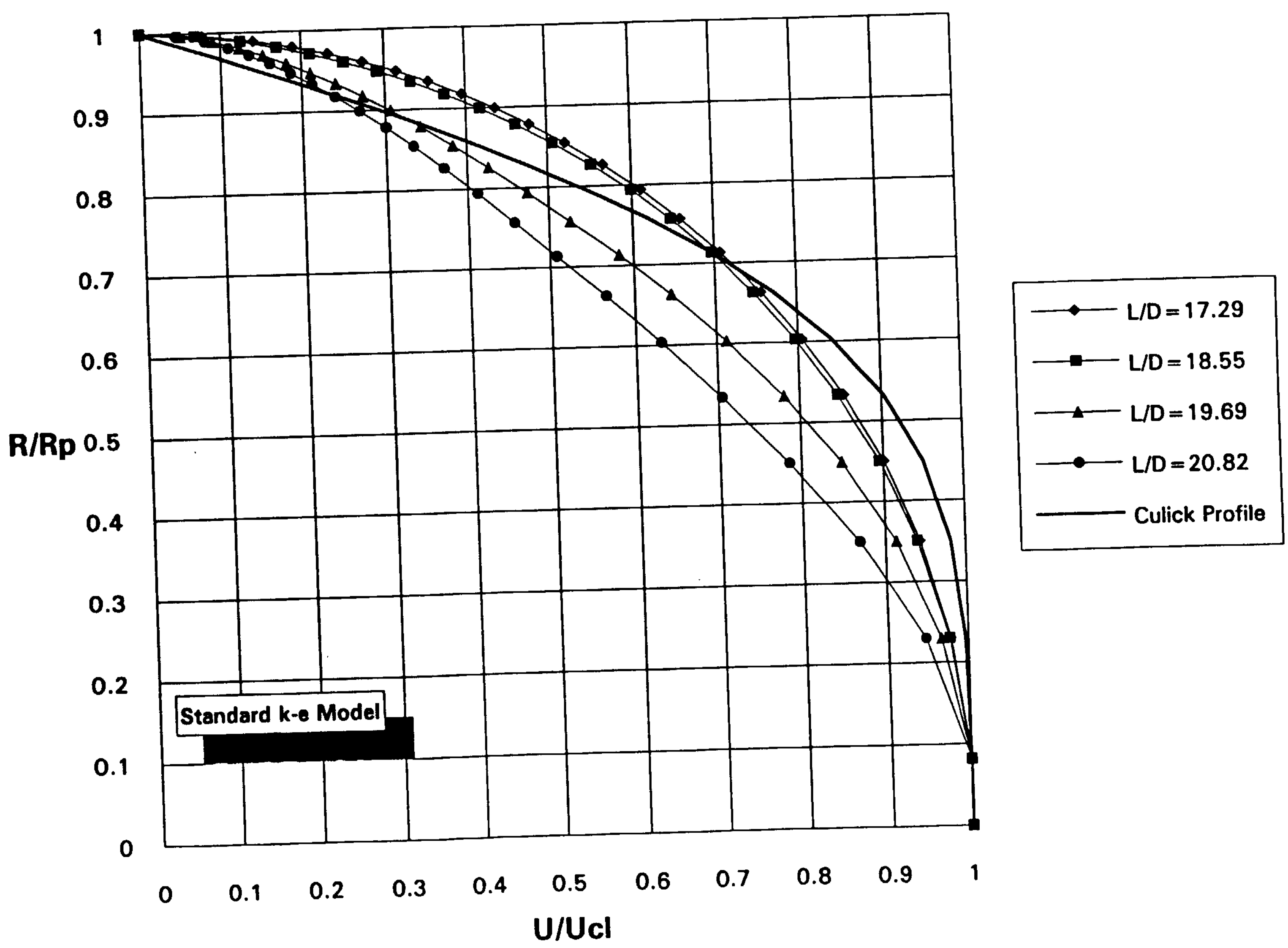

Aft Section

ERCI 08/13/92

Figure 29 ASRM Full-Scale Motor Velocity Profiles

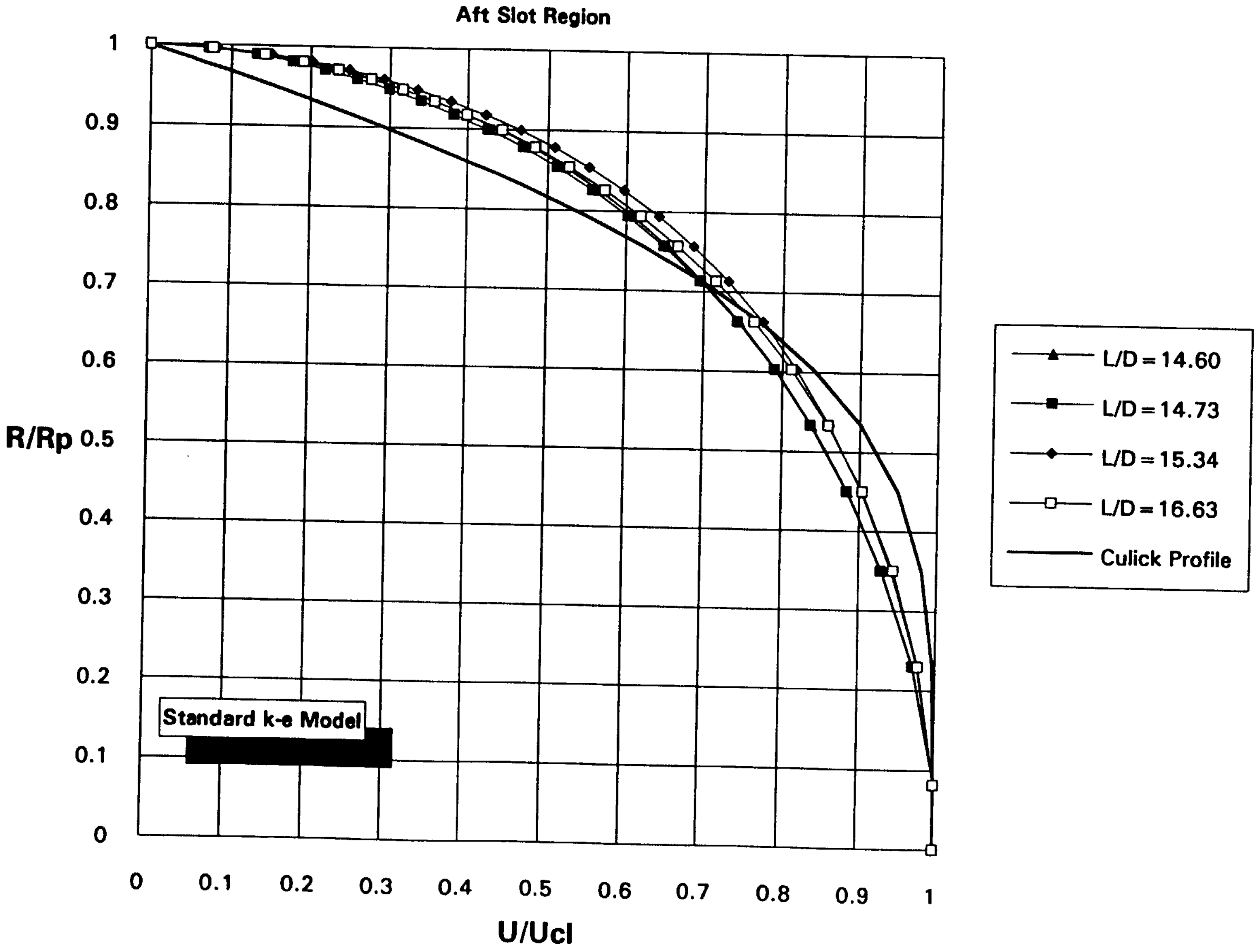

ERCI 08/13/92

Figure 16. Ring 5 Pressure Ratios

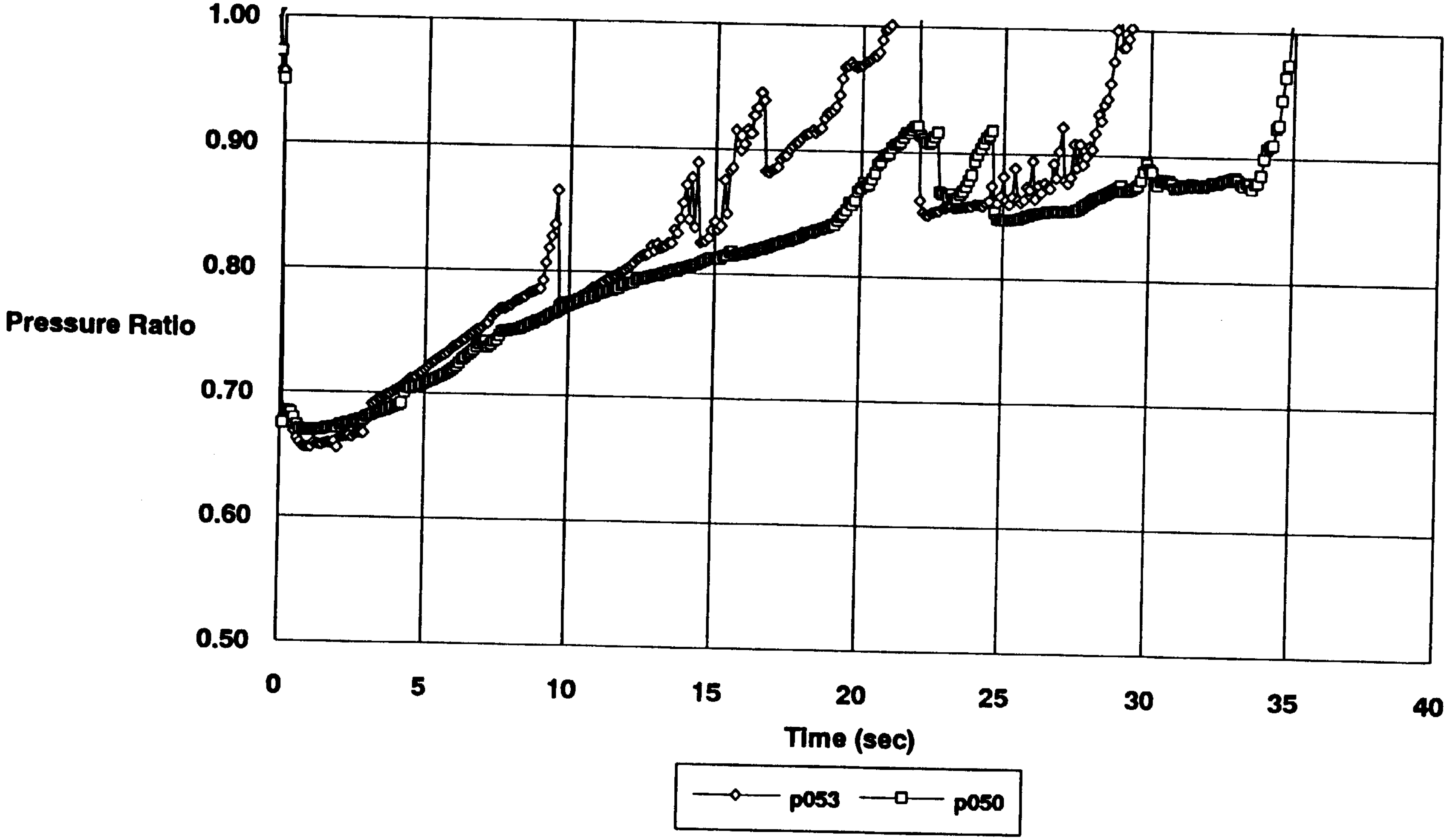

Figure 15. Ring 4 Pressure Ratios

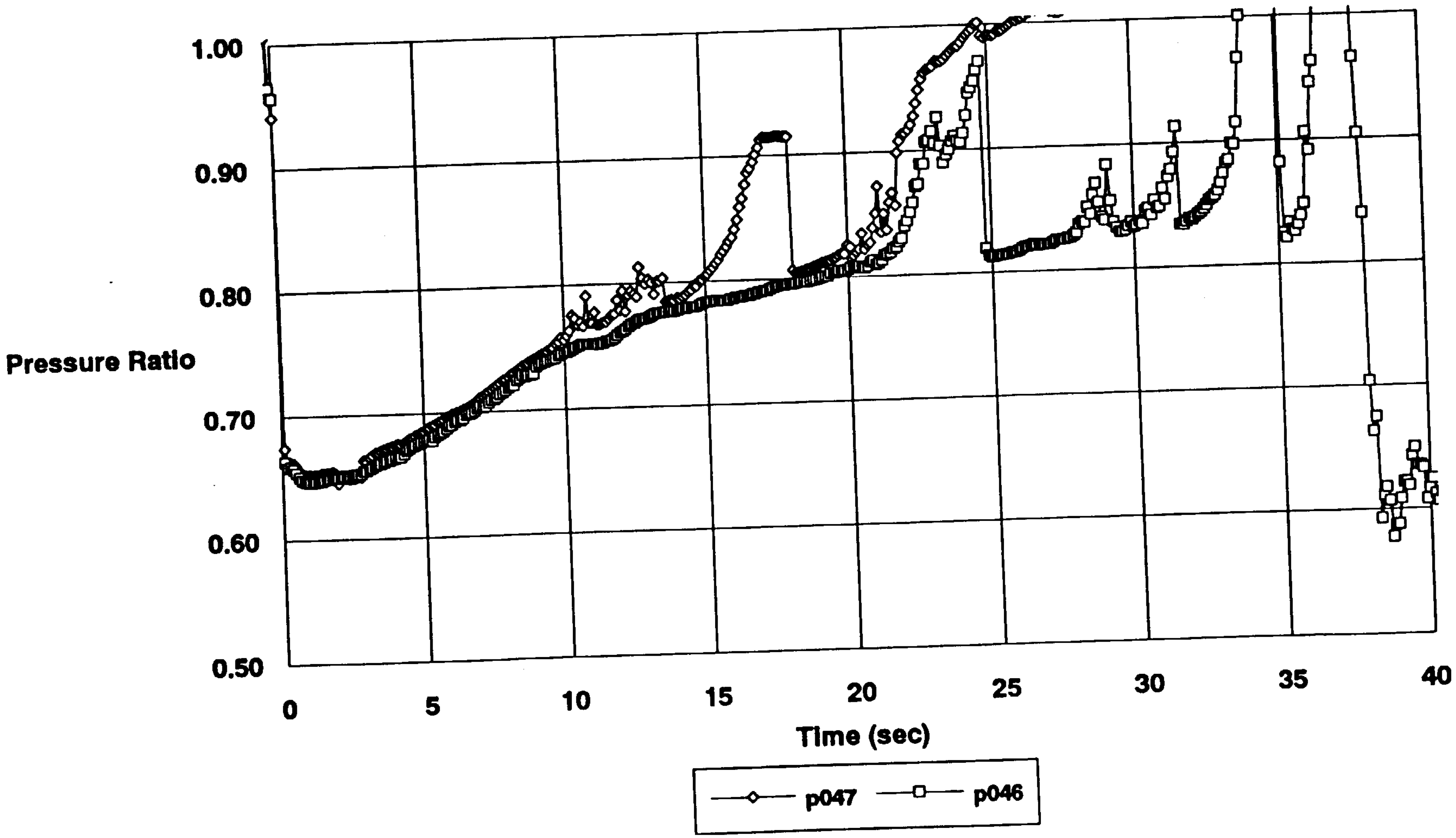

Figure 14. Ring 3 CFD Adjusted Pressure Ratios

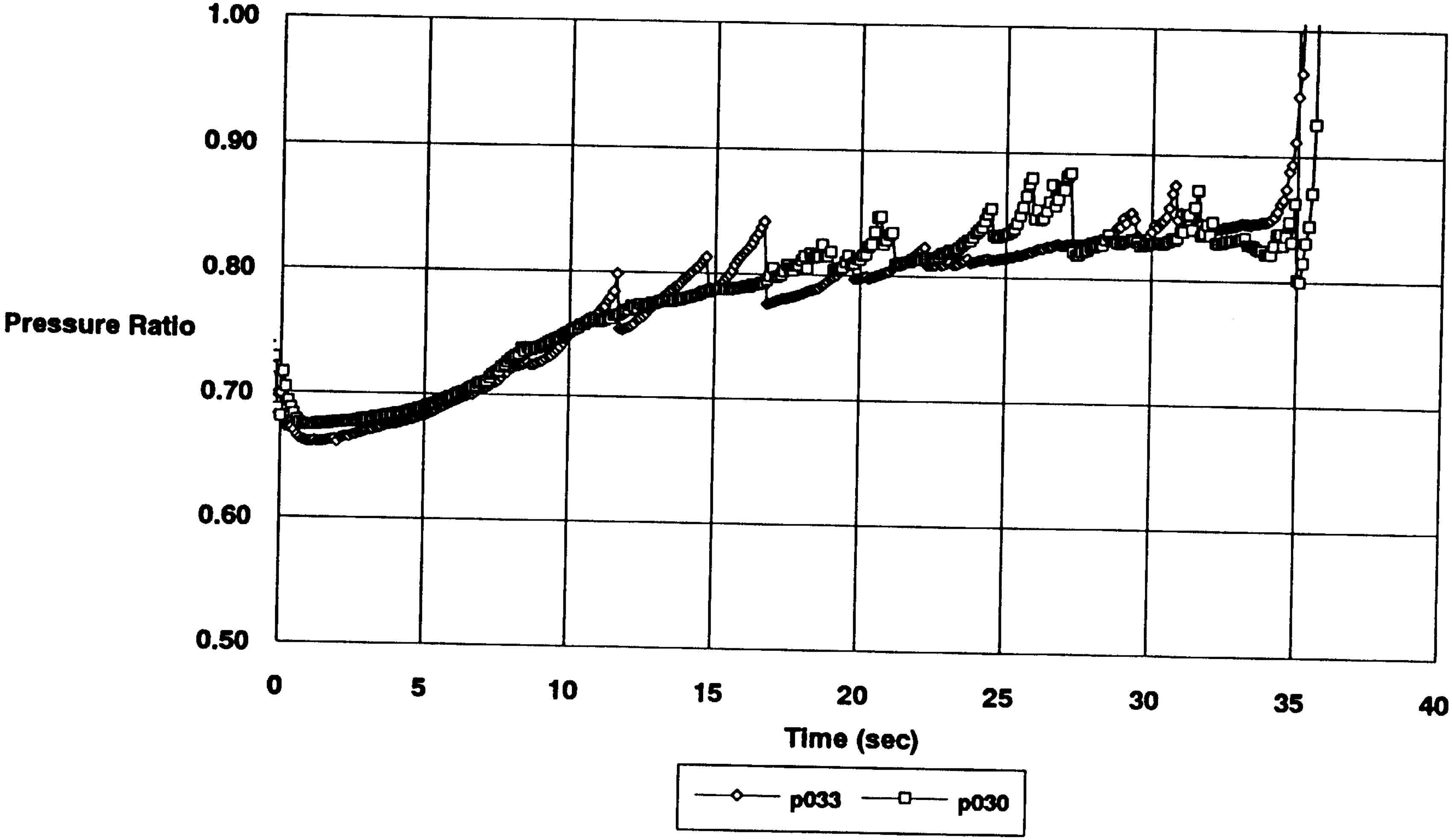

Figure 13. Ring 2 CFD-Adjusted Pressure Ratios

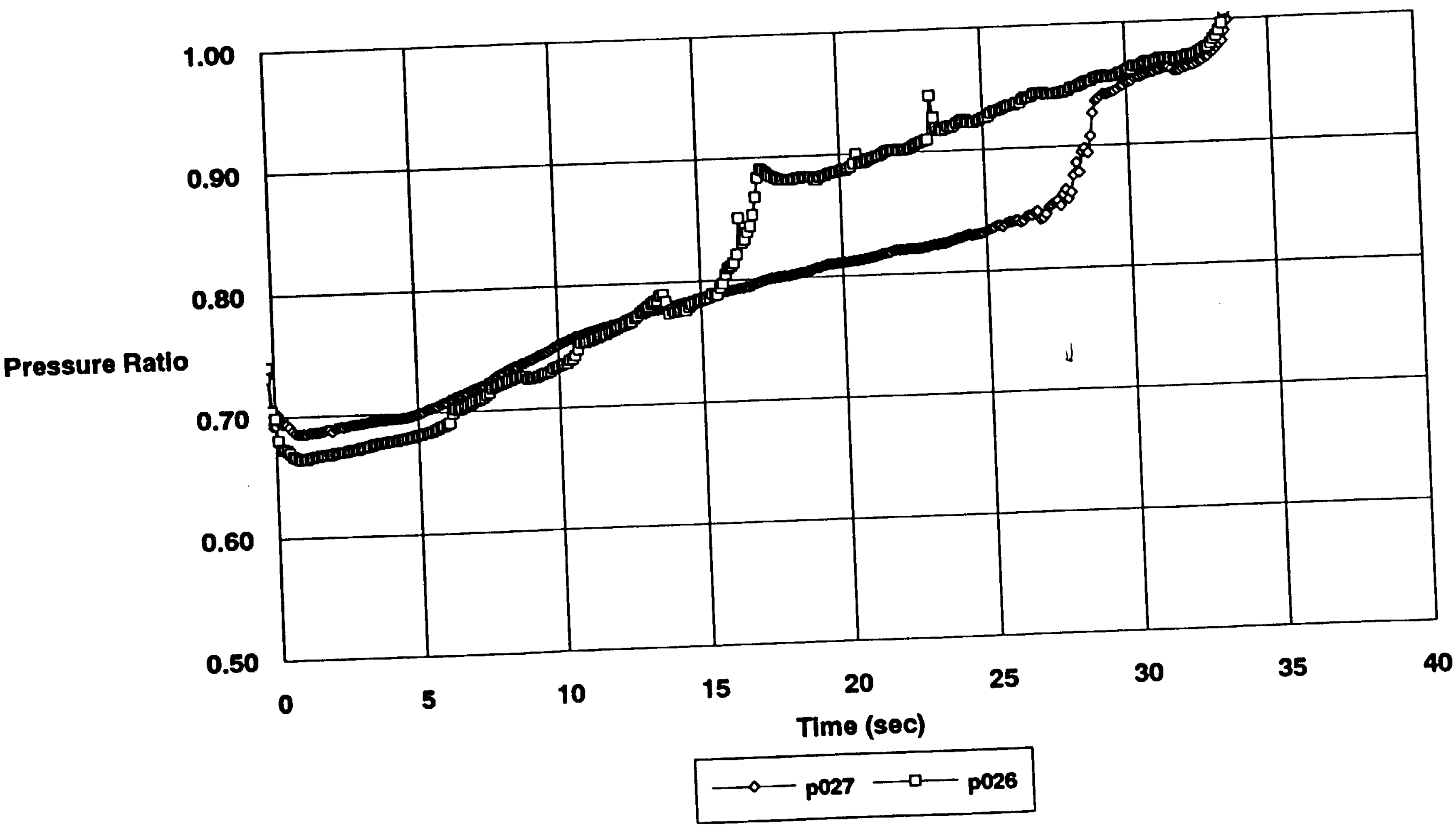

Figure 12. Ring 1 CFD-Adjusted Pressure Ratios

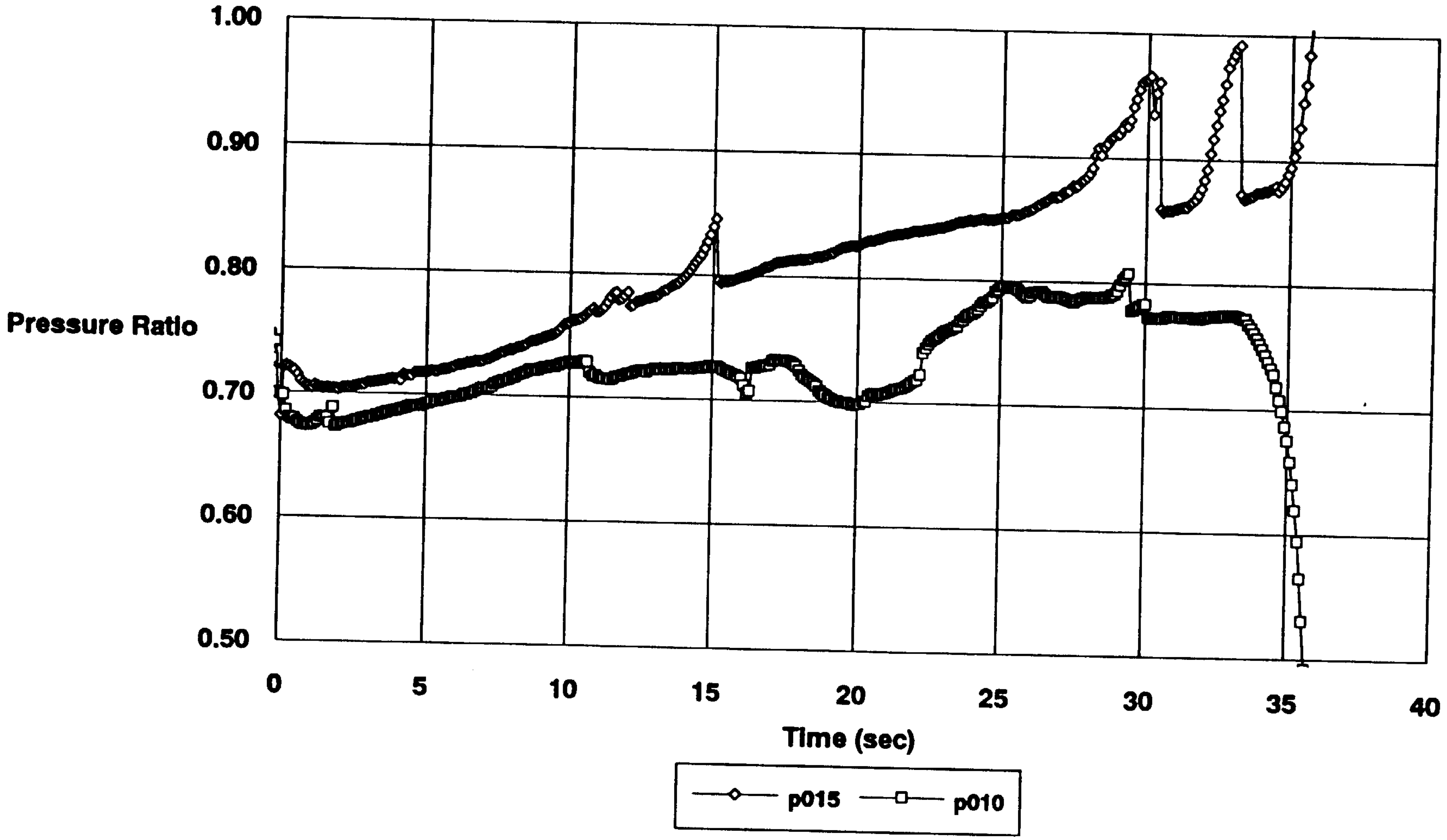

Figure 11. Ring 5 Pressures

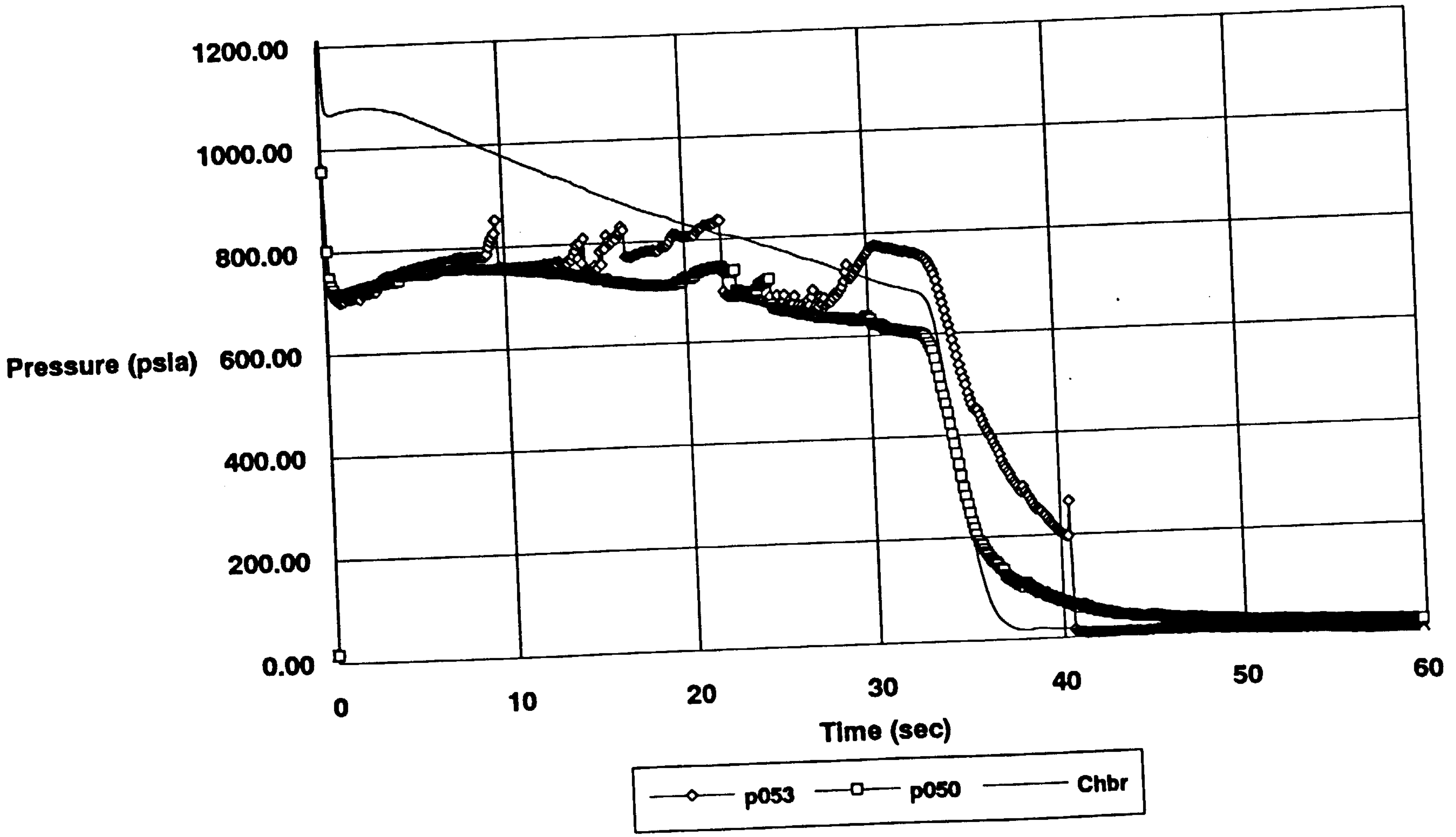

Figure 10. Ring 4 Pressures

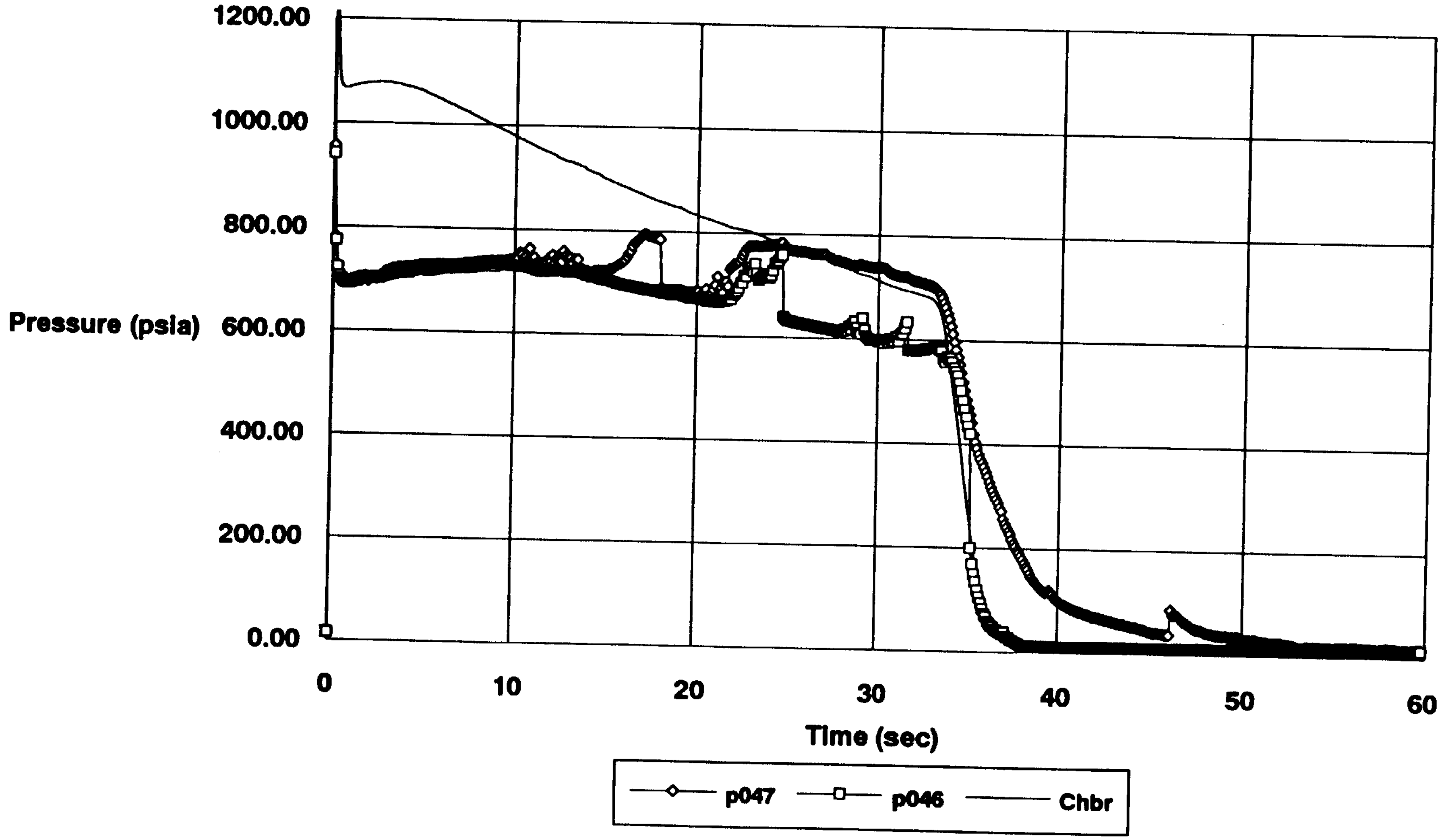

Figure 9. Ring 3 CFD-Adjusted Pressures

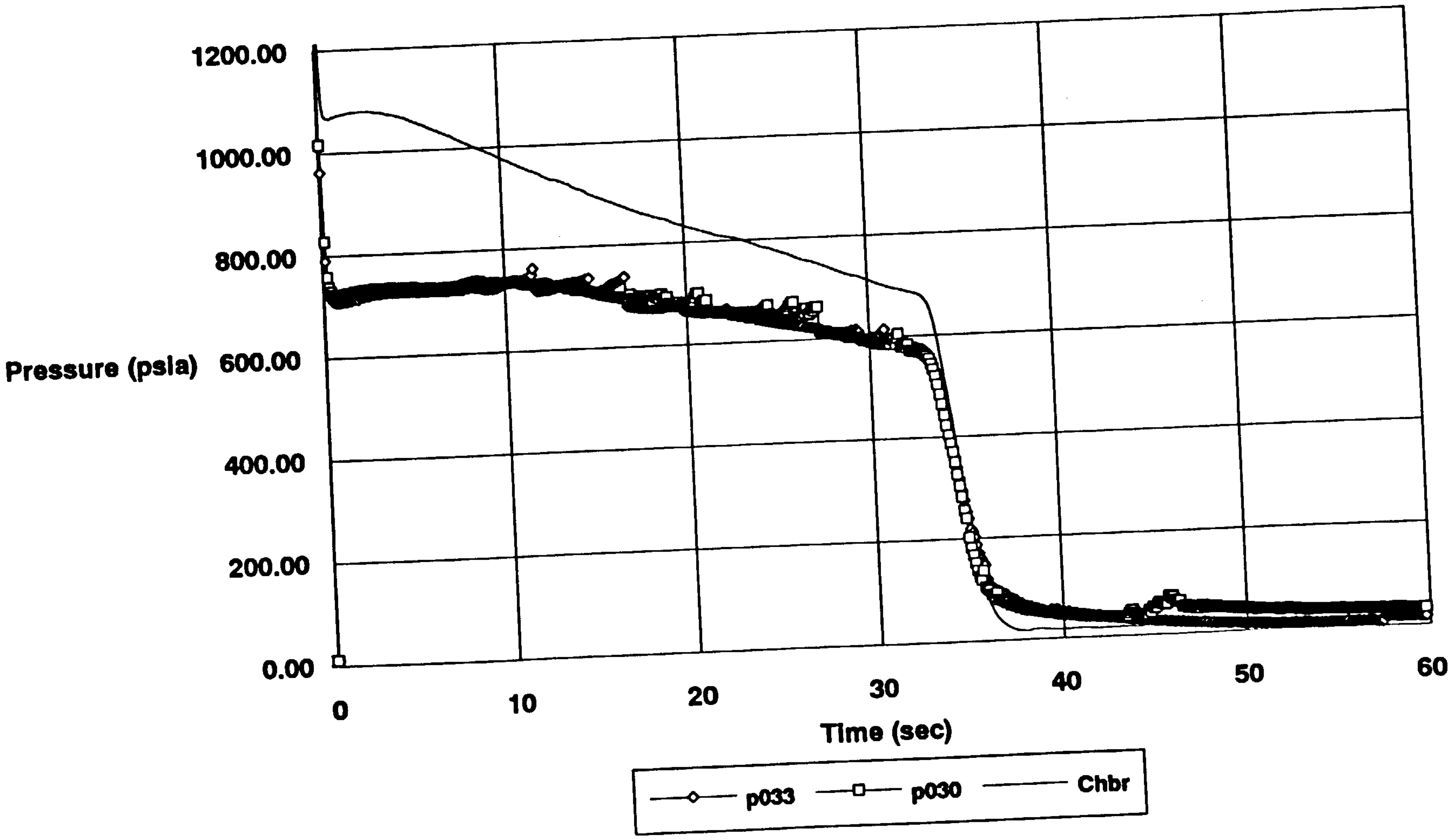

Figure 8. Ring 2 CFD-Adjusted Pressures

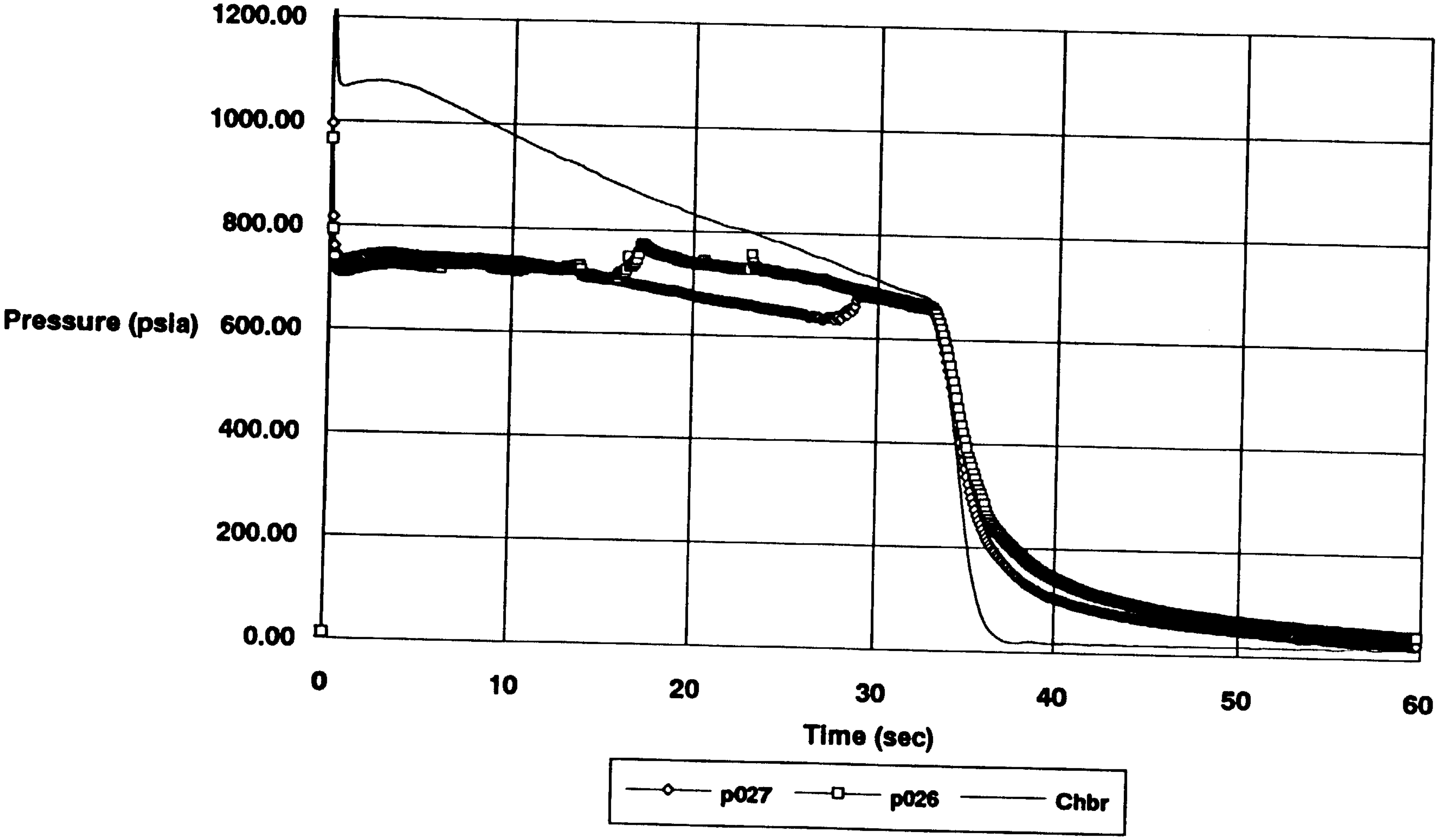

Figure 7. Ring 1 CFD-Adjusted Pressures

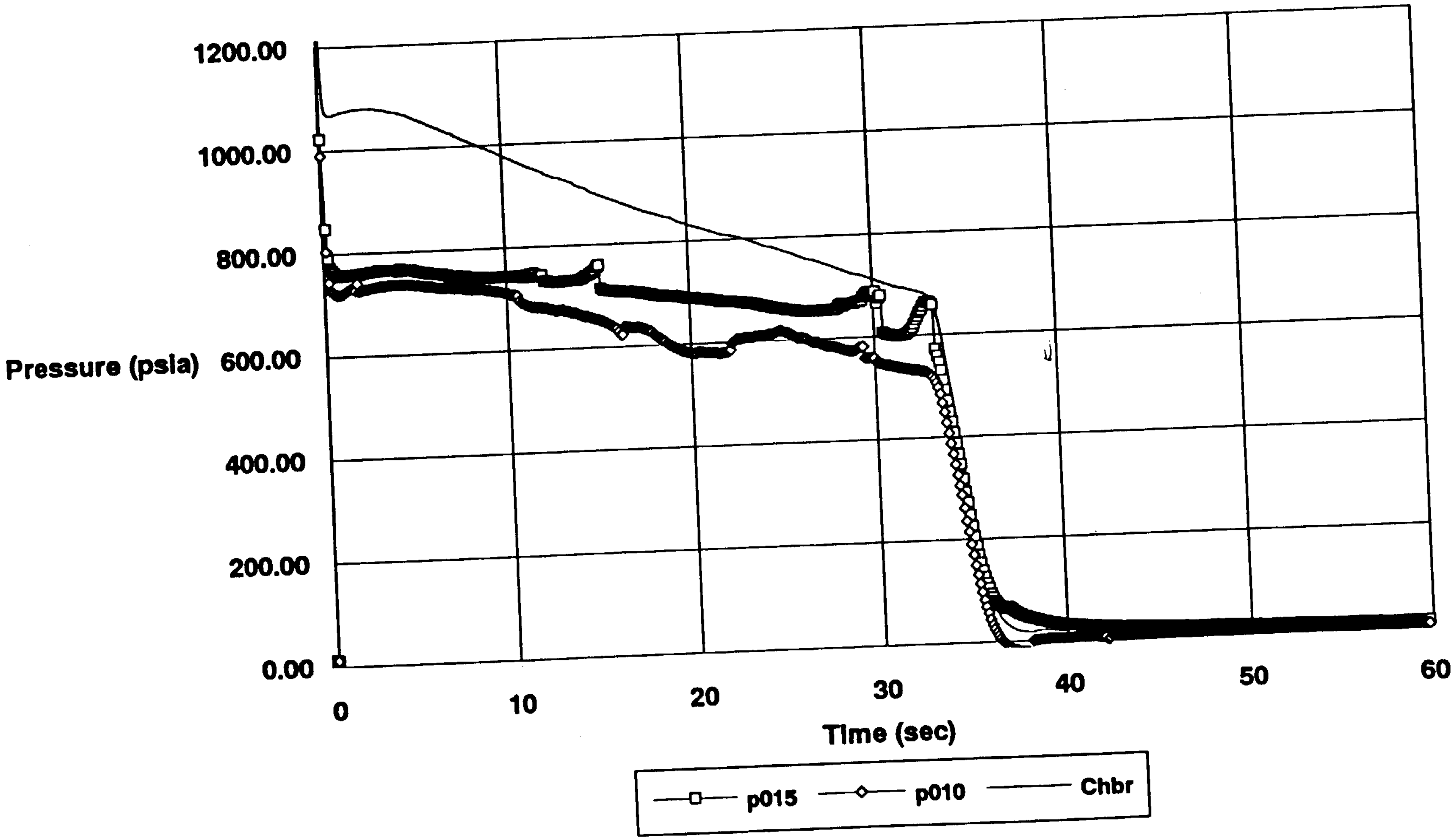

Figure 6. Calibration of Test 3 Using CFD and Test Data Comparisons

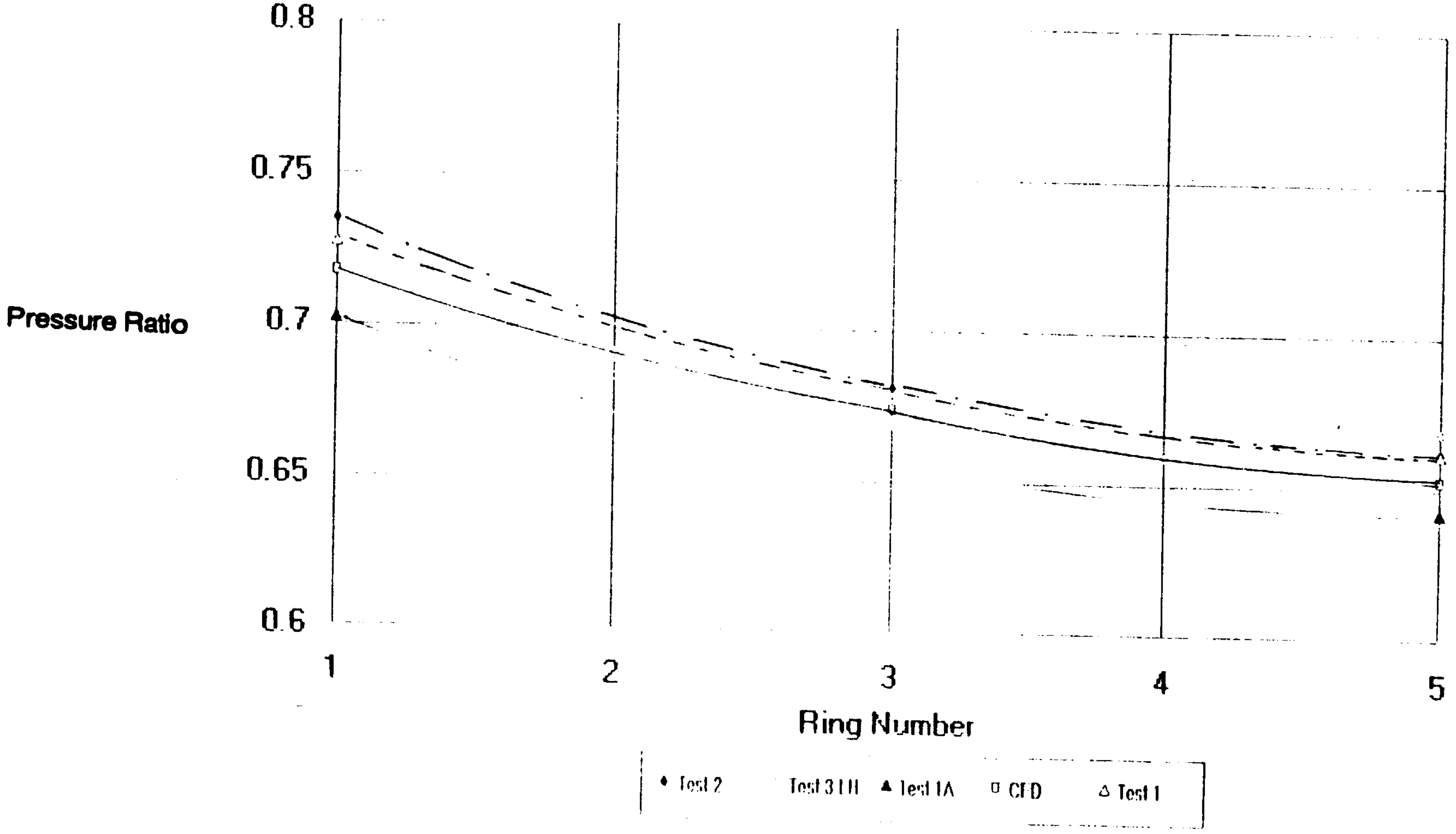

Figure 5. Test 3 Data Calibration Based on a Linear Average of the Pressures

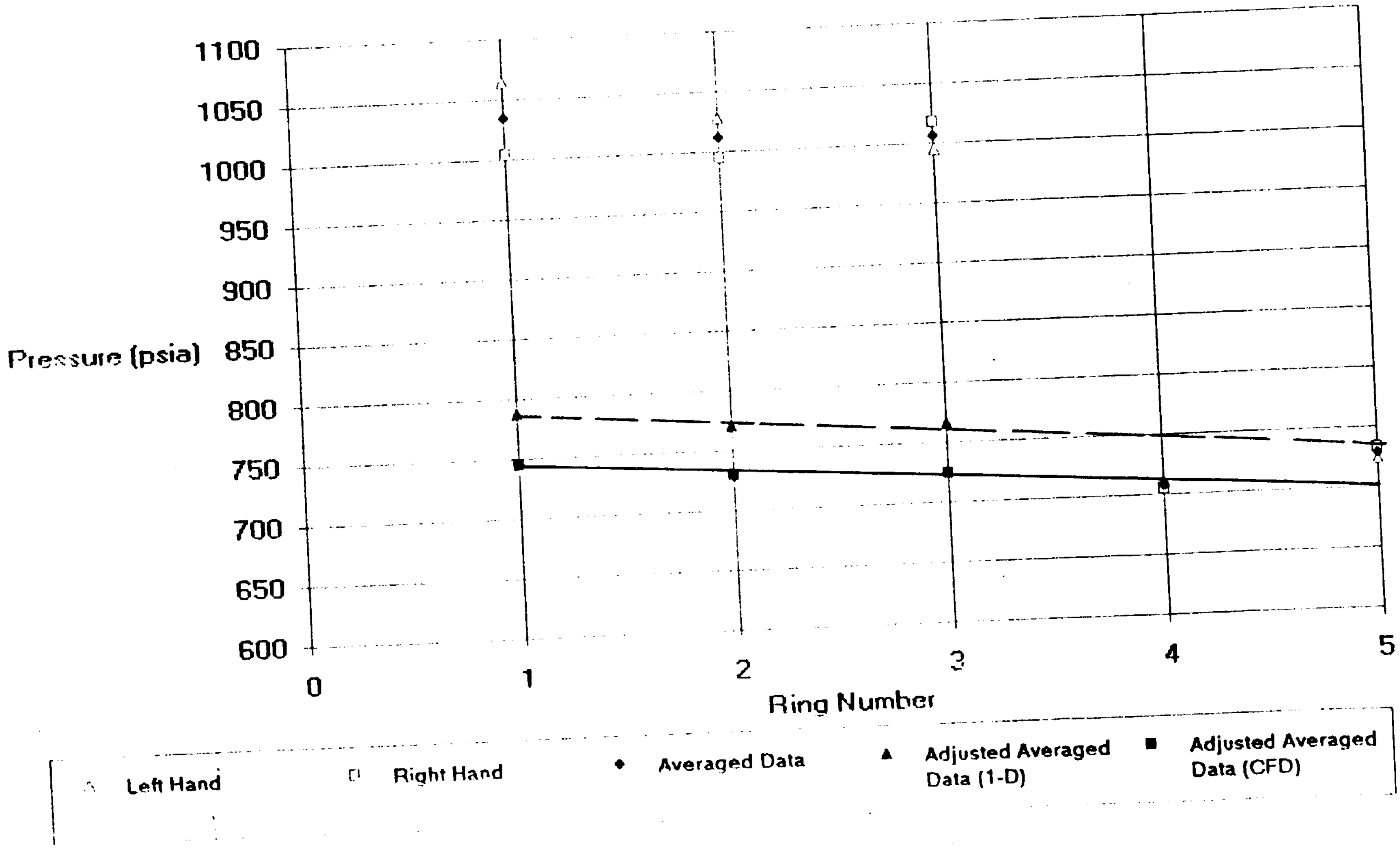

Figure 4. Ignition Blast Tube Static Pressure - LH Segments: NITM-2, Test 3

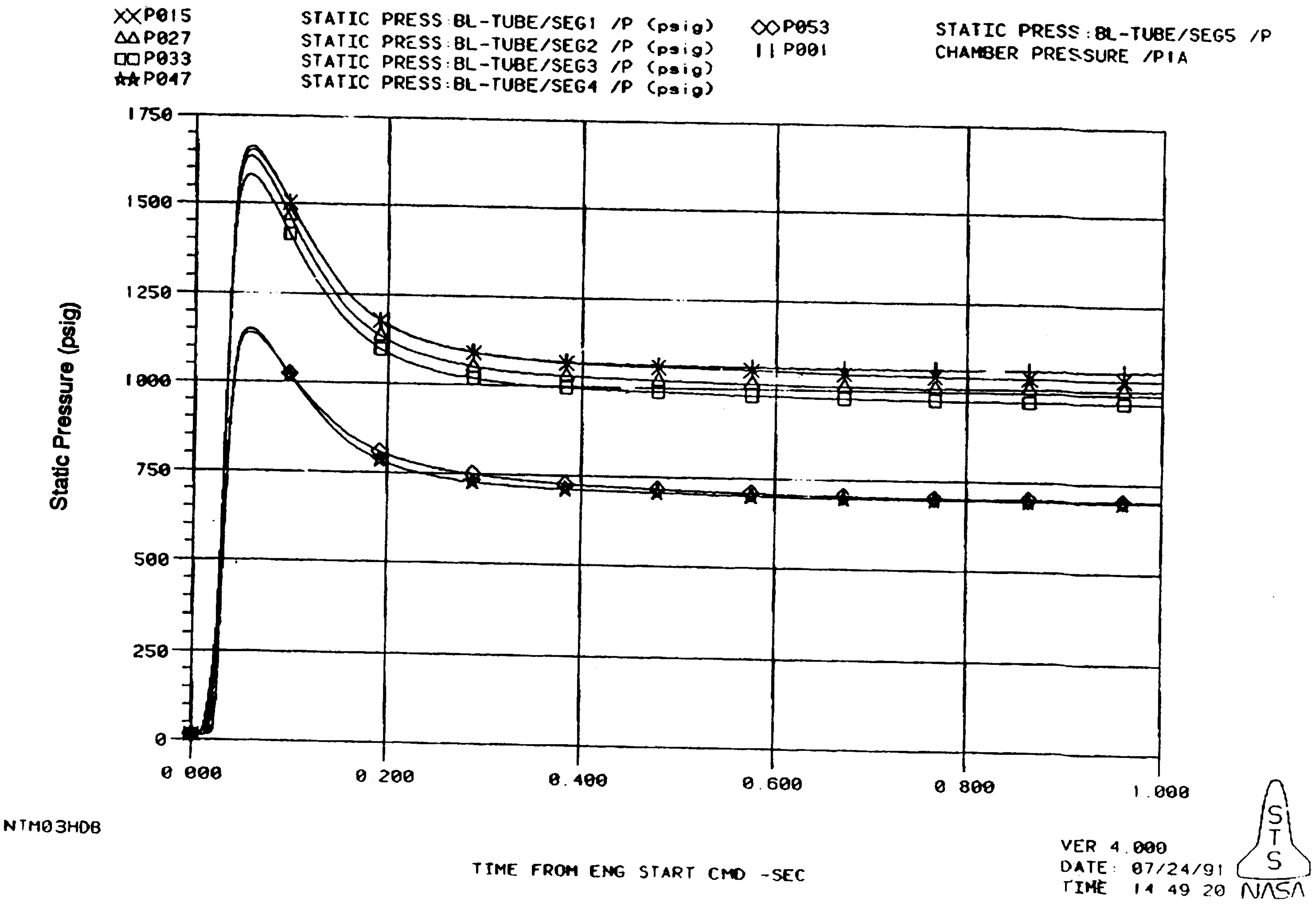

Figure 3. Velocity Profile Comparison at the Inlet of the Two-Inch Motor

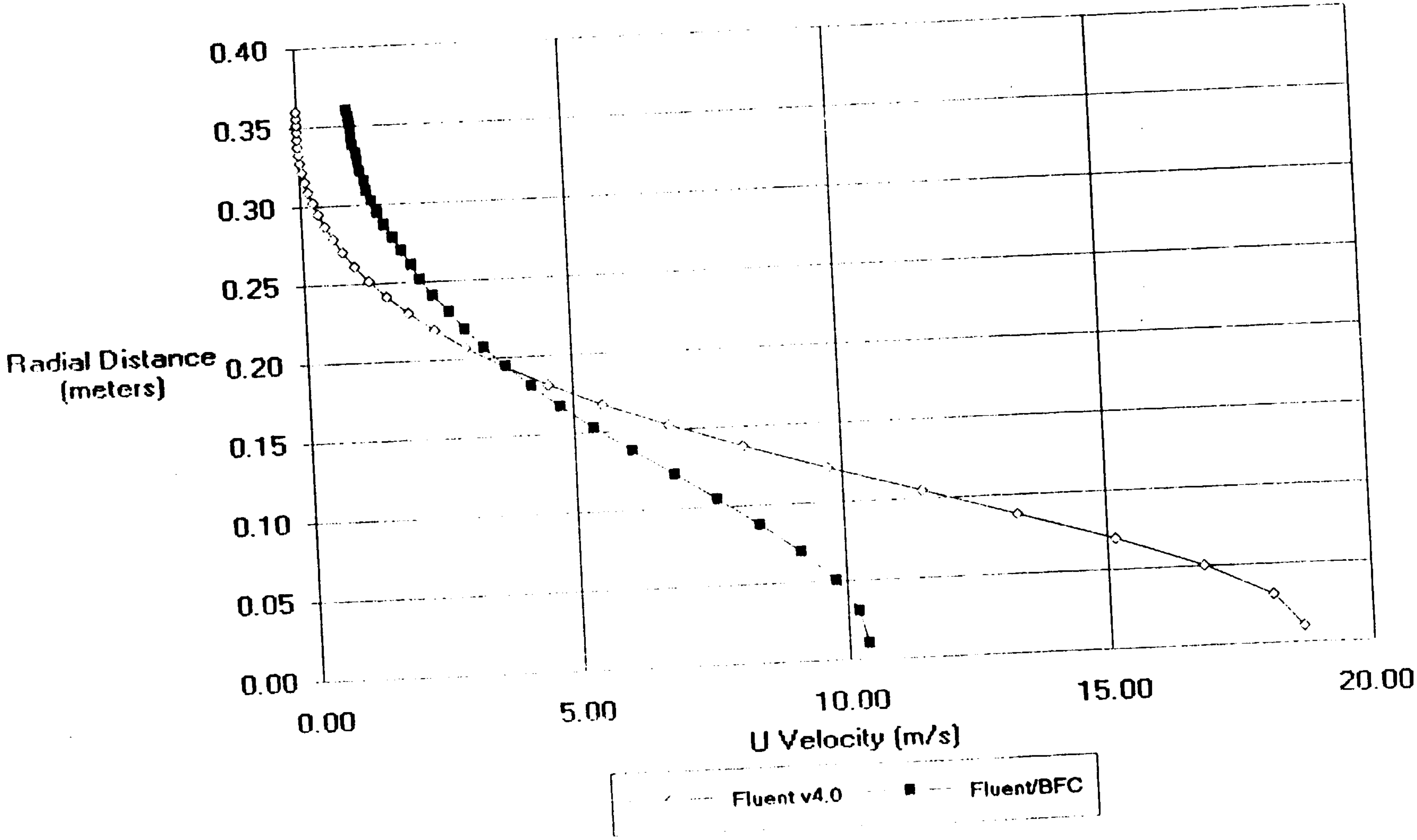

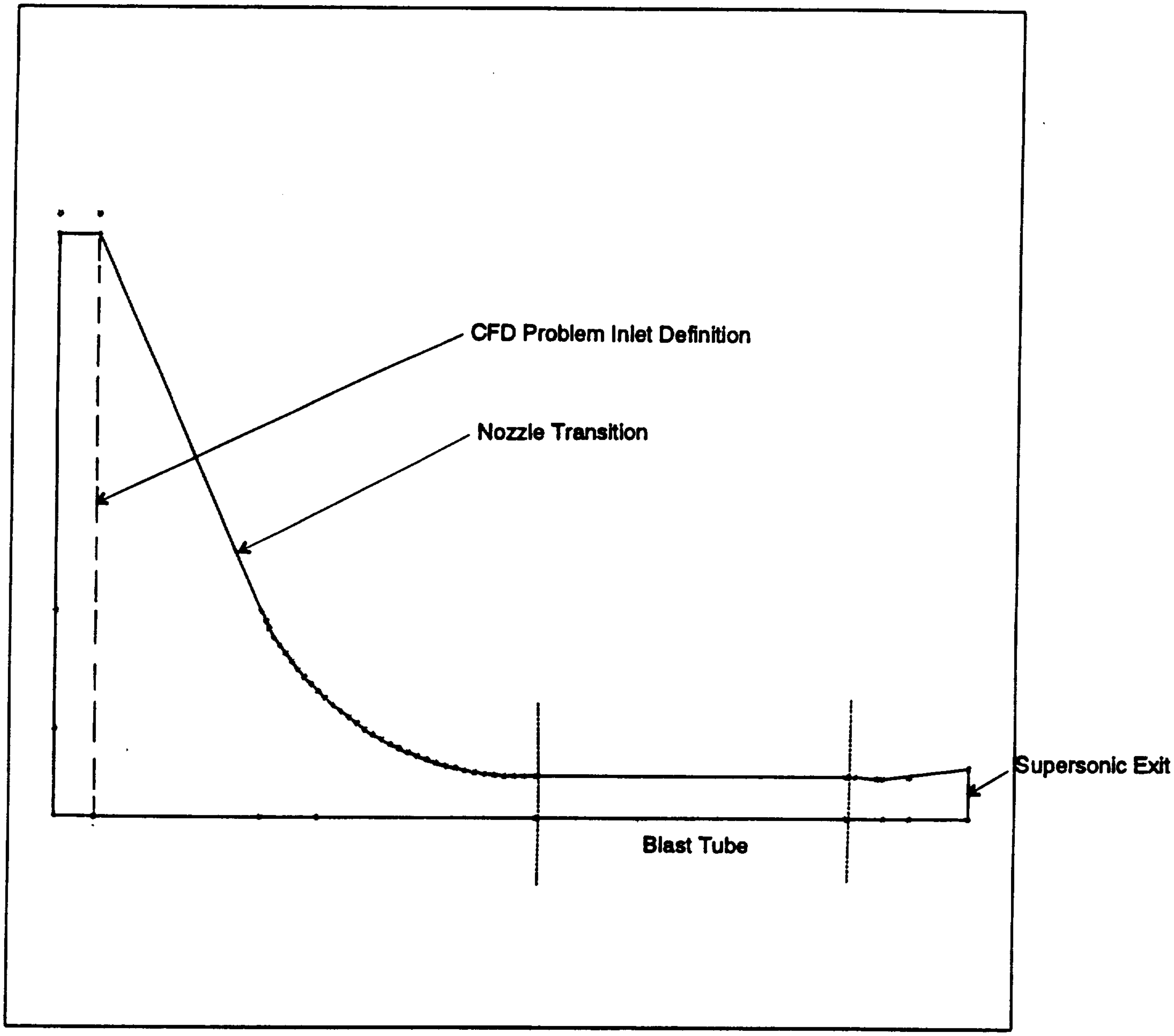

Figure 2. Nominal Design Geometry of the Two-Inch Motor

little lower than either the Test 1 data or the CFD predictions. Both Test 1 and Test 1A match well with the predicted CFD results. Test 2 is shown as a solid diamond. The pressure ratio at the ring segment 1 gauge is higher than the CFD results or any of the previous test results. The pressure readings in the gauges in ring segments 3 and 5 are close to the CFD predictions and also have a pressure drop slope close to the CFD prediction. The pressure drop from gauge 1 to gauge 3 is larger than observed in any other test or in the CFD predictions. The ring segment 1 gauge reading may be in error but the spread in the data is not great enough to say this with any kind of confidence until much more motor test pressure data is collected. The open diamonds represent the adjusted pressure ratio data for the left-hand gauges in Test 3. The pressure ratios for ring segments 1, 2, and 3 were determined by calibrating all the gauges down by an amount such that the ring segment 1 gauge matched the CFD predicted pressure. The correction factor applied to recalibrate the first three ring segment gauges was .7244. The pressure ratios for ring segments 4 and 5 were not adjusted in any way. The measurements match the CFD prediction for all 5 ring segments as well or better than any of the other test after the data for ring segments 1, 2, and 3 have been recalibrated in this way. This is the best estimate of recalibrating the data that can be made without more information and the method makes use of the maximum amount of known information by using previous test results and the CFD predictions. The pressure rise from ring segment 4 to 5 was not predicted in the CFD analysis and the zone of recovery pressure created by the throat was not strong enough to cause a pressure rise on the ring segment 5 gauge. The cause for the pressure rise from ring segment 4 to 5 is not known at this time but will be reassessed after the two-phase flow analysis is performed.

The recalibrated pressure data for each consecutive ring segment plotted separately with the chamber pressure is shown in Figure 7, Figure 8, Figure 9, Figure 10, and Figure 11 for ring segments 1, 2, 3, 4, and 5 respectively. Figure 12, Figure 13, Figure 14, Figure 15, and Figure 16 show the same gauge plots as pressure ratios to the chamber pressure. The gauge pressures plotted as pressure ratios show the erosion occurring in the ring segments as a rise in the pressure ratio. Notice that the pressure ratio begins to rise rapidly in the first five seconds of burn as the walls heat up and erosion rapidly begins. The flow field velocities are also the highest in this early portion of the motor burn before significant erosion of the wall has reduced the blast tube velocities. This is confirmed by the reduction of the slope of the pressure ratios toward the end of the test. The blast tube flow field environment is less stressing and the erosion rate, shown as a reduction in the slope of the pressure ratio, is therefore lower.

The gauges in ring segments 4 and 5 do not read as close as past test but the readings are close enough together so that it is difficult to say that the gauges have a problem on this basis alone.

The gauge pressures in ring segments 1, 2 and 3 also appear very suspect because ring segment 3 reads higher than either ring segments 1 or 2. This means that something must be wrong with the reading on either the gauges in rings 1 and 2 or that the gauge in ring 3 is incorrect because there should not be a pressure rise down the blast tube from ring 1 to ring 3. The pressure drop from the gauge in ring 1 to the gauge in ring 2 is also very small, much smaller than expected so that one would suspect gauge 1 and 2 as being in error. This is also substantiated by interpreting the smaller spread in the gauge readings in ring segment 3 to mean that the ring 3 readings on the left and right-hand side are reading more true. On the basis of the above discussion, the right-hand side gauge pressures in ring segments 1, 2, and 3 do not appear reliable.

Assuming for the moment that the gauges in both the left and right-hand side of segments 1, 2, and 3 are acceptable, a first attempt at a calibration of the data from ring segments 1, 2, and 3 can be made in the following way. Working under the assumption that all the gauges are correct implies that the best way to fit the data is to average the right and left-hand measurements in the various rings. This is shown in Figure 5. The unadjusted right and left-hand measurements are shown in the figure along with the average values as solid diamonds. After the measurements are averaged, the measurements are then adjusted down to either the 1-D pressure ratio at the ring segment 1 gauge or the CFD predicted pressure ratio at this location. The dashed straight line drawn through the adjusted measurements shows that the data adjusted in this way forms a good linear fit to 4 of the 5 gauges. If the 1-D pressure ratio is used, the data fits gauges 1, 2, 3, and 5 well. If the CFD pressure ratio is used, the data fits gauges 1, 2, 3, and 4. Since the pressure drop down the blast tube is not predicted to be linear, another method of performing this data calibration is now explained and evaluated.

A detailed compilation of all the previous test data for test gauges assumed to be good is shown in Figure 6. This figure also shows the CFD predictions made by Fluent/BFC version 3.02 (The prediction for the run which obtained a pressure drop of 68.6 psi down the blast tube was used.). A solid curve has been drawn through the CFD predicted data which clearly does not predict a linear pressure drop. In this analysis the right-hand test gauges in ring segments 1, 2, and 3 have been discarded for the previously discussed reasons of reliability. Test 1 data is plotted as an open triangle and is slightly higher than the CFD predicted results. The pressure drop for Test 1 and that predicted by the CFD code are close but there was no pressure gauge in ring 3 to help assess the shape of the CFD predicted pressure drop curve down the blast tube. Test 1A is shown as a solid triangle. The pressure drop observed down the blast tube is only slightly higher than the CFD results or Test 1 data. Also the pressure ratio is a

Table 8. Test 2 Chamber Pressures and Ring Segment Pressure Ratios

Average Chamber Pressure = 978.6 psia
Time = 0.5 sec

Gauge	Measured Pressure Ratio	Predicted Pressure Ratio
Ring 1, P012	.7349	.7174
Ring 3, P032	.6809	.6739
Ring 5, P051	.6673	.6527
Ring 5, P052	.6616	.6527

Table 9. Test 3 Chamber Pressures and Ring Segment Pressure Ratios

Average Chamber Pressure = 1068.5 psia
Time = 0.5 sec

Gauge	Measured Pressure Ratio	Predicted Pressure Ratio
Ring 1, L1	.9903	.7174
Ring 2, L2	.9547	-------
Ring 3, L3	.9242	.6739
Ring 4, L4	.6596	-------
Ring 5, L5	.6683	.6527

In the process of performing this exercise a very disturbing observation on the data must first be noted. The spread of the data for the pressure gauges in ring segments 1 and 2 is exceptionally larger than in any previous test in which the gauge reading has been considered viable. The spread for the gauges in ring segment 3, although smaller than Ring segment gauges 1 and 2, is still much larger than noted in the past test for multiple working gauges in a single ring. This is shown in Table 10.

Table 10. Pressure Gauge Spread in Ring Segments 1, 2 and 3

	Ring 1	Ring 2	Ring 3
Right-Hand Gauge (psia)	994.3	980.7	994.8
Left-Hand Gauge (psia)	1041.0	1012.3	975.8
Spread in Pressure (psi)	46.7	31.6	19.0

in the material ring segments should not have sensed a pressure near this value if calibrated properly.

This information was given to NASA personnel on August 8th along with some possible sources of the calibration error such as the voltage source, D/A converter, calibration curve error, etc.. This is being investigated at this time. In order to make some use of the data assuming at the moment that no re-calibration of the data can be performed, ERCI has investigated several methods of determining a calibration factor for the data. The best two of these are presented.

Table 6. Test 1 Chamber Pressures and Ring Segment Pressure Ratios

Average Chamber Pressure = 999.7 psia
Time = 0.5 sec

Gauge	Measured Pressure Ratio	Predicted Pressure Ratio
Ring 1, PT1-220	.7272	.7174
Ring 5, PT5-140	.6612	.6527

Table 7. Test 1A Chamber Pressures and Ring Segment Pressure Ratios

Average Chamber Pressure = 988.1 psia
Time = 0.5 sec

Gauge	Measured Pressure Ratio	Predicted Pressure Ratio
Ring 1, P015	.7022	.7174
Ring 5, P050	.6397	.6527
Ring 5, P053	.6417	.6527

The computational grids used by Fluent β-version 4.0 and Fluent/BFC version 3.02 were identical. The grid was comprised of 200 axial computational cells and 35 radial computational cells. The y+ values at the wall for this grid show that the first grid point for all axial stations is within the fully turbulent log-law region which means the grid spacing is close enough to the wall to provide a good prediction of the shear stress using wall functions. The flow field gradients are also reasonably low in both the radial and axial directions. Since these two criteria are satisfied, the grid will be accepted as of high enough resolution to provide a good CFD solution. No actual grid dependency studies have been performed at this time. However, this grid is of higher resolution than grids which have been tested in the past for solution grid dependency.

Test 3 Data Quick-look Data Analysis

The quick-look data package for the Two-Inch Motor, Test 3, was received on August 7th. It was immediately obvious that there was an error in the data for pressure gauges in ring segments 1, 2, and 3 on both the right and left-hand side pressure gauges. Figure 4 shows the pressure data for the gauges in the 5 material ring segments during the first one second of motor burn. Table 5 shows the CFD and 1-D pressure ratio predictions in the blast tube of the Two-Inch Motor. These are for nominal design dimensions of the Two-Inch Motor and not for the exact pre-test dimensions of the Test 3 Motor. The pressure ratios are the local wall static pressure divided by the total motor pressure.

Table 5. CFD Predicted Pressure Ratios

	Ring 1	Ring 5
Run 1, Dp = 42.3 psi	.7231	.6795
Run 2, Dp = 68.0 psi	.7211	.6558
1-D prediction	.7609	.7609

Tables 6, 7, 8, and 9 are also useful in this discussion. These tables show the pressure ratios for Test 1, 1A, 2, and 3 respectively, at one-half second after ignition when the motor start-up transients have cleared. The pressure ratios for ring segments 1, 2 and 3 of Test 3 are well above .9 during the ignition pressure spike and at one-half second burn time. These values are approximately 50% greater than the CFD or 1-D predictions for the pressures in the blast tube. All the other tests have been very close to the CFD and 1-D predictions in the blast tube. The pressure gauges in ring segments 4 and 5 are close to the CFD prediction of the pressure ratio at ring segment 5 for both the start-up pressure rise section of Figure 4 and at one-half second into motor burn. It is assumed that the first three gauges on both the left and right-hand side are incorrectly calibrated. There is another problem noted during the ignition pressure spike. The pressure rises to over 1500 psia which is the maximum pressure to which the gauges are rated. However this should not be a problem since the gauges

Correction of NITM-2 Test 3 Data Using CFD Analysis and Previous Test Results

NITM-2 Test Data and CFD Analysis

A discussion of recently completed CFD results associated with the Two-Inch Motor is presented in this report. Along with the CFD analysis, a review of the quick-look data package on Test 3 of the Two-Inch Motor is presented. The CFD analysis addresses some past issues associated with the Two-Inch Motor. The underprediction of the pressure drop down the blast tube is discussed as well as the effects of two phase flow on the motor flow field.

General Description of The Two-Inch Motor Configuration

The nominal design configuration of the Two-Inch Motor as detailed in Hercules drawing number 10396 was modeled for CFD analysis. The blast tube diameter for this nominal configuration was 2.1 inches and the throat diameter was 2.0 inches. No blast tube or throat pre-test measured diameters for any of the tests are used in this computational analysis. Due to convergence problems with the grid and the need to obtain a solution as quickly as possible, a slightly modified geometry was used in the CFD analysis. Figure 2 shows the nominal Two-Inch Motor geometry. The geometry used to analyze the flow field was modified by moving the inlet one inch forward to the beginning of the nozzle transition as shown by the dashed line in Figure 2. The actual geometry will be re-run at a later time; however, the effect of this modification on the flow field should be insignificant to the conclusions of this analysis.

The boundary conditions applied at the inlet and exit are as shown in Table 1. A supersonic outlet boundary condition is used at the configuration exit. A total pressure boundary condition is used at the configuration inlet with the pressure prescribed as the chamber pressure listed in Table 1. These boundary conditions represent an effective gas analysis where the properties, such as molecular weight and specific heat ratio, are combined values of both the gaseous and particle phases.

Table 1. Physical Properties and Boundary Conditions for the Nominal Two-Inch Motor Geometry

Chamber pressure	6894800 Pa
Molecular weight	29.472
Viscosity	8.68487×10^{-5} kg/m-s
Stagnation temperature	3557 °K
Specific heat	1987.47 J/kg-°K
Inlet kinetic energy	0.16 m^2/s^2
Inlet dissipation rate	0.39 m^2/s^3
Thermal conductivity	0.4293 W/m-°K

ASRM Analysis Drawings List

Drawing Number	Drawing Title
H5005	Aft Case Loaded with Nozzle - 19 Second Burn Time
H5006	Aft Case Loaded with Nozzle - 60 Second Burn Time
H5007	Aft Case Loaded with Nozzle - 115 Second Burn Time
H5008	Center Case Loaded with Nozzle - 19 Second Burn Time
H5101	Aft Case Loaded with Nozzle
H5102	Center Case Loaded
H5103	Forward Case Loaded
H5104	Motor Assembly Loaded
H5109	Nozzle Assembly
H5201	Aft Case Loaded with Nozzle - Deformed Grain
H5202	Center Case Loaded - Deformed Grain
H5203	Forward Case Loaded - Deformed Grain
H5204	Motor Assembly Loaded - Deformed Grain

smoother for this solution and the 4 psi pressure differential between the 0 and 180 degree positions underneath the nozzle nose agrees well with past analyses and cold flow data for RSRM. The resultant forces and hinge moments for this case are shown in the table below.

Internal Hinge Moment Results / 8 Degree Gimbal Angle

Zone	F_y,lb$_f$	F_z,lb$_f$	M_x,in-lb$_f$
Nose Tip - Flex Bearing	9,659	588,211	210,921
Nose Tip - Throat	36,946	2,639,536	1,310,217
Throat - Exit Plane	26,838	-731,971	-452,456
Nose Tip - Exit Plane	63,789	1,906,526	879,780
Total	73,443	2,495,776	1,068,682

The resultant non-restoring hinge moment for this case is 1.069×10^6 in-lbf compared to the previous result of 1.329×10^6 in-lbf from previous results. This non-restoring resultant moment does include a restoring (negative) moment component calculated for the zone from the nozzle throat plane to the exit plane.

Agreement was obtained between all NASA/MSFC ED32 calculated hinge moments and results from ERC. Attention then turned to the effects of off-nominal conditions which may affect the internal aerodynamic hinge moment. The most significant factor may be a lateral or radial shift in the effective nozzle pivot point. Thiokol reported a 3σ value of $\pm$ 1.517 inches for the lateral shift in pivot point. The interface control document permits $\pm$ 2.0 inches. Preliminary results for the hinge moment at the 19 second, 8 degree gimbal angle condition for the plus and the minus 1.517 inches lateral pivot point shift were -2,609,184 in-lb$_f$ and +5,552,851 in-lb$_f$, respectively. These compare with the previous nonrestoring moment result of +1,311,713 in-lb$_f$. Thus a restoring moment result of -2.609×10^6 in-lb$_f$ would have a significant impact on actuator load budgets.

plans for the internal hinge moment analysis were presented by ED32 at USBI. The plans include calculation of the internal hinge moments for RSRM and ASRM at burn times of 19, 60 and 115 seconds. ERC also provided drawings of the propellant and nozzle geometry with x-y coordinates of the surface contour. Also, additional moment calculations were performed for updated CFD solutions as they became available. Solutions based on both surface pressure integration as well as conservation of inlet and exit plant angular moment of momentum were employed and compared to each other. The nozzle was divided into three zones and the moment about the pivot point and the hinge moment was calculated for each zone separately. These three zones are : 1) The nose tip to the flex bearing underneath the nose, 2) the nose tip to the throat plane, and 3) the throat plane to the exit plane. A fourth overlapping zone was defined from the nose tip to the exit plane to serve as a check case. The results are listed in the tables below for the 4 and 8 degree nozzle gimbal angles. Note that positive moments are restoring moments. The "y" axis is radially upward, the "x" axis is radially inward to the paper and the "z" axis is axial along the nozzle centerline.

Internal Hinge Moment Results
4 Degree Gimbal Angle

Zone	F_y, lb_f	F_z, lb_f	M_x, in-lb_f
Nose Tip - Flex Bearing	15,674	609,714	273,864
Nose Tip - Throat	11,838	2,794,947	329,224
Throat - Exit Plane	10,194	-788,555	-259,063
Nose Tip - Exit Plane	22,026	2,006,159	74,964
Total	37,706	2,616,106	344,025

Internal Hinge Moment Results
8 Degree Gimbal Angle

Zone	F_y, lb_f	F_z, lb_f	M_x, in-lb_f
Nose Tip - Flex Bearing	14,344	563,669	241,987
Nose Tip - Throat	71,804	2,662,120	1,832,803
Throat - Exit Plane	48,684	-732,347	-746,139
Nose Tip - Exit Plane	120,578	1,959,357	1,107,766
Total	134,832	2,493,442	1,328,651

Efforts continued on the calculation of the nozzle hinge moment due to the internal aerodynamic forces. An updated solution for an 8 degree gimbal angle at a burn time of 19 seconds was obtained from ED32. The wall pressure profiles were much

Internal and External Nozzle Torque Analysis

Computer codes to calculate the nozzle forces and moments about the nozzle pivot point were developed toward this analysis. Two codes for the internal flow were developed; one which calculates forces and moments from integrating the wall pressure distribution and one which calculates forces and moments from the inlet and outlet plane momentum and pressure forces. The codes were checked out using one-dimensional test cases. The wall pressure code was successfully ported to the IBM RISC workstation at ERC. They are able to receive CFD data from MSFC/ED32 flow field solutions. Nozzle pivot point moments were determined for ASRM and RSRM burn times of approximately 19, 60 and 115 seconds at gimbal angles of 4 and 8 degrees.

Also, a separate code was developed to integrate the external nozzle surface pressure distribution to obtain the nozzle forces and moments about the pivot point due to the space shuttle external flow environment. The wall pressure data was taken from wind tunnel data on a 2 percent scale shuttle model. This was test number IA119. The calculations are being performed for the external nozzle geometry represented in ERC drawing H6004-1 for the RSRM geometry. The model scale geometry and pressure tap locations are presented in ERC drawing H6501-1 for the SRB aft skirt and nozzle region of the two percent shuttle model.

When the hinge moment analysis for the external flow was completed the results were plotted and delivered to ED33. The pressure distributions for over 130 shuttle model wind tunnel tests were integrated and scaled to RSRM/ASRM flight conditions and full scale geometry. The external geometry of the aft section of the SRM nozzle and skirt for the 2% scale Shuttle model is shown in ERC drawing H6501-1. This drawing also shows an overlay comparison of the model geometry and the current RSRM nozzle and SRB skirt geometries. The analysis accounted for the differences in nozzle length by proportional adjustments in pressure tap locations. The external geometry of the full scale SRB nozzle and skirt is shown in drawing H6004-1. These drawings are available upon request and reduced scale versions are included in the ED33 presentation on the external hinge moment analysis.

The external hinge moments were calculated for various vehicle pitch and yaw angle and nozzle pitch plane gimbal angles at various vehicle Mach numbers. These results were presented to the Chief Engineer's office by ED33 as well as USBI. A request was received to translate the calculated pitch and yaw plane moments to the actuator rock and tilt planes. This axis transformation was accomplished for selected runs and the results were plotted and presented to the Chief Engineer's office by ED33.

Preliminary CFD solutions from ED32 personnel were used to calculate the internal aerodynamic hinge moments for both a 4 degree and 8 degree nozzle gimbal angle. These results indicated an overall non-restoring torque but the absolute values were not released since the CFD solutions were preliminary and not fully converged. The

Igniter Analysis

The ASRM igniter motor was test fired with the multi-port closure and the measured motor chamber pressure was considerably higher than predicted by Aerojet. ERC had expected this result due to Aerojet's failure to properly treat the aerodynamic effect of the sharp edged, multi-port nozzles in the analysis of the internal ballistic performance of the igniter motor. ERC concerns were documented in RID PDR-M-06-120 which was submitted and approved at the February, 1991, ASRM PDR held in Iuka, MS. Calls about this motor test result were received from the Chief Engineer's office and the Solid Propulsion Branch. The main flow discharge coefficient was of significant interest to us because of the sharp edged oval holes which should have resulted in a higher than expected motor operating pressure. Aerojet did report a nozzle efficiency of 0.92 and higher than expected pressures although the reasons were not agreed to by all. Cold flow tests using an existing Experimental Branch test rig and facilities were proposed to determine the exact magnitude of the effective multi-port discharge coefficient and to evaluate prospective design solutions. Interest was expressed in cold flow testing of the igniter closure and ports by the Chief Engineer's office, but coordination and input from Aerojet would have been required.

Figure 11. ASRM Surface Pressure Distribution #2, #6, #7 & #8
CFD Solution, Grain Geometry #1, #4, #5, #6 & #7 @ 90 Deg. F

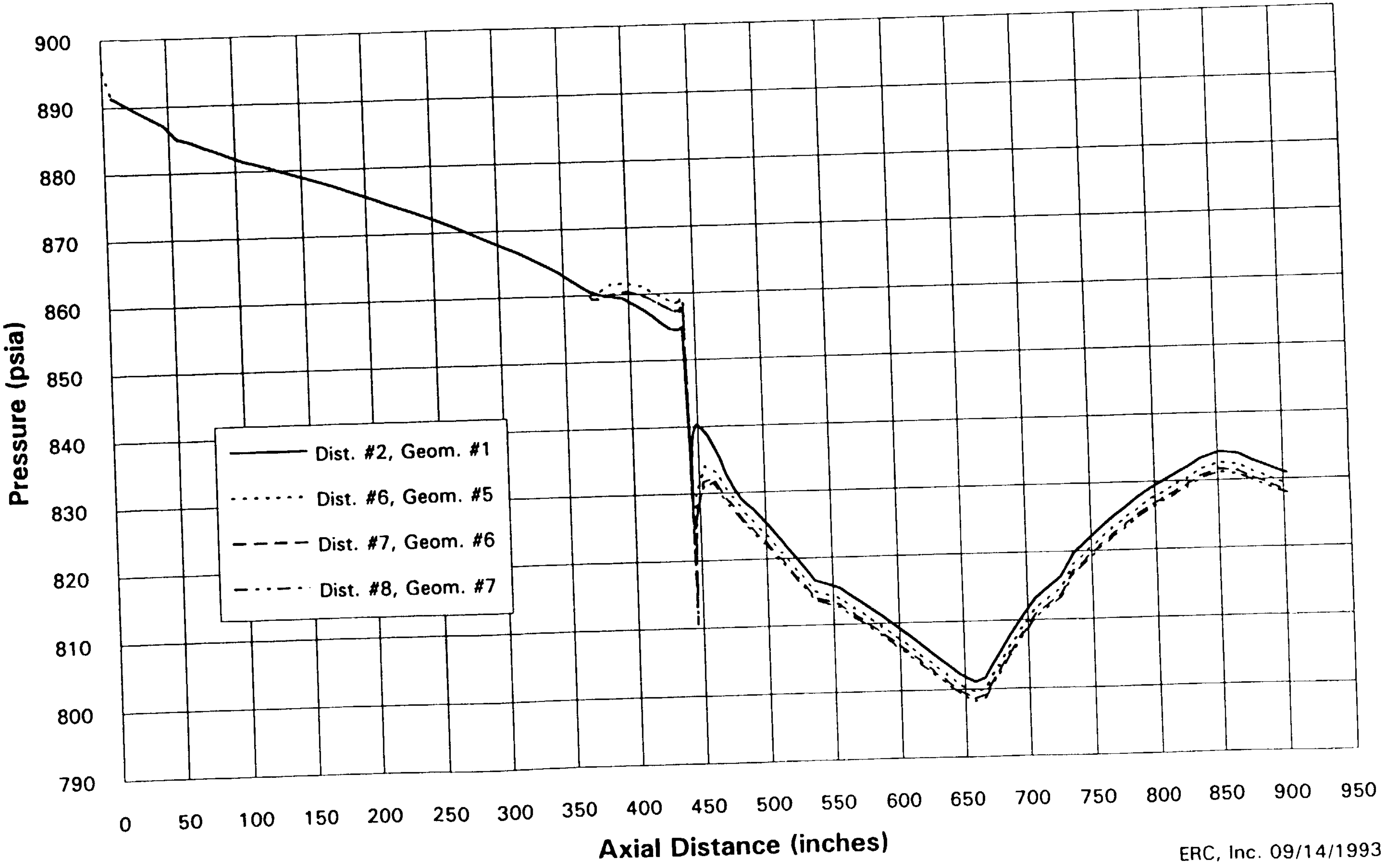

ERC, Inc. 09/14/1993

Figure 10. ASRM Axial Pressure Distribution #2, #5, #6, #7 & #8 CFD Solution, Grain Geometry #1, #4, #5, #6 & #7 @ 90 Deg. F

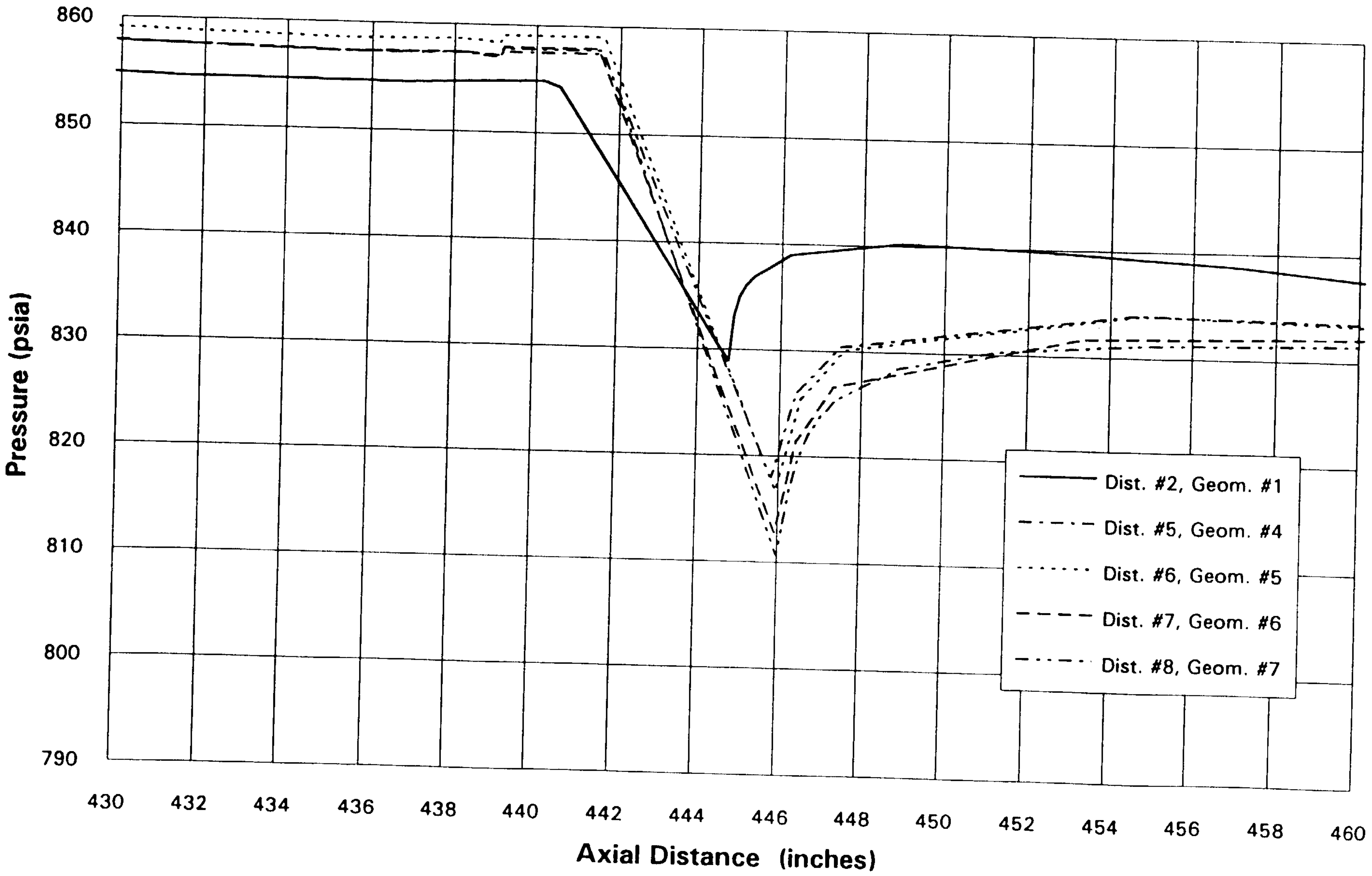

ERC, Inc. 09/14/1993

Figure 9. ASRM Radial Pressure Distribution #8 in the Aft Slot CFD Solution, Grain #7 @ 90 Deg. F

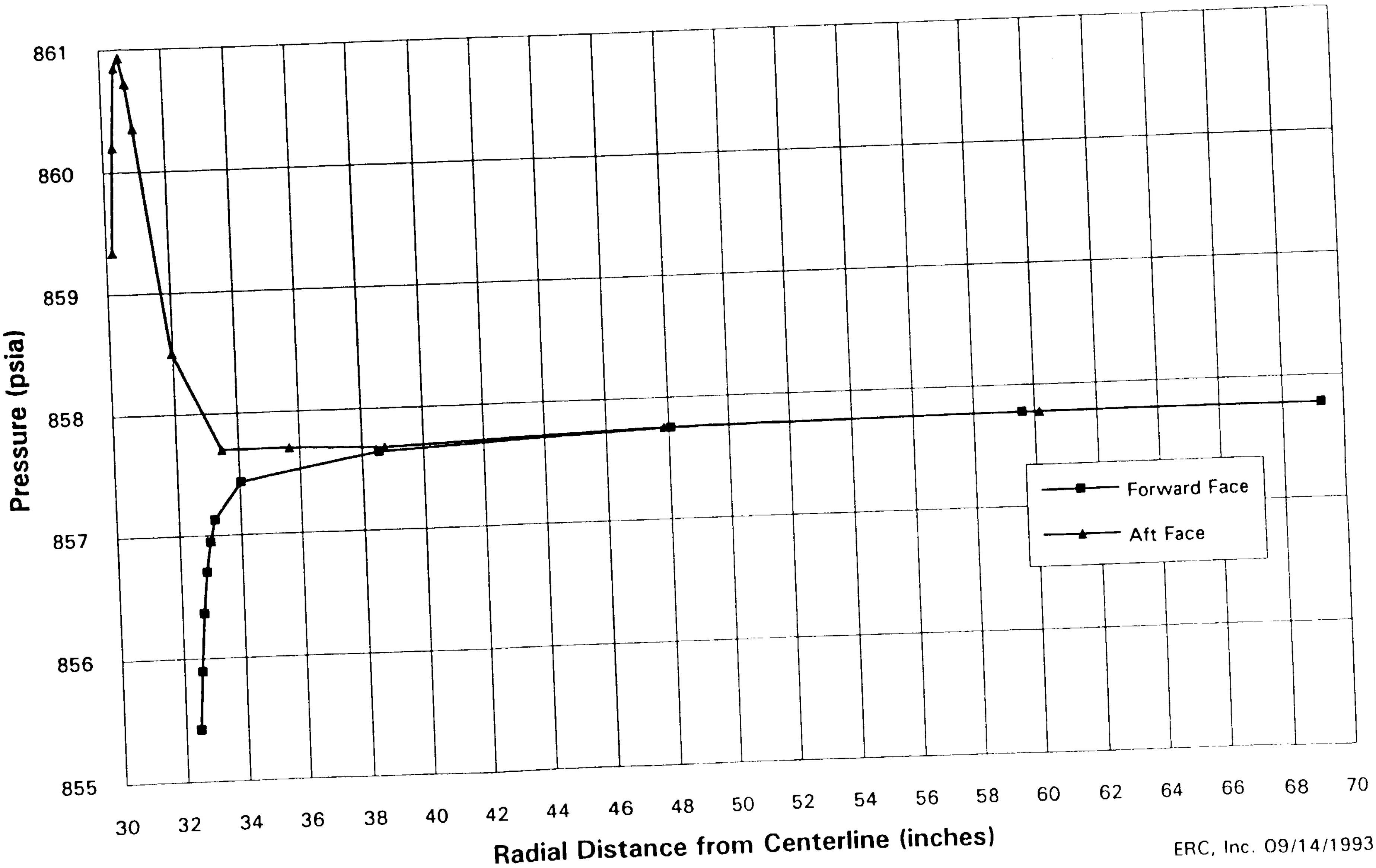

ERC, Inc. 09/14/1993

Figure 8. ASRM Deformed Aft Slot Maximum Delta P as a Function of Geometry Number

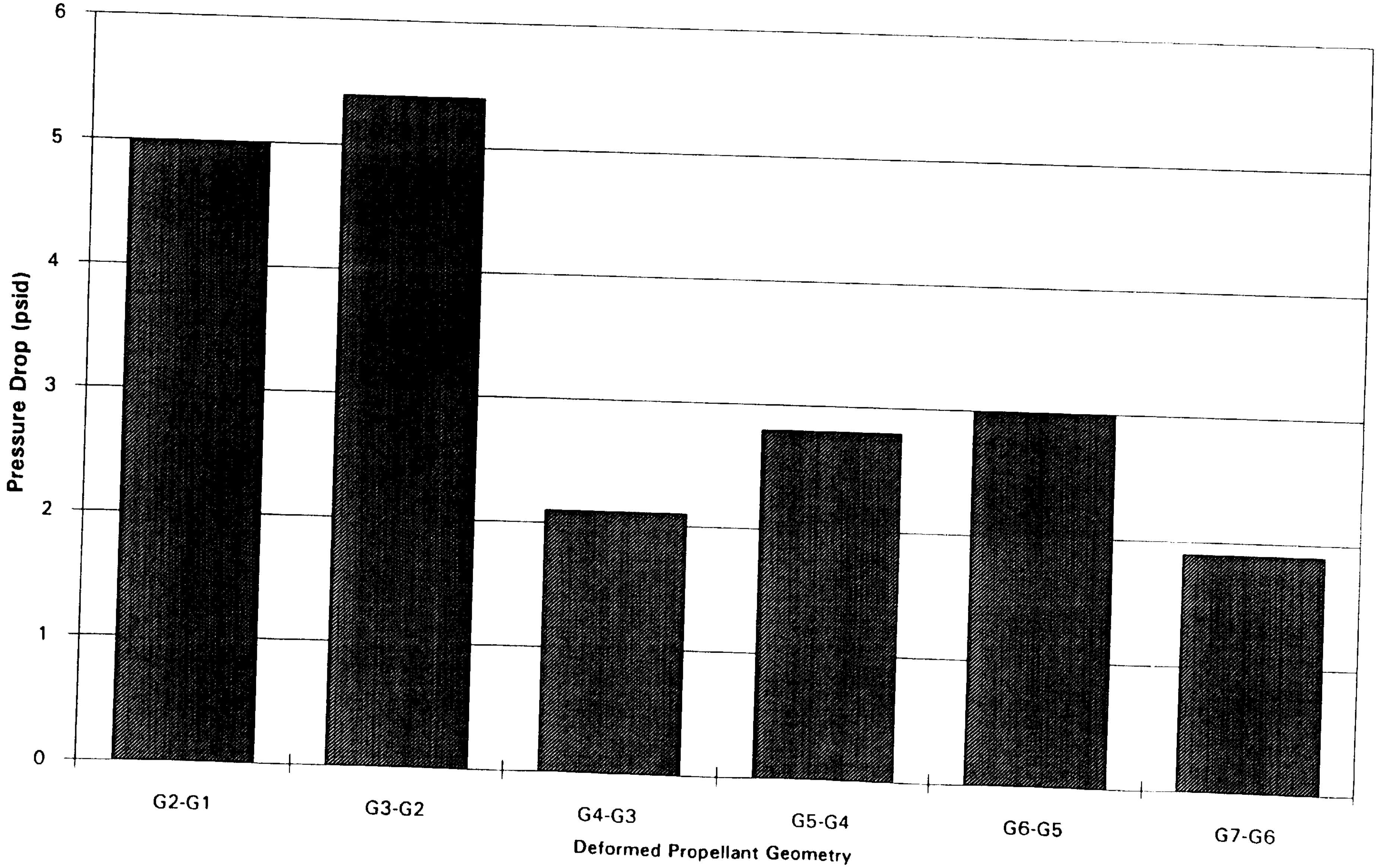

ERC, Inc. 09/10/1993

Figure 7. ASRM Aft Slot Maximum Slot Pressure Differential @ 90 Deg. F

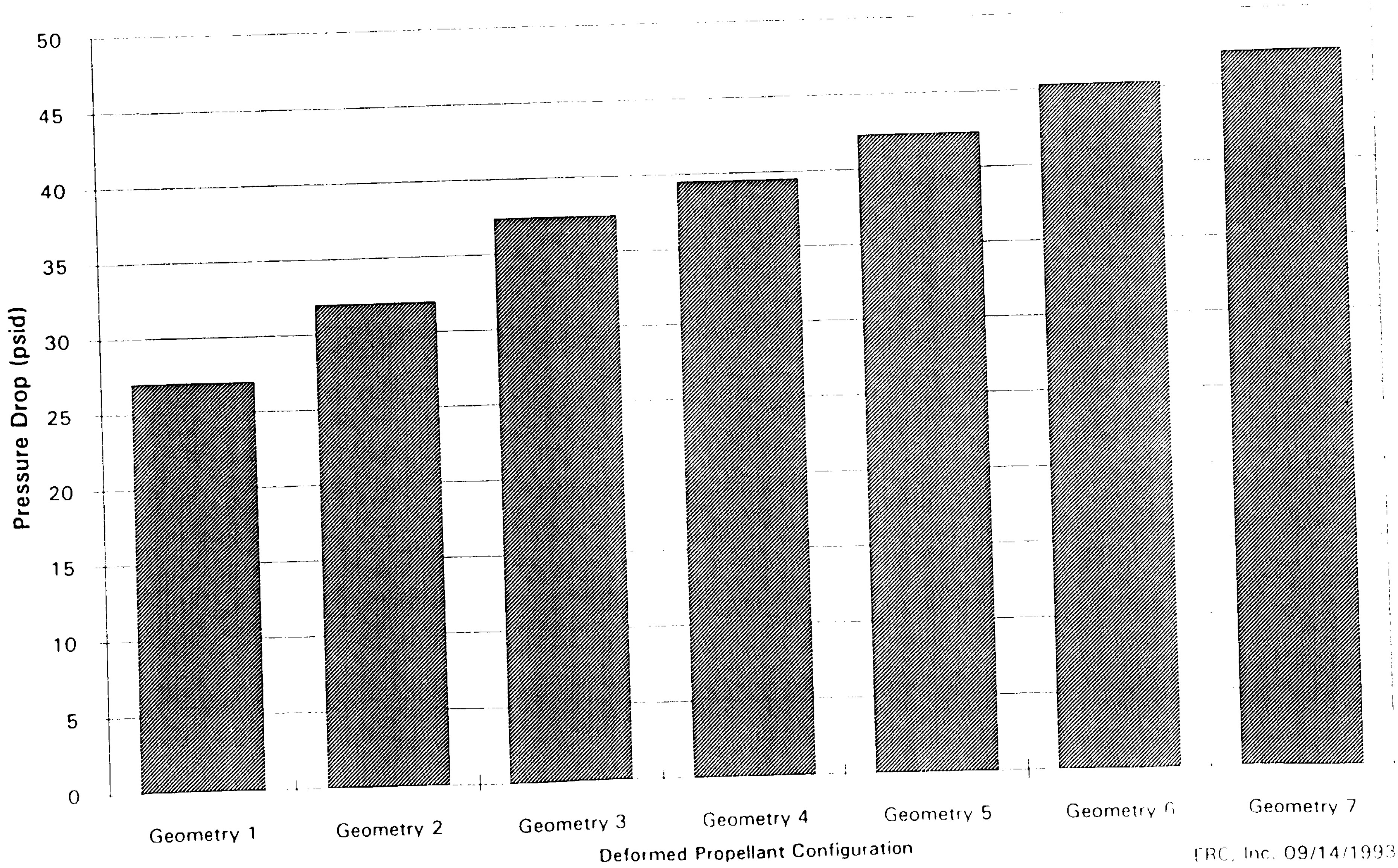

ERC, Inc. 09/14/1993

Figure 6. ASRM Deformed Aft Slot Analysis Step Height Variation as a Function of Geometry Number

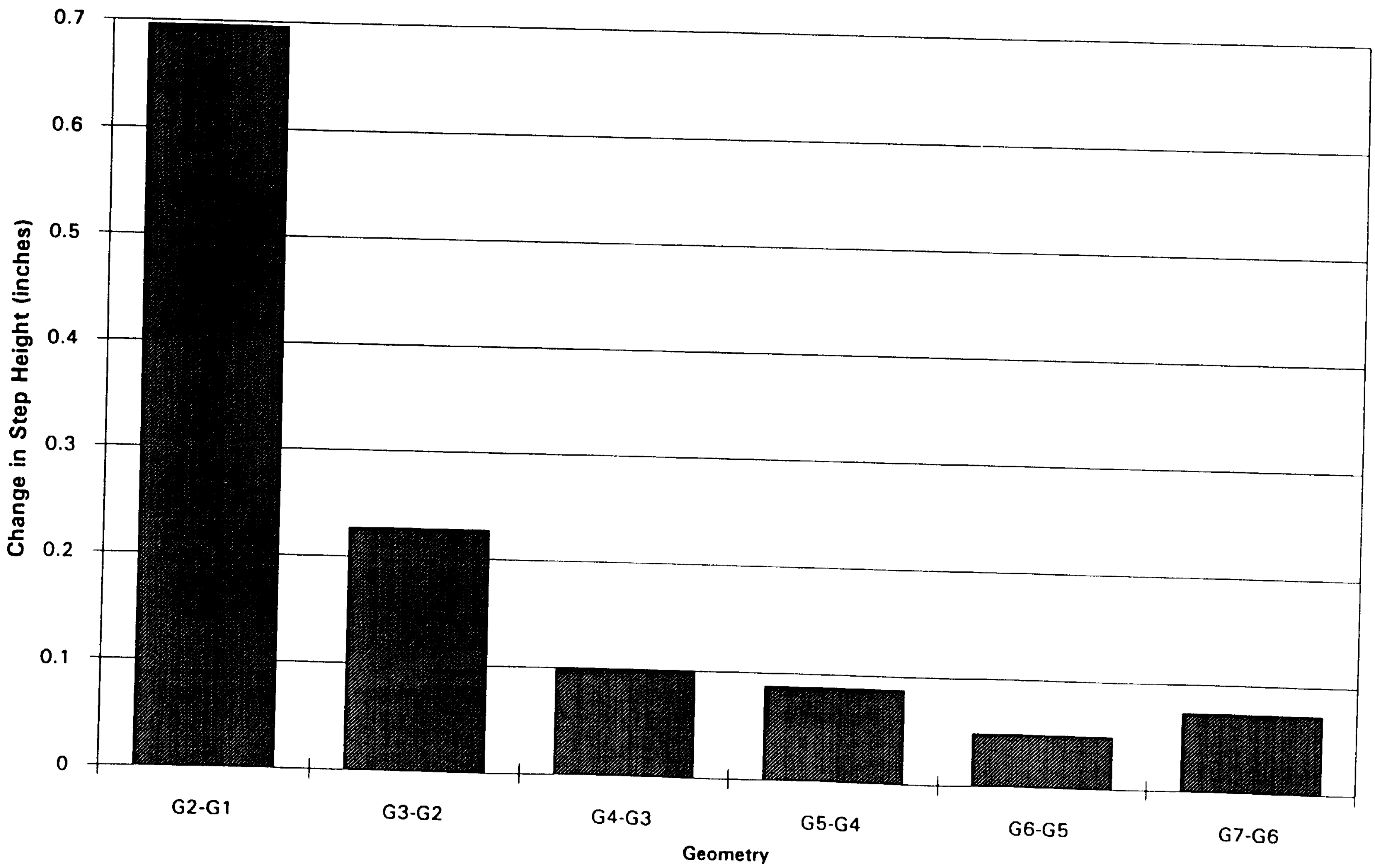

ERC, Inc. 09/14/1993

Figure 5. ASRM Deformed Aft Slot Analysis Slot Width Variation as a Function of Geometry Number

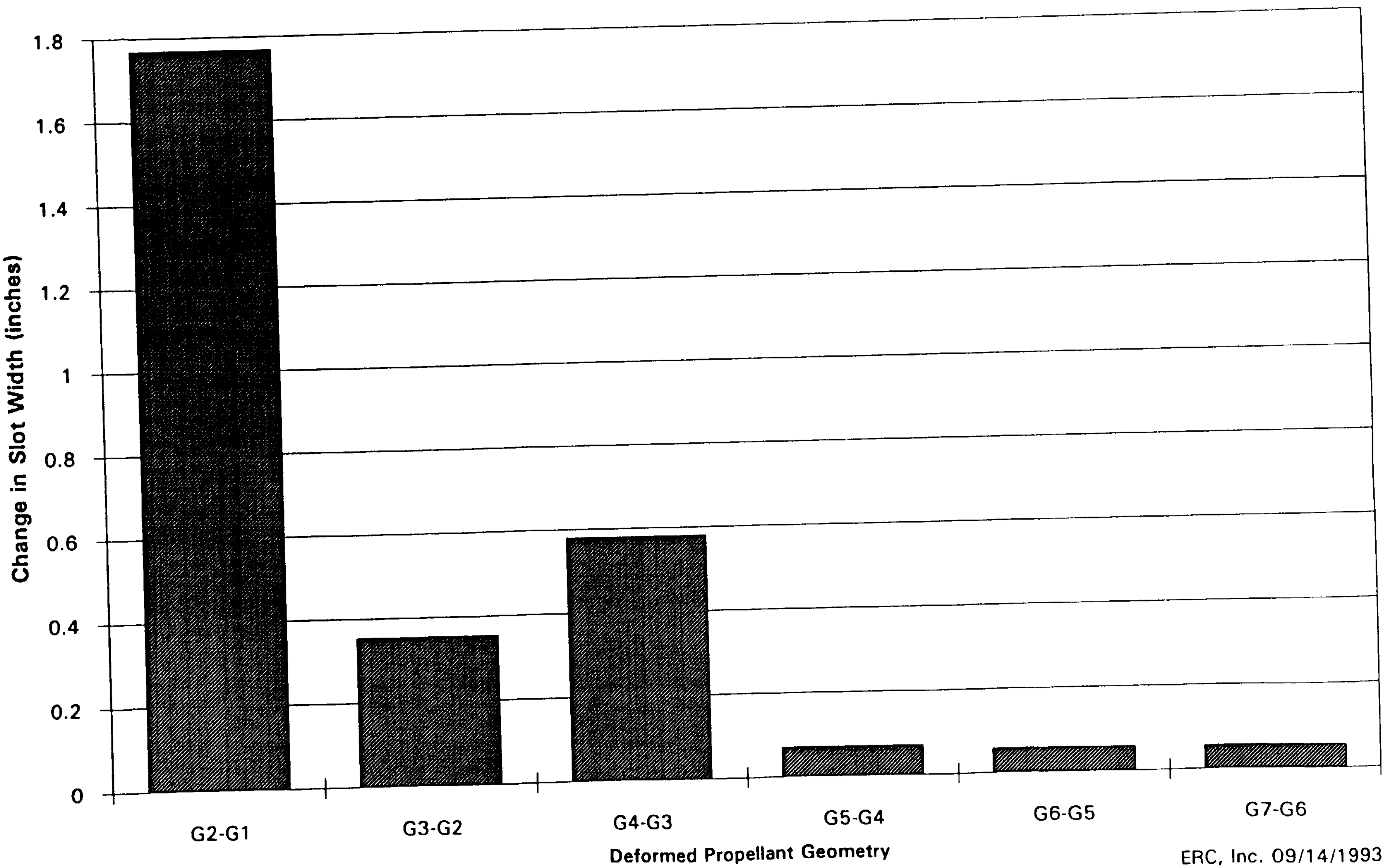

ERC, Inc. 09/14/1993

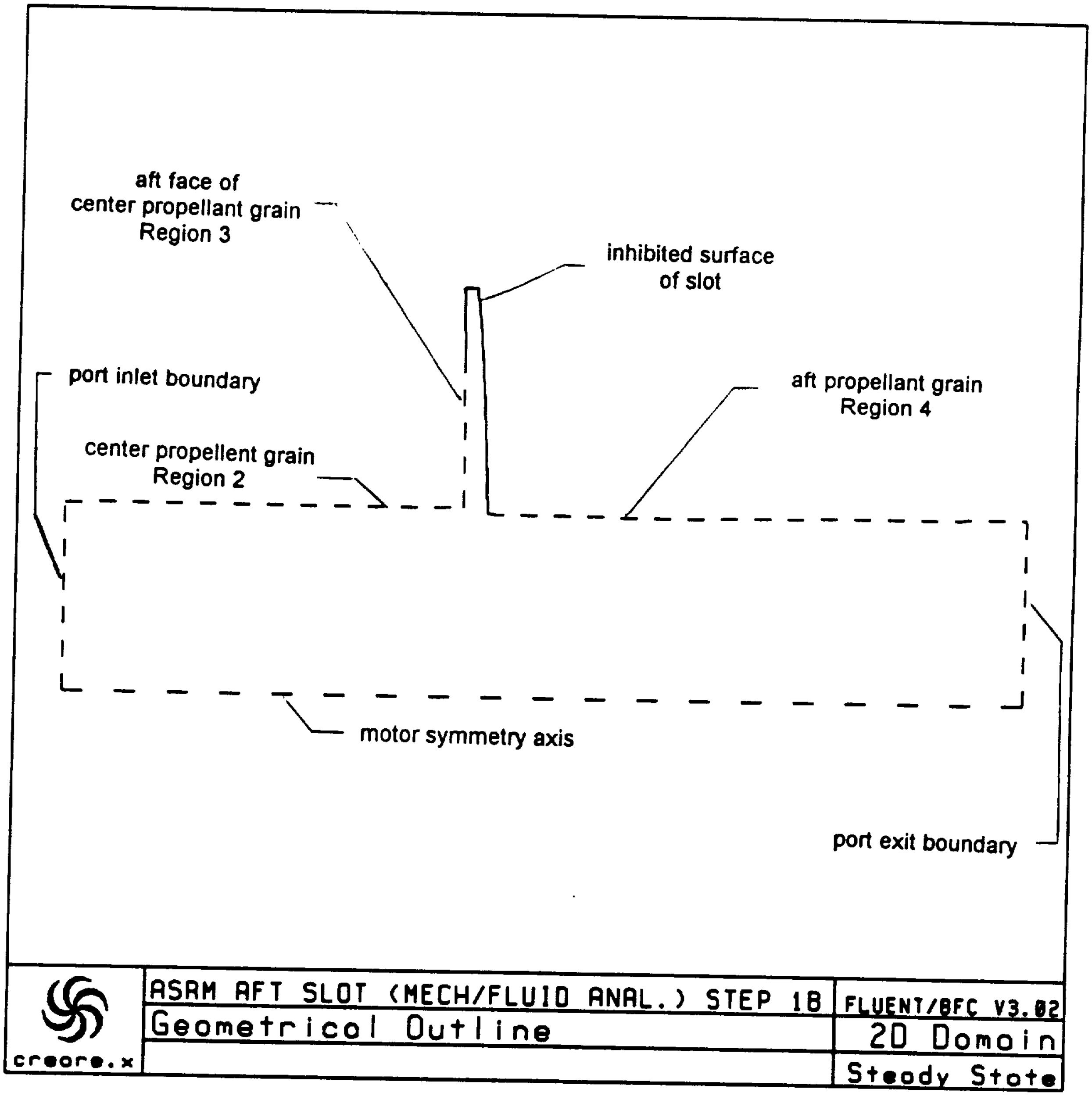

Figure 4. Boundary Condition Types used in the ASRM Aft Slot Deformed Grain Analysis

pressure differential remained about the same for the next two iterations and a decrease of approximately 1 psi for the latest geometry comparison between, G7-G6 was noted. The pressure distribution in the slot region is very similar between geometry 6 and geometry 7 illustrating that the slot deformations are not affecting the flow solution as much as for previous solutions. In conclusion, these figures show that the iterations of the coupled mechanical/fluid dynamic analysis are converging to a stable deformed grain configuration.

The CFD analysis for geometry 7 follows the same method as performed for the other deformed geometries. The grid resolution in the port was 180x30. The grid resolution in the aft slot was 30x50. The grid resolution near the wall was checked to be sure that the distance between the wall and the first node has remained approximately constant through all the runs.

The results of the analysis for geometry 7 are presented in this paragraph. Figure 9 shows a plot of the pressure drop from the bottom of the aft slot where the flow is stagnant to the port exit of the slot flow. Both the forward face (aft face of the center propellant segment) and the aft face (forward face of the aft propellant segment) of the slot are plotted. The aft face of the slot shows a pressure rise coincident with the recirculation region present on the downstream slot face. This recirculation zone was not present in the very early deformed geometry solutions but has developed as the slot width and step height increased. Figure 10 shows the static pressure distribution in the motor port. The pressure distribution for deformed grain geometries Number 1, Number 4, Number 5, Number 6 and Number 7 are compared in the plot. All the solutions show that the pressure drop is very sharp between the slot faces and the port wall at the downstream corner of the slot. The position of the aft corner of the center grain remained almost constant from geometry 6 to geometry 7 with all the movement in the slot occurring due to movement of the aft propellant grain segment. The pressure distribution for geometries 6 and 7 are very similar. The distributions follow one another much closer than for the previous iterations. It would be expected that another iteration on the geometry would show less movement than occurred between iteration 6 and 7. Figure 11 shows the pressure distribution on the center and aft propellant grains. Only a portion of the center and aft propellant grain segments were modeled. The curve in Figure 11 was generated by combining the CFD pressure distribution from the aft slot region analysis with the ballistic run pressure distribution upstream and downstream of the CFD problem domain.

and a zero gradient flux boundary condition on all variables in the axial coordinate direction was used at the port exit boundary.

The iteration process was continued from iteration 1 through iteration 7. Analysis results associated with the final aft slot deformed grain, geometry 7, and a summary of the final results of the completed coupled mechanical/fluid dynamic analysis for the 90 degree F propellant storage temperature are presented in this report. Representatives from NASA, Sverdrup and ERCI met on August 30, 1993 to discuss the complete analysis. The pressure distribution for the final deformed grain geometry 7 was discussed along with the previous deformed geometry results. It was decided that the analysis would be concluded based on the small changes in slot geometry over the last three geometry iterations.

Analysis of the ASRM aft slot deformed grain for geometry 7 was completed during the month of August. Table 3 shows a summary of how the slot geometry has changed for the 7 deformed geometries considered in this analysis.

Table 3. ASRM Deformed Slot Step Height and Slot Width Changes

Deformed Geometry	Step Height	Slot Width
1	1.054 inches	4.080 inches
2	1.750 inches	5.849 inches
3	1.977 inches	6.202 inches
4	2.076 inches	6.608 inches
5	2.164 inches	6.678 inches
6	2.213 inches	6.735 inches
7	2.286 inches	6.790 inches

Figure 5 shows a plot of the change in the slot width from geometry to geometry for the 7 deformed configurations analyzed. The slot width is the axial distance from the aft port corner of the center grain segment to the forward port corner of the aft grain segment. The changes in slot width from geometry to geometry have been below 0.1 inches since the change in the motor case boundary conditions between geometry 3 and 4. Figure 6 shows the change in the step height from geometry to geometry. The step height is the difference between the radius of the aft port corner of the center grain segment and the forward port corner of the aft grain segment. The changes in step height have also remained well below 0.1 inches since the change in case boundary conditions between geometry 3 and geometry 4. Figure 7 shows a comparison of how the maximum pressure drop (change in pressure between the bottom of the aft slot and the forward port corner of the aft grain segment) changes from geometry to geometry. The pressure differential for geometry 7 is also included in this figure which was not shown in the July monthly report. Figure 8 shows the increase in the maximum slot pressure differential from geometry to geometry. The maximum pressure differential jumped at the change in the motor case boundary conditions. Since that time, the

Figure 28. ASRM Full-Scale Motor Velocity Profiles

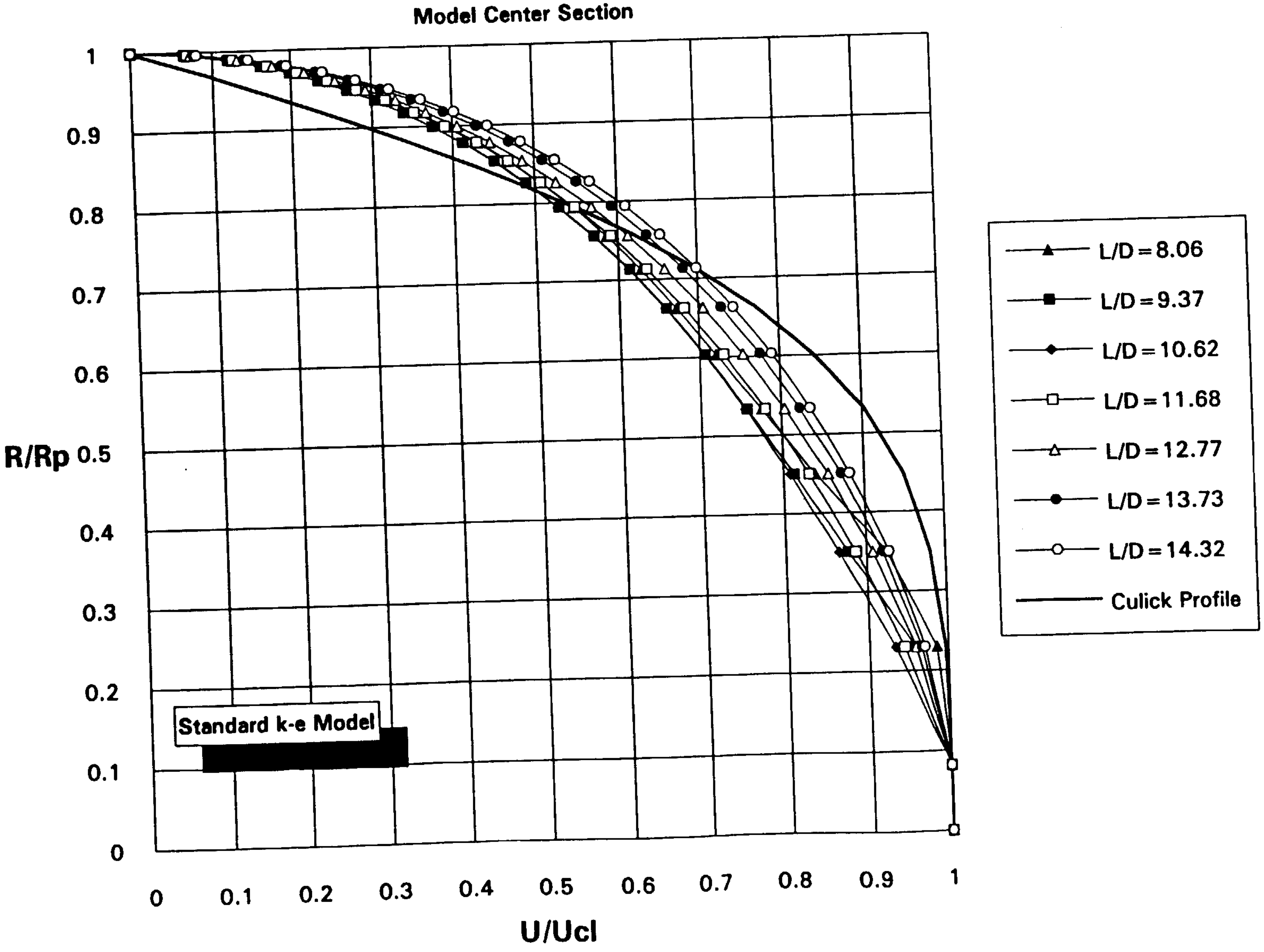

ERCI 08/13/92

Figure 27. ASRM Full-Scale Motor Velocity Profiles

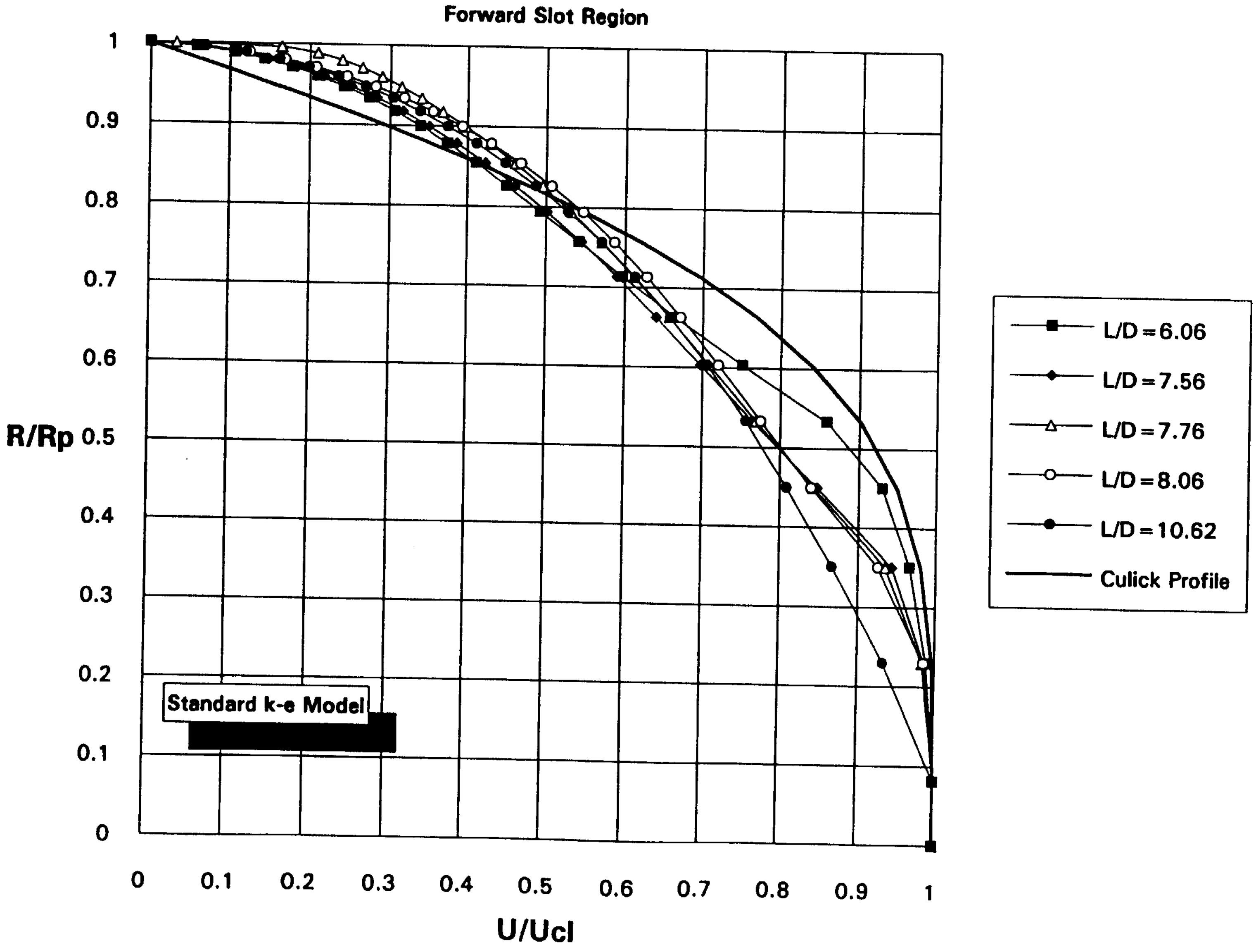

ERCI 08/13/92

Figure 26. ASRM Full-Scale Motor Velocity Profiles

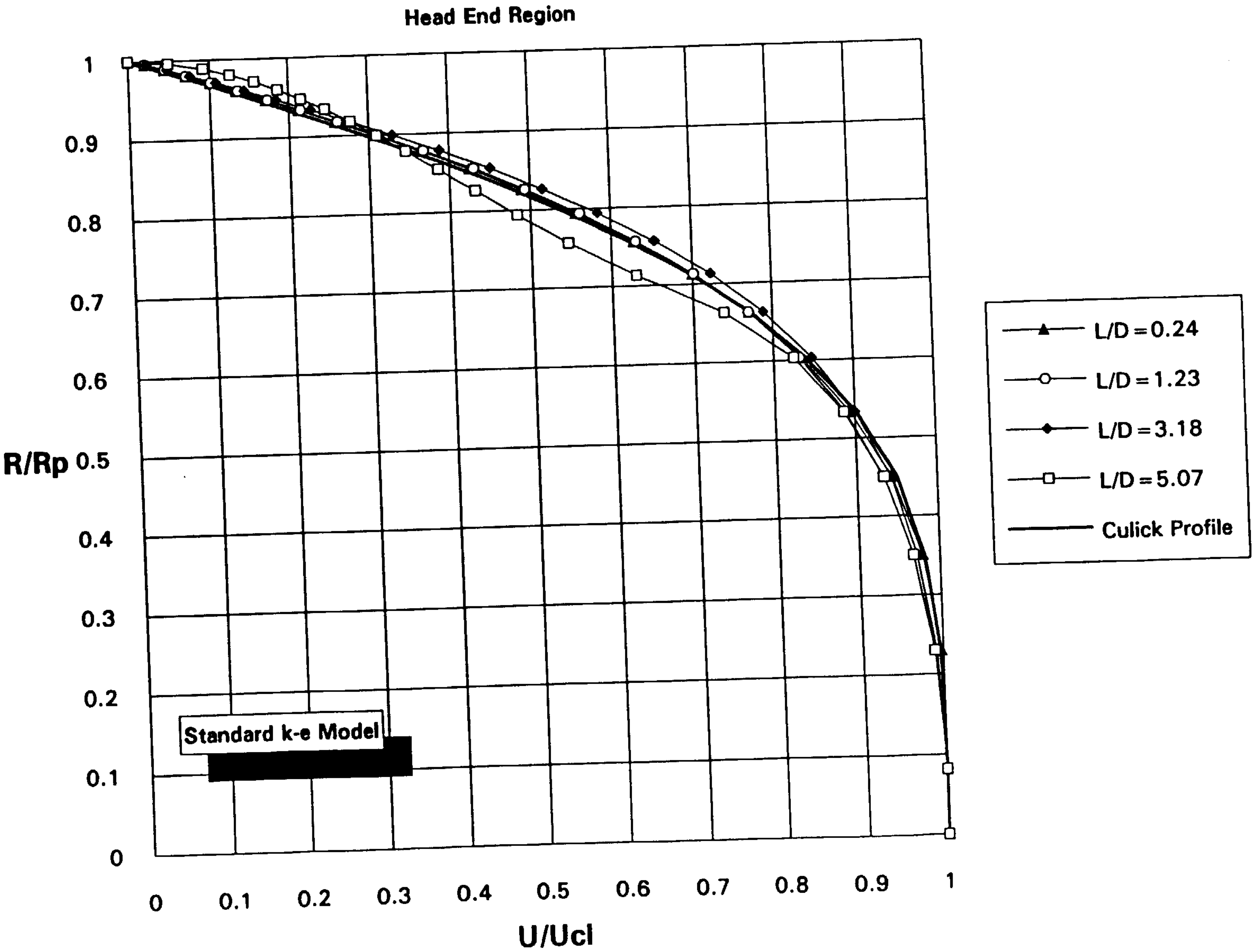

ERCI 08/13/92

Figure 25. ASRM Full-Scale Motor Velocity Profiles

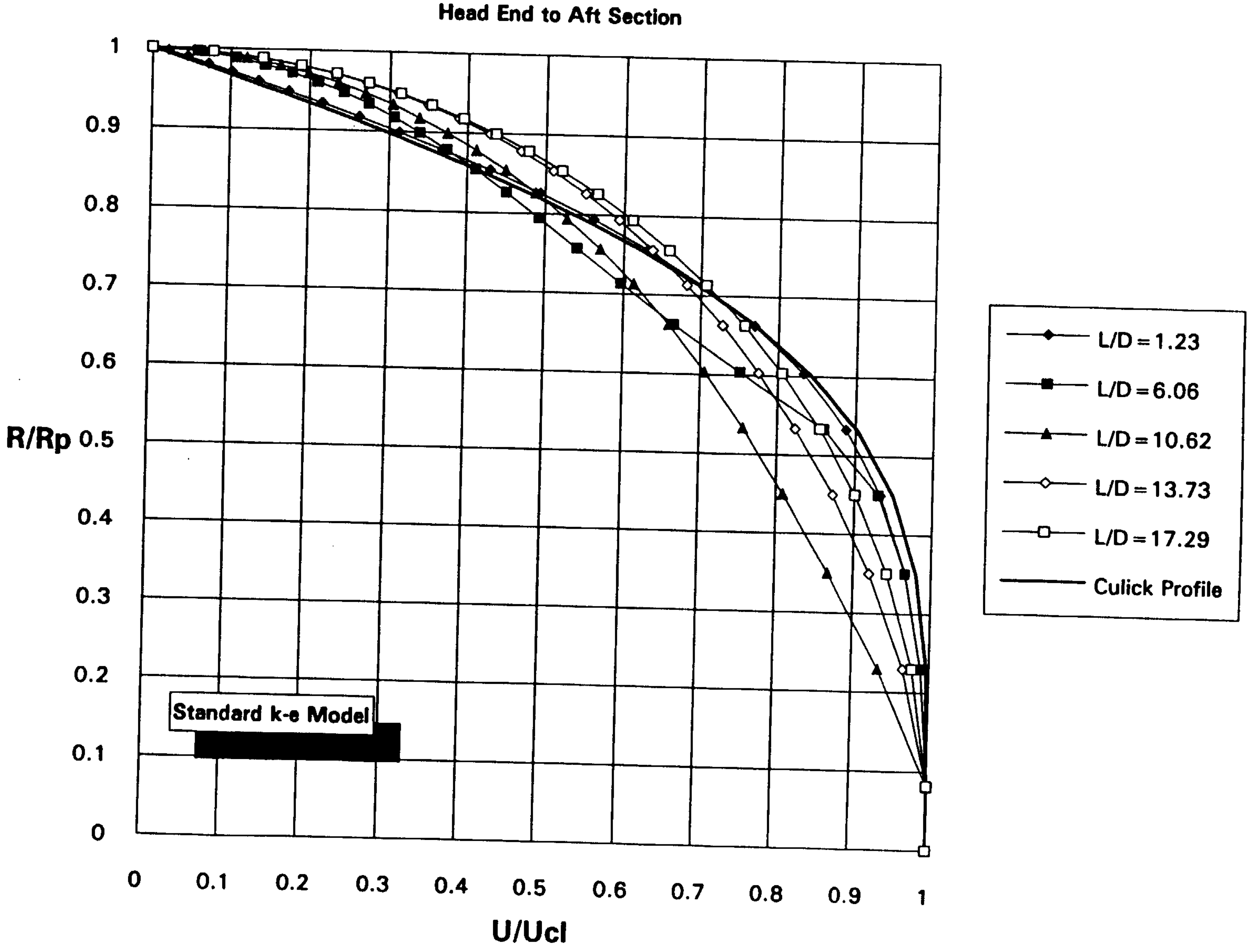

ERCI 08/13/92

Figure 24. ASRM Full-Scale Motor Total Pressure

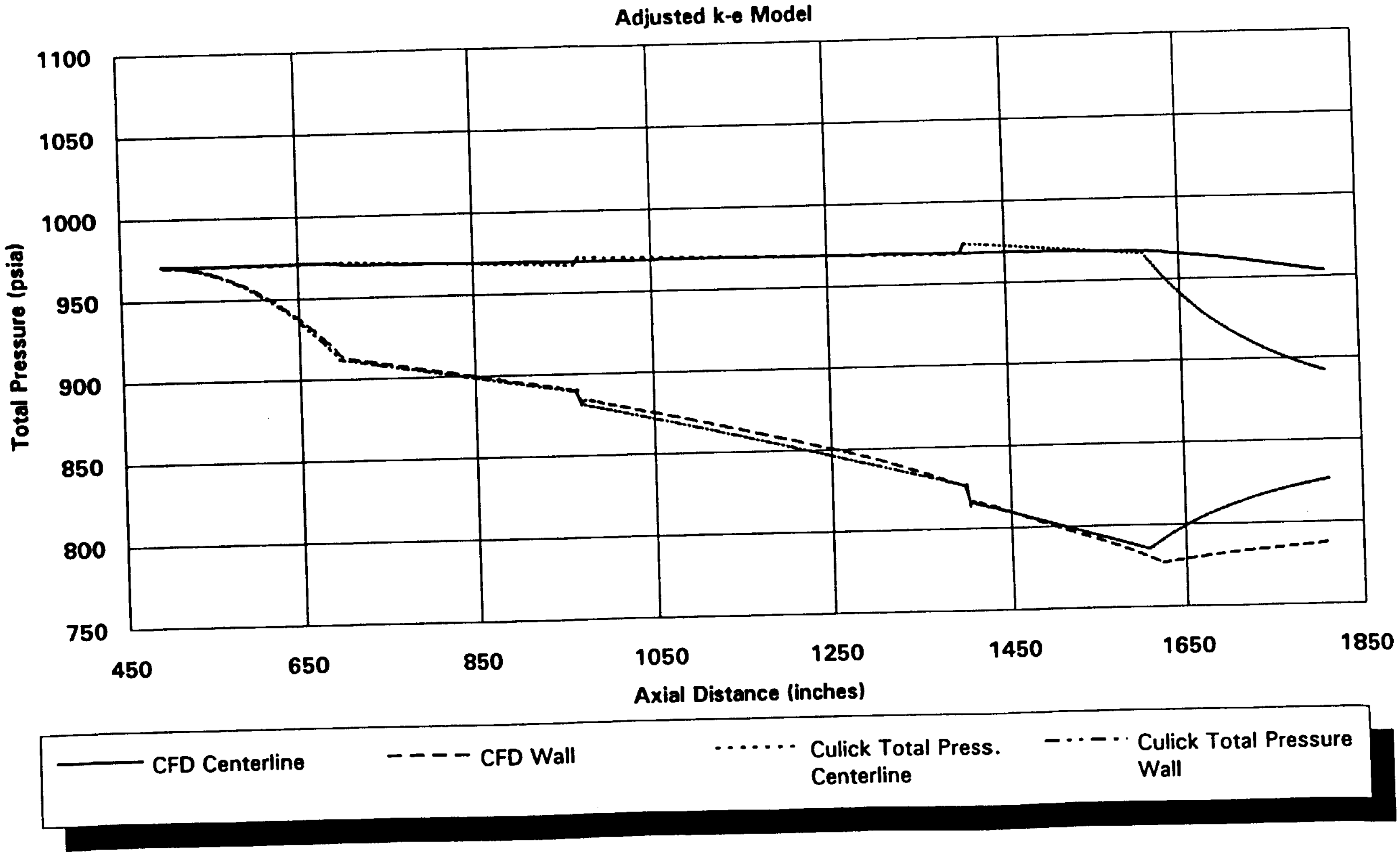

Adjusted k-e Model

Figure 23. ASRM Full-Scale Motor Total Pressure

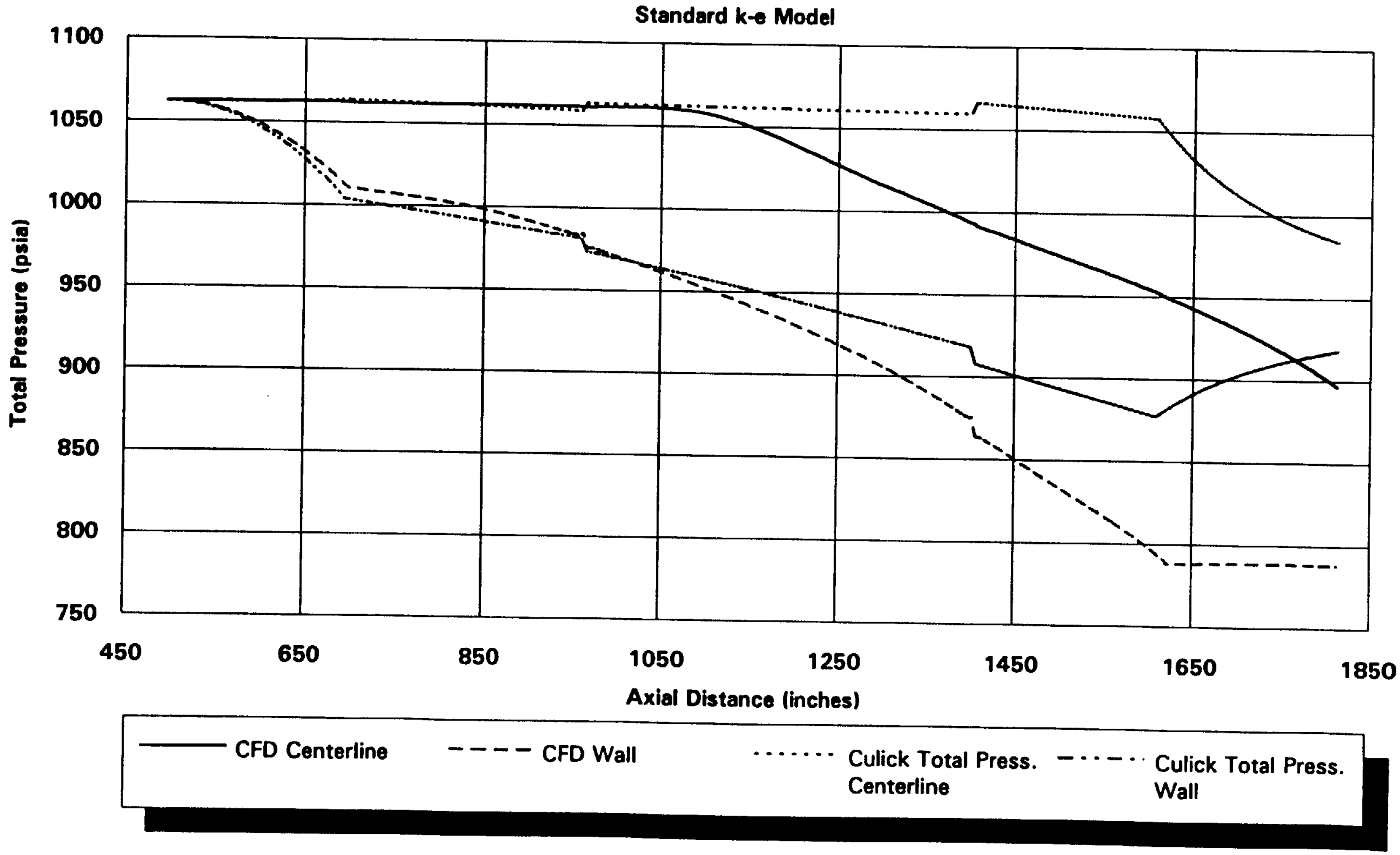

ERC, Inc. 08/13/92

Figure 22. ASRM Full-Scale Motor Static Pressure

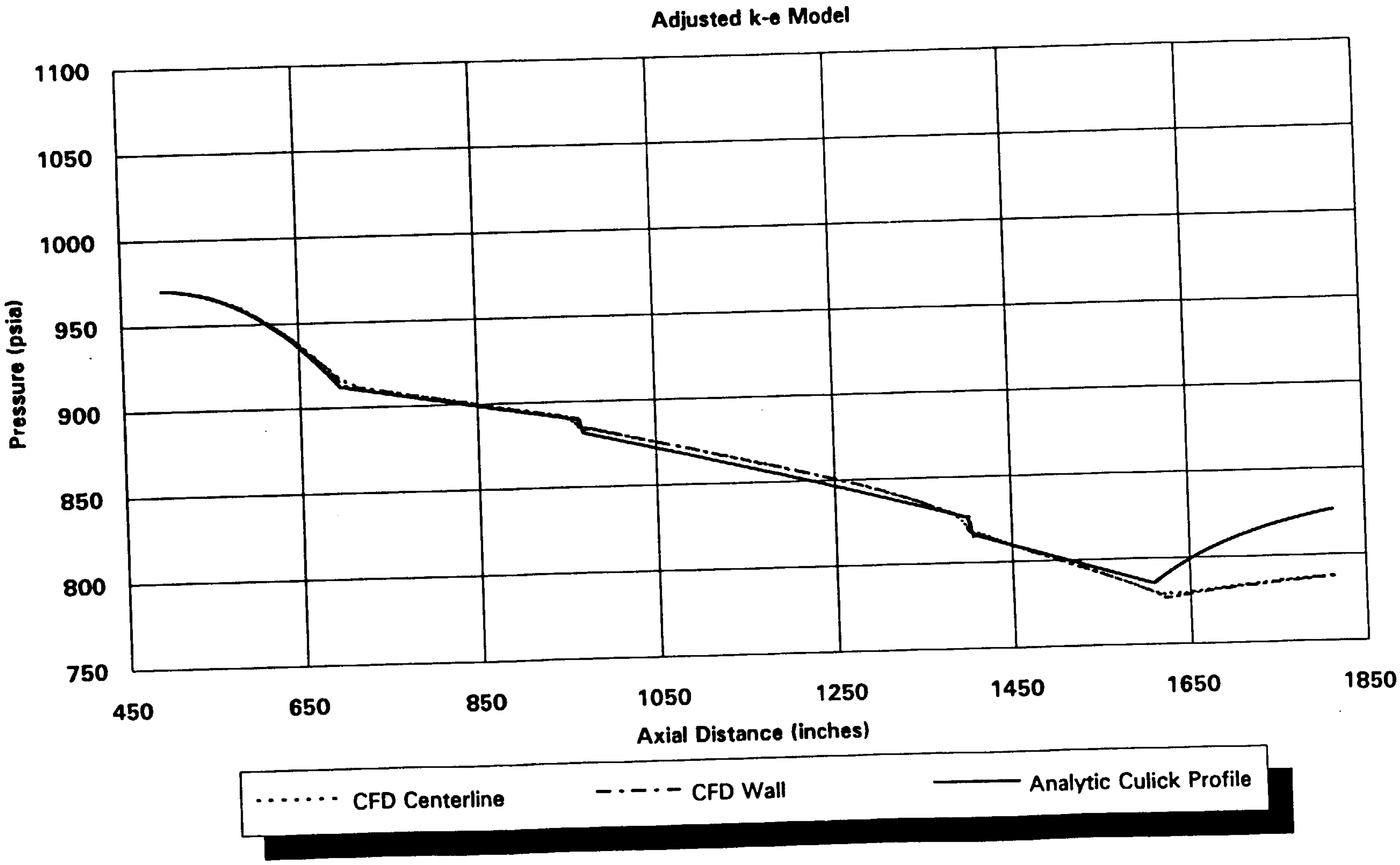

ERC, Inc. 08/13/92

Figure 21. ASRM Full-Scale Motor Static Pressure

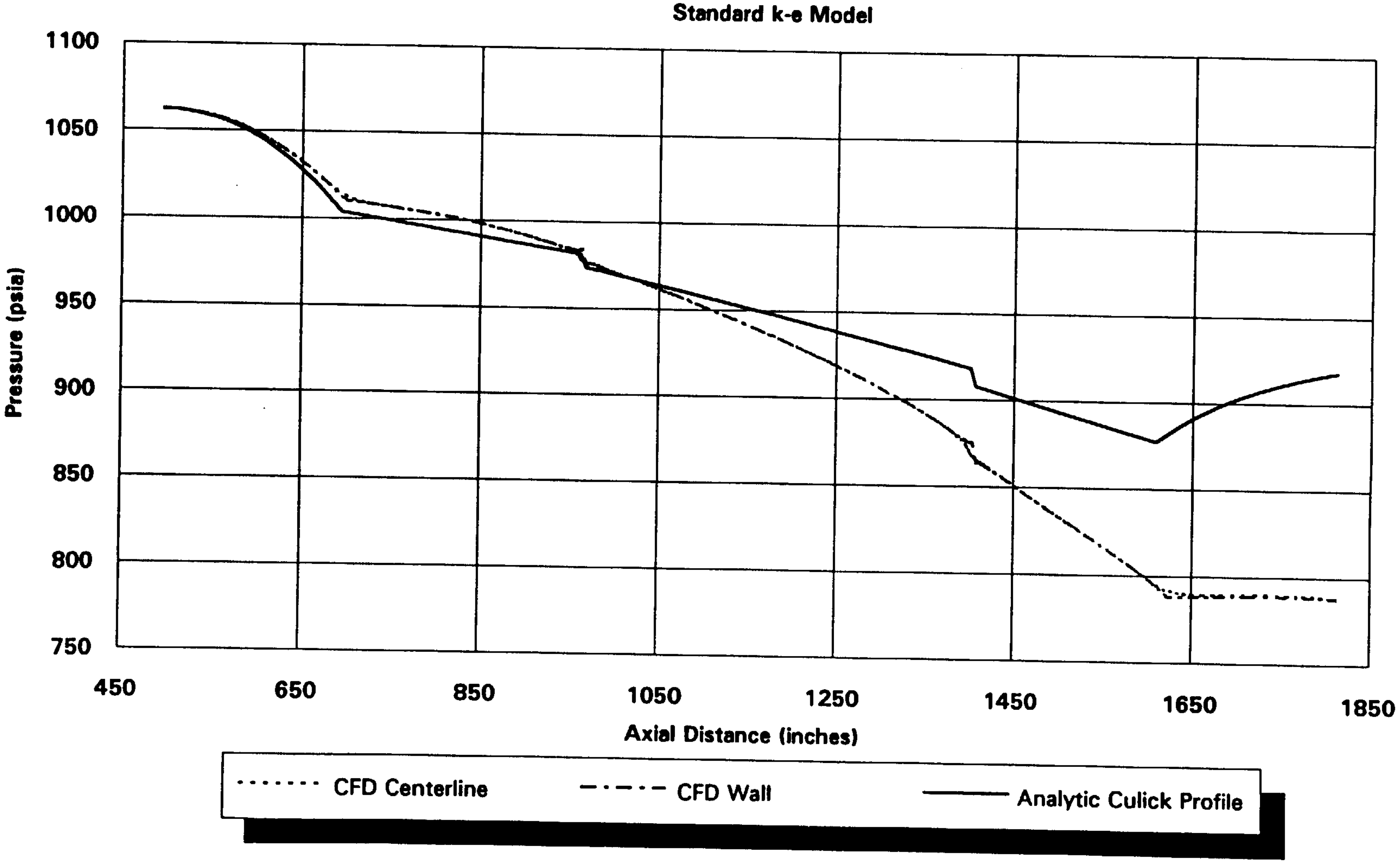

ERC, Inc. 08/13/92

Figure 20. ASRM Full-Scale Motor Mach Number

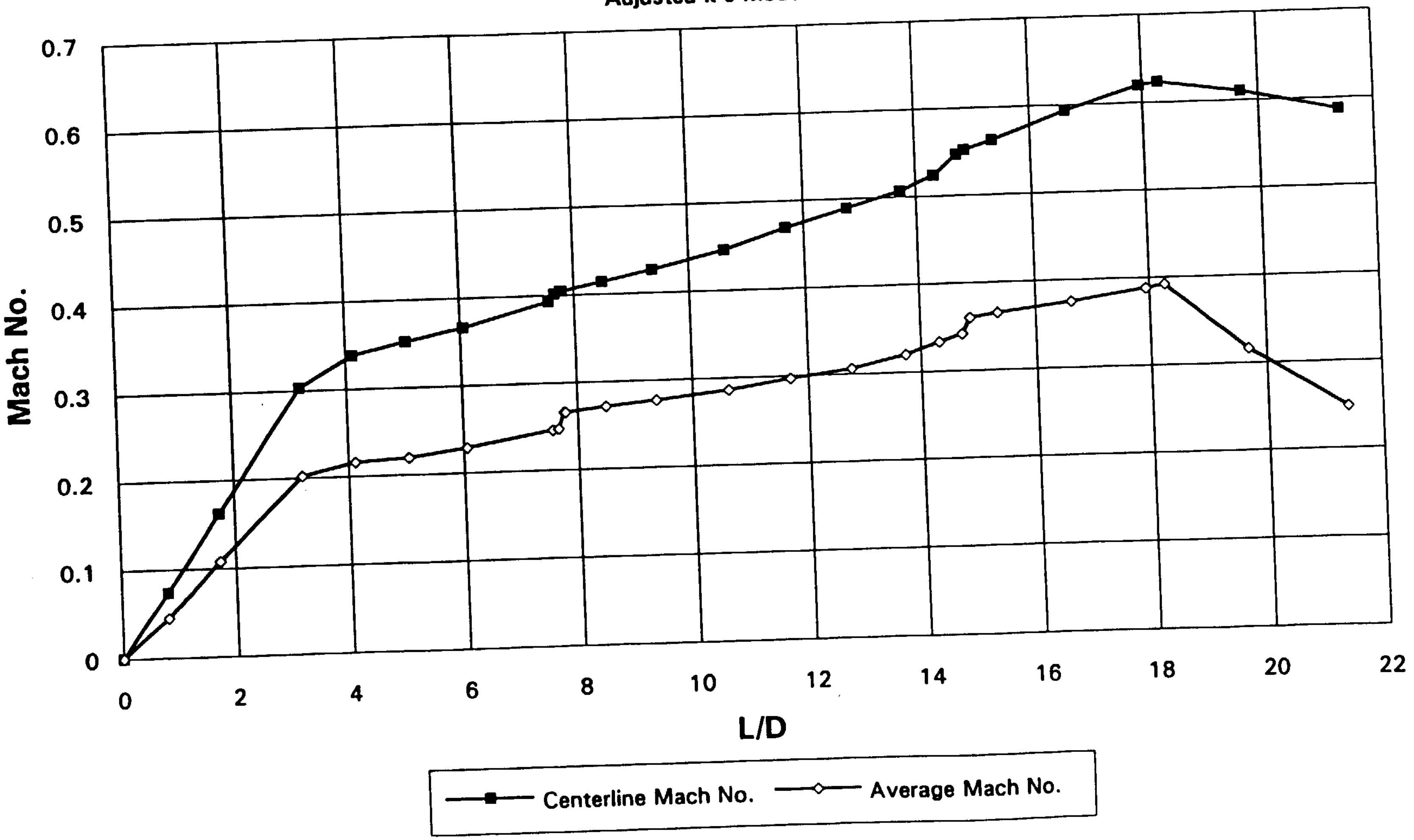
Adjusted k-e Model

ERCI 08/13/92

Figure 19. ASRM Full-Scale Motor Mach Number

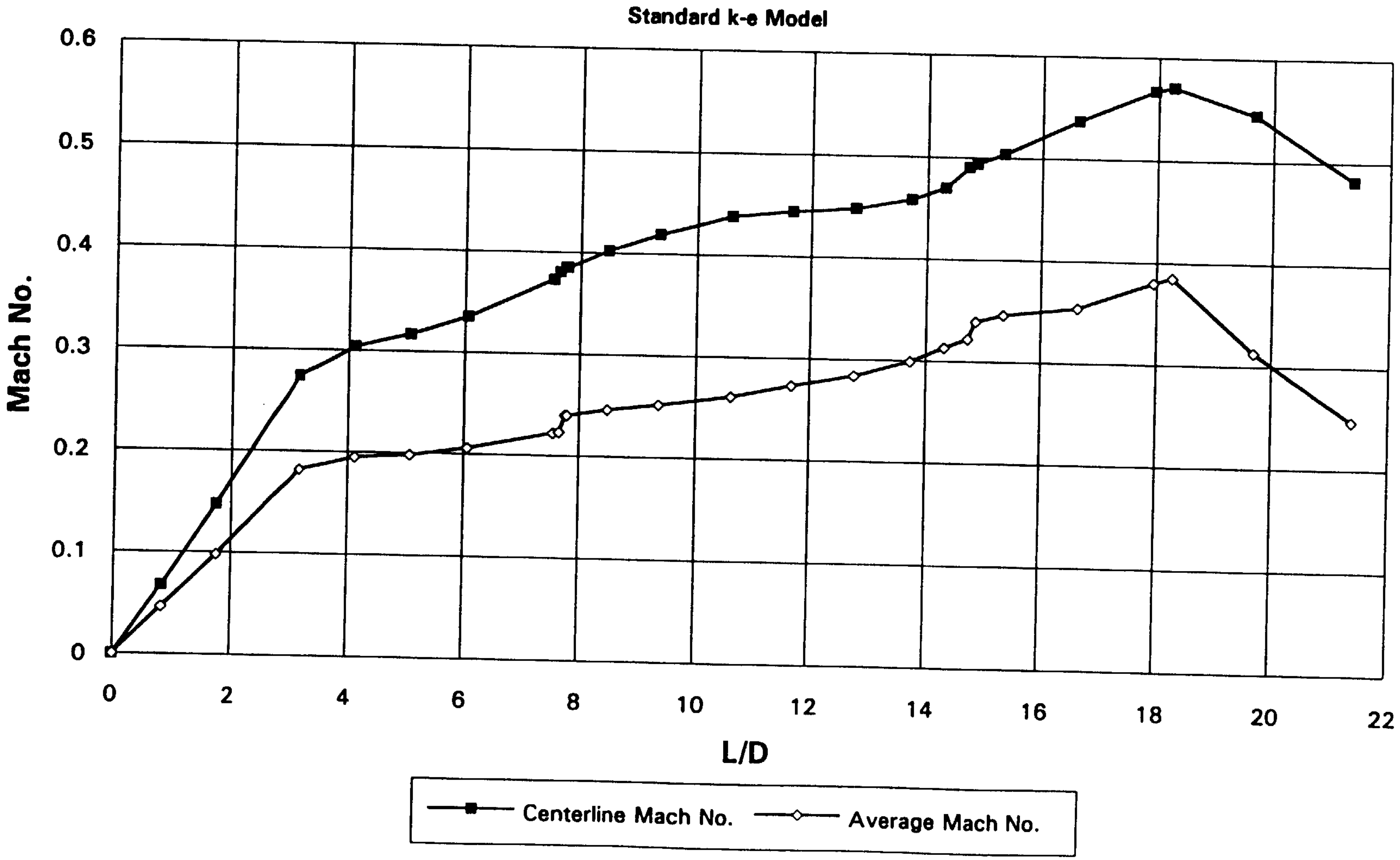

ERCI 08/13/92

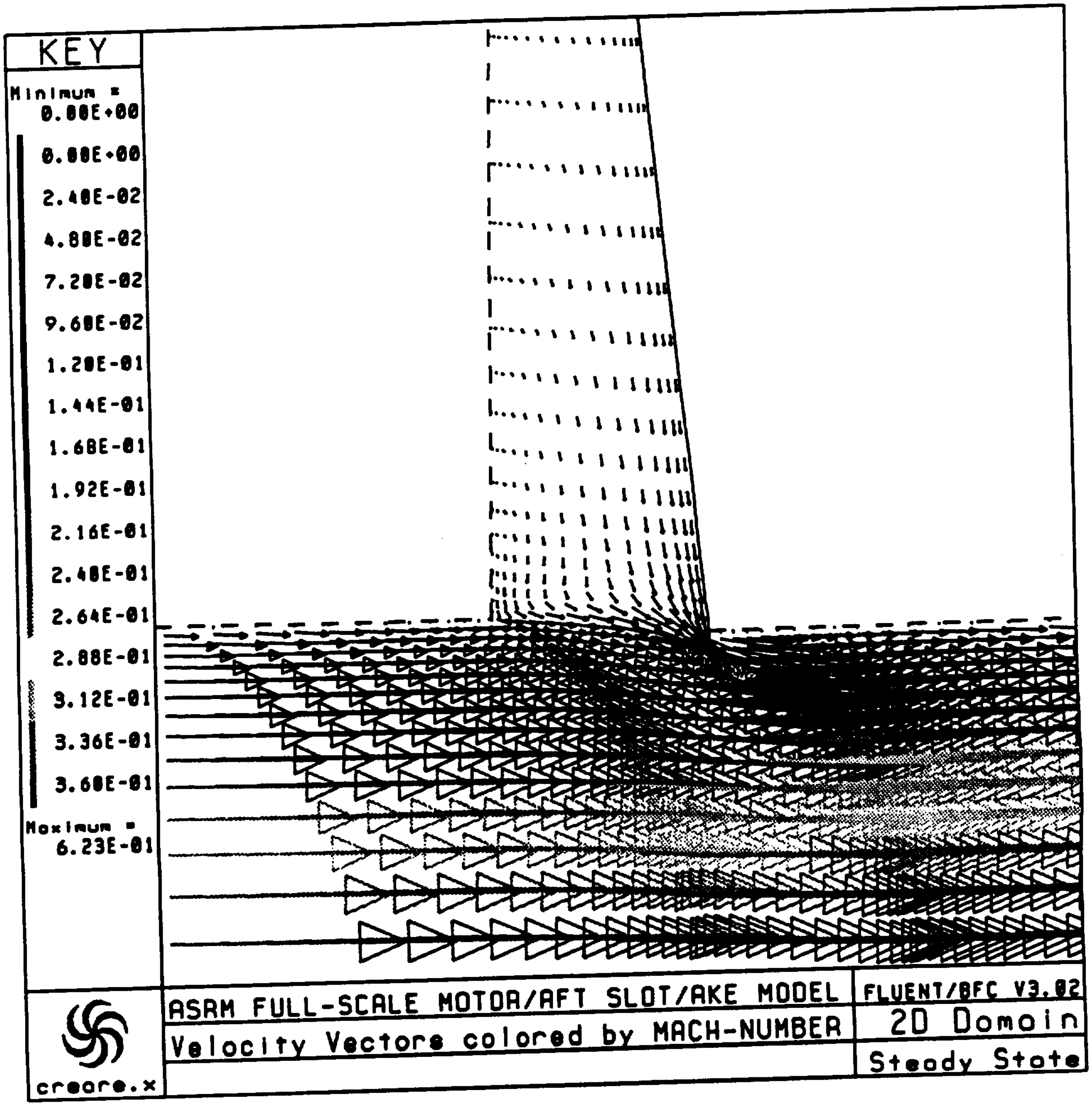

Figure 18. Velocity Field in the Aft Slot Region, AKE Model

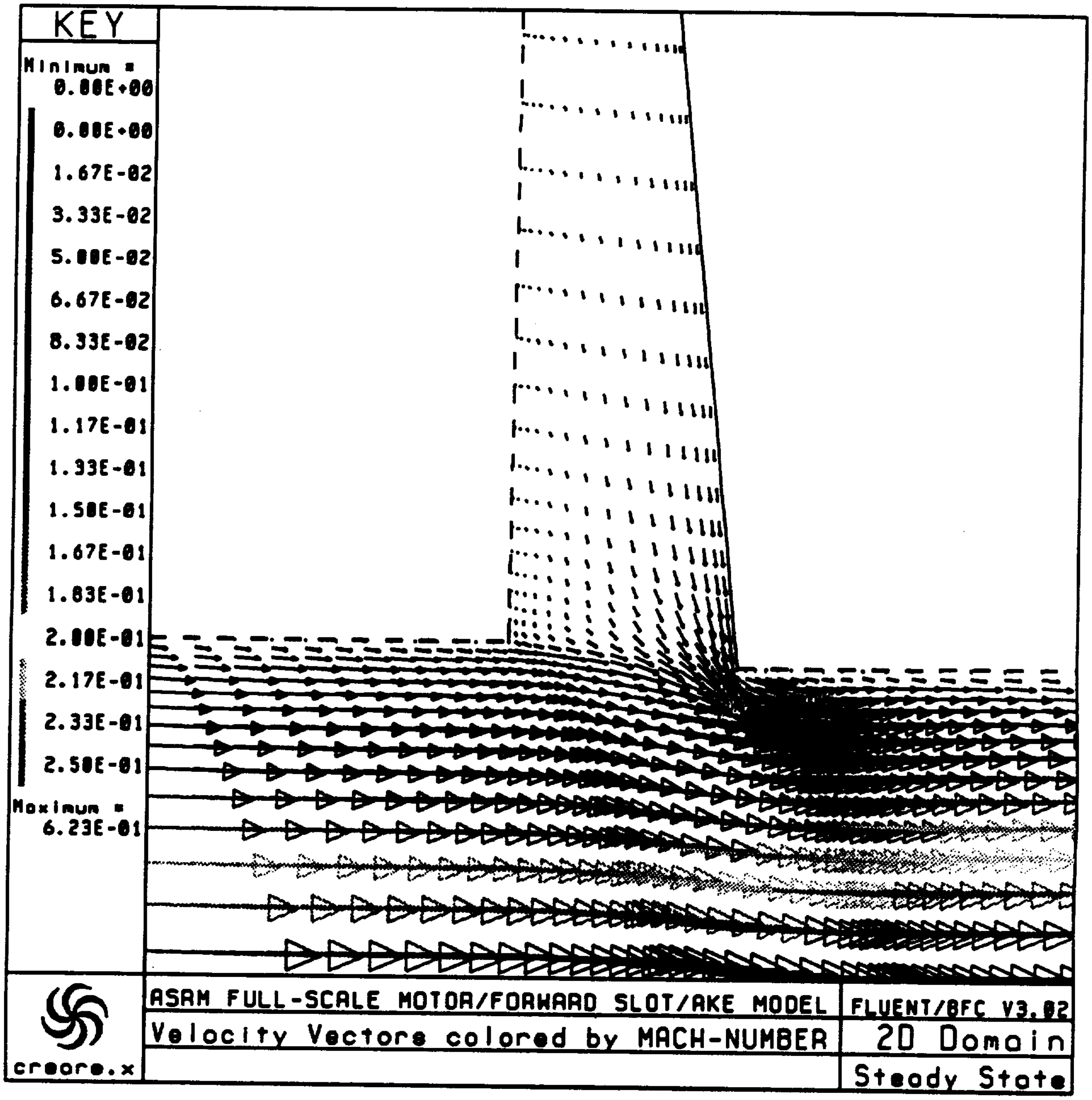

Figure 17. Velocity Field in the Forward Slot Region, AKE Model

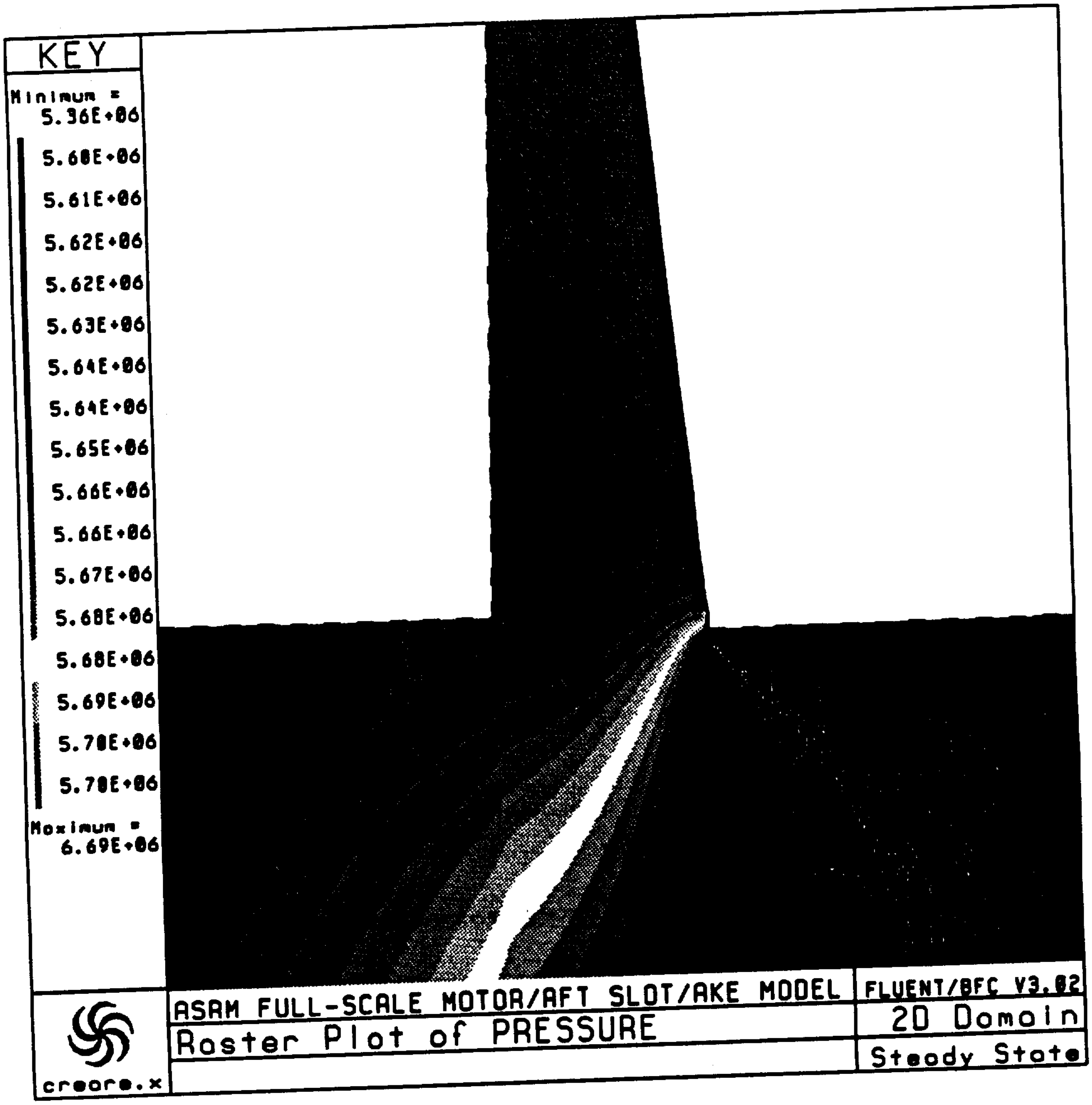

Figure 16. Static Pressure in the Aft Slot Region, AKE Model

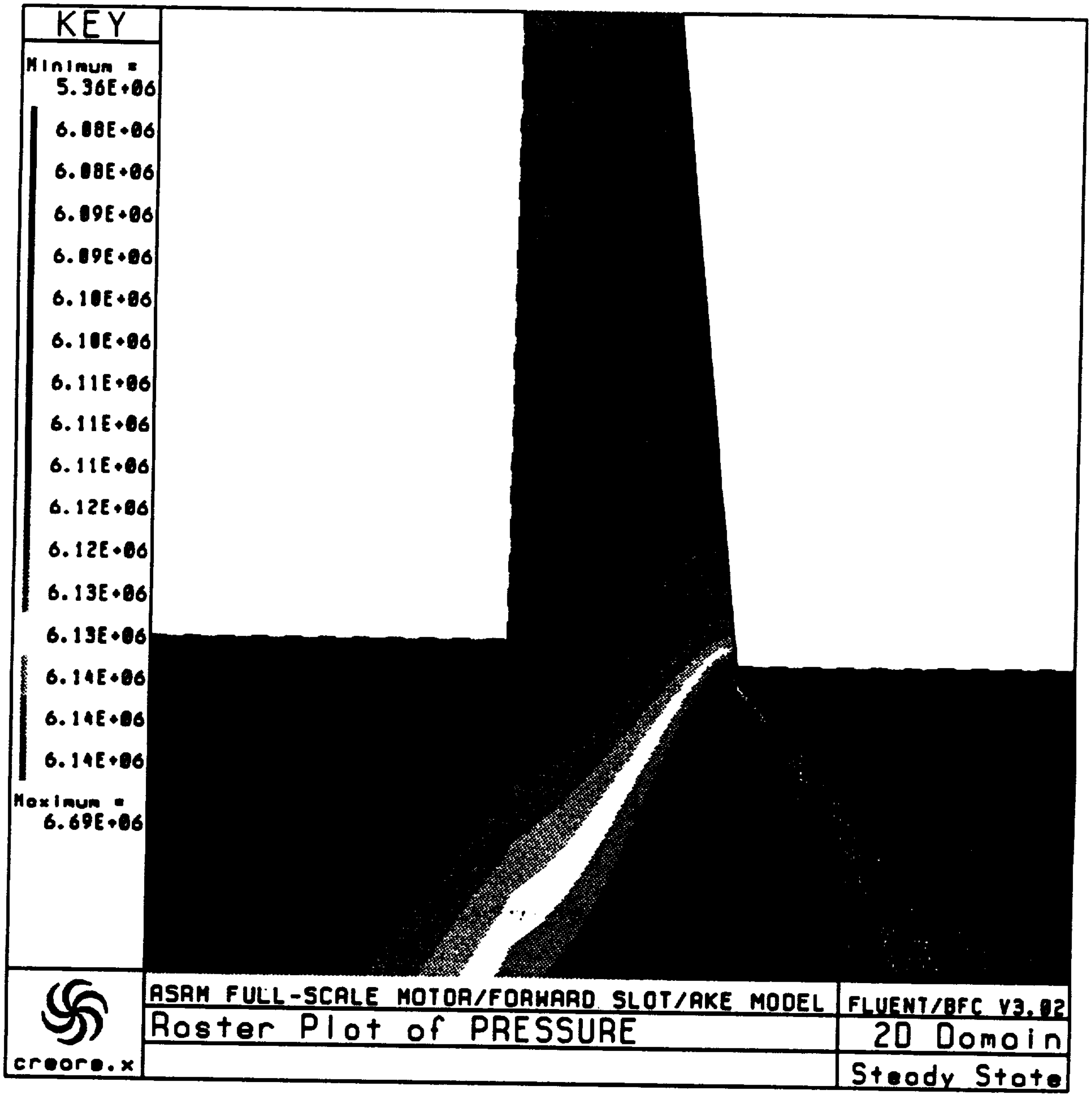

Figure 15. Static Pressure in the Forward Slot Region, AKE Model

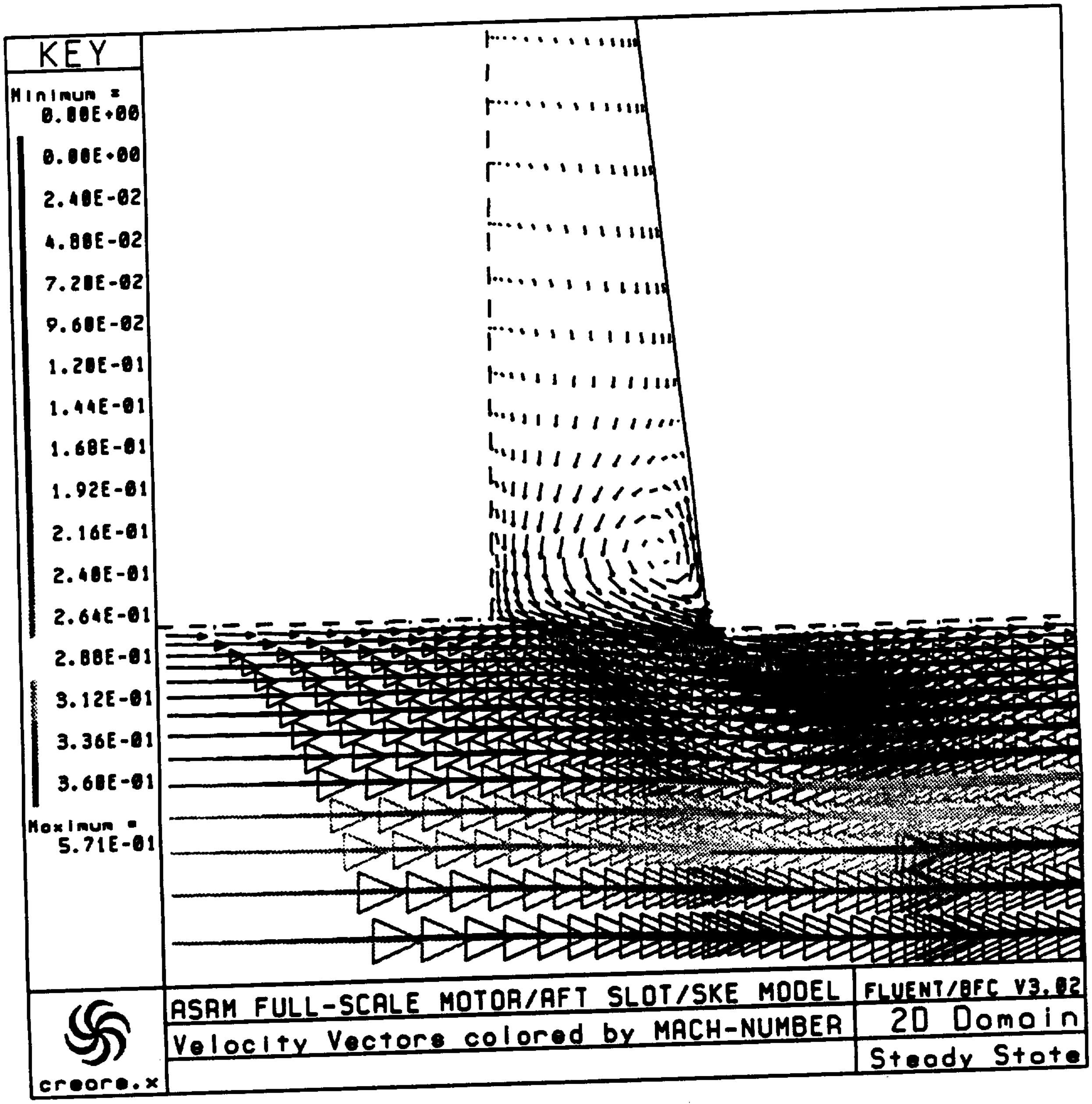

Figure 14. Velocity Field in the Aft Slot Region, SKE Model

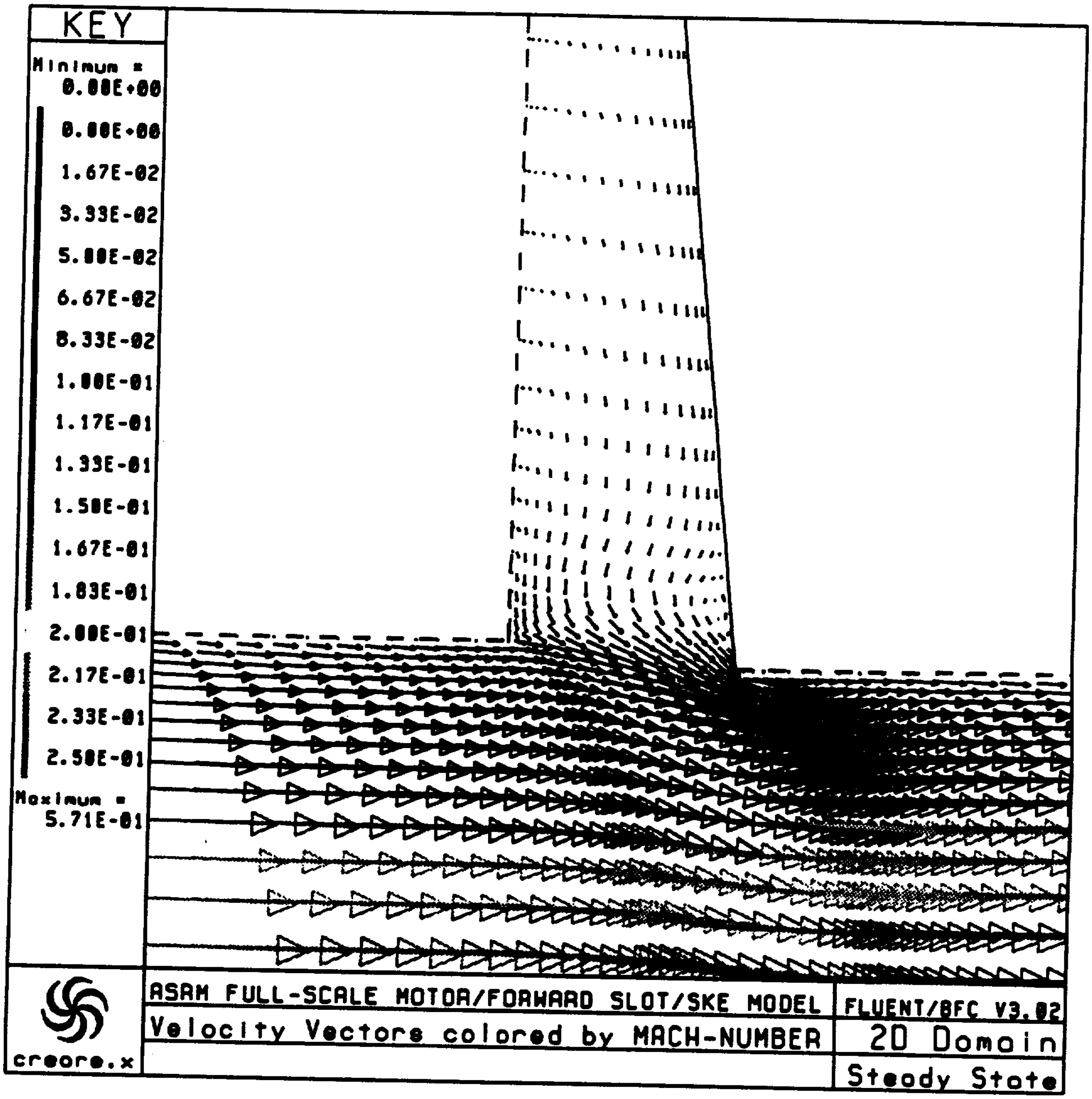

Figure 13. Velocity Field in the Forward Slot Region, SKE Model

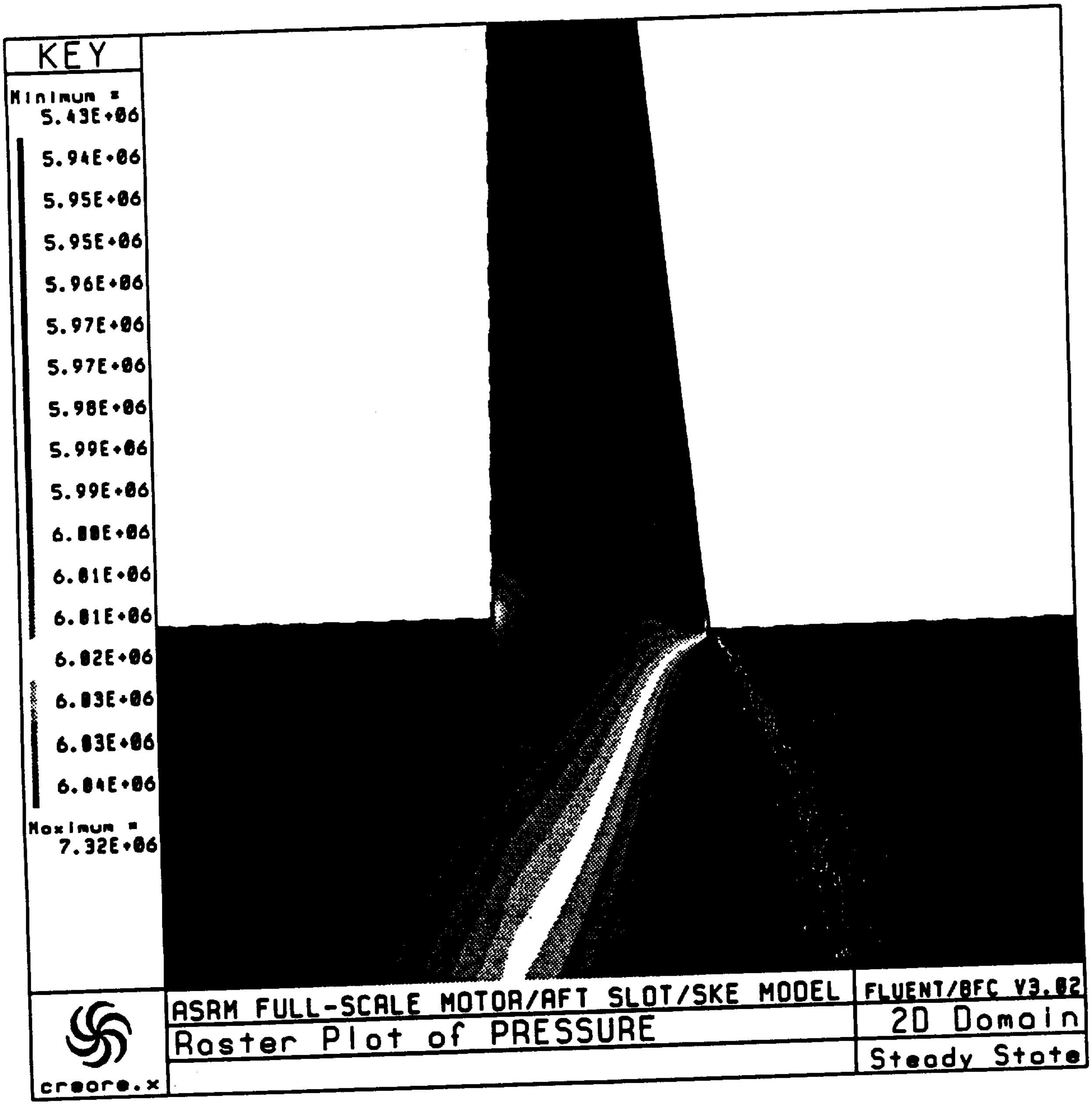

Figure 12. Static Pressure in the Aft Slot Region, SKE Model

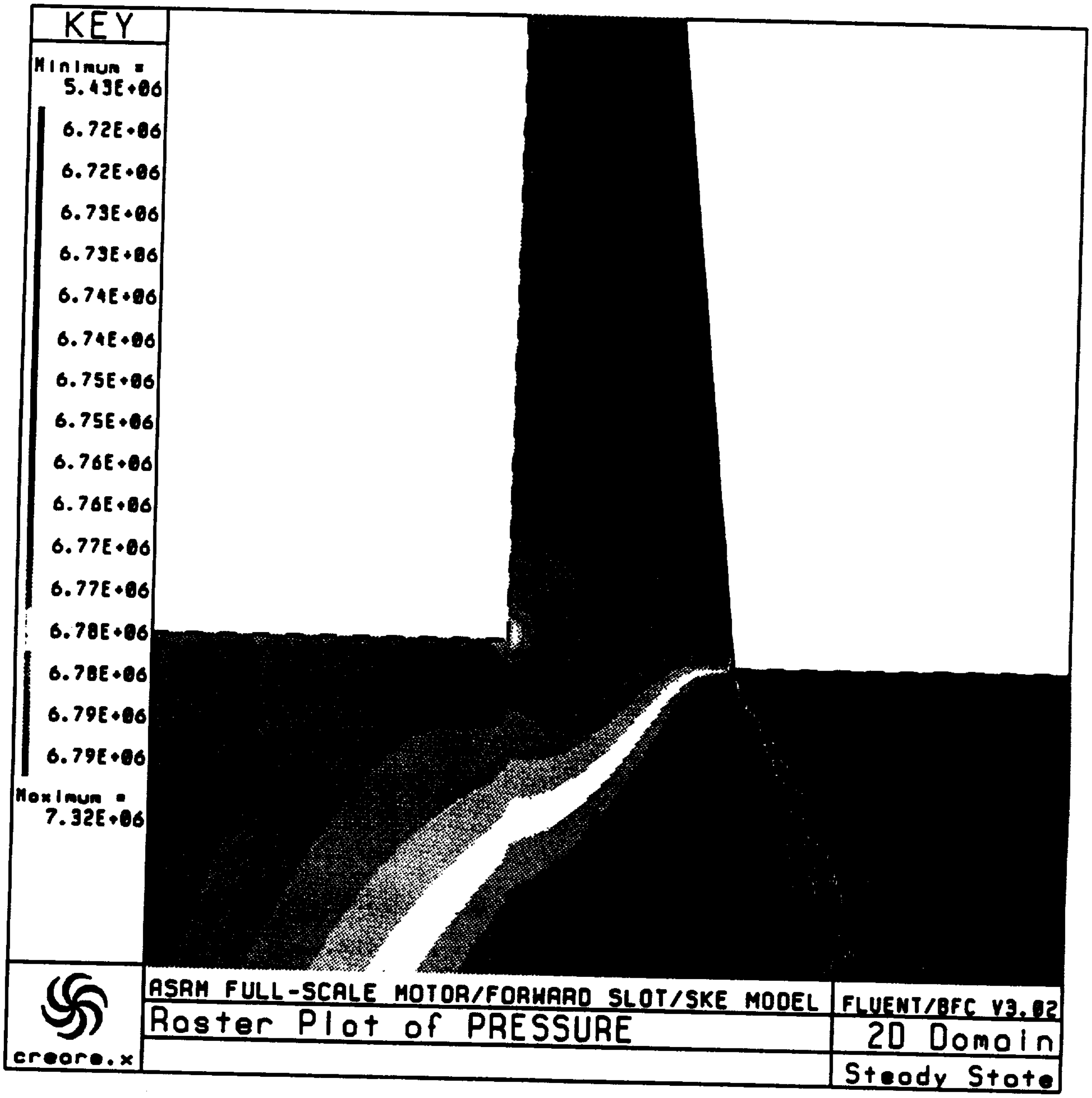

Figure 11. Static Pressure in the Forward Slot Region, SKE Model

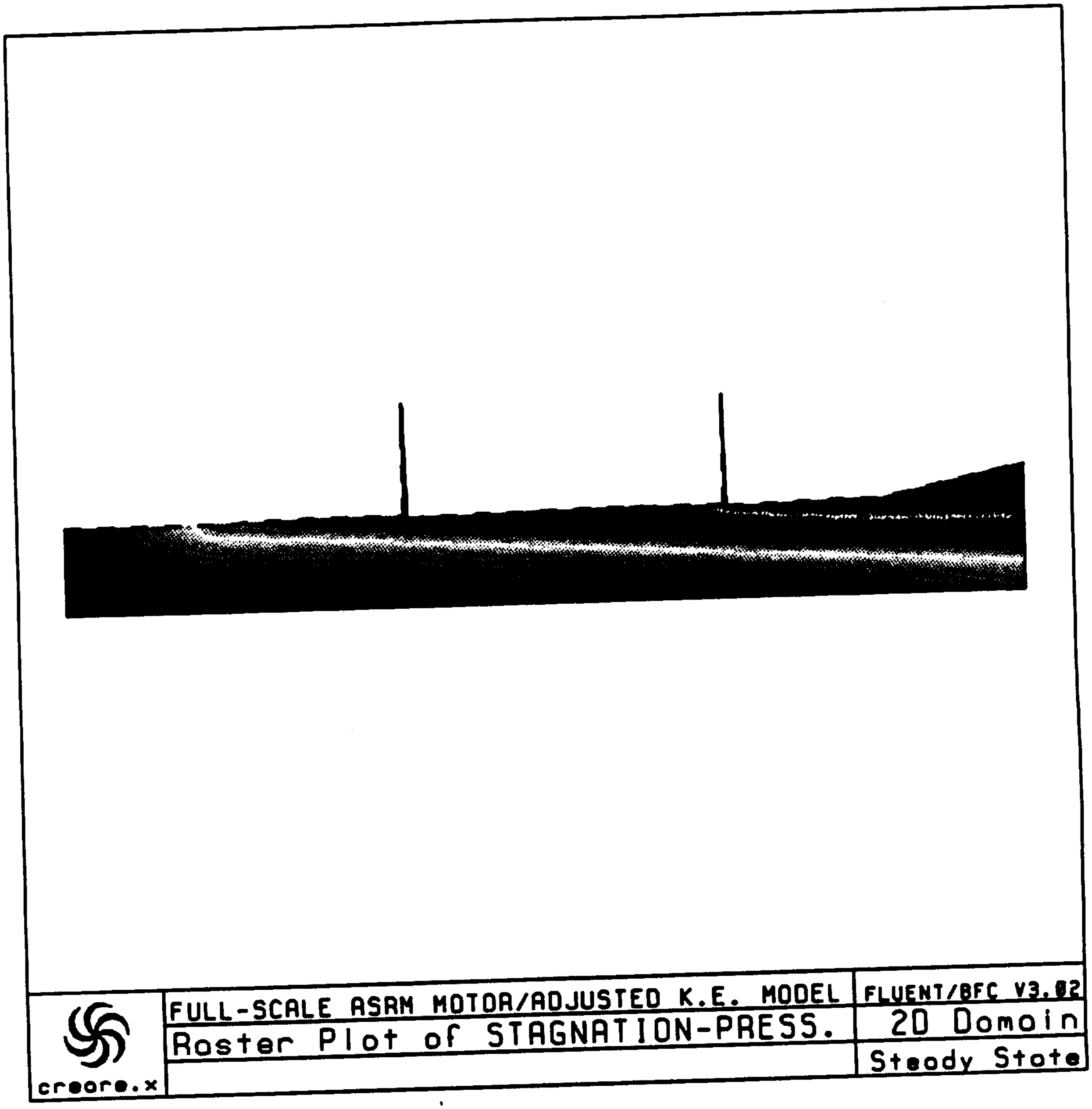

Figure 10. Total Pressure Raster Plot for the ASRM Full-Scale Motor, AKE Model

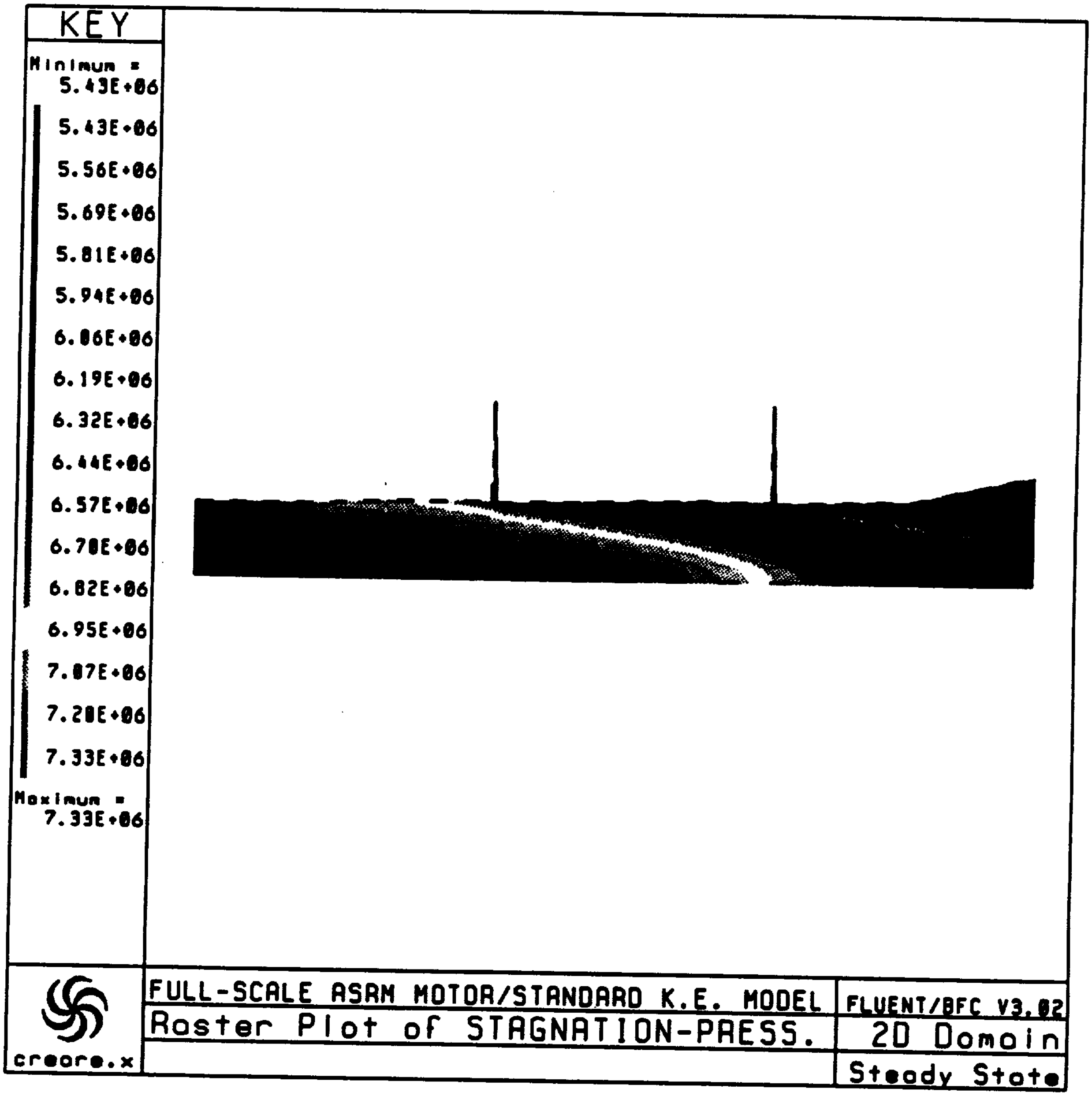

Figure 9. Total Pressure Raster Plot for the ASRM Full-Scale Motor, SKE Model

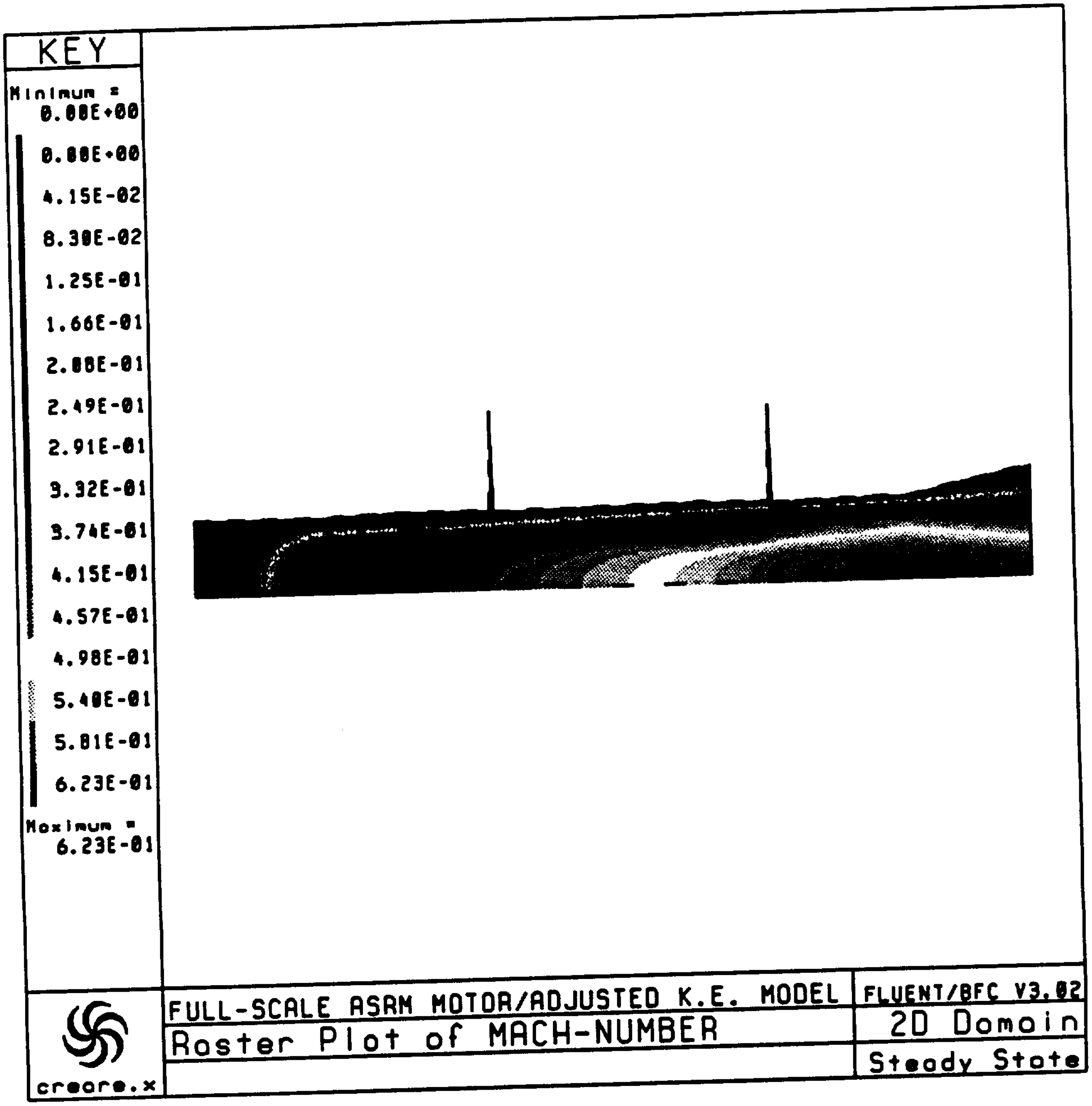

Figure 8. Mach Number Raster Plot for the ASRM Full-Scale Motor, AKE Model

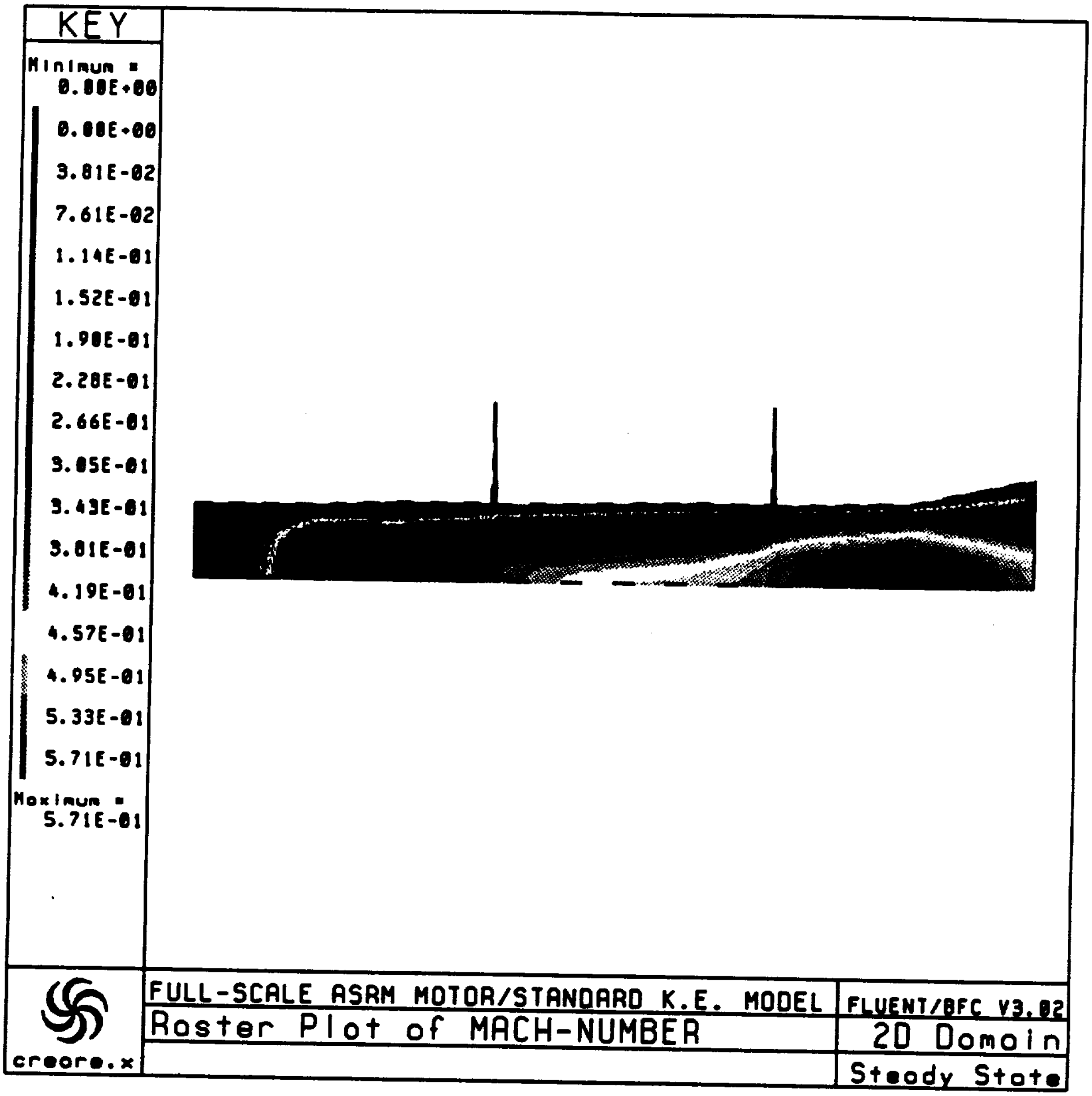

Figure 7. Mach Number Raster Plot for the ASRM Full-Scale Motor, SKE Model

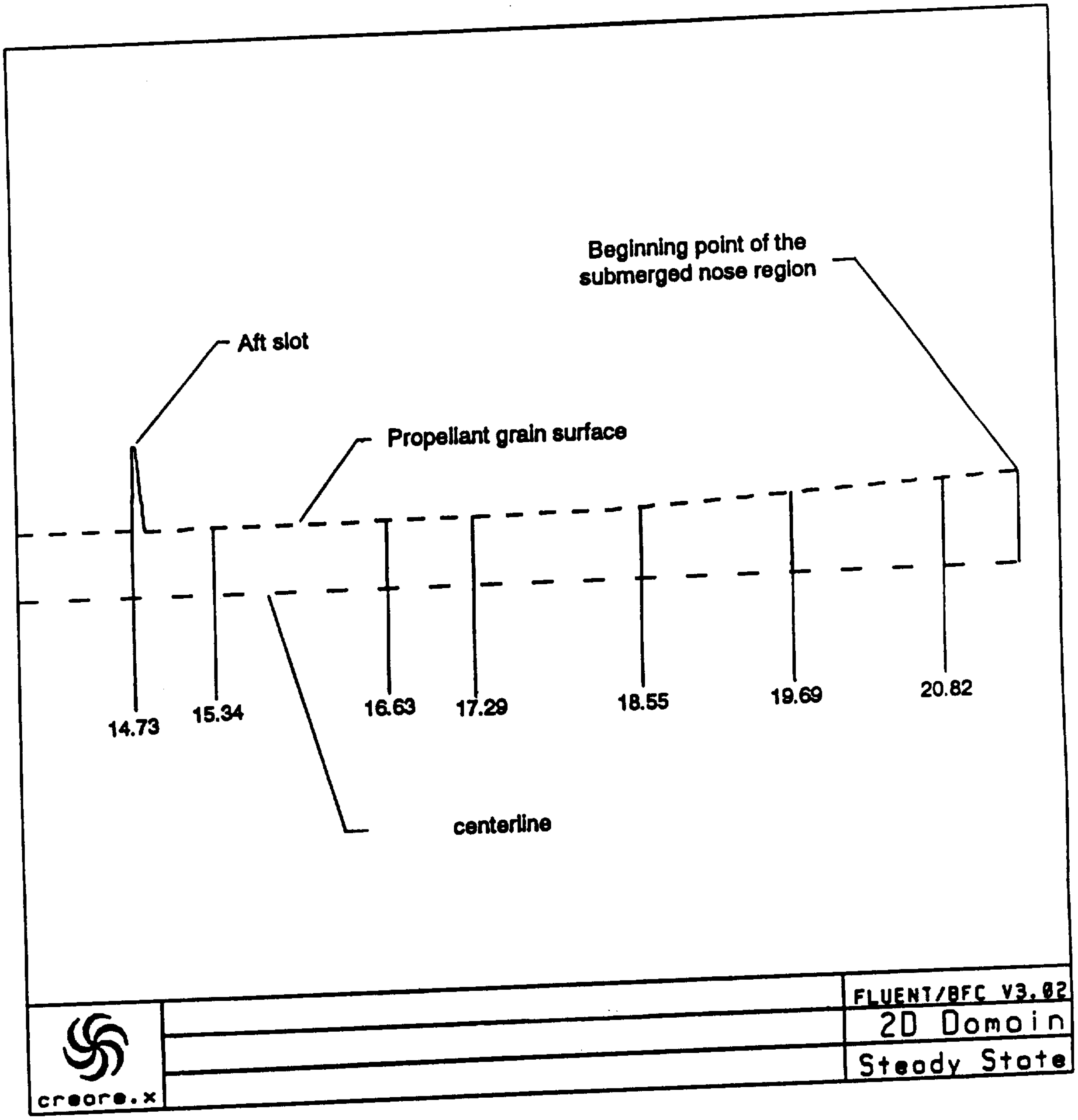

Figure 6. Aft Propellant Segment of the ASRM Full-Scale Motor

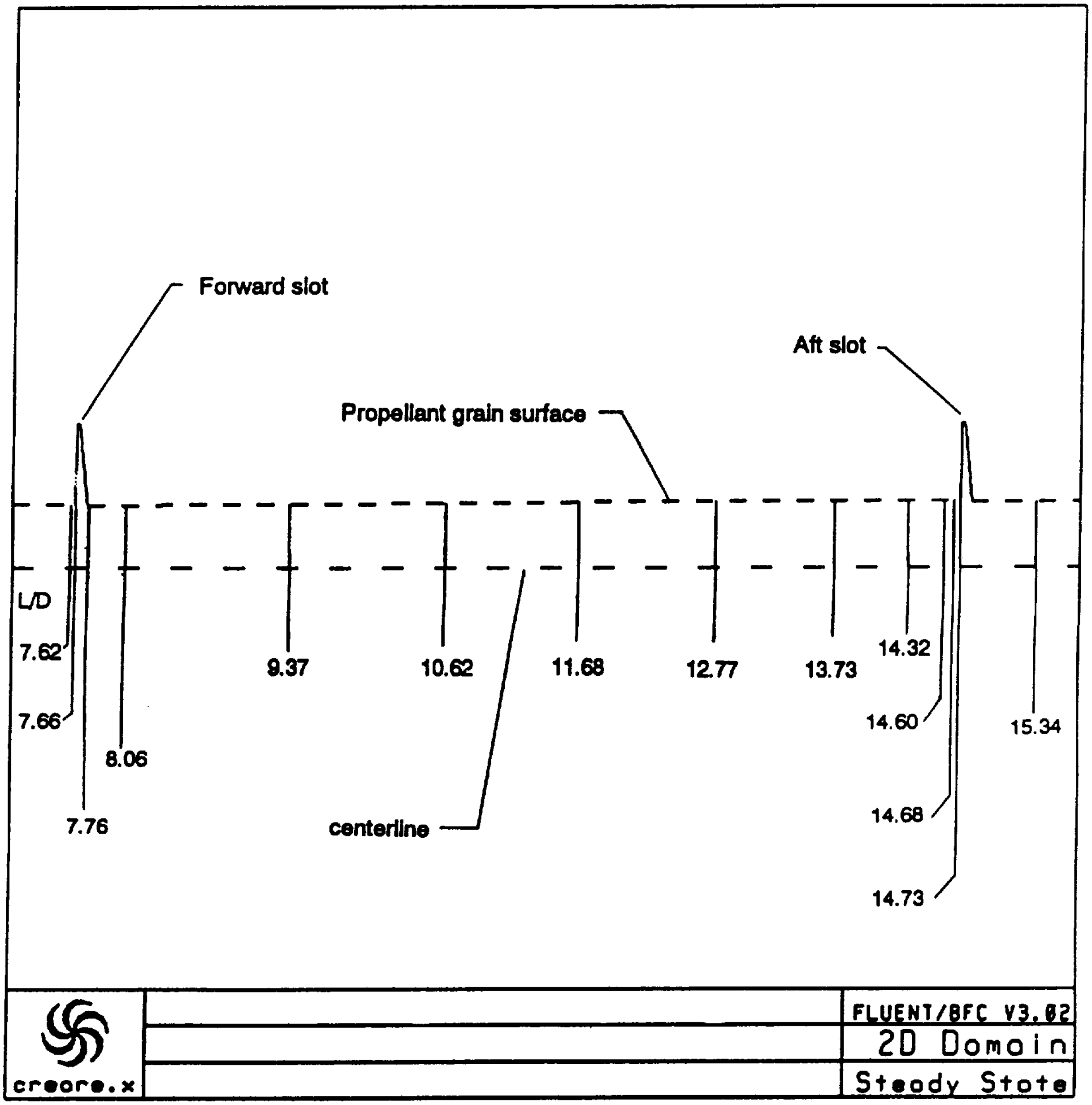

Figure 5. Center Propellant Grain Segment of the ASRM Full-Scale Motor

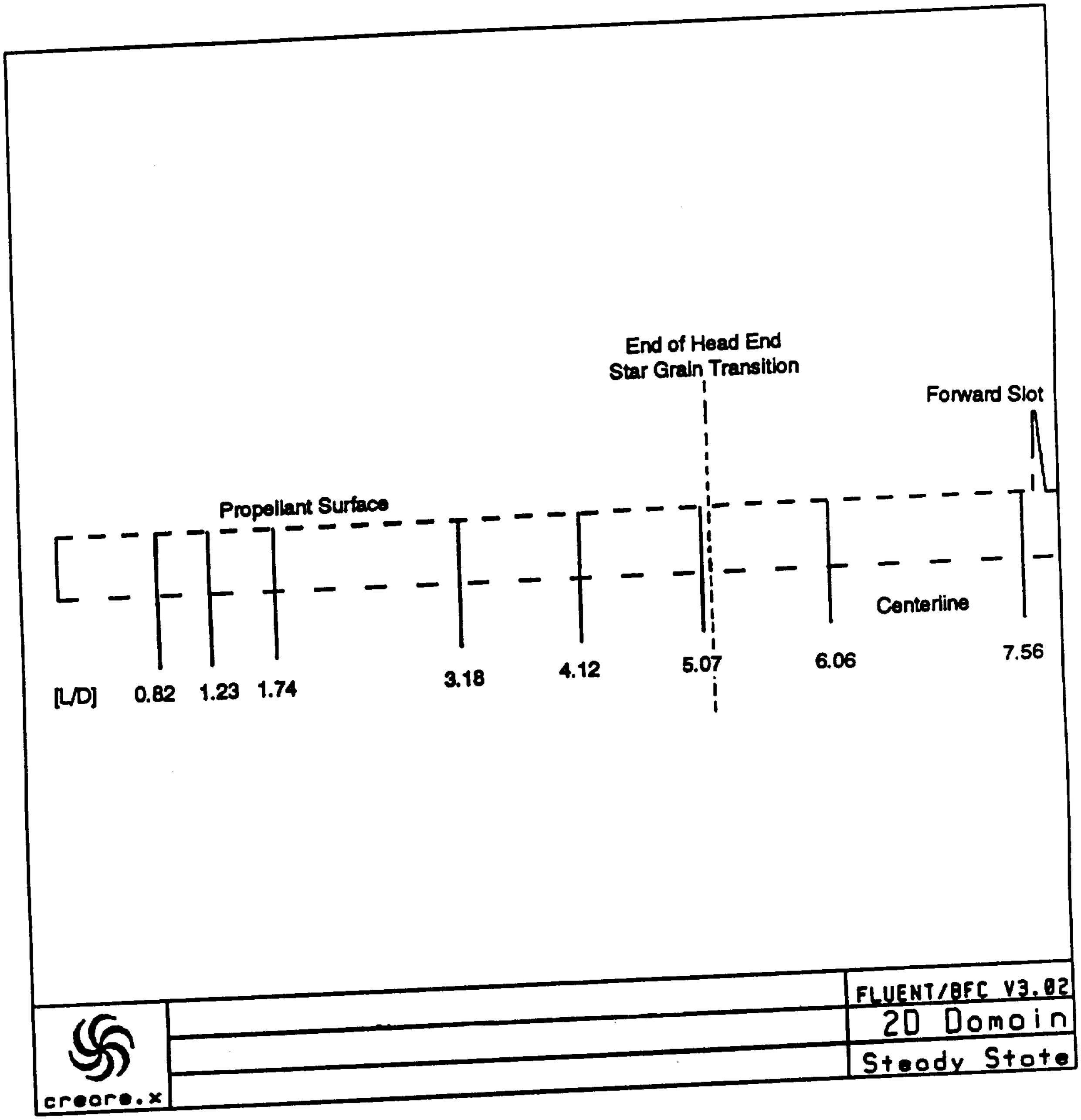

Figure 4. Forward Propellant Grain Segment of the ASRM Full-Scale Motor

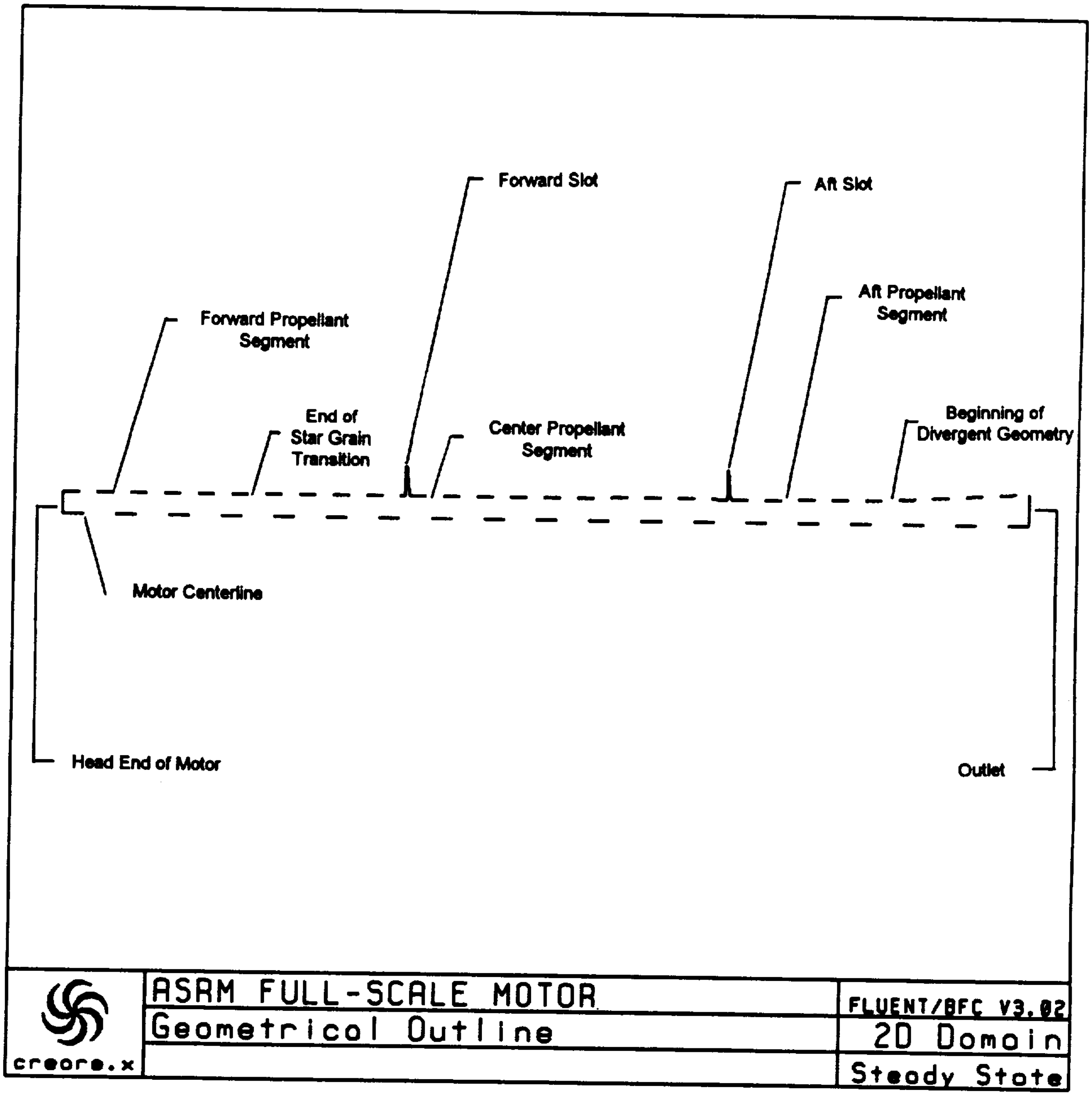

Figure 3. Nomenclature Diagram for the ASRM Full-Scale Motor

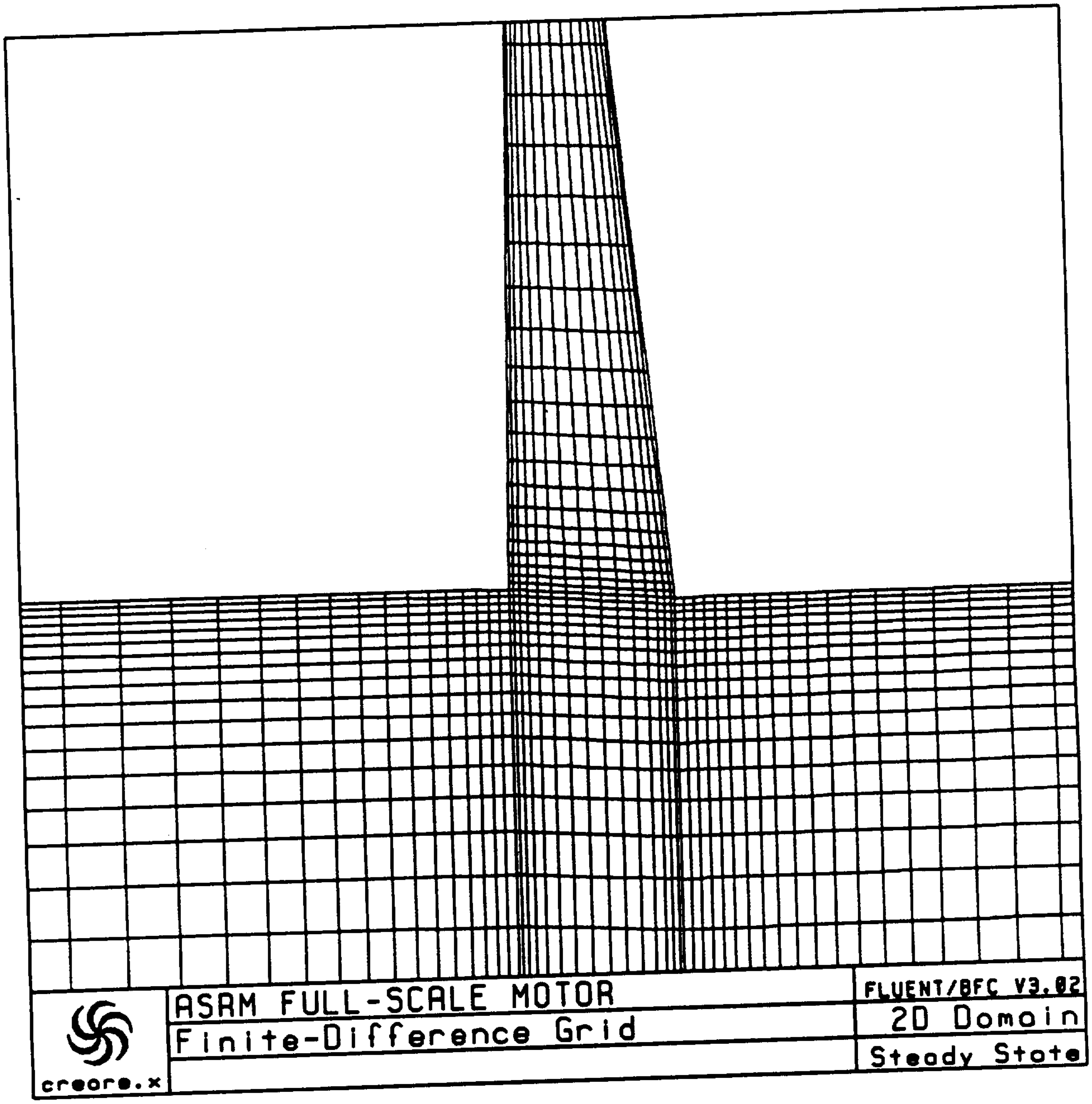

Figure 2. Enlarged View of Computation Grid in the Slot Region of the ASRM Full-Scale Motor

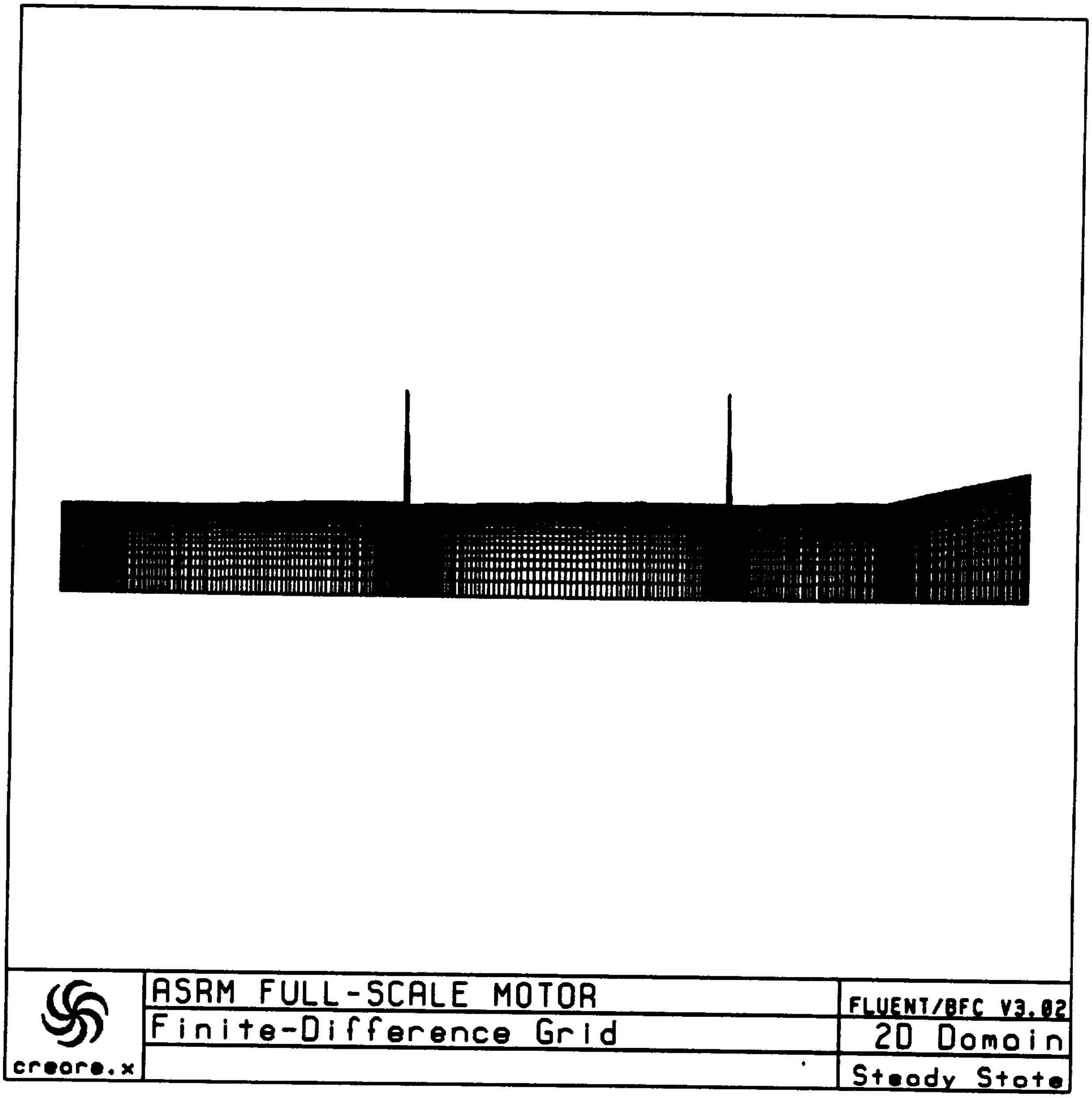

Figure 1. Computational Grid for the ASRM Full-Scale Motor Deformed Grain Configuration

2. Transition of the model axial velocity profiles does not begin until the immediate vicinity of the forward slot. There is evidence of the beginnings of turbulence upstream of the forward slot as observed in the normalized turbulent kinetic energy profiles but the transition is very slow upstream of the forward slot. The forward slot contributes to the onset of turbulence and the transition process speeds up somewhat downstream of the forward slot.

3. Maximum turbulence levels are below 2 % for all regions of the model except in the aft section where the simulated propellant grain undergoes slope change causing a drastic increase in area ratio of the model port.

4. Results for the ASRM full-scale motor are very similar to those obtained for the Technology model and some direct comparisons will be shown in the August monthly report.

26 it becomes immediately apparent that the AKE motor solution is different. The process of transition has not yet started in the AKE model solution for those L/D's plotted in Figure 45. A small growth in the normalized turbulent kinetic energy profile at an L/D of 6.06 signals the possible beginnings of transition upstream of the forward slot but the axial velocity profiles show insignificant change upstream of the slot region. Figure 46 shows the velocity profiles in the forward slot region where the slot does seem to have a significant effect on the velocity profiles and the transition process. Most of the change in the velocity profiles is concentrated near the mass injection wall in this region of the motor. Although the beginnings of transition are evident in the region of the forward slot for the AKE model solution, the transition process is much less rapid than the process predicted by the SKE model. Figure 47 illustrates this well by showing the transition of the velocity profiles along the center section of the motor between the forward and aft slots. The transfer of kinetic energy between the motor centerline and the wall is much less for the AKE model than for the SKE model. This will again be illustrated when the normalized turbulent kinetic energy profiles are observed for the AKE model solution. The level of turbulence is much lower near the model centerline than for the SKE model solution. Figure 48 shows the velocity profiles in the vicinity of the aft slot and Figure 49 shows the velocity profiles in the aft section of the motor. As seen for the SKE model, the simulated propellant grain geometry change has a drastic effect on the velocity profiles in the aft section of the motor. Figure 50 shows a plot of the u-velocity profiles in the aft section of the motor for the AKE solution. These profiles, just as those shown for the SKE solution, are not normalized to the centerline velocity so that the actual shape of the profiles in the divergent section of the motor can be seen. Figures 51 to 62 show the normalized turbulent kinetic energy profiles for the AKE model solution at specified L/D ratios from the motor head end to the aft end. These are the same L/D's as plotted for the SKE model solution and can be directly compared. The comparative results can be summarized by noting that the growth of a turbulent energy peak near the wall occurs much later for the AKE model solution and the continued growth in turbulence level is slower for the AKE model solution. The maximum turbulence level up to the propellant geometry flare in the aft section of the model is less than 2 % for the AKE model solution. This is approximately 5 % less than the same level observed for the SKE model solution. Another clearly discernible feature of the AKE model normalized kinetic energy profiles is that the centerline turbulence levels are much lower than for comparative L/D ratios for the SKE model. As previously observed, there is a drastic change in the velocity profiles aft of the propellant geometry flare in the aft section of the motor and the normalized turbulent kinetic energy for the AKE model solution shows a drastic change in the turbulence profile at an L/D of 20.82, Figure 62.

Several concluding observations will now be made to summarize the CFD solution for the ASRM full-scale motor flow field predictions presented in this monthly report.

1. The AKE turbulence motor solution is indicated as the better CFD solution since it matches both the analytic results and the CSD experimental data much better than the SKE solution.

The normalized axial velocity profiles in the motor port illustrate transition of the flow from laminar to turbulent flow. The profiles for the SKE solution will be discussed first. The velocity profiles also show the detailed physical changes in the flow as the hot propellant gas flows down the motor port. The normalized axial velocity profiles are plotted in comparative figures for different regions of the ASRM motor port. Figure 25 shows an overall view of how the axial velocity profile changes down the motor port. The velocity profiles in the head end of the motor rapidly form profiles very close to a Culick profile. This occurs very near the head end of the motor as illustrated in Figure 26. As the flow approaches the forward slot, transition has already begun to occur for the SKE model solution. This is illustrated by the 5.07 L/D velocity profile in Figure 26. As flow continues to move down the motor port to the aft end, the velocity profiles become more flattened or turbulent in nature. Figure 27 shows the disturbance of the velocity profiles in the forward slot region. Figure 28 best illustrates the continued transition of the velocity profile to a fully turbulent character. Most of the transition in the axial velocity profiles occur in the center segment of the motor coincident with the slope change of the static pressure in the motor port noted in the discussion of Figure 21. Figure 29 shows that there is only a small alteration of the axial velocity profile at the aft slot. And Figure 30 shows the velocity profiles in the aft section of the motor. The L/D of 17.29 is downstream of the aft slot and just prior to the slope change in the simulated propellant geometry. Notice in Figure 3 how the aft propellant grain flares outward as the motor nozzle is approached. This geometry change drastically alters both the axial and radial velocity profile in the motor port. Figure 31 shows a plot of the u-velocity profiles in the aft section of the motor. These profiles are not normalized profiles and so present the progression in the actual shape of the profile down the divergent aft section. The turbulent kinetic energy is also redistributed over the port as will be shown in the sequence of plots for the normalized turbulent kinetic energy. The sequence of figures from Figure 32 to Figure 43 show the normalized turbulent kinetic energy at specified L/D ratios sequentially down the motor port. The normalized turbulent kinetic energy level is highest along the centerline of the flow field near the head end of the motor just as seen in the experimental data for the CSD cold flow test discussed in the May 92 monthly. The normalized kinetic energy level drops rapidly until an L/D of about 5.07 where a peak begins to develop near the mass injection wall. This peak is very pronounced by the 6.06 L/D as shown in Figure 35. The peak begins to grow and widen as the flow moves down the motor port. A maximum of 8.5 % turbulence level is reached in the aft end of the motor. This is much higher than the levels noted in the CSD coldflow test data although test conditions are different. These high levels of turbulence can be associated somewhat with the excessive pressure drop down the motor port predicted by the SKE model.

The normalized axial velocity profiles for the AKE model solution are much different when compared with those already presented for the SKE model solution. Figure 44 shows the sequence of velocity profiles at selected L/D ratios from the model head end to the aft end. Figure 45 shows the axial velocity profiles at various L/D ratios in the head end of the motor prior to the forward slot. When Figure 45 is compared to Figure the velocity profile is changing drastically (L/D from about 10 to 15). Since the SKE model causes a much more rapid transition to turbulent flow, the velocity profiles are much flatter than for the AKE model. This is collaborated by observing that the centerline Mach number is affected less for the AKE model than for the SKE model. The abrupt slope change in the center section of the motor (L/D from about 10 to 15) observed in Figure 19 for the SKE model is not present in the AKE model solution. Unlike the SKE model results, the AKE model predicts very little change in the slope of the Mach number for the flow near the centerline of the motor. One final comparative note, the sharp drop in the Mach number from an L/D of 18 to 21 is caused by a change in the propellant geometry in the aft section of the motor. The area ratio increases rapidly in the aft section of the motor due to the divergent propellant geometry. The centerline Mach number for the AKE solution is not as affected by the motor geometry change as is the centerline Mach number for the SKE model. Again, this is due to a difference in the dissipation of energy predicted when using the two models and this will be illustrated when the velocity and kinetic energy of turbulence profiles are shown.

An analytic model was developed at ERCI and discussed in the May 92 monthly report. This model uses a similarity velocity profile assumption to compute the flow characteristics of the ASRM full-scale motor by means of an analytic solution. Either of two velocity profiles may be assumed for the analytic solution. The code can use either a bulk velocity profile, as used in some ballistic codes, or a Culick velocity profile.

Figure 21 shows a comparison between the static pressure predicted by the CFD code using the SKE model and the static pressure predicted by the analytic Culick profile solution. The plot shows that the SKE model over predicts the pressure drop down the motor port by a substantial amount. From the head end to the forward slot the results of the solutions are close, but downstream of the forward slot at an axial distance of approximately 1000 inches the results diverge. This divergence in the solutions is due to two factors. The prediction of transition to turbulent flow upstream of the forward slot is both premature and too rapid. The actual transition of the velocity profiles will be discussed later. Figure 22 shows a comparison between the predicted static pressure in the motor for the CFD solution using the AKE model and the predicted static pressure using the analytic Culick profile solution. The CFD and analytic solutions match closely. The CFD code develops a slightly different slope as the transition process continues down the port. The only other difference exists in the aft section where the port diameter increases rapidly. The differences in the solutions in the aft section of the motor are due to drastic changes in the CFD predicted velocity profiles in this region and this will be discussed later in this report. Figures 23 and 24 show the comparison between CFD and analytic total pressure predictions for the SKE and AKE models, respectively. The same observations discussed for the static pressures in the model apply to the total pressure comparison plots. For the SKE model solution the total pressure along the centerline begins to drop rapidly once transition occurs. As shown in Figure 23, the transition phenomenon in the CFD solution using the AKE model is delayed and not as rapid. The total pressure along the centerline is not significantly affected until the aft section of the motor.

of the total pressure is the same for the two solutions. In the low velocity region of the head end the total pressure is approximately constant. As the mass injection increases, the port Mach number increases and a velocity profile begins to develop. This causes the development of the stratified layers seen in the plot in the radial direction. This is strictly related to the higher dynamic pressure at the motor centerline as the flow velocity increases. The SKE model predicts a much greater drop in both the centerline and wall total pressure as the flow progresses toward the nozzle. As shown in Figure 10, there is only a small loss in total pressure at the centerline at the aft end of the motor port using the AKE model. Figures 11 and 12 show raster plots of the pressure in the forward and aft slot regions respectively for the SKE model results. Figures 13 and 14 show the corresponding velocity field for the forward and aft slots predicted using the SKE model. The relative size of the velocity vectors is directly related to the flow Mach number. There is a recirculation region along the downstream face of the slot for both the forward and aft slots. The recirculation region is stronger for the downstream slot since the port Mach number is greater at the aft slot. The stronger port flow at the aft slot causes the flow emanating from the slot to be more restricted than the flow from the forward slot. The recirculation region forms a restriction to the passage of the slot mass flux into the port region. This creates a region of higher velocity flow along the upstream slot face. This is evidenced in the pressure plots, Figures 11 and 12. There is a high pressure region on the downstream slot face and a low pressure region on the upstream slot face. This can also be noted by observing the strength of the flow near the upstream face of the slot in Figures 13 and 14. The AKE model solution does not show a recirculation region in the slots. Figures 15 and 16 show the pressure raster plots for the forward and aft slots respectively and Figures 17 and 18 show the velocity field for the forward and aft slots. The velocity distributions near the wall are different for the solutions using the SKE and the AKE models. This causes the restriction on the flow from the slot to be less for the AKE solution and therefore no recirculation region is generated on the downstream slot face.

The remainder of the discussion of the analytical results will be devoted to a detailed discussion of the physical phenomena predicted for the ASRM full-scale motor. Predictions will be shown and discussed for the static and total pressure in the motor and for the axial velocity component at various L/D ratios in the motor port. The normalized kinetic energy of turbulence profiles in the motor will also be shown. These predictions will provide a better understanding of the details of what is happening in the motor.

Figures 19 and 20 respectively, show a plot of the centerline and average Mach numbers predicted in the motor port using the SKE model and the AKE model . The Mach number increases very rapidly in the head end section of the model from an L/D of 0 to 4. This is due to the larger amount of mass flow emanating from the head end star grain propellant region. The SKE model predicts transition to turbulent flow much faster than the AKE model. In reference to the SKE model Mach number prediction, there is a depression in the slope of the centerline Mach number in the region where

Section 2	2.58 m/s(8.45 ft/s)	2.87 m/s(9.42 ft/s)
Section 3	2.80 m/s(9.19 ft/s)	3.05 m/s(10.01 ft/s)
Section 4	3.43 m/s(11.25 ft/s)	3.5 m/s(11.48 ft/s)

Section 1 includes the propellant from the head end to the end of the star grain transition section of the forward propellant grain segment. Section 2 includes the continuation of the forward propellant grain from the end of the star grain transition section to the end of the forward propellant segment which ends in the forward slot. Section 3 includes all of the center propellant grain segment which begins at the aft corner of the forward slot and ends in the aft slot. Finally, section 4 includes the aft propellant grain segment excluding the propellant behind the submerged nose nozzle. A no-slip velocity boundary condition was utilized along inhibited or non-propellant surfaces located in the motor head end and in the slots. A symmetry boundary condition was used along the motor centerline axis of symmetry. All surfaces were considered to be adiabatic. A static pressure boundary conditions was utilized at the aft end outlet of the motor. The static pressure was specified as 788 psia, which was obtained from ballistic simulation of the full-scale motor. The total mass flow rate for the propellant surfaces modeled was 5293 kg/s (11670 lbm/s). For the SKE model solution, the total computed mass flow rate was 5290 kg/s (11663 lbm/s). The computed mass flow rate is within less than 0.06% of the desired mass flow rate for the motor. The total computed mass flow rate for the AKE model solution was 5327 kg/s (11744 lbm/s). This is within 0.7% of the desired mass flow rate for the motor. This problem exhibited a rather slow convergence rate and both solutions required over 10000 iterations to achieve convergence.

Just as for the Technology model analysis presented in the July monthly report, the SKE model and the AKE model were used in the CFD code to solve for the ASRM full-scale motor internal flow field. These results will be presented together in a comparative fashion.

A general overview of the flow field results using the SKE model and the AKE model will be given before discussing the actual physics of the internal flow in the ASRM motor. Figures 4, 5, and 6 show constant axial planes at specific L/D ratios in the motor chamber. The ratios are those for which data is plotted in the results section of this report on the ASRM motor flow field. Figure 4 shows the region of the motor from the head end to the forward slot while Figure 9 shows the center propellant grain between the forward and aft slots. Figure 10 shows the aft section of the motor from the aft slot to a point just upstream of the submerged nose of the nozzle. These figures will be helpful throughout the discussion of the flow field results. These figures may also be referenced as needed to determine the location of a specified L/D ratio mentioned in the text. Figures 7 and 8 show color raster plots of the predicted Mach number in the flow field using the SKE and AKE models, respectively. These figures show that the centerline Mach number changes more rapidly when using the SKE model than when using the AKE model. Figures 9 and 10 show raster plots of the total pressure in the motor using the SKE and AKE models, respectively. The general trend regions were resolved using 16 axial cells and 31 radial cells. Figure 1 shows the grid used in this analysis. The y-axis is stretched by a 4x magnification factor in order to show more of the grid structure than could be shown on an unmagnified grid plot. Figure 2 shows a closeup of the grid in the slot region. This figure readily shows that the grid lines have been clustered near the propellant grain and solid wall surfaces. The figure also shows that the grid line spacing was smaller in regions where higher flow variable gradients were expected to exist. The two flow field solutions for the ASRM full-scale motor, one using the standard $\kappa-\varepsilon$ model (**SKE**) and the other using the adjusted $\kappa-\varepsilon$ model (**AKE**), were calculated using the same computational grid. An analysis is currently underway to determine the sensitivity of the flow solution to the grid resolution. In this run the grid has been refined in the radial direction and at the axial direction in axial locations where the highest flow gradients were observed in the predicted flow solution using the original 411x23 grid.

The basic thermochemical properties and boundary conditions used in the analysis were:

M, molecular weight	29.489
μ, dynamic viscosity(Pa-s)	9.423×10^{-5}
C_p, specific heat(J/kg- K)	2484.63
T_o, Stagnation Temperature(K)	3525

Figure 3 shows a plot of the ASRM full-scale motor configuration considered in this analysis. The figure is labeled to show the terminology used in this discussion. A velocity boundary condition was used at the propellant grain surface. The correct velocities for the forward, center and aft propellant surfaces were not known directly. The velocities were obtained by the following iterative process. The mass flow rates computed for the undeformed grain ASRM full-scale motor by the NASA ballistic code SPP were used as the mass flow rates for this analysis. The mass flow rate, however, does not directly translate into a velocity boundary condition. A port pressure estimate for the various sections must also be obtained. The initial estimate of the pressure distribution in the port of the model was determined from an analytic code. Given this information, a velocity was obtained from the mass flow rate equation, ($m=\rho VA$) and the ideal gas law. This velocity estimate was then used to converge the flow field in the motor to an intermediate convergence level. At this point the calculated mass flow rates based on the initial guess pressure field were compared to the desired mass flow rates for each section. A new velocity boundary condition was computed from this information. This iteration of the velocity boundary condition for the motor continued until the mass flow rates computed by the CFD code matched the target mass flow rates which originated from the ASRM full-scale motor ballistics run. The final computed velocity boundary conditions associated with the four sections of the ASRM full-scale motor are shown below.

	SKE model	**AKE model**
Section 1	14.64 m/s(48.03 ft/s)	16.18 m/s(53.08 ft/s)

Full Motor Port Analysis

The CFD analysis of the SAF Technology Model was presented in the June 1992 monthly report. The Technology Model is a 10% scaled model of the full-scale ASRM deformed motor geometry. It is designed to operate at full-scale motor Reynolds numbers. Since the Technology Model will be used to experimentally assess the internal flow field in the full-scale motor, it is necessary to analyze both of the configurations and compare the predicted flow fields in order to assure good similarity between the flow field existing in the model and the flow field existing in the full-scale motor. This monthly will present the analysis of the full-scale ASRM motor deformed grain geometry flow field and the subsequent monthly report for August will analyze the similarity of the flow fields predicted for the Technology Model and the full-scale ASRM motor. Both of the analyses were performed with Fluent/BFC version 3.02. As for the analysis of the Technology Model, the full-scale ASRM motor analysis was performed using a standard $\kappa-\varepsilon$ model and an adjusted $\kappa-\varepsilon$ model. A full explanation of these models can be found in the May 1992 monthly report. The adjusted $\kappa-\varepsilon$ model provides the better match to the experimental data and will be presented as the baseline turbulence model.

The geometry description used to construct the full-scale ASRM Motor computational grid was taken from ERCI drawings H5201-1, revision A, H5202-1, H5203-1 and H5204-1. The dimensions specified in the drawings were used except in the head end region. ERCI drawing H5203-1 shows a star grain propellant configuration in the head end of the motor. The star grain propellant flares into the cylindrical port geometry in the transition region shown in the drawing. This section of the motor was modeled analogously to the head end of the Technology model configuration. From the end of the transition at the cylindrical port, upstream to the head end of the motor, the propellant grain was modeled as a cylindrical port with a radius equivalent to the star grain configuration flow area. The flow area in the star grain region was calculated and the equivalent cylindrical radius was computed. This equivalent radius was very close to the port radius at the end of the star grain transition so the analysis was further simplified by modeling the ASRM full-scale motor head end region as a cylindrical port of radius equal to the radius of the motor port at the end of the star grain transition. This allows the head end to be modeled with a consistent flow area but without the three-dimensional complexity of the actual star grain configuration. This simplification is important since the flow field for the full motor chamber from the head end to the nozzle nose is being modeled. If the star grain configuration were modeled the required number of computational cells would increase dramatically. The effects of the star grain propellant configuration on the internal flow in the motor will need to be investigated separately.

The computational grid was chosen to be identical in size to the computational grid for the Technology model reported in the July monthly. This allows the two solutions to be directly compared at exactly the same physical locations. The grid contained 411 axial computational cells and 23 radial computational cells in the port region. The slot

Figure 19. Pressure Distribution on the Front and Back Faces of the Fwd Slot, Undeformed Geometry

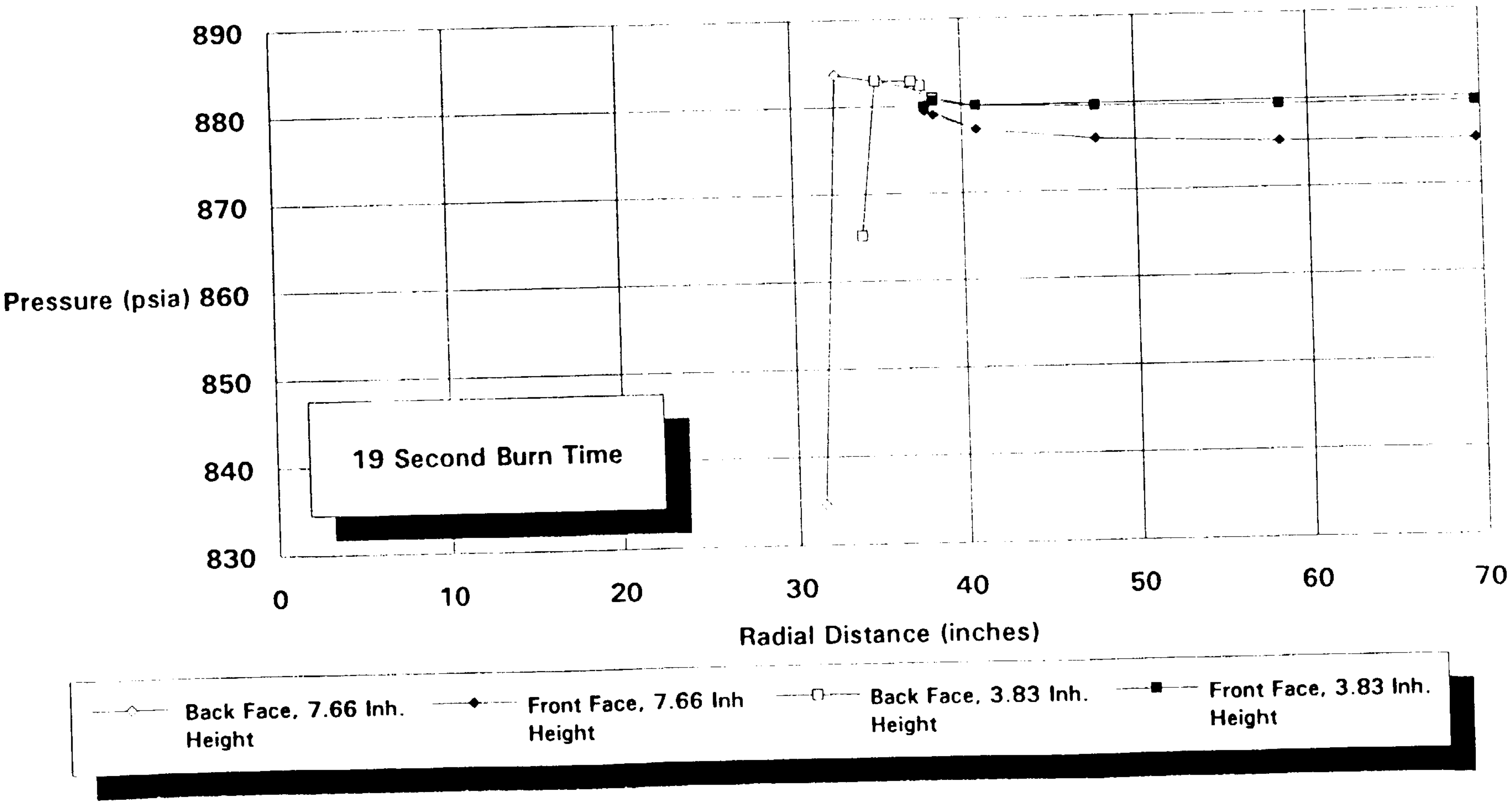

Figure 18. ASRM Fwd Slot Undeformed Grain Port Pressures On the Surface and at the Motor Centerline

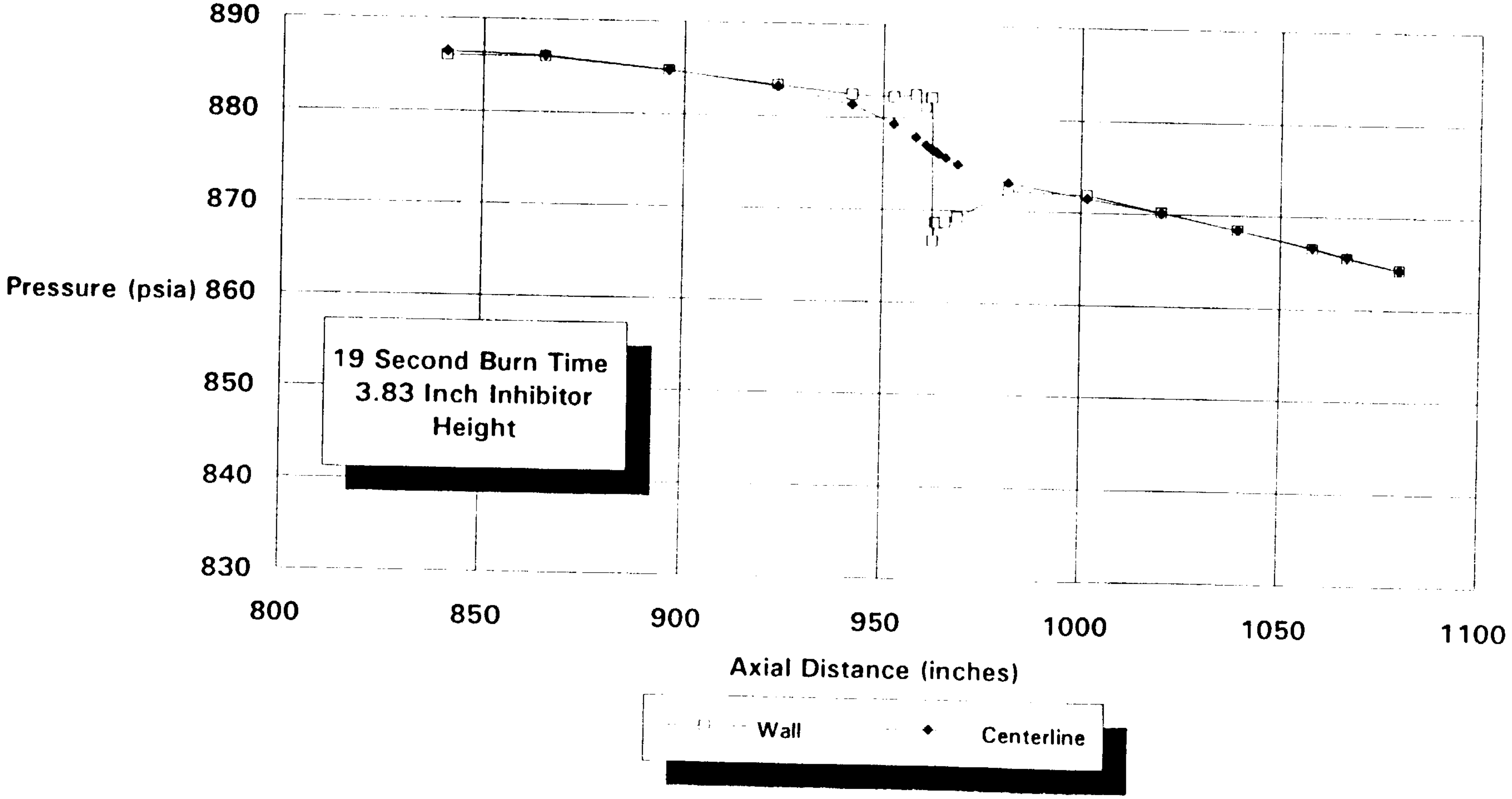

Figure 17. ASRM Fwd Slot Undeformed Grain Port Pressures On the Surface and at the Motor Centerline

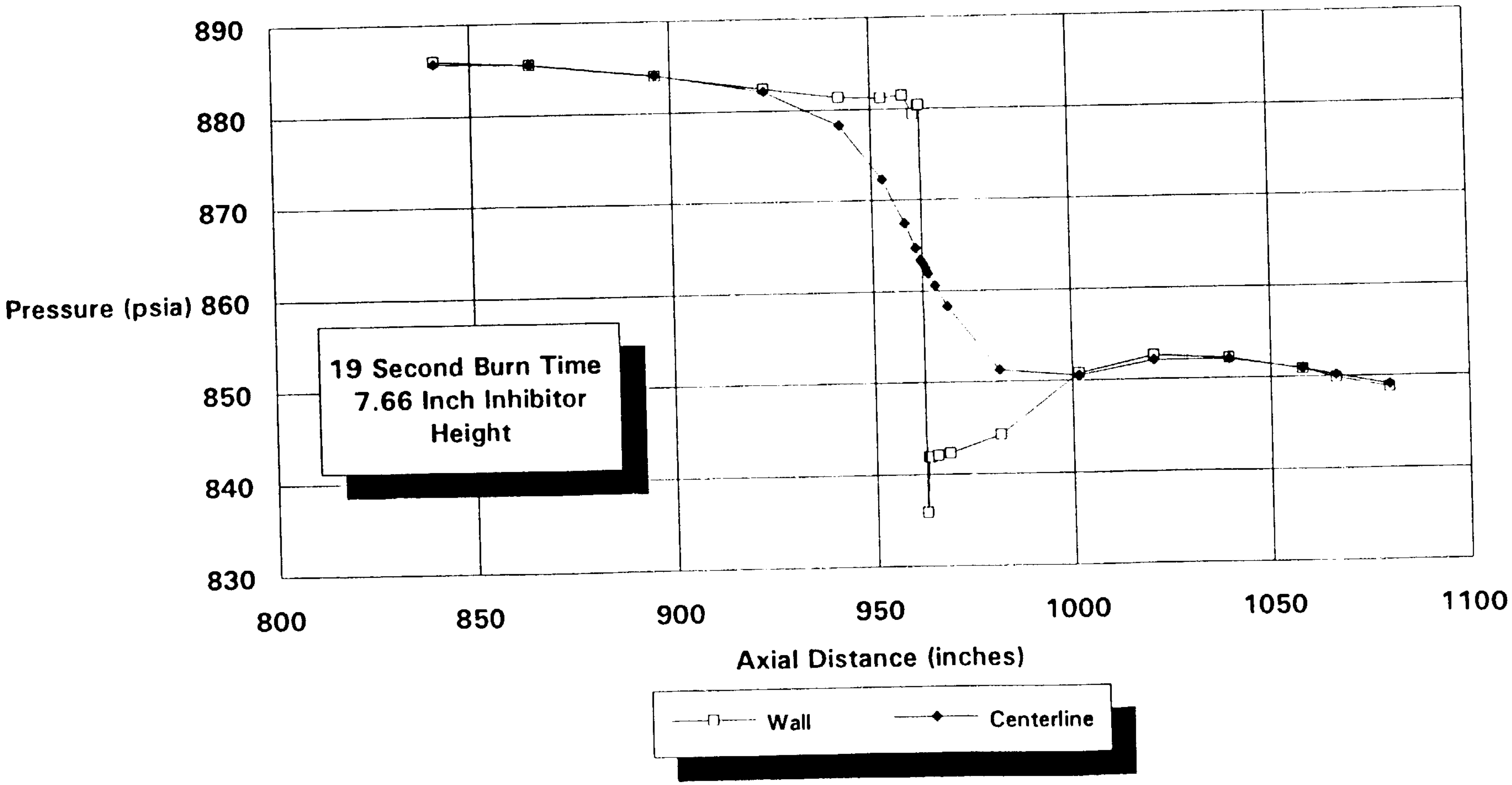

Figure 16. Pressure Distribution on the Front and Back Faces of the Aft Slot, Undeformed Geometry

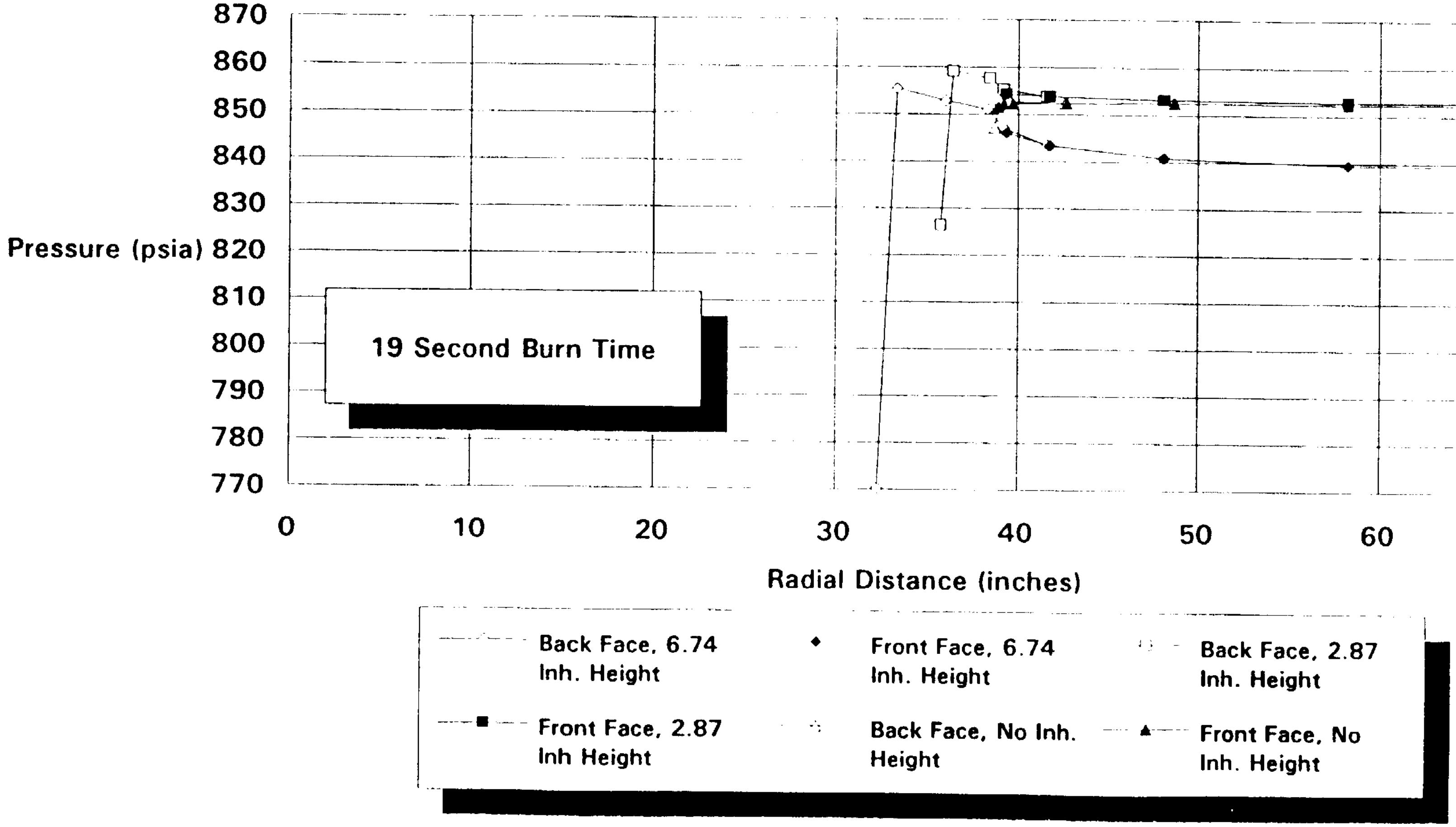

Figure 15. ASRM Aft Slot Undeformed Grain Port Pressures On the Surface and at the Motor Cenerline

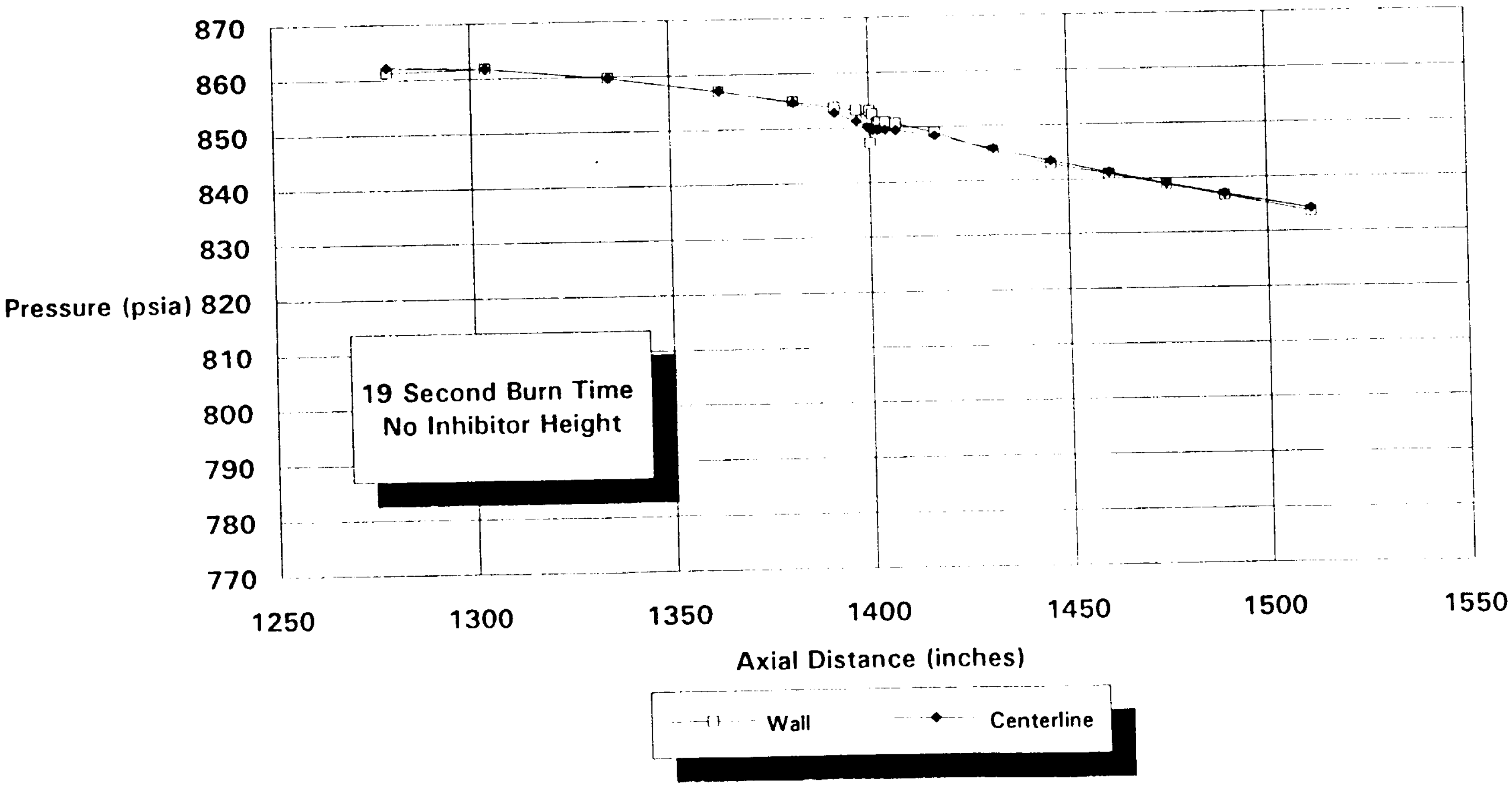

ERCI - 1/8/92

Figure 14. ASRM Aft Slot Undeformed Grain Port Pressures On the Surface and at the Motor Centerline

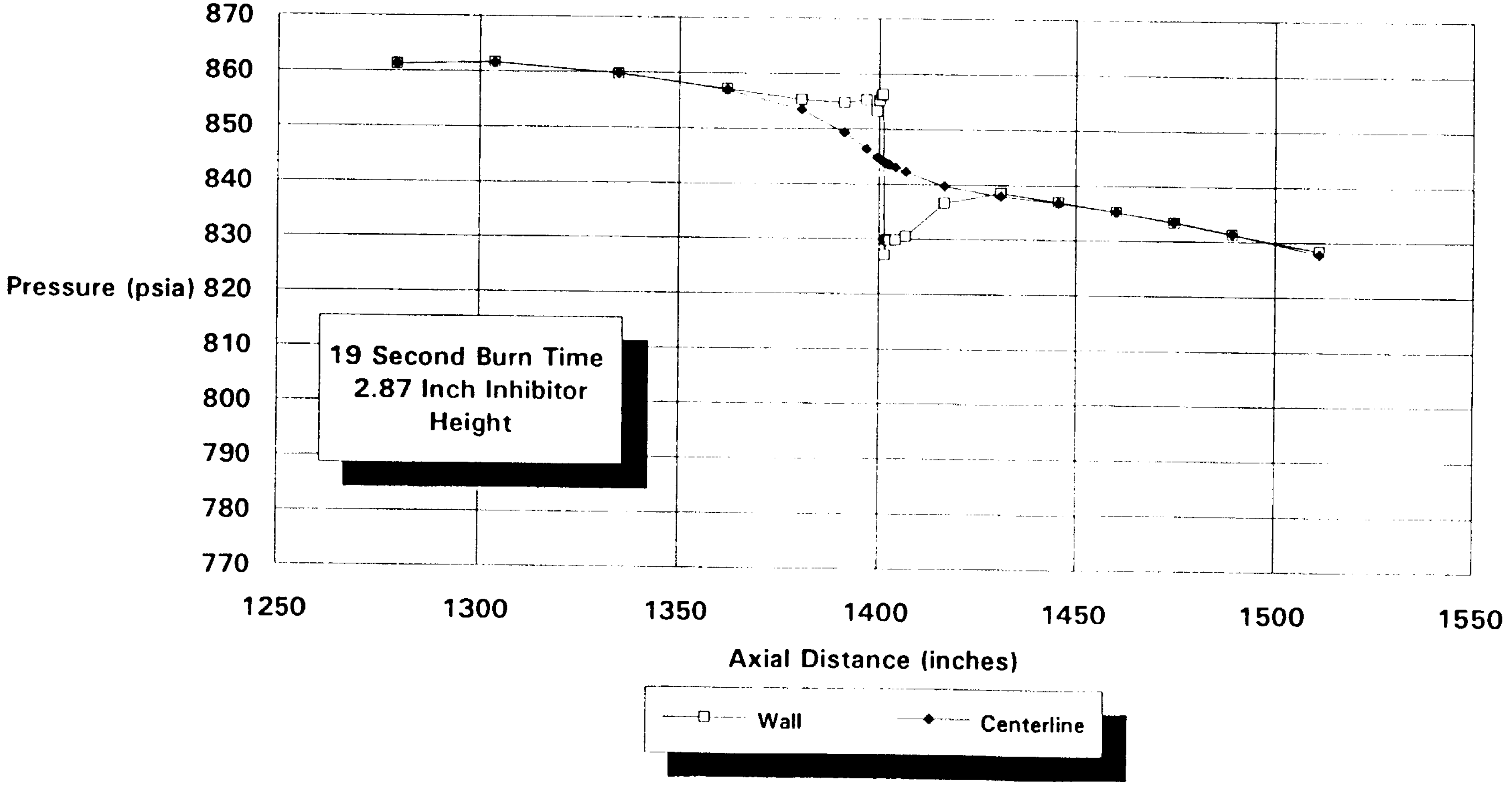

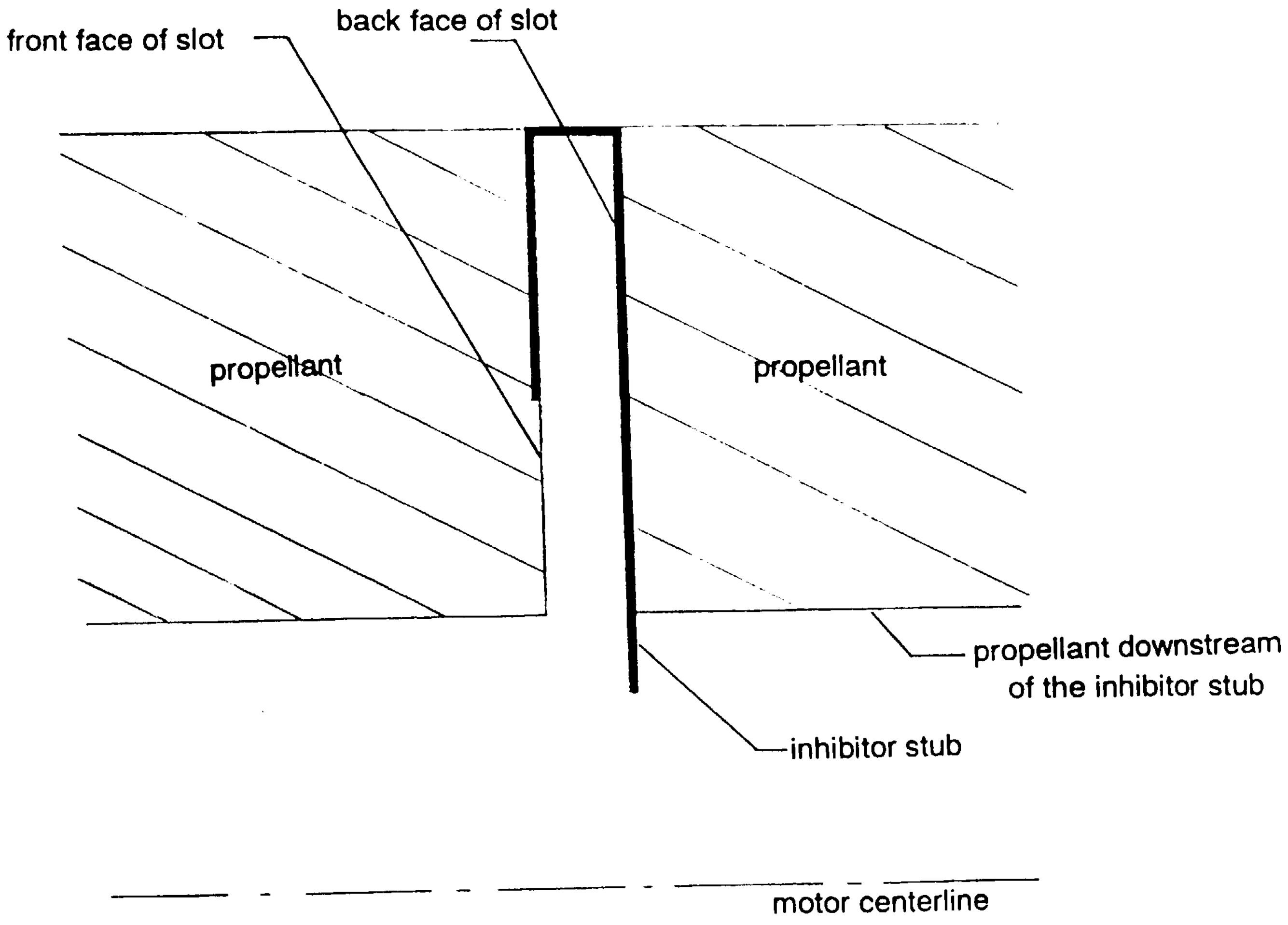

Figure 13. Illustration of the Slot/Inhibitor/Propellant Geometry in the ASRM Motor

Figure 12. ASRM Aft Slot Undeformed Grain Port Pressures On the Surface and at the Motor Centerline

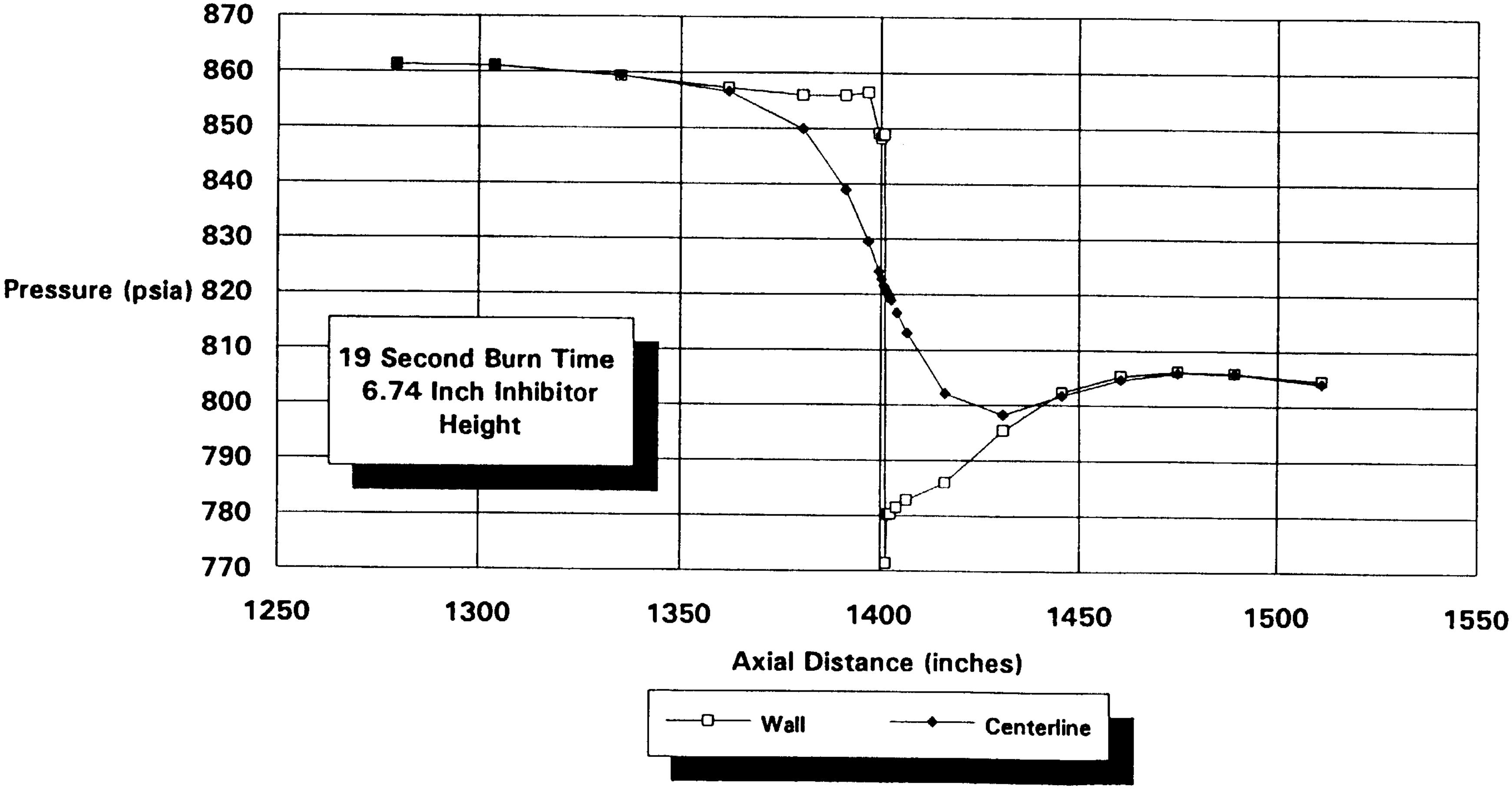

ERCI - 1/8/92

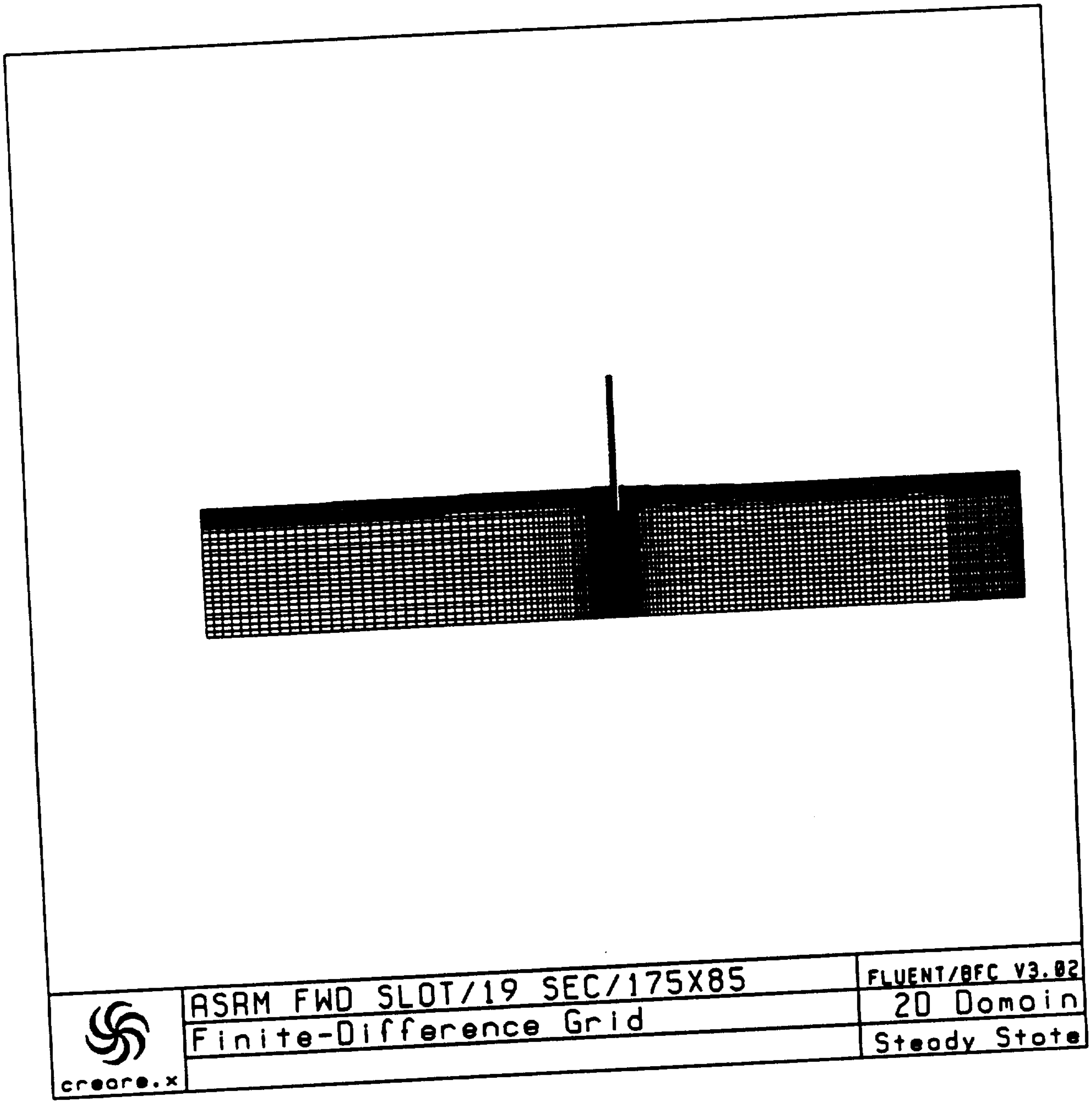

Figure 11. ASRM Forward Slot Computational Grid for the 19 Second Configuration

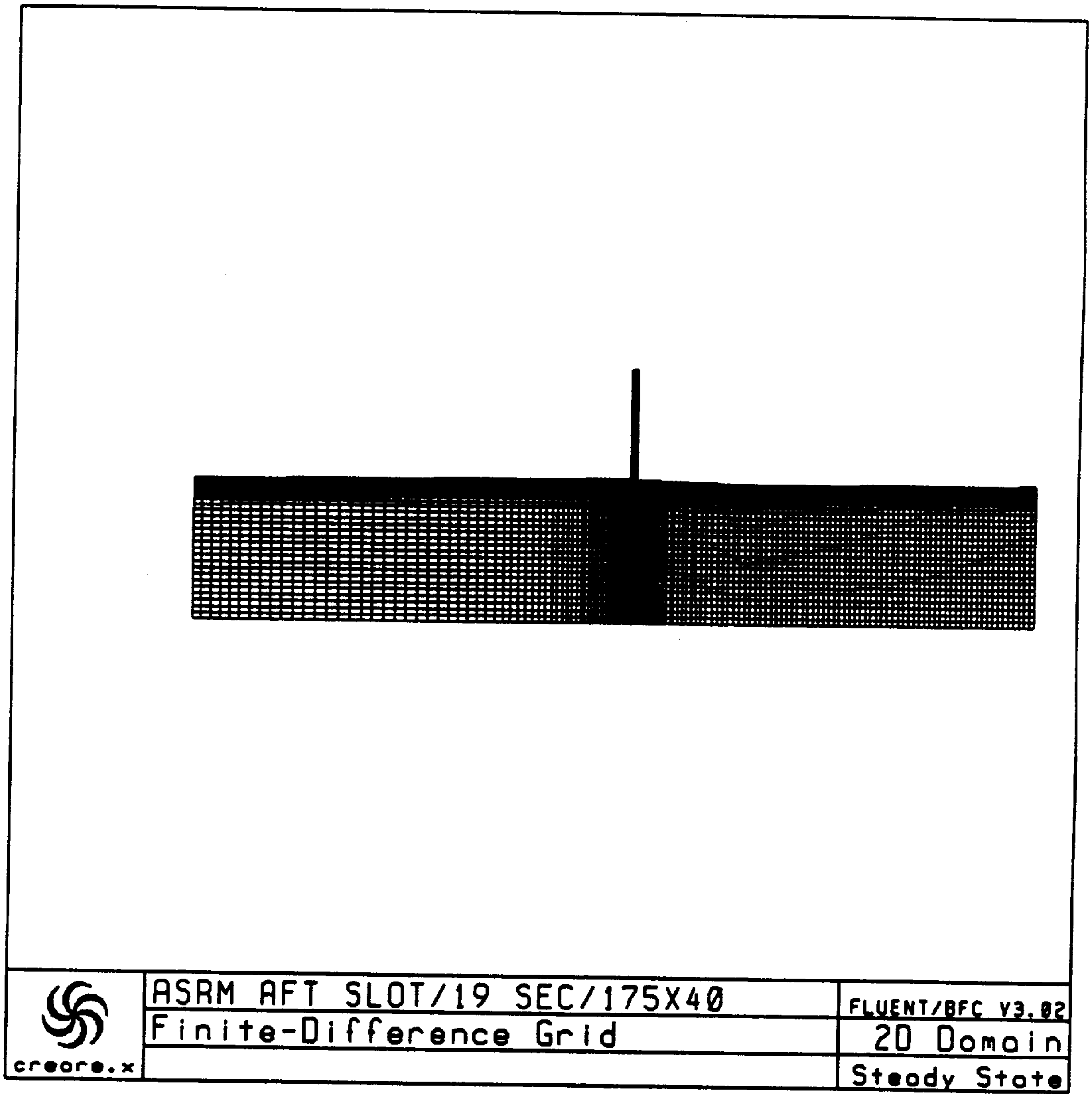

Figure 10. ASRM Aft Slot Computational Grid for the 19 Second Configuration

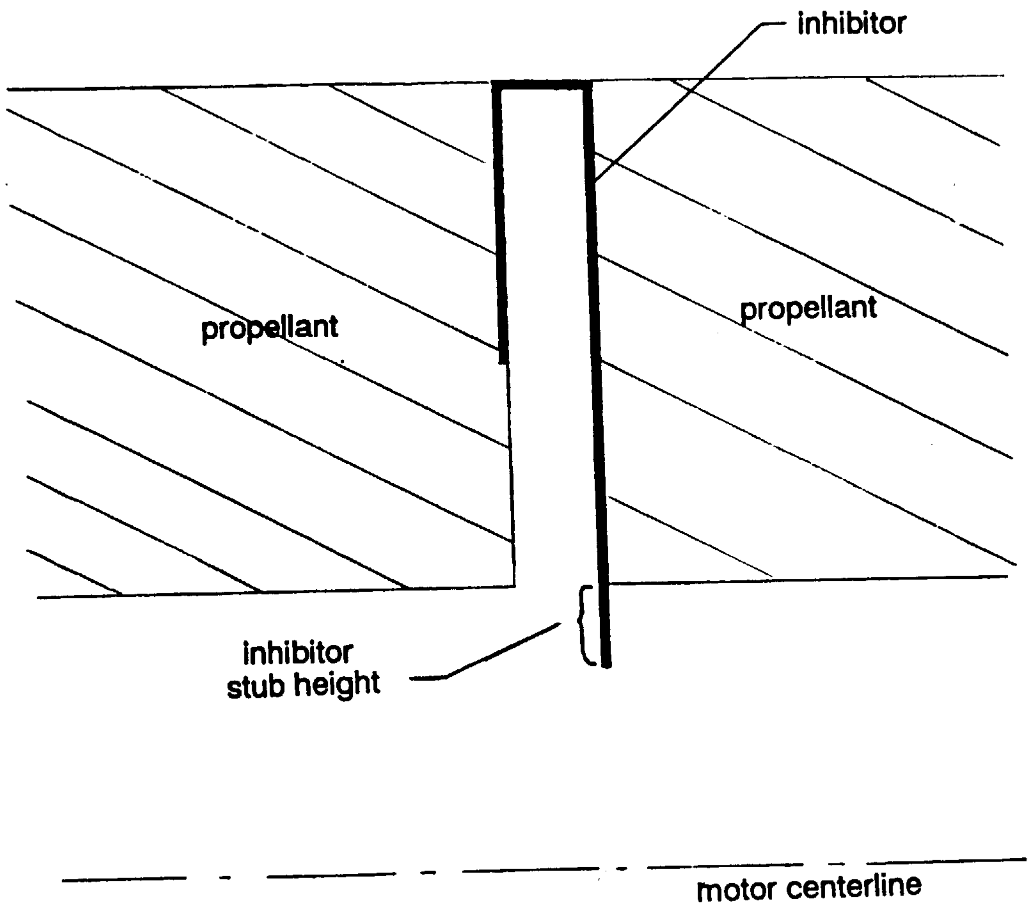

Figure 9. Inhibitor Stub Geometry in the Slot Region at 19 Seconds Burn Time

Figure 8. Pressure Distribution on the Front and Back Faces of the Fwd Slot, Undeformed Geometry

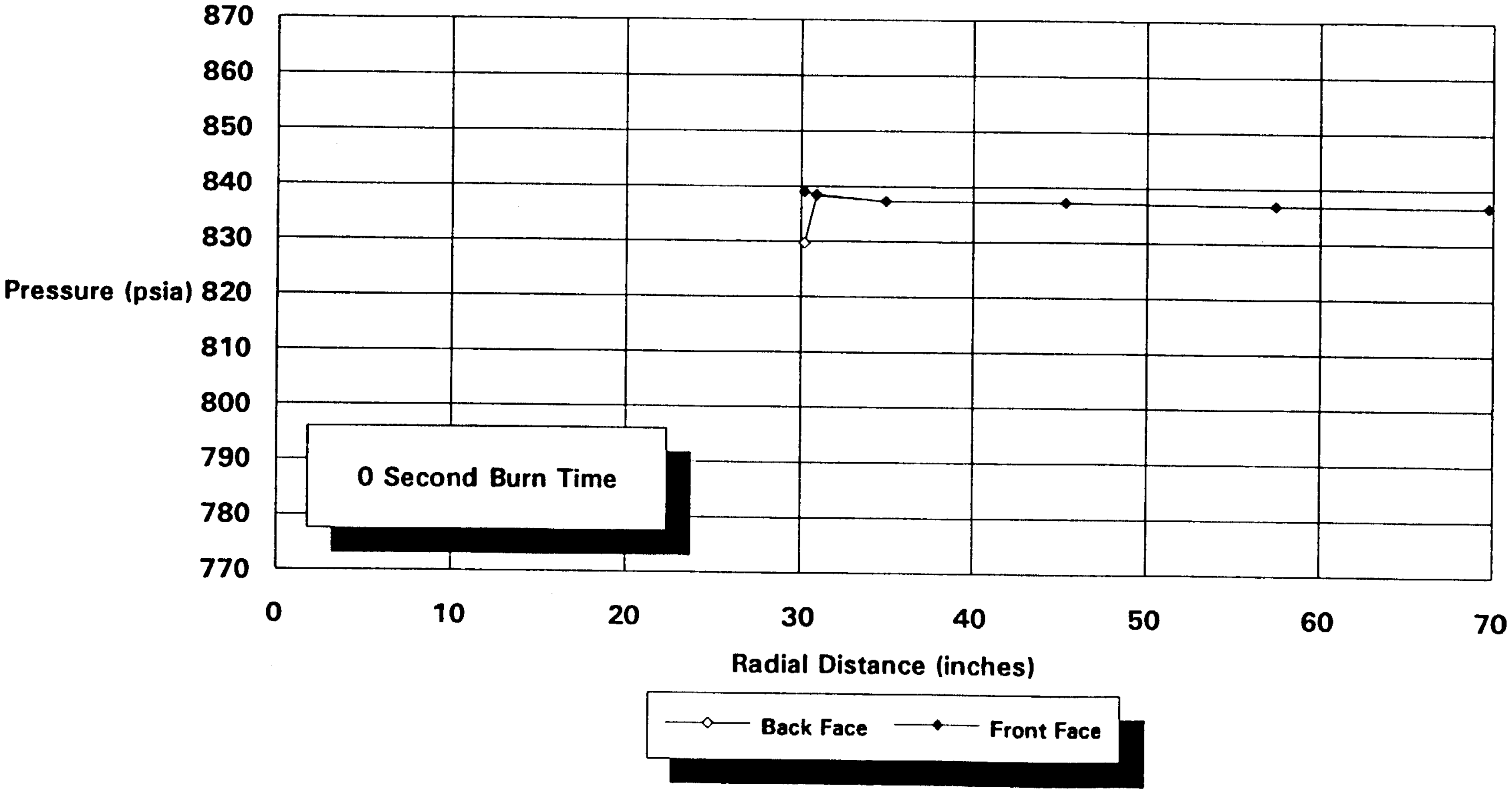

ERCI - 1/8/92

Figure 7. Pressure Distribution On the Front and Back Faces of the Aft Slot, Undeformed Grain

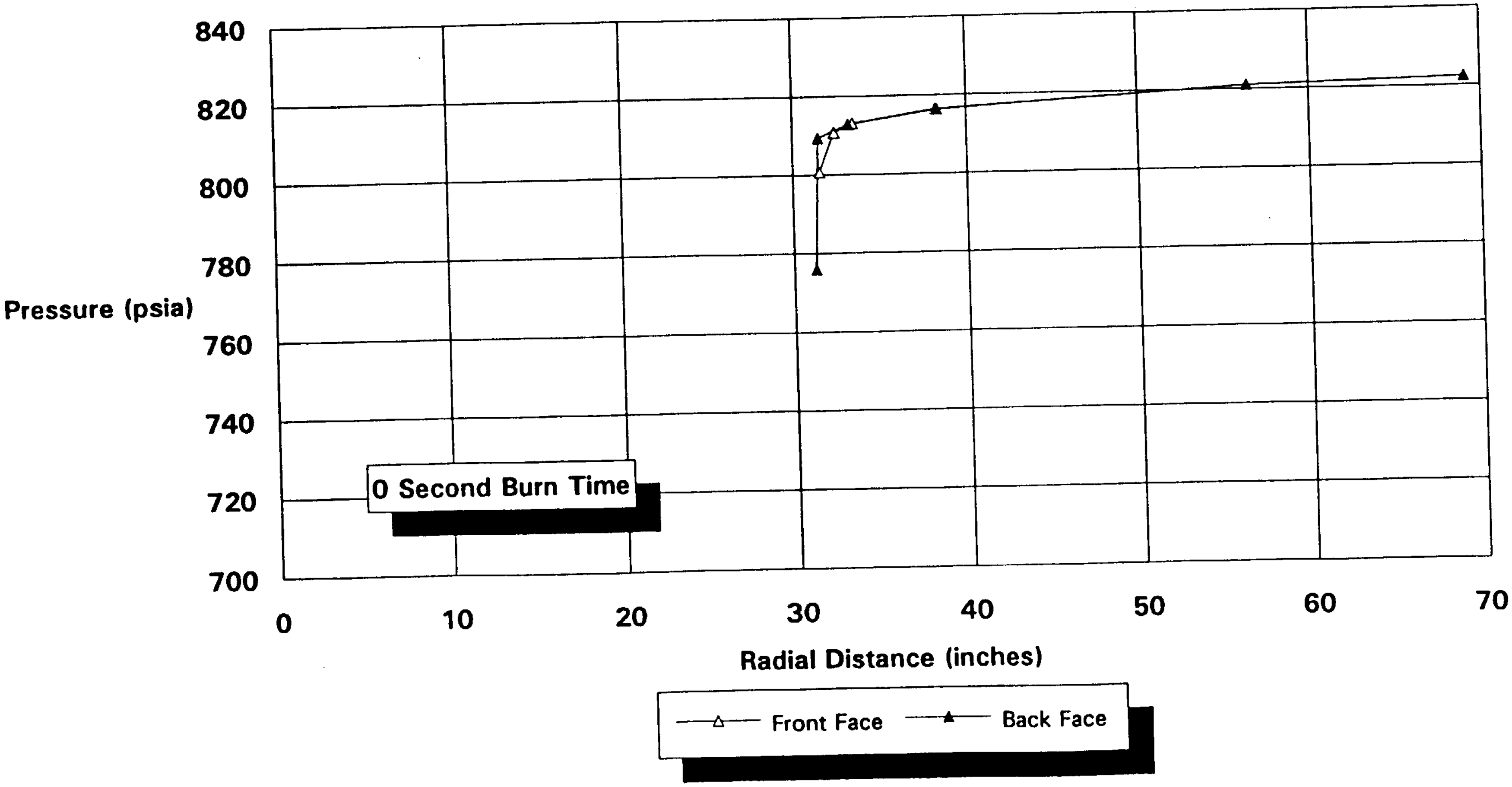

ERCI - 1/8/92

Figure 6. ASRM Fwd Slot Undeformed Grain Port Pressures On the Surface and at the Motor Centerline

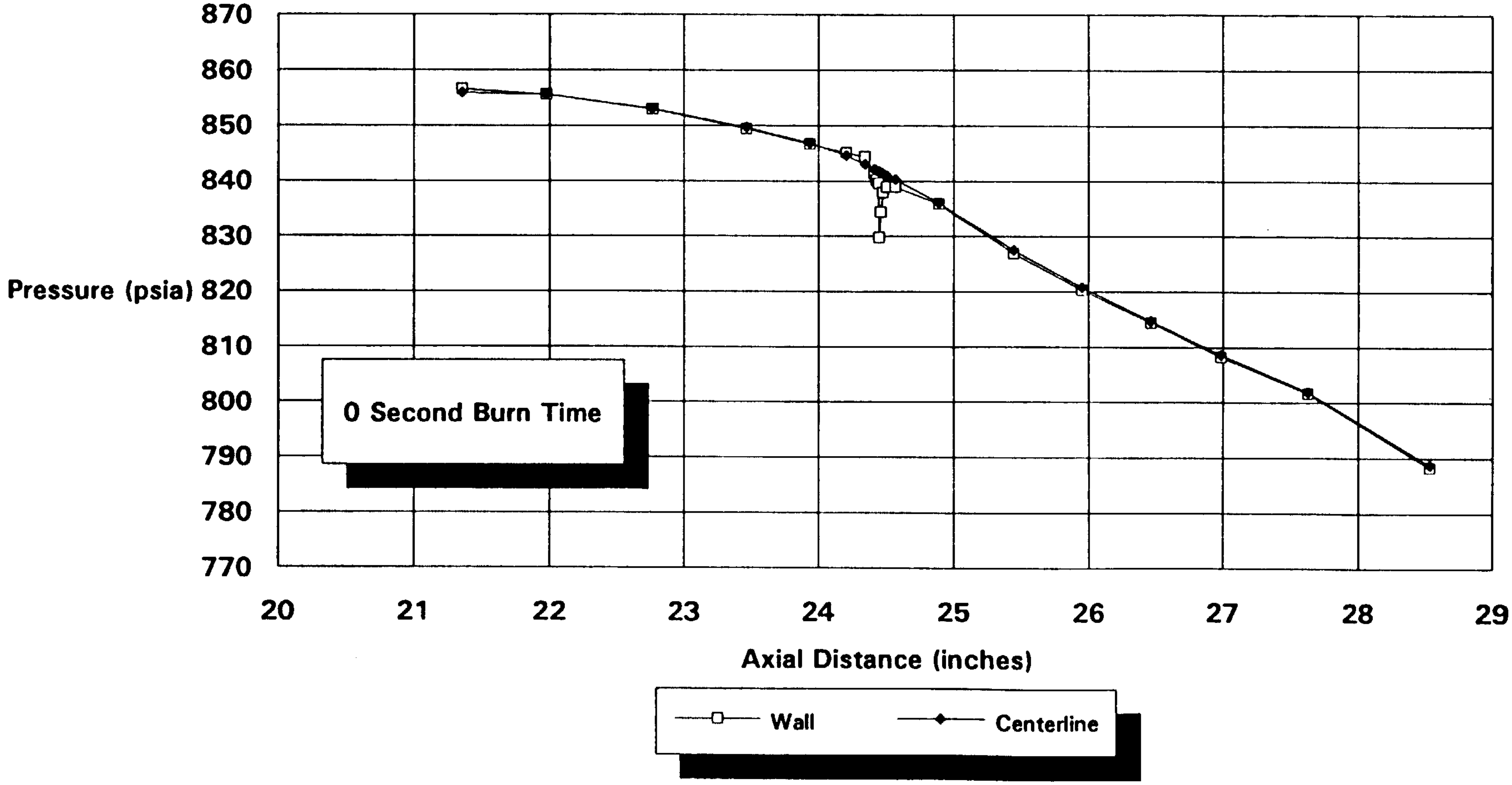

ERCI - 1/8/92

Figure 5. ASRM Aft Slot Undeformed Grain Port Pressures On the Surface and at the Motor Centerline

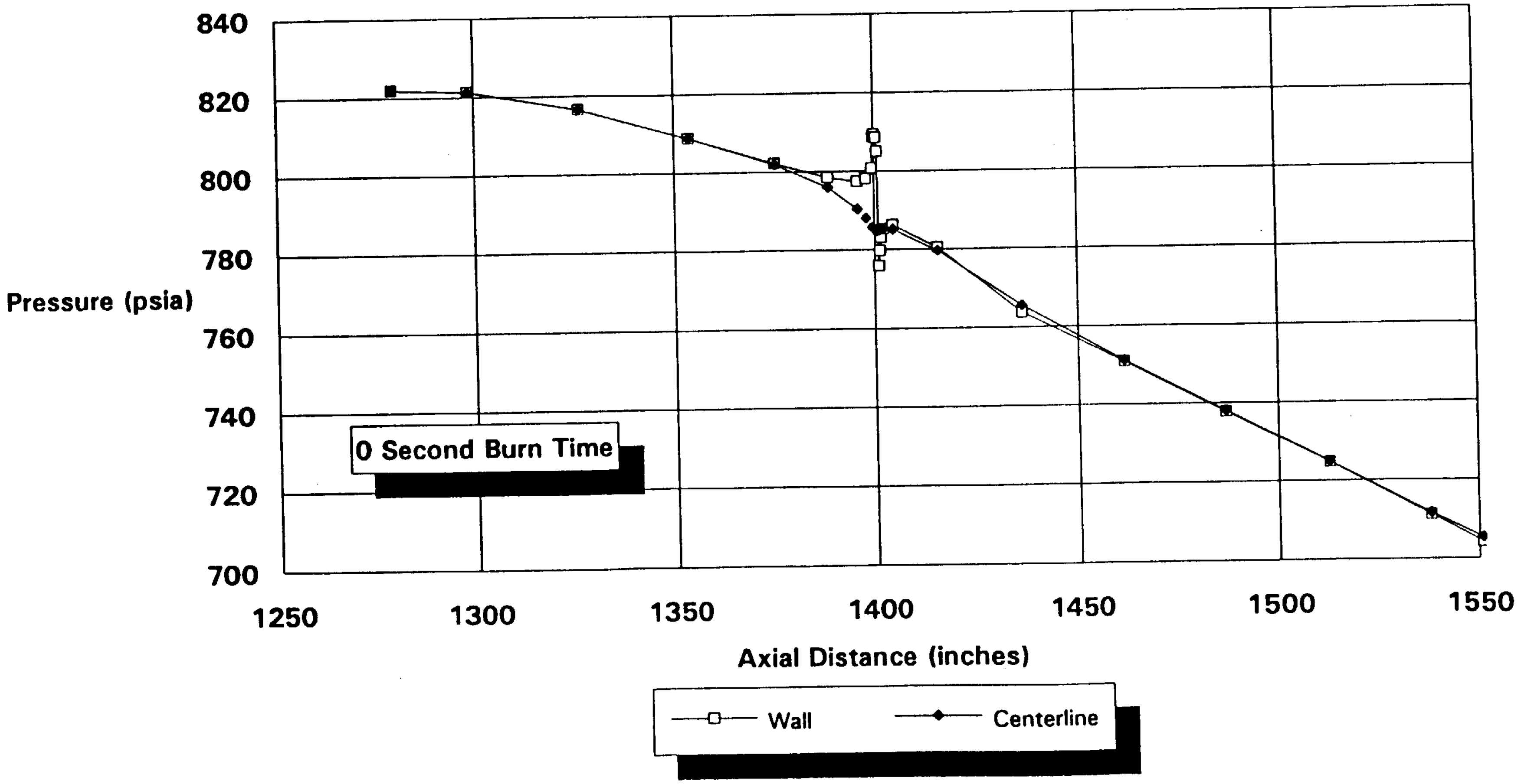

ERCI - 1/8/92

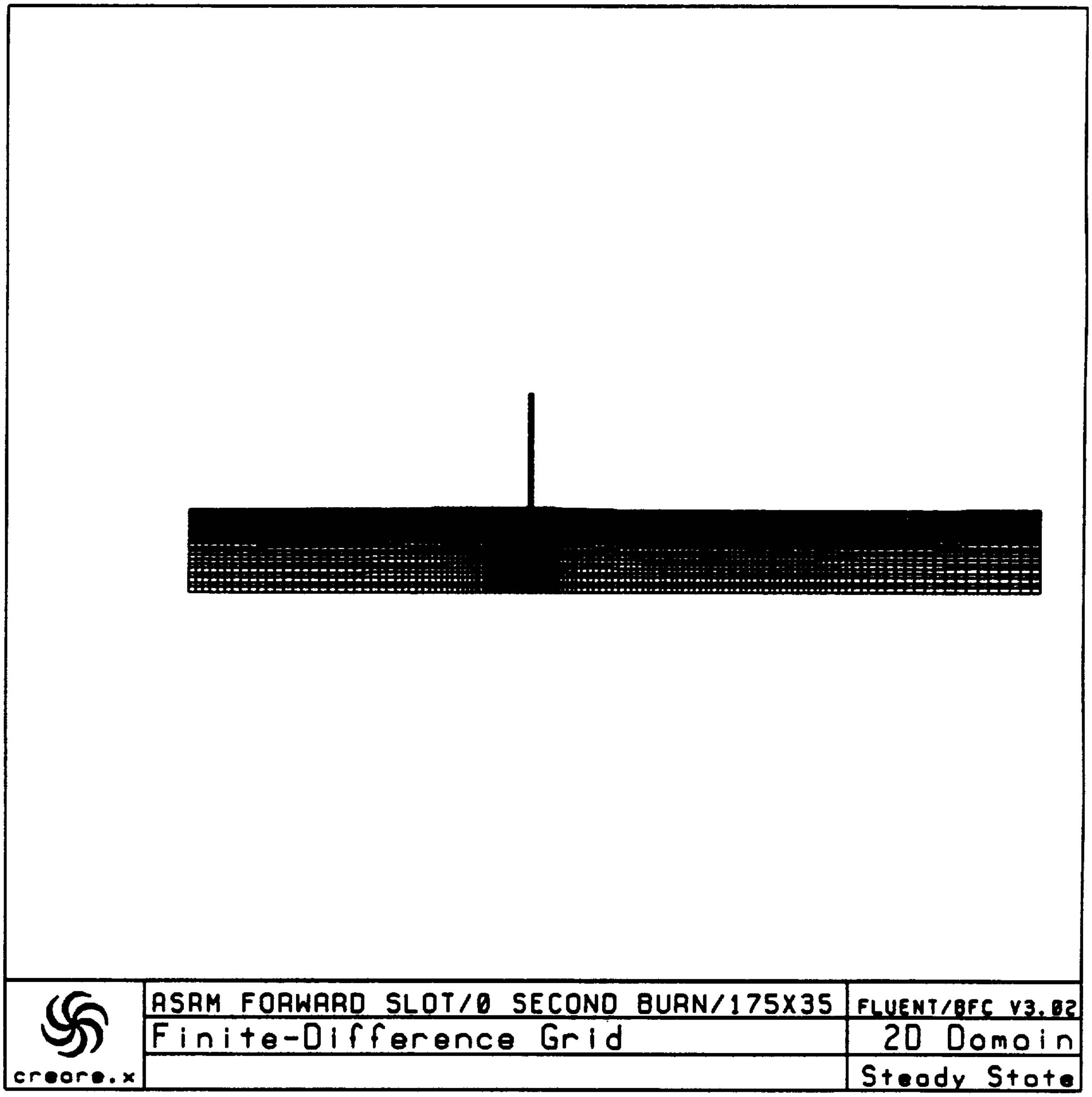

Figure 4. ASRM Forward Slot Region Computational Grid

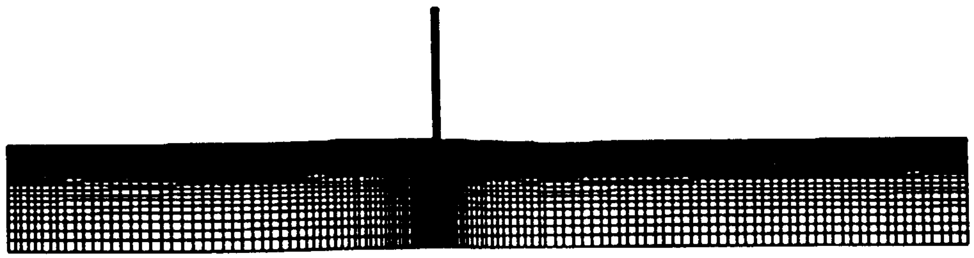

Figure 3.   Aft Slot Region Computational Grid

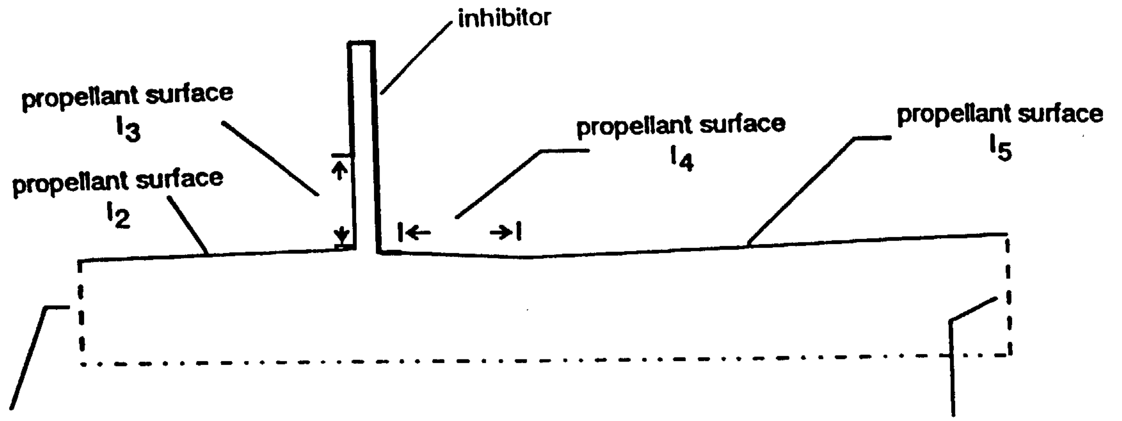

Figure 2. Boundary Conditions at the Constraining Surfaces of the ASRM Aft Slot

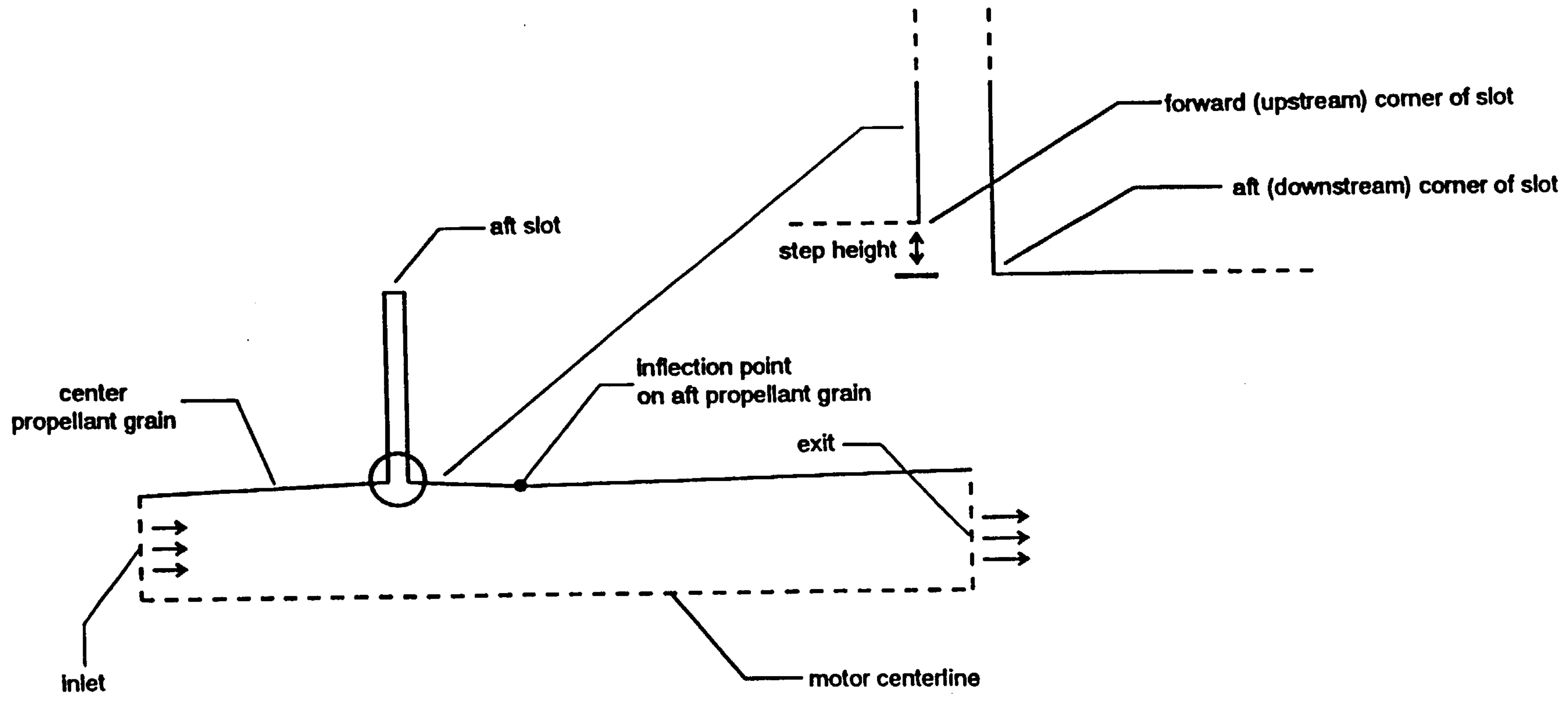

Figure 1. ASRM Aft Slot Geometry

inhibitor was not analyzed for the forward slot since the flush stub height of the aft slot showed no problems.and since the aft slot is more stressing than the forward slot.

The CFD analyses involving the 0 second and 19 second burn time configurations of the ASRM forward and aft slot regions have revealed several points. There are no large pressure gradients existing on the significant areas of the propellant grain at the 0 second burn time. This is due to the design of a small step height between the forward, center and aft grain segments at the motor field joints. These analyses were for the non-deformed propellant grain geometry. At least one further analysis should be performed which couples the mechanical stress and flow field for the more stressing aft slot region. This would insure that there are still no problems for the deformed grain propellant.

Even though the port velocities are reduced at the 19 second burn time, the analyses performed for the various inhibitor heights show potential problems induced by the inhibitor stubs at the field joints. An investigation of realistic estimates of the inhibitor heights and their downstream declination angles should be investigated. This information should then be used in an interactive coupled analysis between the flow field and propellant structural effects at the field joints.

Inlet Static Pressure	:	886.0 psia
Average Port Velocity	:	521.2 ft/s
Stagnation Temperature at the Inlet	:	6317.6 °R
Ratio of Specific Heats	:	1.128
Propellant Injection Velocity	:	9.956 ft/s
Molecular Weight	:	29.295
Mass Flow Rate (Inlet)	:	5963 lbm/s
CFD Calculated Mass Flow Rate (Inlet)	:	5944 lbm/s

Section 5 Conclusions

Due to erosive effects, the inhibitor height will not remain "full height" as described earlier in this section but this case shows a worst scenario in these analyses. If there is not problem induced in the flow field at this height then no further inhibitor analyses are needed. However, the flow field is significantly impacted if the full inhibitor stub height protrudes into the port. This inhibitor stub generates the same problems as generated by a large step height between the upstream and downstream propellant surfaces. Figure 12 shows the pressure drop down the port for the aft slot, full inhibitor stub height case. There is a very large pressure drop between the front and back surfaces of the inhibitor stub which would tend to bend the inhibitor in the downstream direction. Another important feature is that there is a large pressure load difference between the pressure on the back slot face of the downstream propellant surface and the propellant surface in the port downstream of the inhibitor stub, see Figure 13. This is due to the blockage of port flow and recirculation region created by the inhibitor stub. This creates a large surface pressure gradient on the propellant grain downstream of the slot. The pressure drop down the port for the eroded height inhibitor stub is shown in Figure 14. The magnitude of the pressure drop is greatly reduced, but is still of sizable magnitude and the pressure drop is distributed over a sizable area of the propellant surface downstream of the slot. Figure 15 shows the pressure drop down the port for the flush stub height inhibitor case. This case compares with the 0 second burn time configuration of the aft slot region since there is nothing protruding into the port but the pressure drop is negligible in this case since the port velocities are much lower that those existing in the 0 second burn configuration of the motor. Figure 16 shows the pressure drop down the front and back surfaces of the slot continued down to the bottom of the inhibitor stub protruding into the port flow. The figure shows the results for all the stub heights and illustrates that the pressure forces caused by the impingement of the port flow on the inhibitor stub has an impact on the pressures in the slot.

Similar results are noted for the forward slot analyses except that the magnitude of the effects are reduced due to the lower port velocity in the forward end of the motor. Figure 17 shows the pressure drop down the port for the full stub height inhibitor case and Figure 18 show the pressure drop for the eroded stub height case. Figure 19 shows the pressure drop down the front and back surfaces of the slot continued down to the bottom of the inhibitor stub protruding into the port flow. A flush stub height

The case with no stub height (the inhibitor is level with the propellant grain) will not be run. The first stub height is for an inhibitor height of 7.66"(full height). The second stub height is 3.83"(eroded height). This height represents a smaller erosion rate than used for the aft slot. This stub height represents an erosion of only one-half the propellant burn back rate. This lower erosion rate and higher stub geometry for the forward slot was used because of the lower velocities present in the forward end port. As the discussion of the analyses of the forward and aft slot proceeds, keep in mind that the stub heights are not the same for the forward and aft slots, but are as specified in the preceding discussion.

Figures 10 and 11 show the computational grids for the flush inhibitor stub height configuration of the aft and forward slots respectively. There are 175 axial grid lines for both the forward and aft configurations. Forty grid lines are used in the radial direction instead of 35 for the 0 second burn time configuration since the port radius is larger due to propellant burn back. The resolution of the grid near the propellant surface remains approximately the same as in the 0 second burn time configuration grid. The grids for the various inhibitor stub height configurations are also slightly different due to the geometric differences in the immediate vicinity of the slot but grid spacings are used for the different configurations such that the grid spacing relative to the bottom of the inhibitor stub height remains constant.

The boundary conditions utilized at the inlet, exit, propellant and inhibitor surfaces are identical to those discussed for the 0 second configurations of the motor. However, the numerical values of these boundary conditions are different. These are given in Tables 3 and 4 for the aft and forward slot respectively.

Table 3. Aft Slot Boundary Conditions for the 19 Second Burn Time Configuration

Aft Slot

Inlet Static Pressure	:	861.3 psia
Average Port Velocity	:	746.25 ft/s
Stagnation Temperature at the Inlet	:	6317.6 °R
Ratio of Specific Heats	:	1.128
Propellant Injection Velocity	:	10.135 ft/s
Molecular Weight	:	29.295
Mass Flow Rate (Inlet)	:	8846 lbm/s
CFD Calculated Mass Flow Rate (Inlet)	:	8824 lbm/s

Table 4. Forward Slot Boundary Conditions for the 19 Second Burn Time Configuration

Forward Slot

slot region. The pressure drops down the back face of the slot for both the forward and aft slot configurations was not problematically large. Figure 7 and Figure 8 show the pressure drop down the front and back slot surfaces for the aft and forward slot respectively. Another important point to note in Figure 5 and Figure 6 is that the lowered pressure at the downstream corner of the slot is confined to a small area and does not cover a large area on the downstream propellant grain. The jet formed by the flow emanating from either the forward slot or the aft slot causes the port flow to be diverted toward the motor centerline which causes a large portion of the momentum loss in this region of the motor. The other major source of momentum loss is the loss due to having to accelerate the normal flow from the propellant surface in the axial direction down the port.

Section 4 Results for the 19 second burn time motor configurations

Results for the forward and aft slot 19 second burn time configurations are presented in this section. A significant feature present in these analyses which was not present in the 0 second burn time analyses is presence of an inhibitor stub protruding into the port flow. An illustration of the inhibitor stub geometry is shown in Figure 9. The back face of the slot propellant at 0 seconds burn time is bonded to an inhibitor so that as the propellant burns back from its original position, the inhibitor remains at its initial height. This creates a situation such that as the propellant grains upstream and downstream of the slot continue to burn back, a portion of the inhibitor remains which protrudes into the port flow field. The actual amount of the inhibitor remaining depends upon the erosion rate. Also, since the inhibitor is flexible, the stub will be inclined at some downstream angle. In all the analyses performed on the slot/port flow interaction, no attempt has been made to determine exactly how much of the inhibitor remains protruding into the port. Instead, the approach in this report has been to perform a parametric analysis on the inhibitor height to determine any adverse effects in the port generated by the inhibitor stub. The various inhibitor stub heights are also perpendicular to the propellant surface downstream of the slot and no attempt at this stage has been made to determine the effects of inclination of the inhibitor stub. The purpose of the parametric analyses discussed will give a good indication of the need for further analyses related to the inhibitor stub.

Three inhibitor stub heights are considered for the more stressing aft slot configuration. An inhibitor stub height of 6.74"(full height) which represents the height of the original height of the stub at 0 seconds burn time. An inhibitor stub height of 2.87"(eroded height) which represents an inhibitor erosion rate of almost two-thirds that of the burn rate of the propellant. This stub height is a little more than one-third the original height of the inhibitor at 0 seconds burn time. And an inhibitor stub height of 0"(flush) which represents a case in which the inhibitor is eroding at the same rate as the propellant is burning and does not protrude into the port.

Since the port velocity is lower in the forward slot region, the slot/port flow interaction is not as stressing. Only two inhibitor stub height cases will be run for the forward slot.

U_{avg} : average velocity
r_p : port radius
r : radial location
U : velocity at radial location "r"

A zero gradient boundary condition was used at the port exit. The propellant and inhibitor surfaces were considered to be adiabatic.

Table I. Aft Slot Boundary Conditions for 0 Second Burn Time Configuration

Aft Slot

Inlet Static Pressure	821.9 psia
Average Port Velocity	1177.5 ft/s
Stagnation Temperature at the Inlet	6345 °R
Ratio of Specific Heats	1.128
Propellant Injection Velocity	13.467 ft/s
Molecular Weight	29.489
Mass Flow Rate (Inlet)	8682 lbm/s
CFD Calculated Mass Flow Rate (Inlet)	8562 lbm/s

Table 2. Forward Slot Boundary Conditions for 0 Second Burn Time Configuration

Forward Slot

Inlet Static Pressure	855.9 psia
Average Port Velocity	877.5 ft/s
Stagnation Temperature at the Inlet	6345 °R
Ratio of Specific Heats	1.128
Propellant Injection Velocity	9.9837 ft/s
Molecular Weight	29.489
Mass Flow Rate (Inlet)	6178 lbm/s
CFD Calculated Mass Flow Rate (Inlet)	6103 lbm/s

The maximum Mach number at the centerline for the 0 second aft slot problem was just over 0.7 which is more stressing than the forward slot problem which had a maximum Mach number of 0.55. The average Mach number at the forward slot configuration inlet was .253 while the average Mach number at the aft slot configuration inlet was .339.

Figure 5 shows the pressure drop down the port at the motor centerline and at the propellant surface for the aft slot and Figure 6 shows the port pressures for the forward that no significant negative findings are reported in the ASRM slot/port flow interaction analyses.

Section 3 Results for the 0 second burn time motor configurations

Results for both the forward and aft slot, 0 second burn time configurations, will be discussed in this section, but a full presentation of the 0 second burn time aft slot results with color plots can be found in the September monthly report. Also, a complete set of color plots describing the motor flow field information is contained in the presentation documentation given by ERCI on January 8, 1992 at the ASRM Internal Flow TIM. This is a more complete package than the September monthly report and contains plot results for all the slot/port flow interaction problems discussed in this report.

The detailed geometric description for the aft slot is specified in ERCI drawings H5001-1B and H5004-1B while the geometric description for the forward slot was obtained from ERCI drawings H5002-1B, H5003-1B and H5004-1B. Figure 3 shows the computational grid for the 0 second aft slot configuration and Figure 4 shows the computational grid for the 0 second forward slot configuration. Some grid sensitivity was performed for these runs and it was determined that all the grids used provided adequately resolved solutions. There are 155 axial grid lines and 35 radial grid lines in the port for the aft slot configuration. The slot region is resolved by 85 radial grid lines and 10 axial grid lines. The same axial resolution upstream of the slot was used for the solution of the forward slot/port flow interaction but more grid lines were used downstream of the slot since the exit location was chosen further downstream of the slot. A total of 175 axial grid lines and 35 radial grid lines were used to resolve the port flow for the forward slot problem. The slot was resolved by 85 radial grid lines and 13 axial grid lines.

Both the forward and aft slot configurations were solved as axi-symmetric problems with the plane of symmetry being the motor centerline. The boundary condition numerical values for the 0 second burn time runs are shown in Table 1 and Table 2 for the aft slot and the forward slot respectively. These boundary conditions were obtained from the NASA/MSFC SPP ballistic simulation. A normal velocity boundary condition was specified at the propellant surfaces with the appropriate propellant injection velocity taken from Table 1 or Table 2. The inhibitor surfaces were modelled using a no-slip wall boundary condition. A Culick velocity profile was assumed as the port flow velocity profile at the inlet. The Culick profile was based on the average 1-D velocity at motor station 1279.512" for the aft slot and the motor station at 840.83" for the forward slot. Both of these motor reference stations were obtained from the ASRM motor coordinate reference system used in the ERCI drawings. The equation used to compute this velocity profile is:

$$U = \frac{\pi}{2} U_{avg} \cos\left[\frac{\pi}{2}\left(\frac{r}{r_p}\right)^{2}\right]$$

Slot/Port Flow Interaction Analysis

Section 1 Introduction

This document describes the analyses which have been performed on the ASRM full-scale motor involving the interaction between the slot and port flows. Results are discussed for two burn time geometric configurations. The first is the 0 second burn time geometry and the second is the 19 second burn time geometry. Results for the slot/port flow interaction at both the forward and aft field joints are presented for both of these propellant geometric configurations. All the results presented in this report are for non-deformed motor geometries; that is, no curing, propellant slump, thermal cooldown, gravity loading or motor pressure loading effects have not been included in determining the shape of the propellant geometry. A coupled analysis investigating the interaction between the mechanical forces acting on the propellant grain and the motor internal flow field will be performed at a later time in conjunction with NASA/MSFC mechanical analysts.

Section 2 General Features of the Slot/Port Flow Interaction Problem

Figure 1 shows the general features of the ASRM aft slot motor geometry. Since these features are similar to the features observed for all the slot/port flow interaction analyses, this figure will be used to describe the general features of interest for these problems. Also, Figure 2 is a similar figure illustrating the boundary surfaces for the slot/port flow interaction problems. Analytical results involving a variety of geometric configurations and boundary conditions were desired to adequately analyze the slot/port flow interaction in the ASRM motor. For this reason, it was not feasible to calculate the full motor flow field from the head end of the motor to the nozzle for each CFD run. This requires the motor to be sectioned into analytical regions of interest around the forward and aft slot. These regions must be chosen in such a way as to minimize the effects of solving only a portion of the motor flow field.

The Inlet and the Exit shown in Figure 1 are the beginning and the end of the section chosen for analysis. The slot/port flow interaction is the main feature of the flows considered in this monthly report so the inlet location must be chosen so that the upstream effects of the slot on the port flow are negligible. The inlet location for the problems in this report is located approximately two motor port L/D's upstream of the slot or 120 inches. This location should fulfill the requirement that the upstream effects of the slot flow are negligible at the inlet. The exit is chosen far enough downstream so that the flow field gradients created by the slot/port flow interaction are no longer important. In the slot region shown in the inset of Figure 1, a very important feature to the slot/port flow interaction problem is illustrated. This is the step height between the front and back faces of the propellant grain. This feature was found to be crucial to the problems encountered in the Titan IV SRMU analysis. As a important point to note in the analyses reported in this monthly, the step heights at both the forward and aft slots in the ASRM motor are much less than those for the Titan IV. This is the major reason

A copy of the motor case, case insulated, case loaded, and nozzle drawings was obtained and an effort was initiated to update all ERC drawings to the ASRM PDR configuration. A number of errors and inconsistencies were discovered which were worked directly with Aerojet.

The final summary memo report of the activities and recommendations of the Castable Inhibitor Review Team was presented to the ASRM Chief Engineer and Propulsion System management. The presentation was made by David Ricks with all team members present. The discussion of the team findings was intensive, but the recommendations were accepted including the major request that Lockheed/Aerojet review the report and prepare a comprehensive response to the detailed test and analysis plans for development and qualification of the castable inhibitor. The castable inhibitor was viewed as an increased design risk by the team.

ASRM Full Scale Motor Design Investigations

A memorandum was prepared to explain the rationale for using cold flow models of the ASRM design to help qualify the propellant and nozzle design and to validate the CFD models of the internal flow field. This memo was in response to an internal Aerojet memo which questioned the necessity of additional cold flow validation data for the ASRM program.

The hyperbolic spiral nose design for ASRM was checked by comparing an ERC design with the Aerojet design. The designs are close except for a "flat" zone in the Aerojet design just upstream of the throat. Improvements to an existing ERC code, HYPER, were made to accomplish this task.

An ASRM nozzle technical interchange meeting was attended and supported at the Lockheed/ASRM Progress Center location. The nozzle design and the aerothermal analyses were reviewed at this meeting. At a follow-on splinter meeting on the bearing torque problems, it was learned by ED33 that the static pivot point of the nozzle had changed from 23.3 to 17.6 inches aft of the throat plane. An overlay drawing, ERC 5005-X, was prepared to show the effect of the pivot point change on the position of the nozzle nose at a gimbal angle of 8 degrees. The effect of the nozzle pivot shift was to translate the nozzle approximately 0.8 inches laterally in a direction perpendicular to the nozzle axis in the 8 degree position.

The nozzle nose geometry had also changed slightly since the creation of the drawings of the ASRM aft case and nozzle, at 19 seconds burn time, H5005-1. This change was evaluated in a new overlay drawing, H5005-X. It is too late for this change to be incorporated into the ASRM cold flow model which was being produced at this time.

Preparations were initiated for a CFD TIM to be held at NASA/MSFC on January 8, 1992. The participants will be ED32, Aerojet and ERC. The topic were the status of flow field analyses for the full scale motor and for ASRM cold flow models. ERC covered analyses of the forward and aft slots at burn times of zero and 19 seconds. Details of the specific test objectives for the ASRM aft section/nozzle cold flow model 538C to be used at the NASA/SRMAFTE facility were presented. The design ground rules and approach were also presented at the meeting. Some material was presented on the validation of the design goals using a combination of CFD analytical results and experimental results. The CFD analyses investigating the slot/port flow interaction at the ASRM motor field joints was also presented.

The ASRM PDR was supported by participation on the Nozzle, Propellant and Liner, Insulation, and Igniter Review Teams. The CFD and aerothermal analyses and sections of the D & V plan were reviewed. Numerous written requests for more information (PDR Request Form) and two RID's resulted from this review. One RID pertained to the lack of a ballistic and flow analysis of the multi-port igniter and the other RID pertained to a deletion of cold flow validation testing for the CFD models.

Figure 36. Pressure Contours In The Aft Slot Region Of Configuration 4.

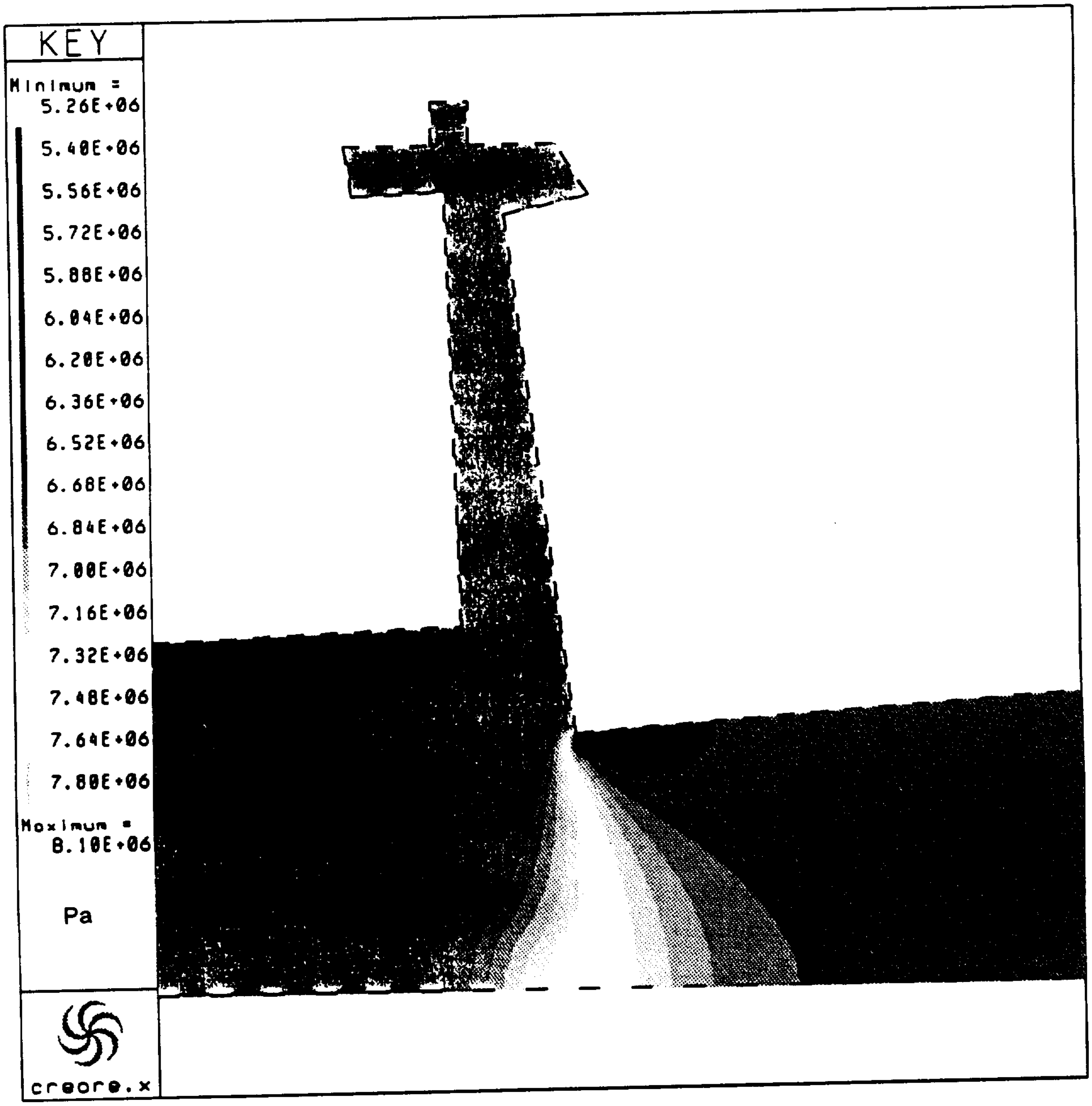

Figure 35. Pressure Contours In The Aft Slot Region Of Configuration 3.

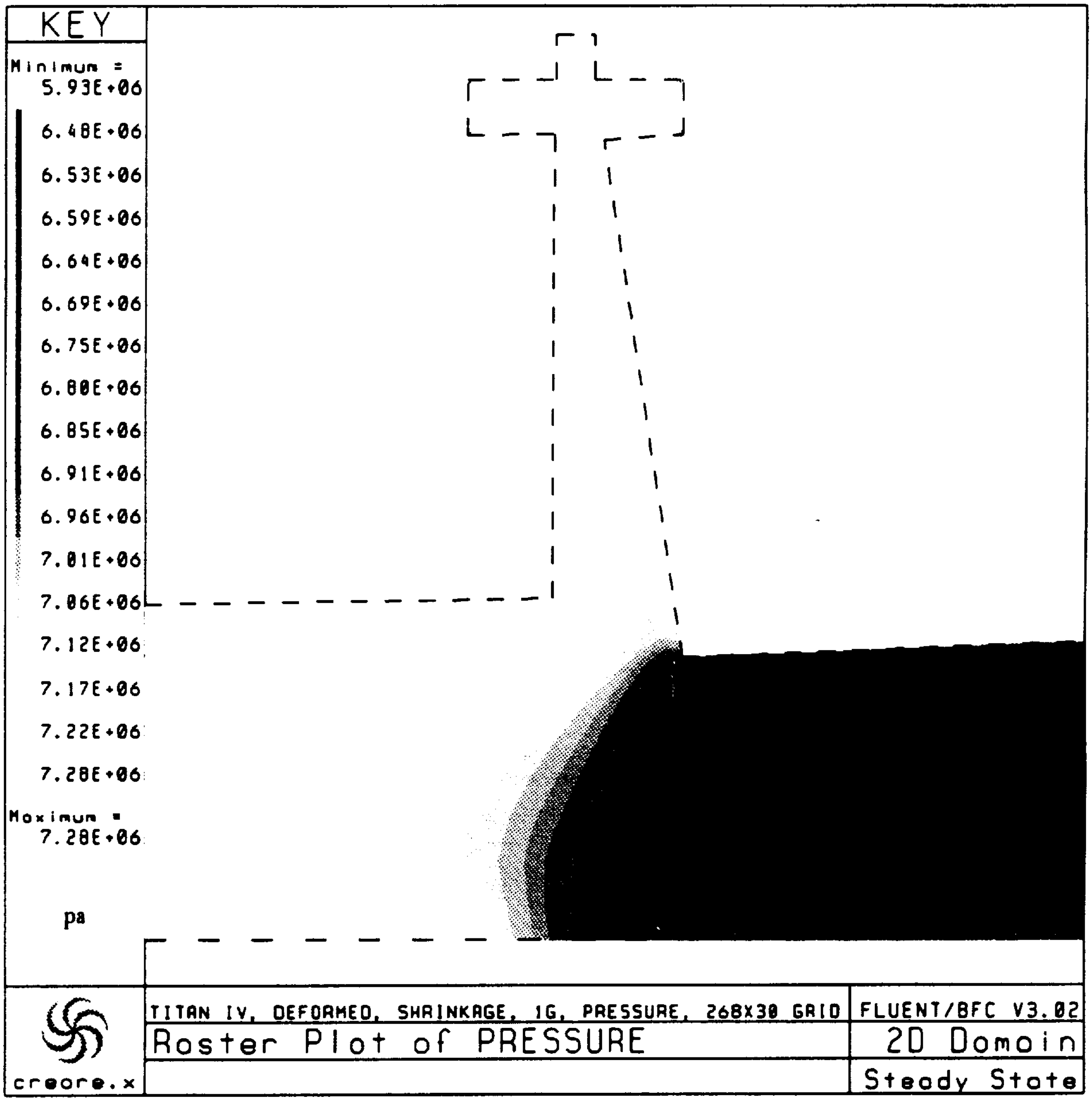

Figure 34. Pressure Contours In The Aft Slot Region Of Configuration 2.

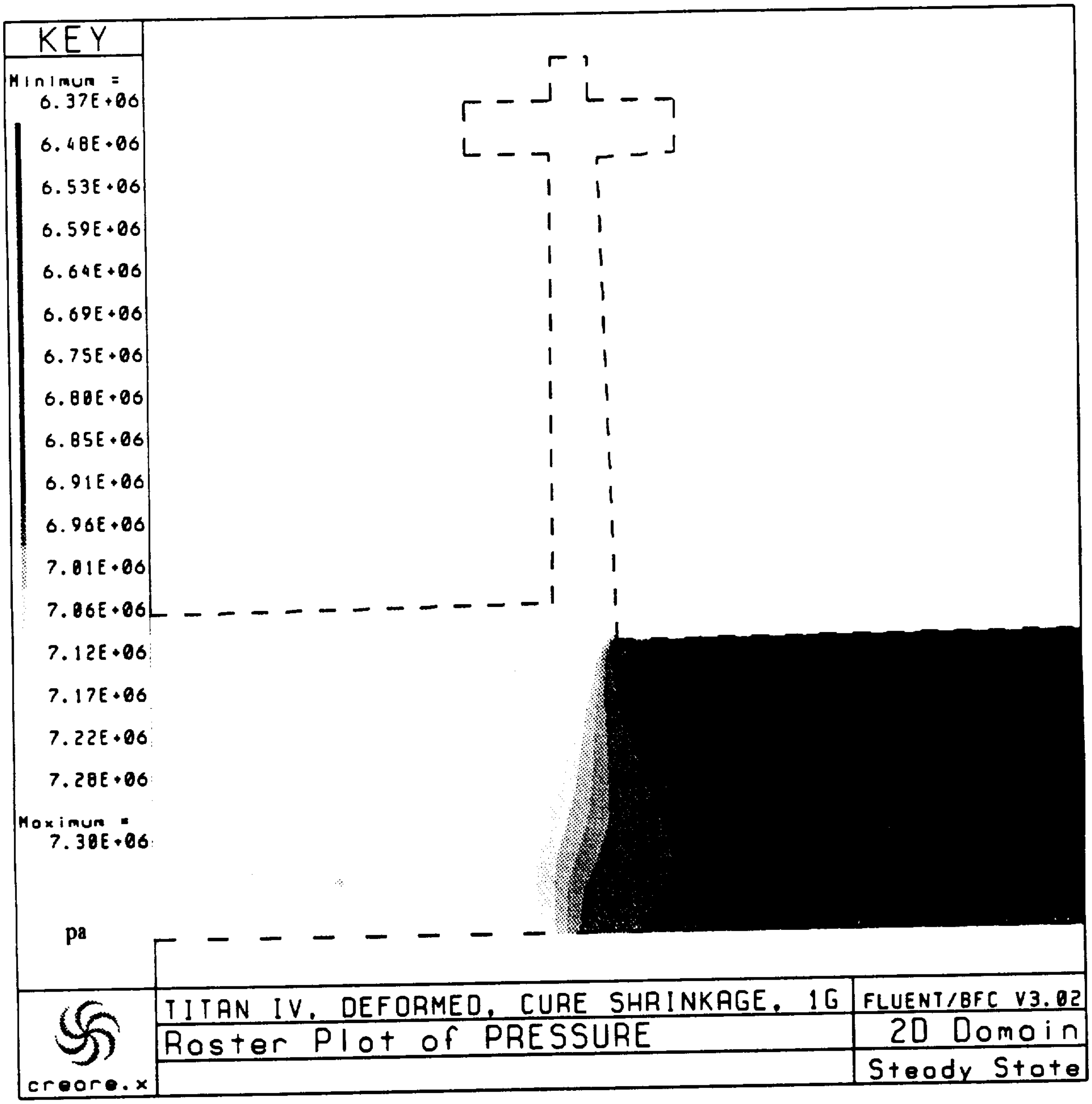

Figure 33. Pressure Contours In The Aft Slot Region Of Configuration 1.

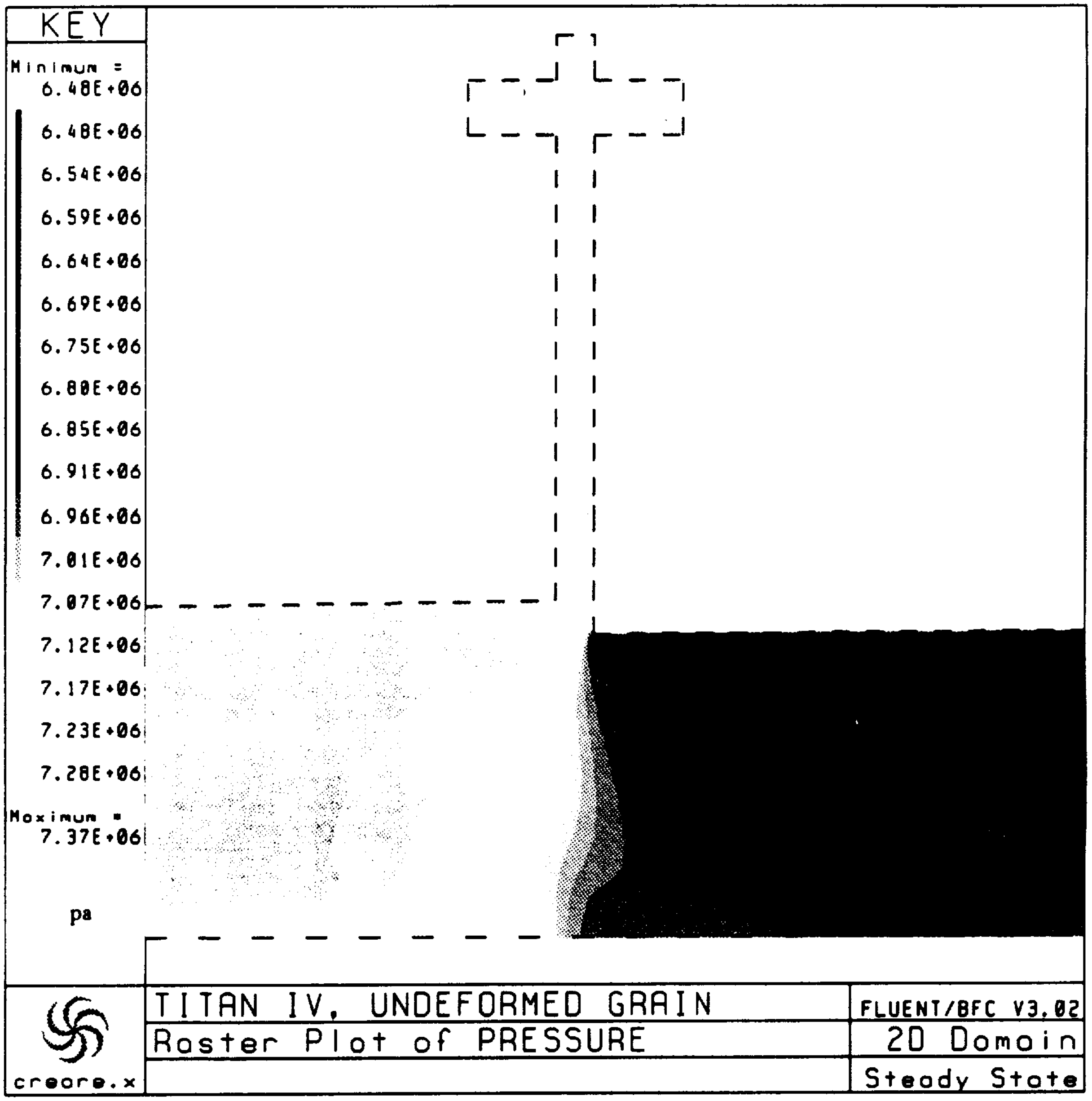

Figure 32. Port Surface Pressure for Aft Segment, Configuration 4.

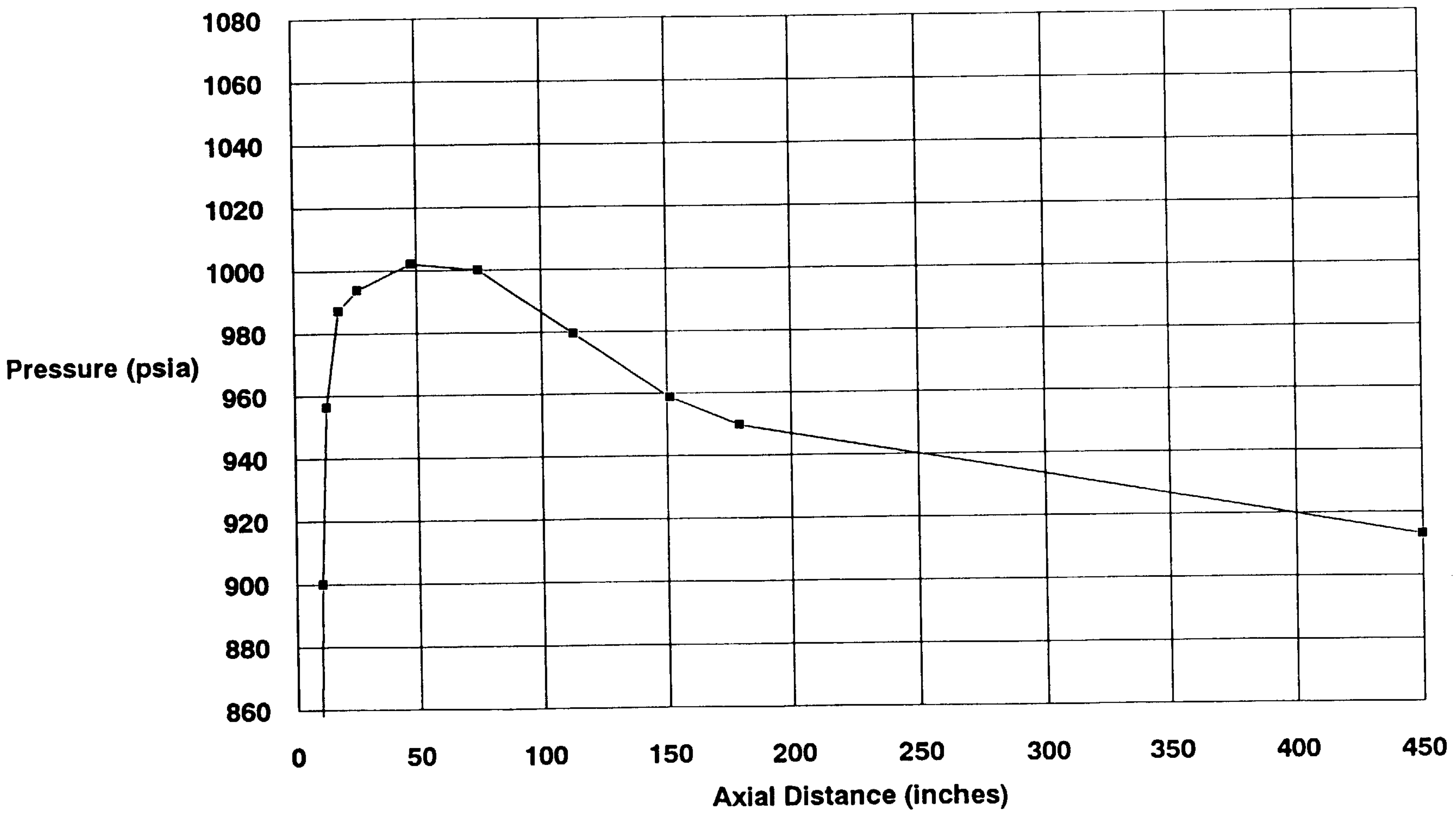

Figure 31. Port Surface Pressure For The Center Segment, Configuration 4.

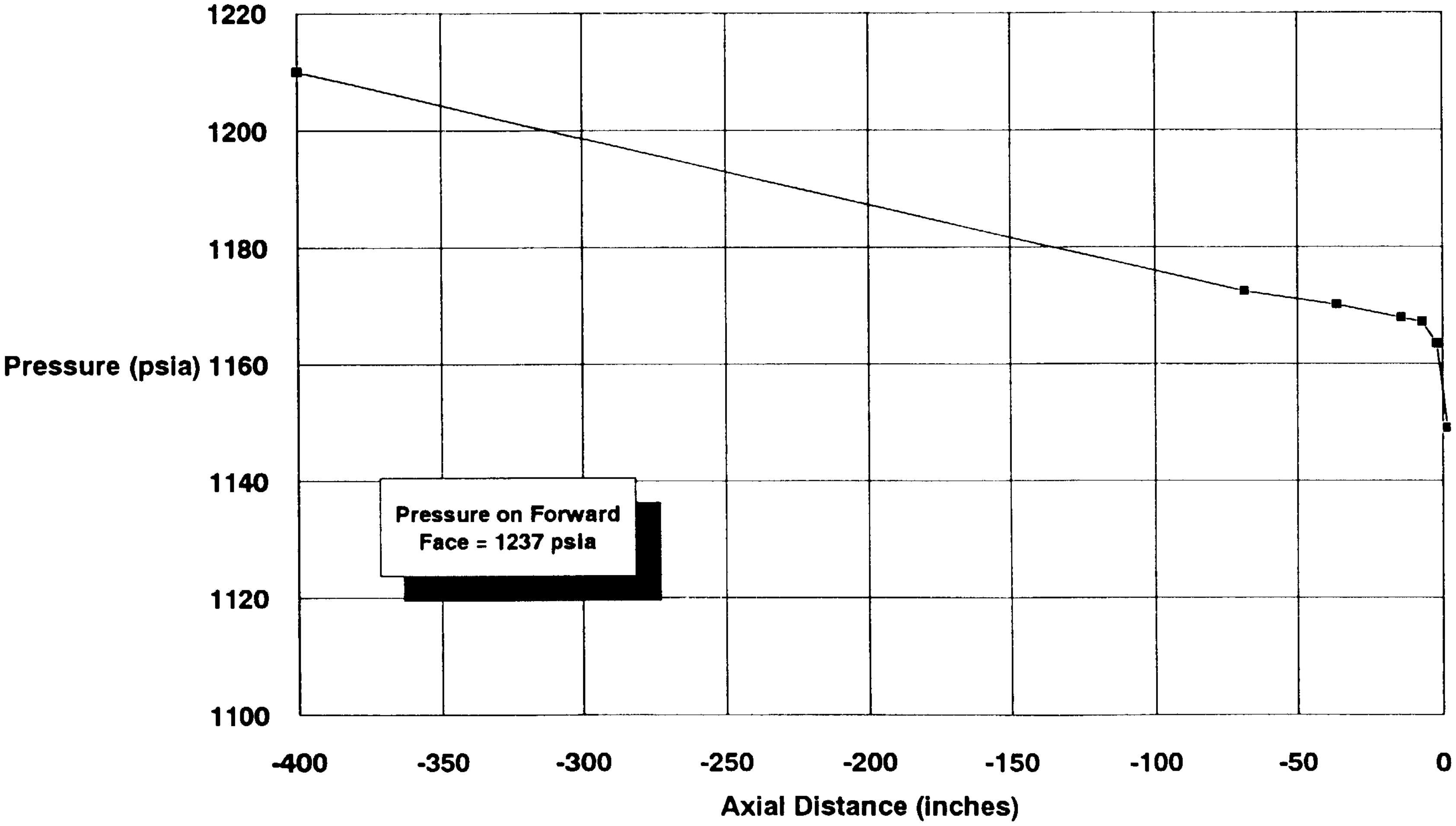

Figure 30. Flow Field Mach Number Contours For Configuration 4.

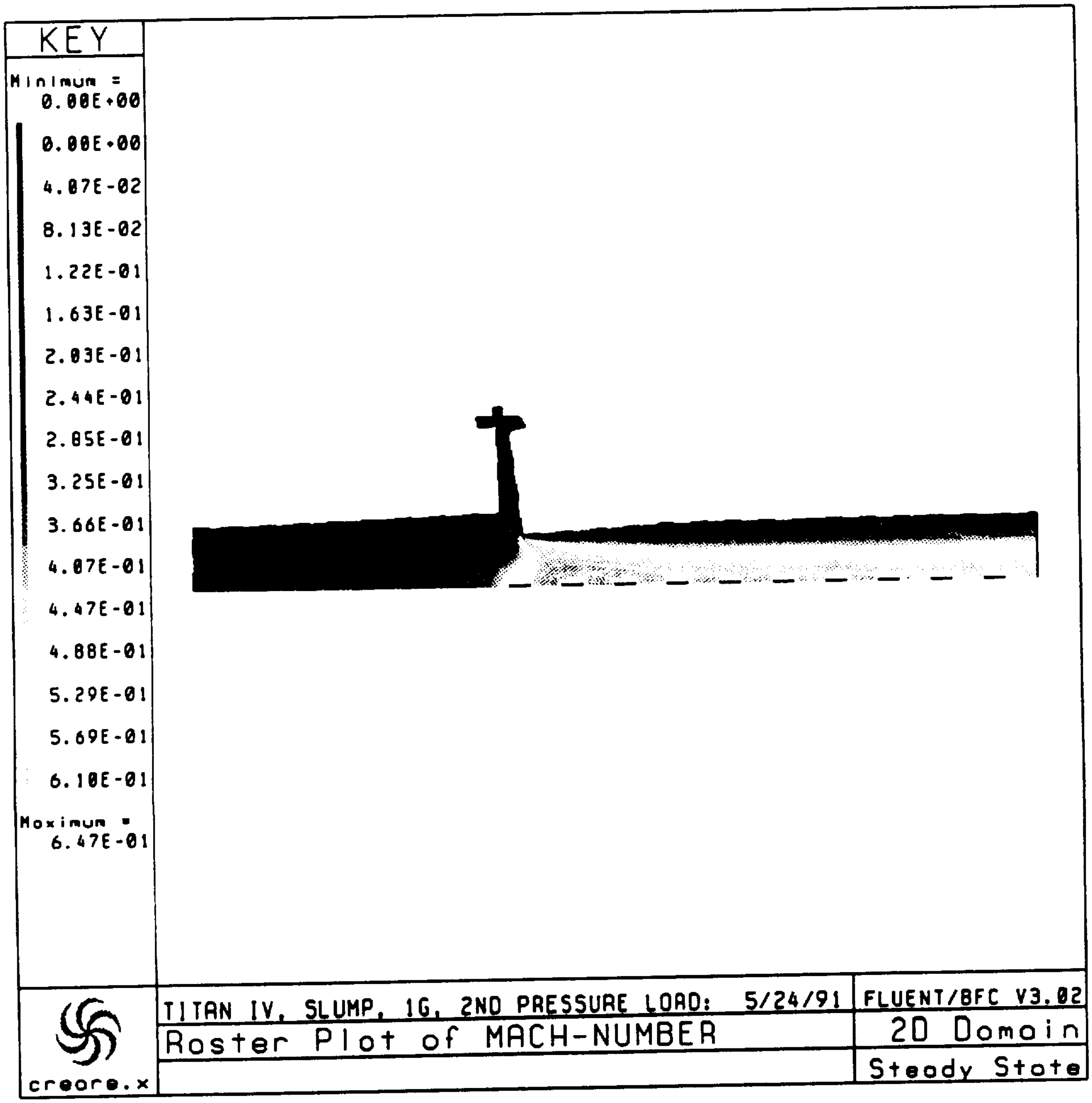

Figure 29. Velocity Vector Flow Field In The Aft Slot Region Of The Motor For Configuration 4.

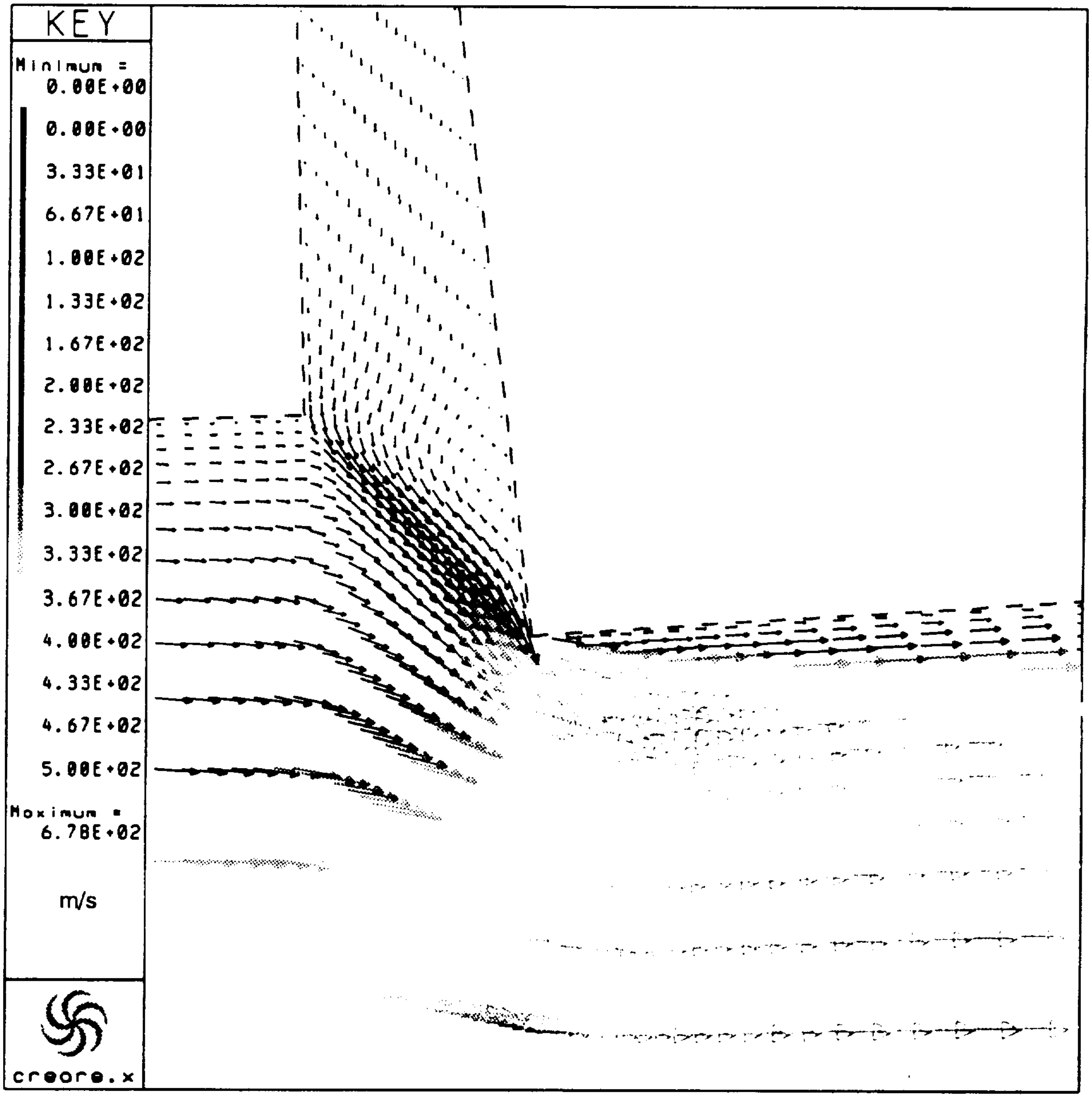

Figure 28. Pressure Distribution On the Upstream and Downstream Faces of the Aft Slot, Configuration 4

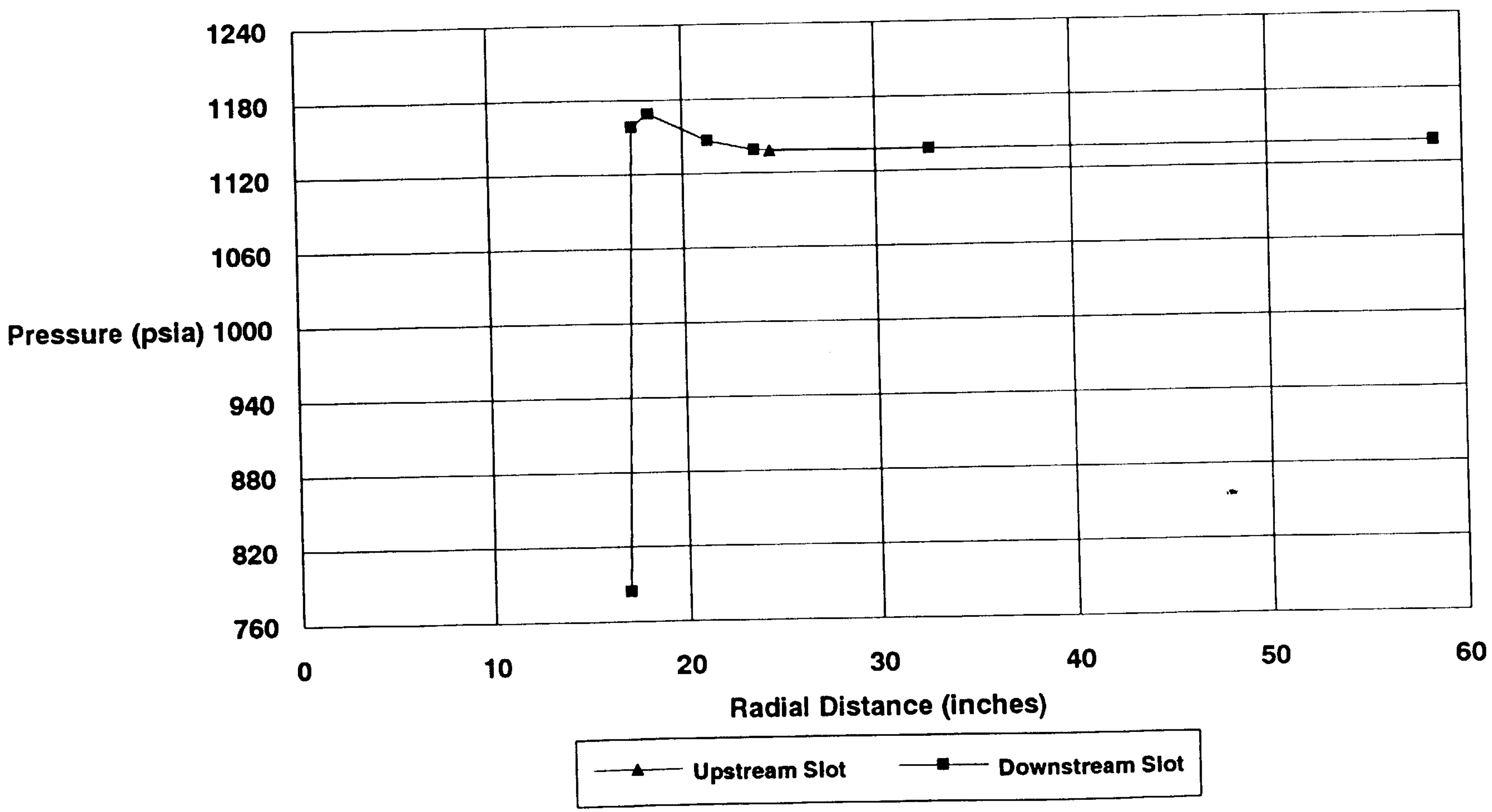

Figure 27. Configuration 4 Port Pressures On the Surface and At the Motor Centerline

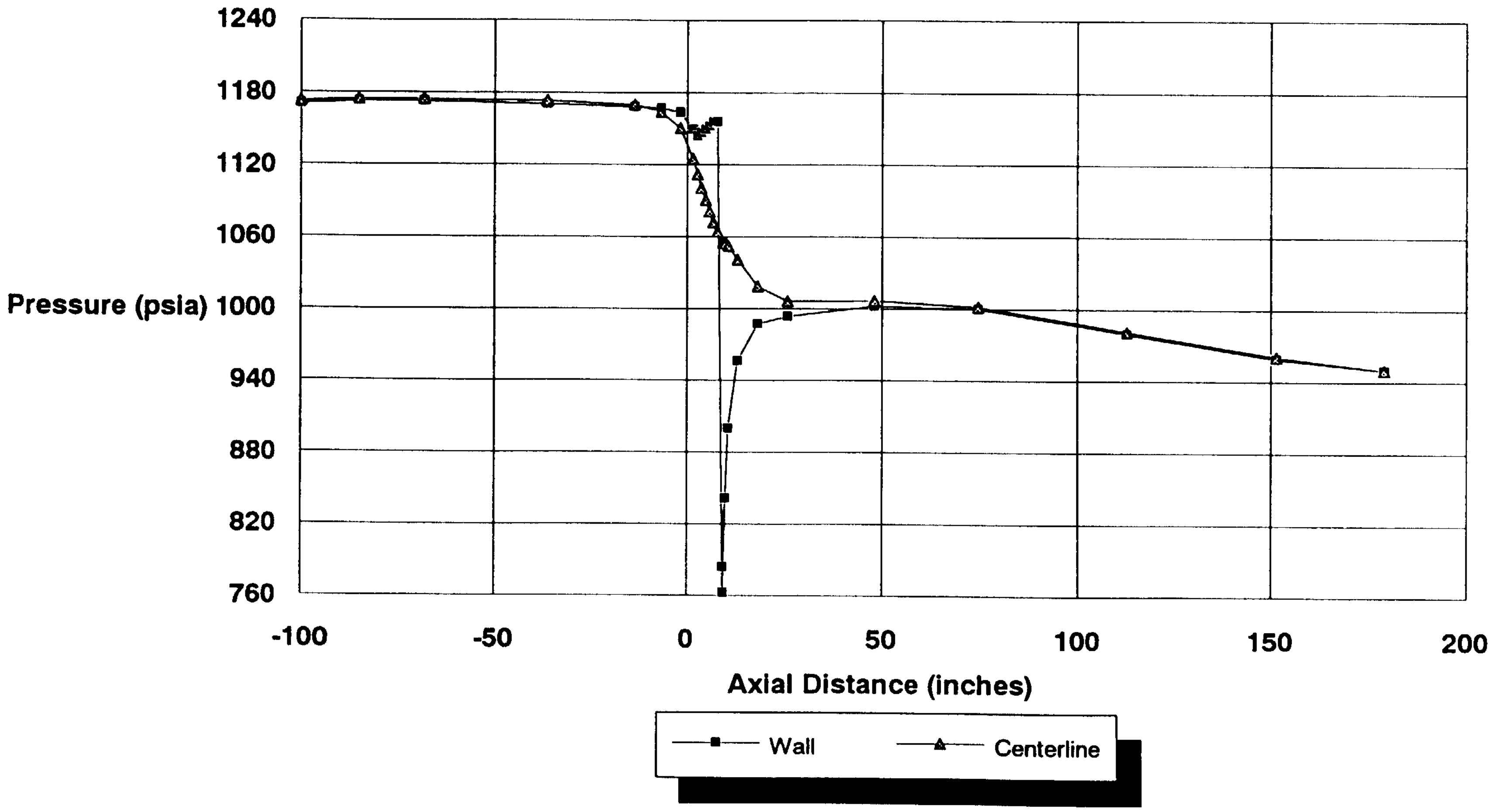

Figure 26. Port Surface Pressure for the Aft Segment, Configuration 3

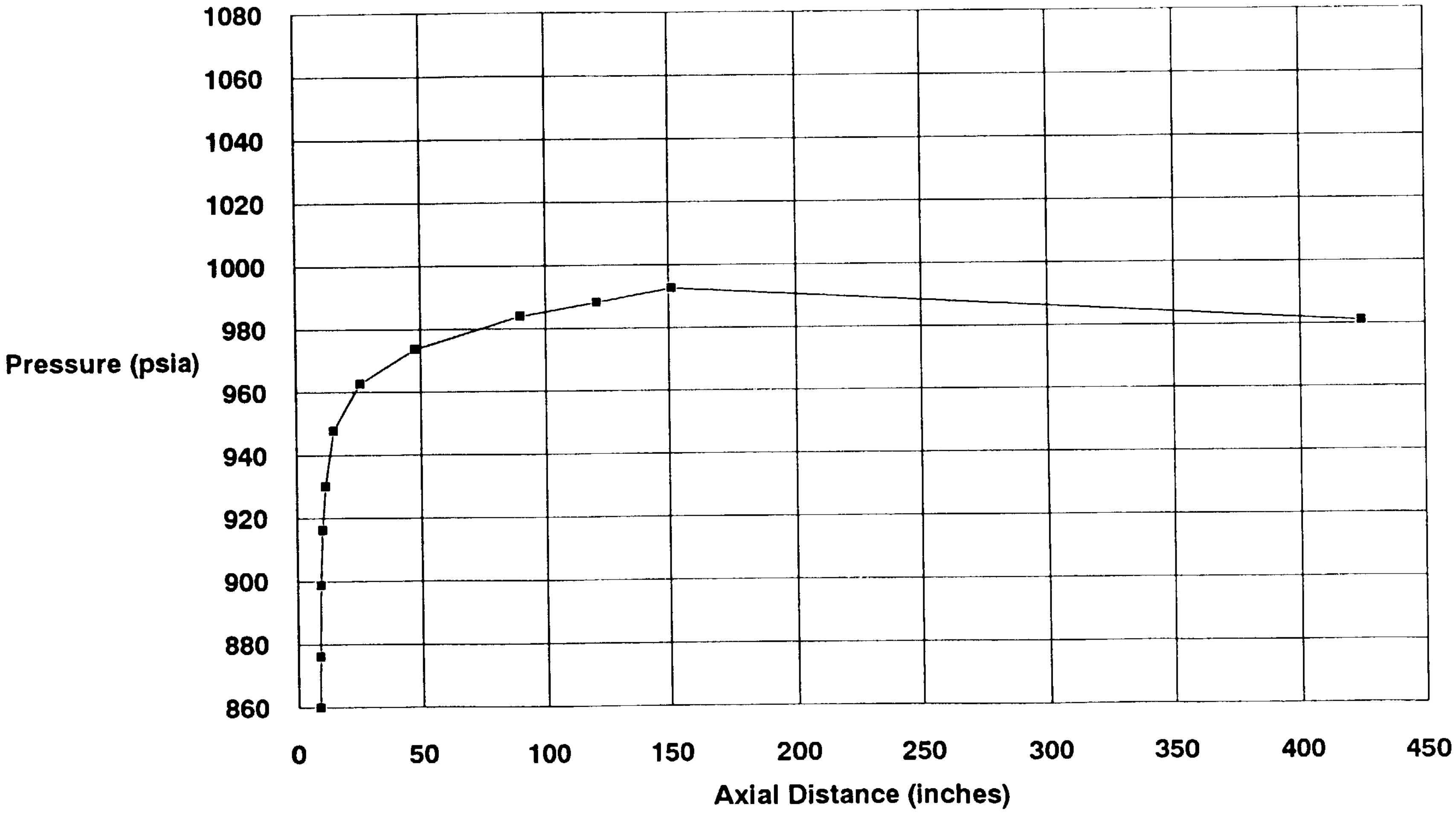

Figure 25. Port Surface Pressure for the Center Segment, Configuration 3

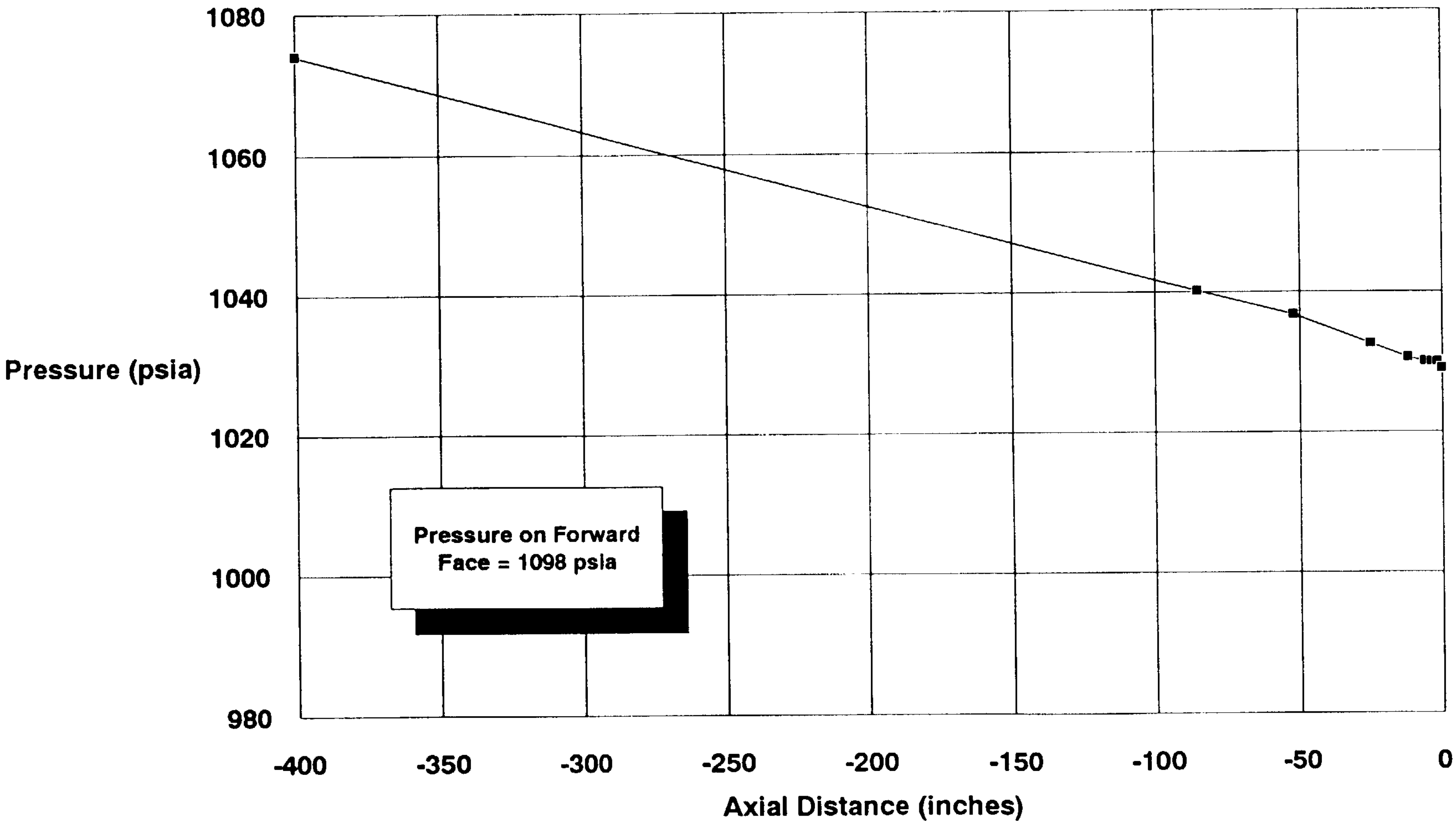

Figure 24. Pressure Distribution On the Upstream and Downstream Faces of the Aft Slot, Configuration 3

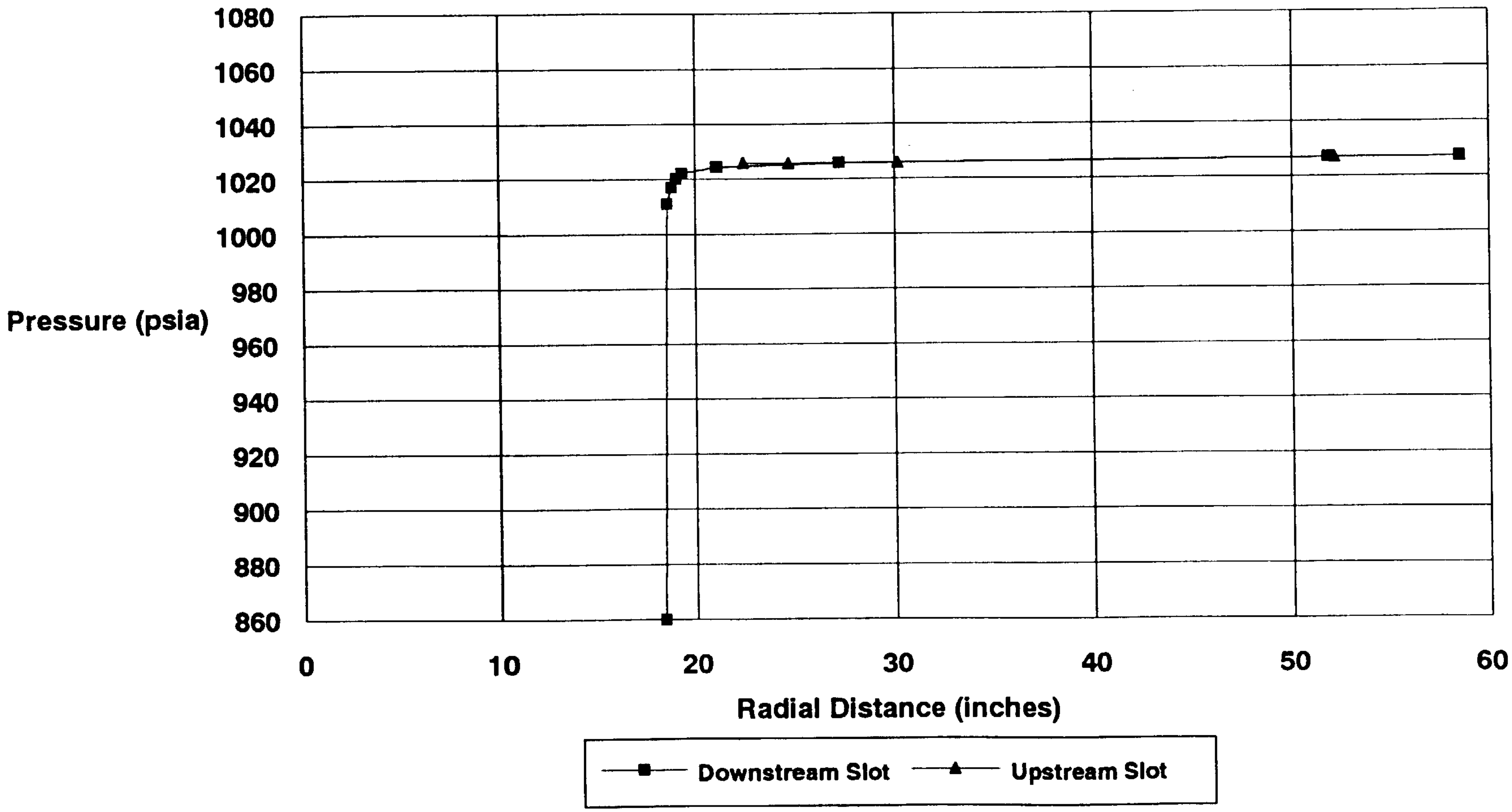

Figure 23. Flow Field Mach Number Contours For Configuration 3.

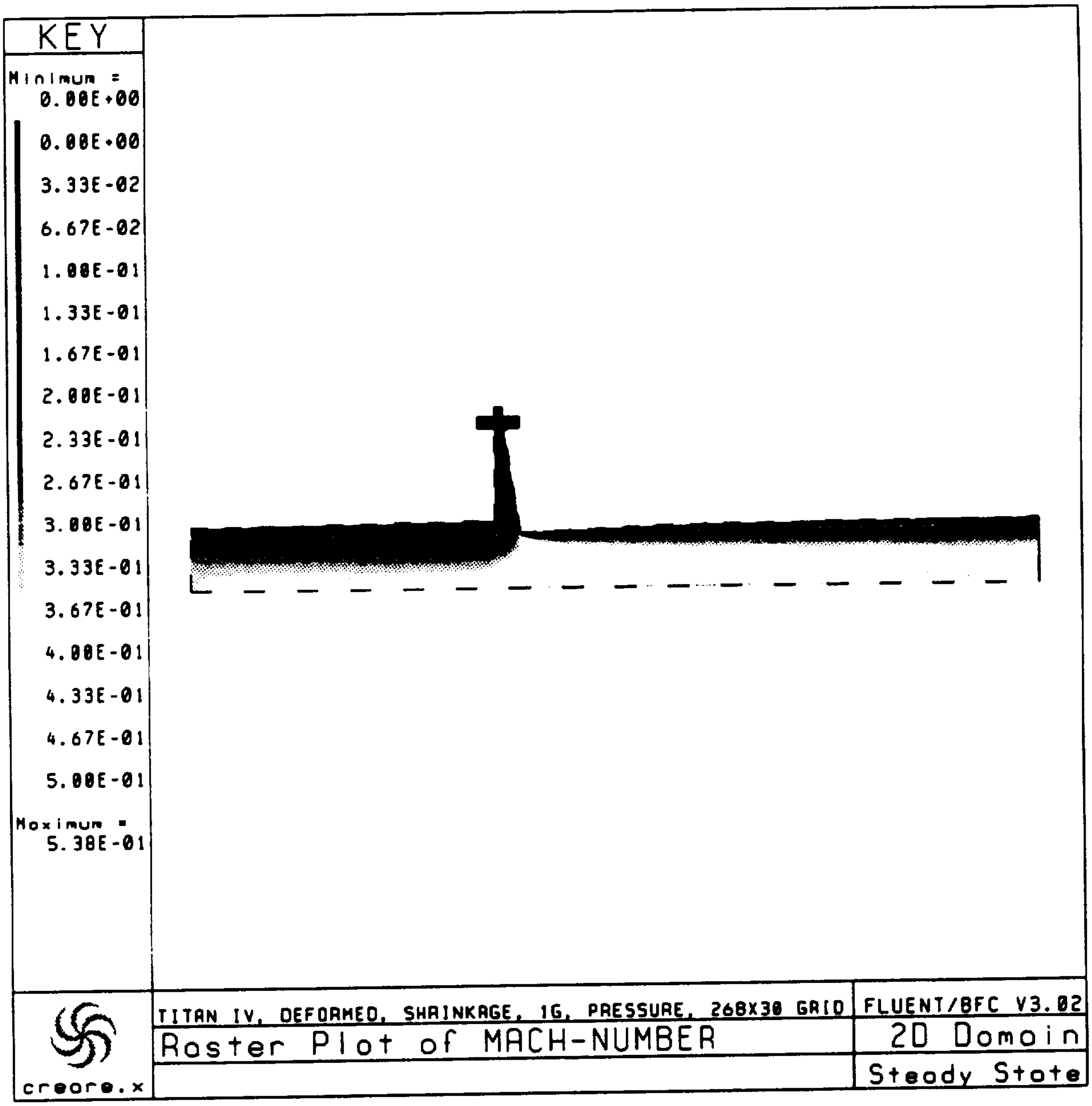

Figure 22. Velocity Vector Flow Field In The Aft Slot Region Of The Motor For Configuration 3.

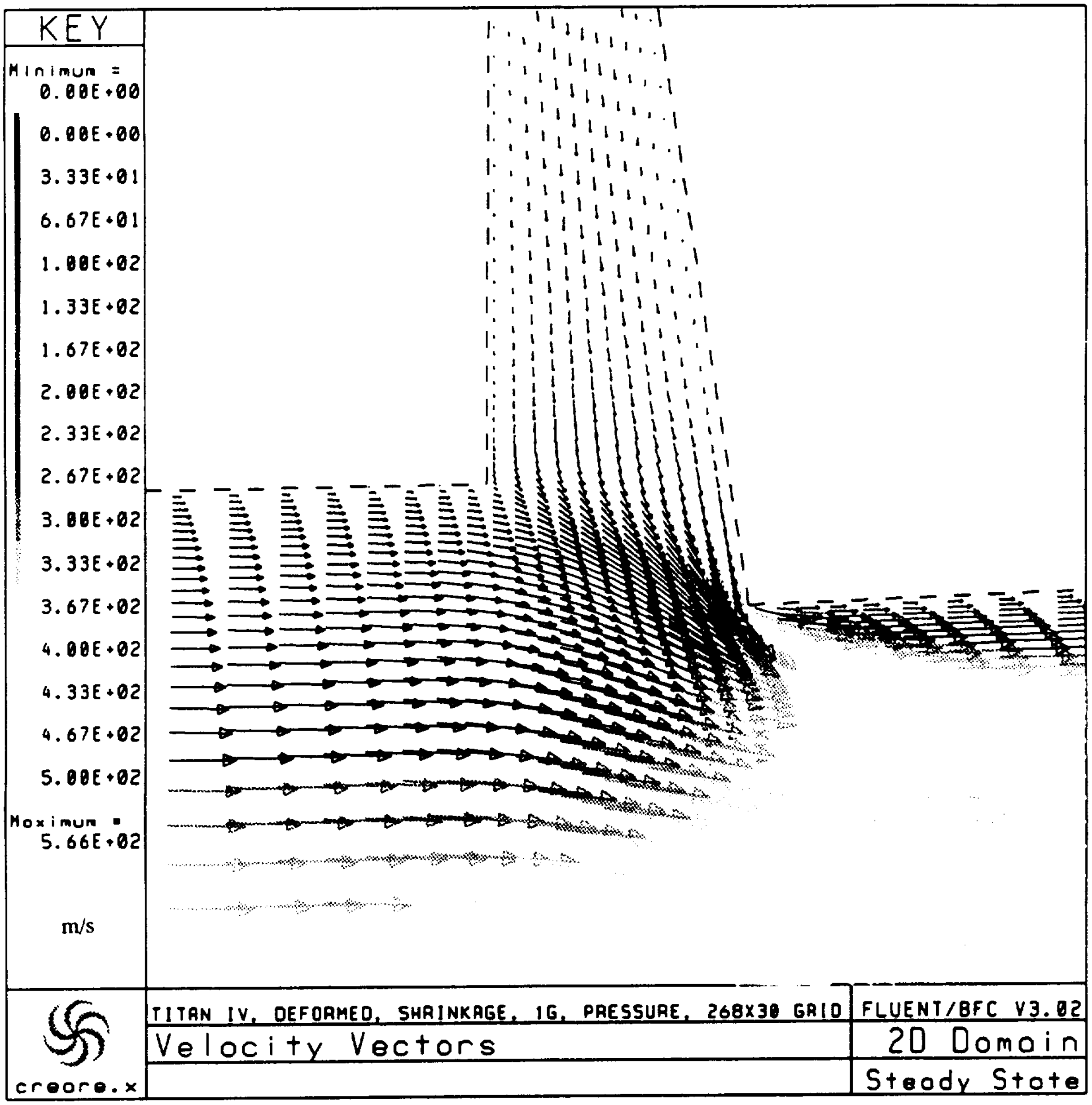

Figure 21. Configuration 3 Port Pressures On the Surface and At the Motor Centerline

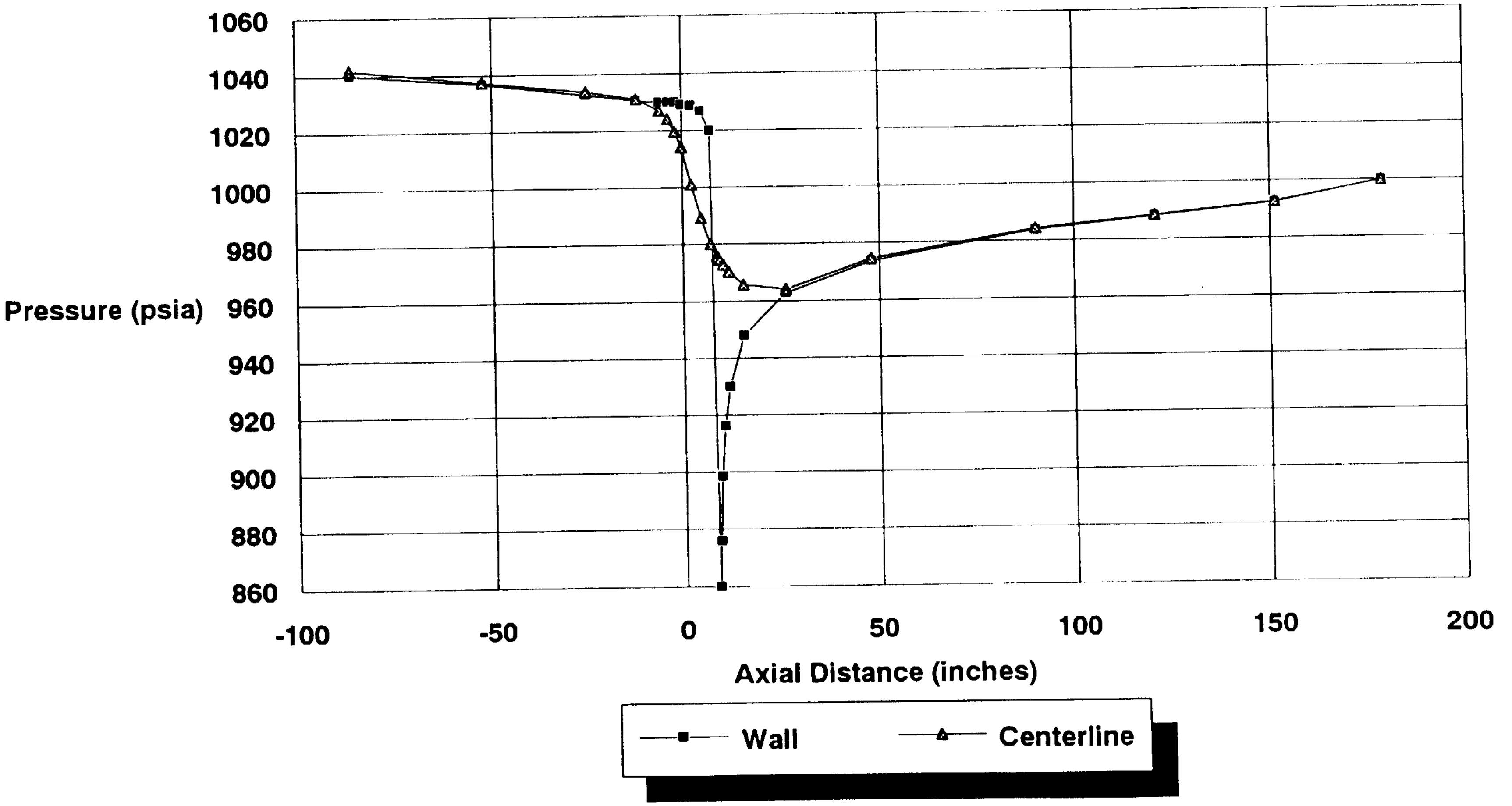

Figure 20. Port Surface Pressure for the Aft Segment, Configuration 2

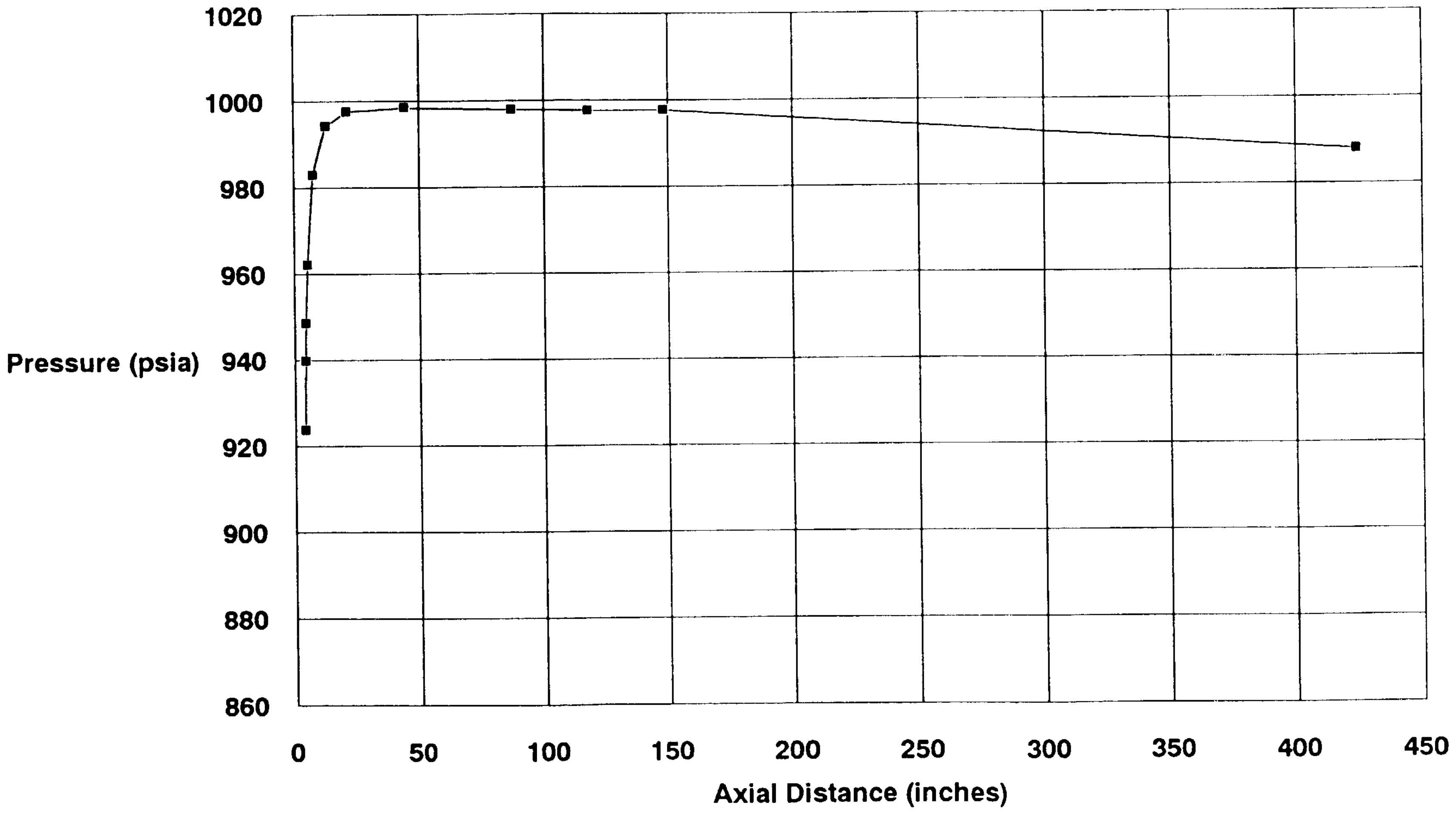

Figure 19. Port Surface Pressure for the Center Segment, Configuration 2

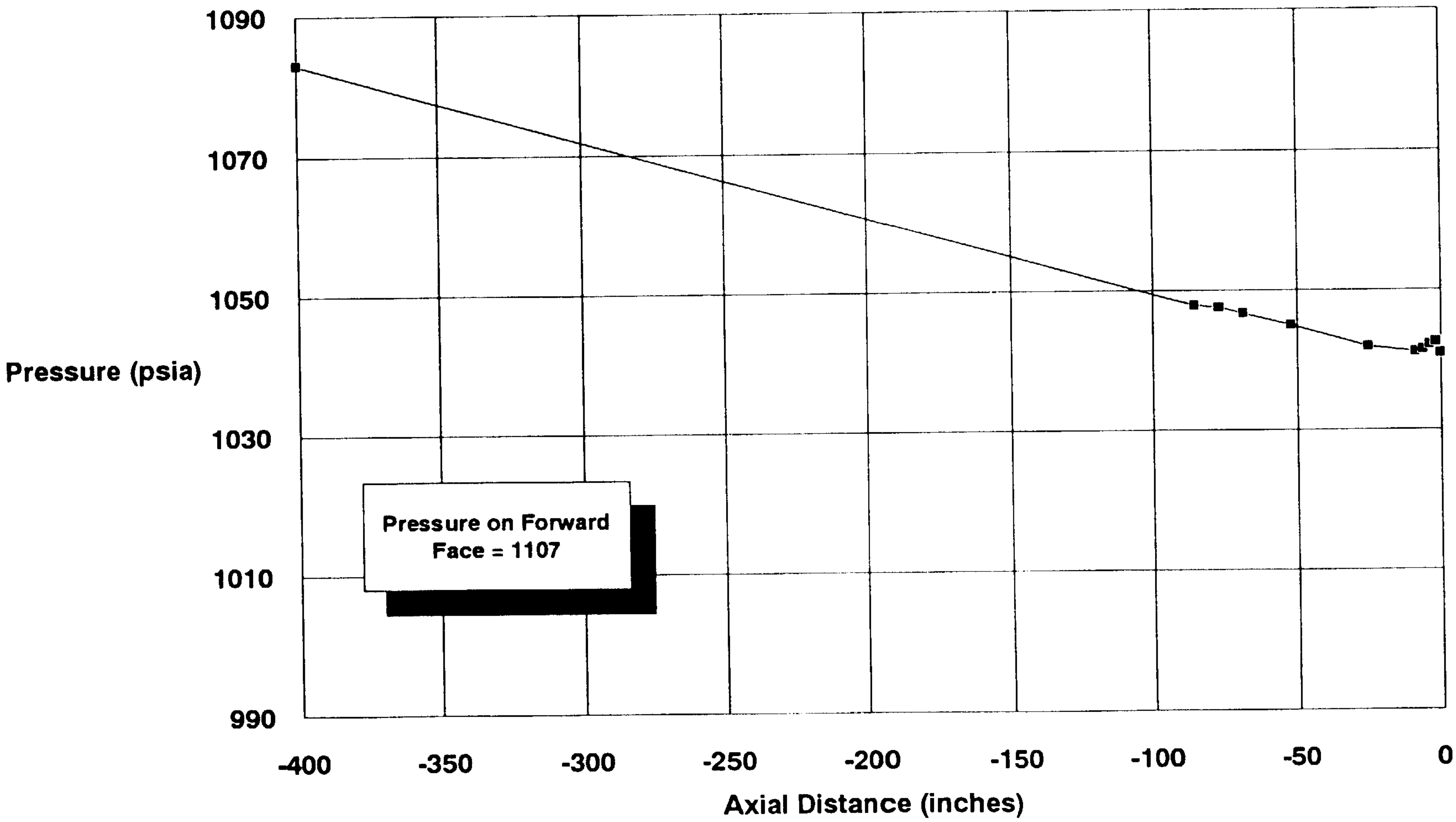

Figure 18. Pressure Distribution On the Upstream and Downstream Faces of the Aft Slot, Configuration 2.

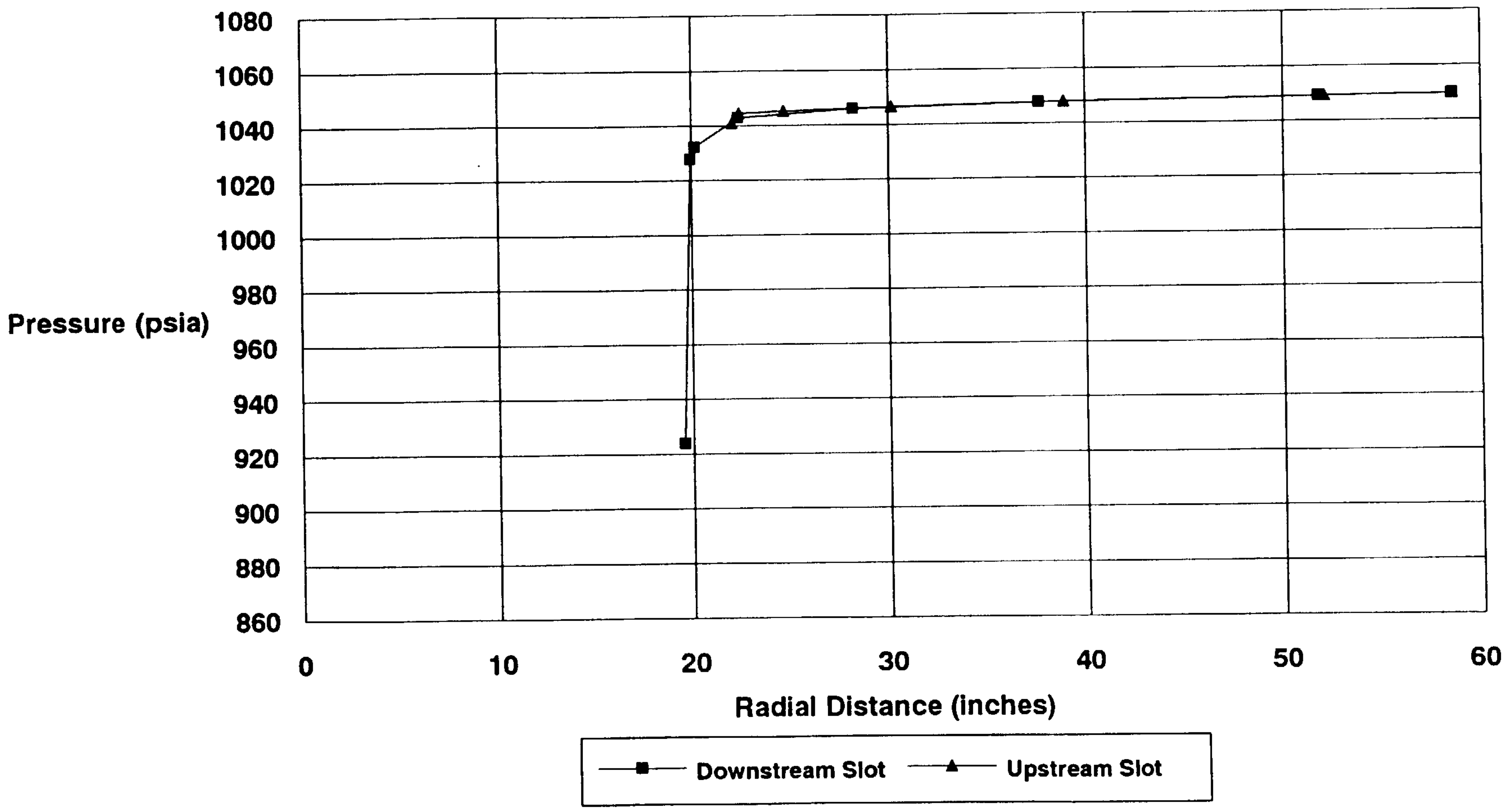

Figure 17. Flow Field Mach Number Contours For Configuration 2.

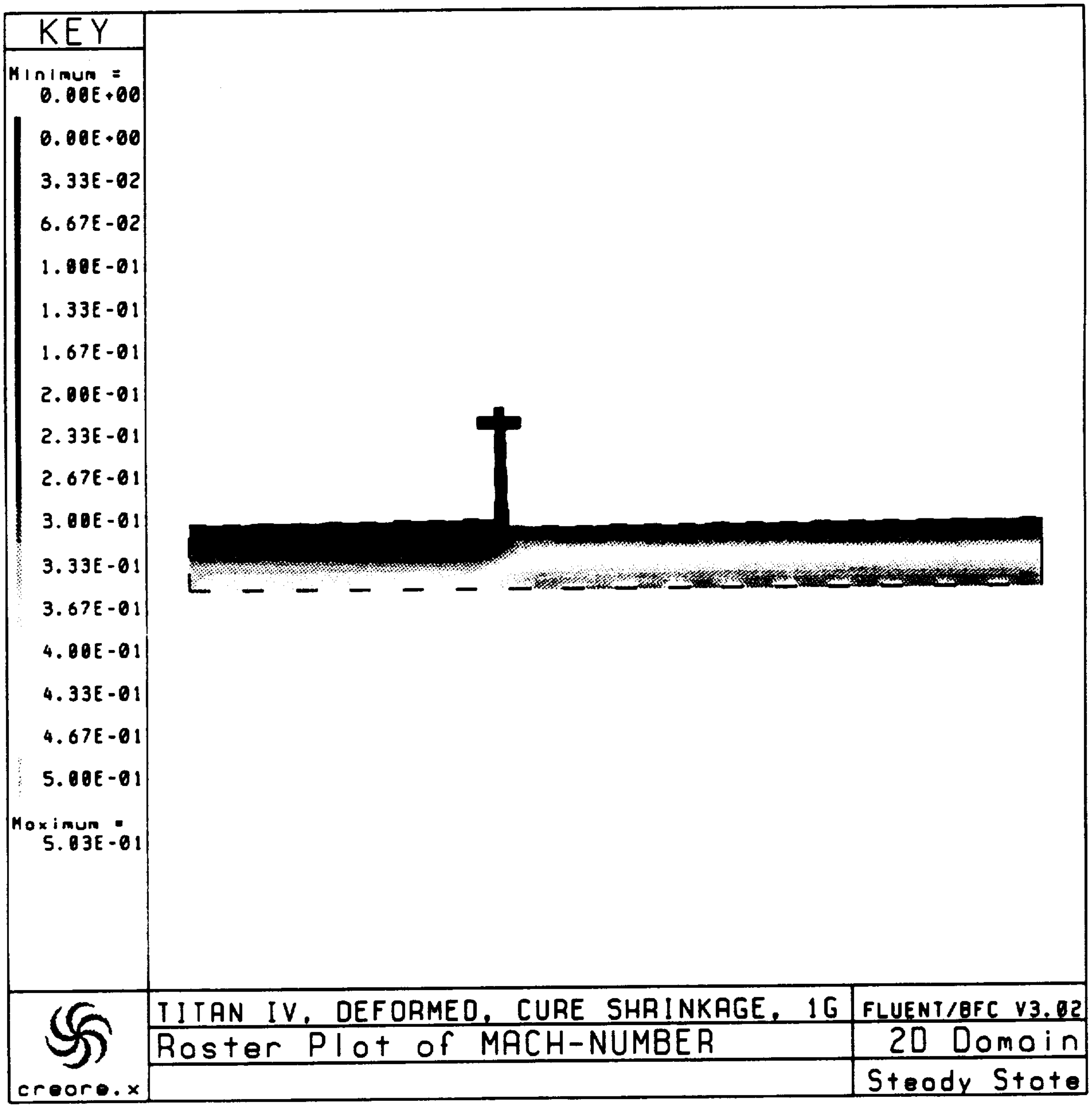

Figure 16. Velocity Vector Flow Field In The Aft Slot Region Of The Motor For Configuration 2.

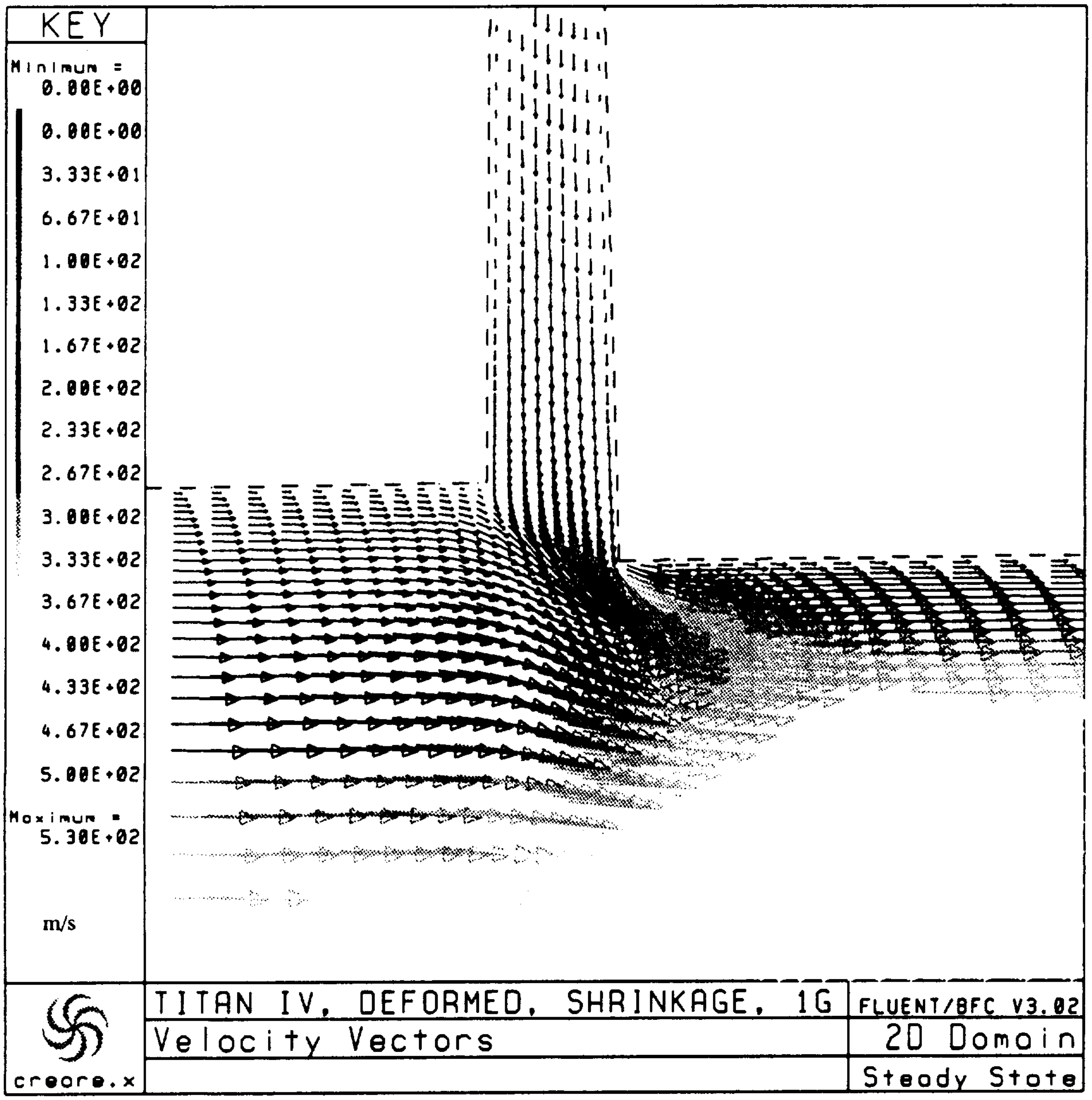

Figure 15. Configuration 2 Port Pressures On the Surface and at the Motor Centerline

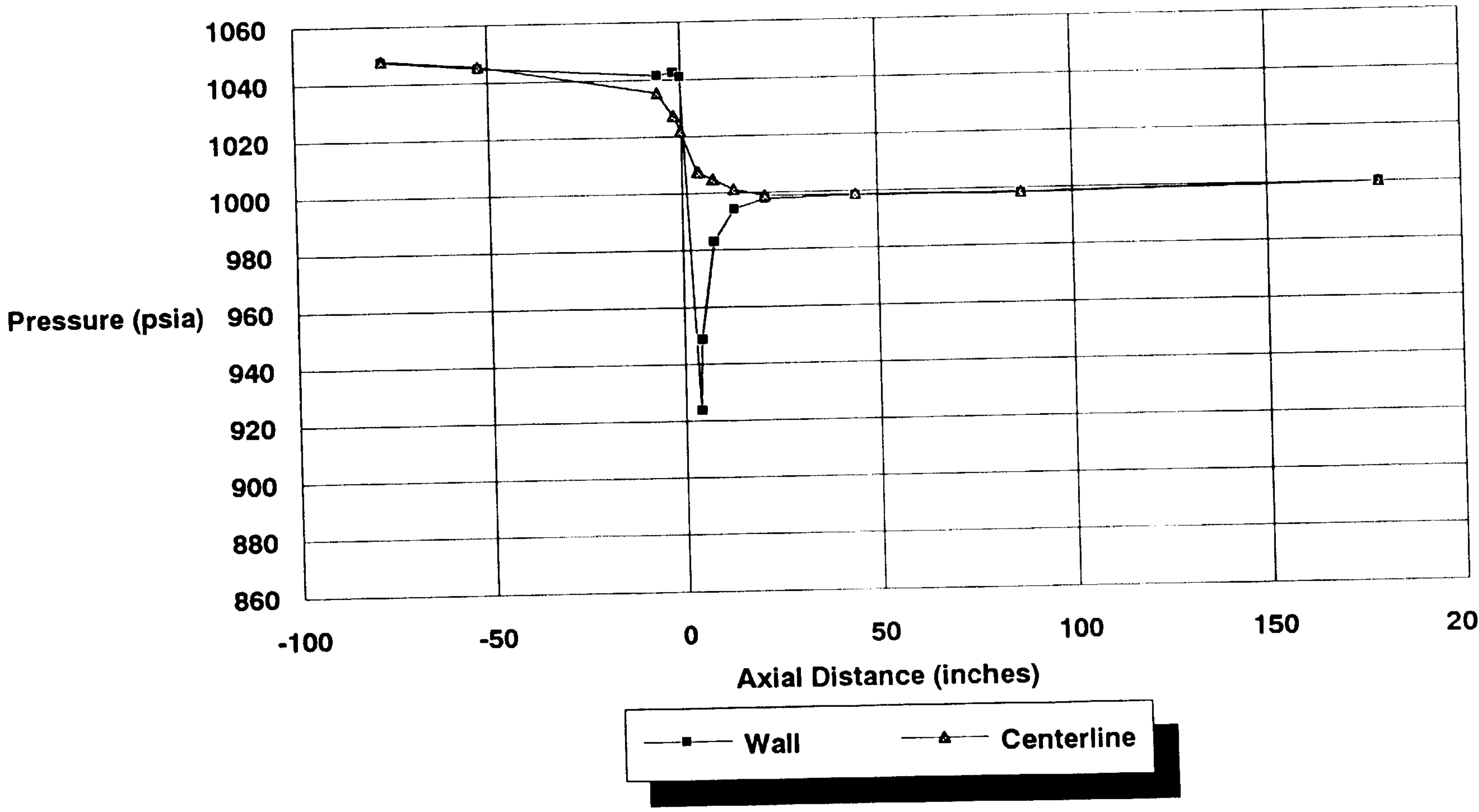

Figure 14. Port Surface Pressure for the Aft Segment, Configuration 1

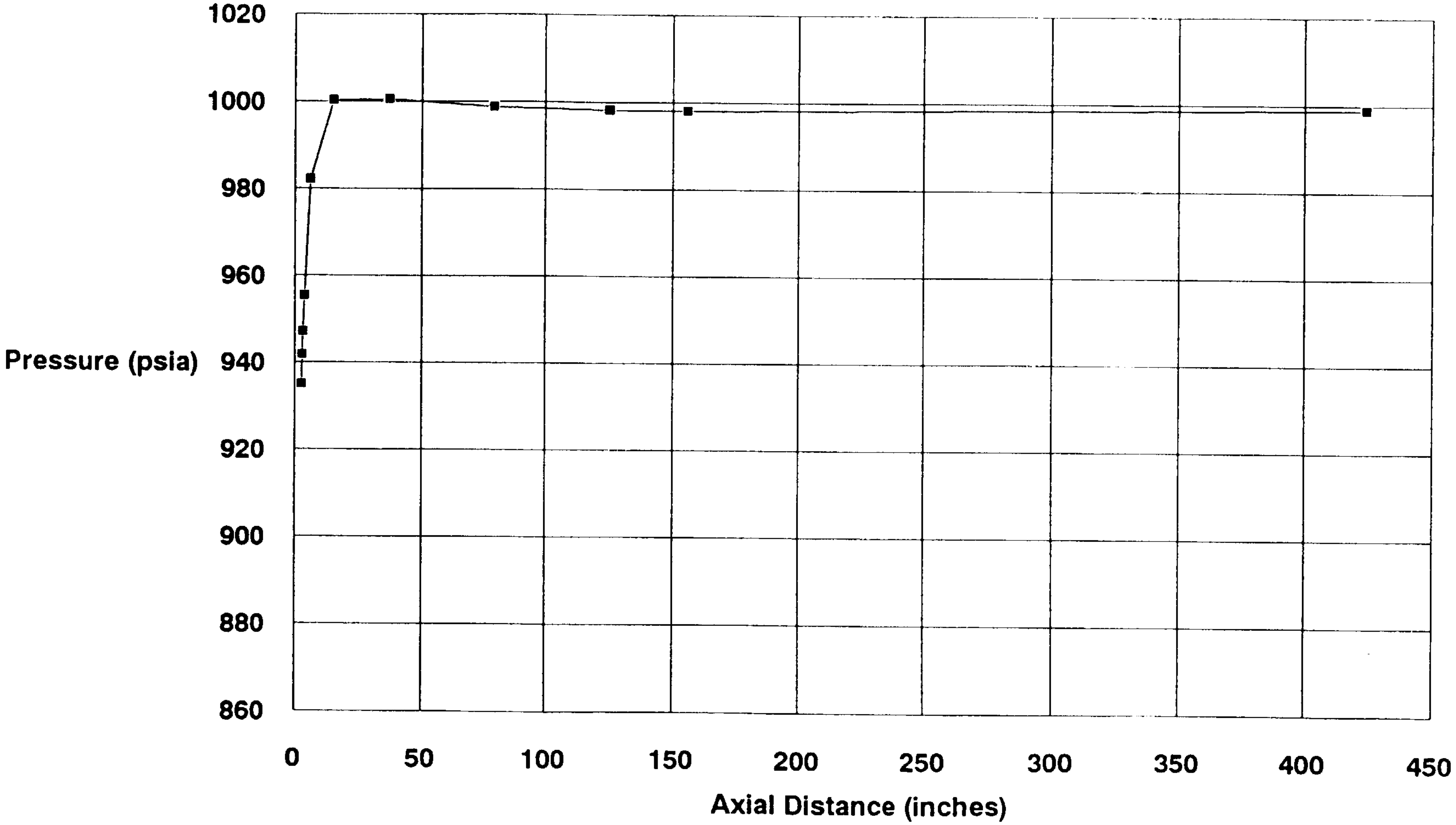

Figure 13. Port Surface Pressure for the Center Segment, Configuration 1

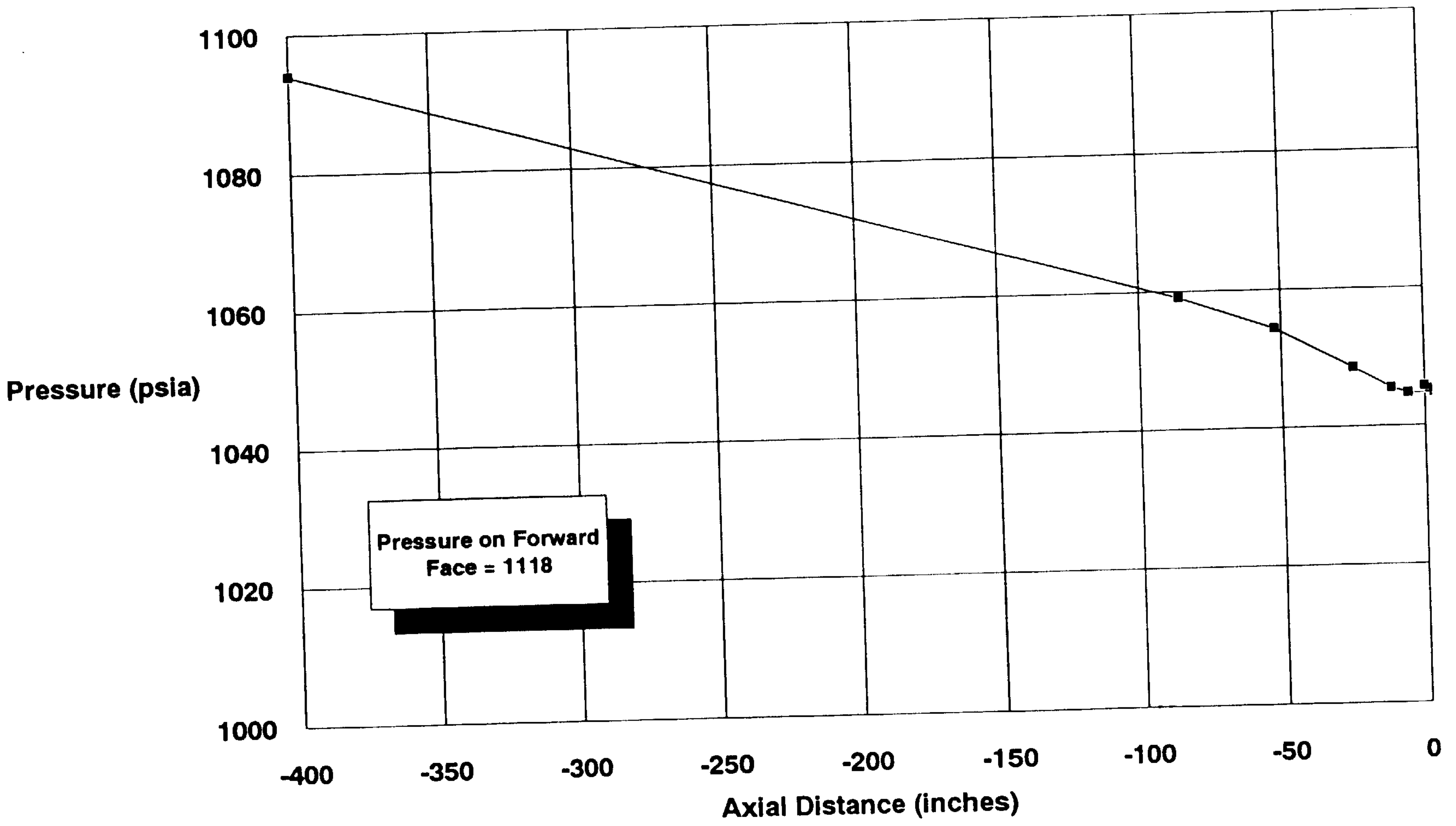

Figure 12. Pressure Distribution On the Upstream and Downstream Faces of the Aft Slot, Configuration 1

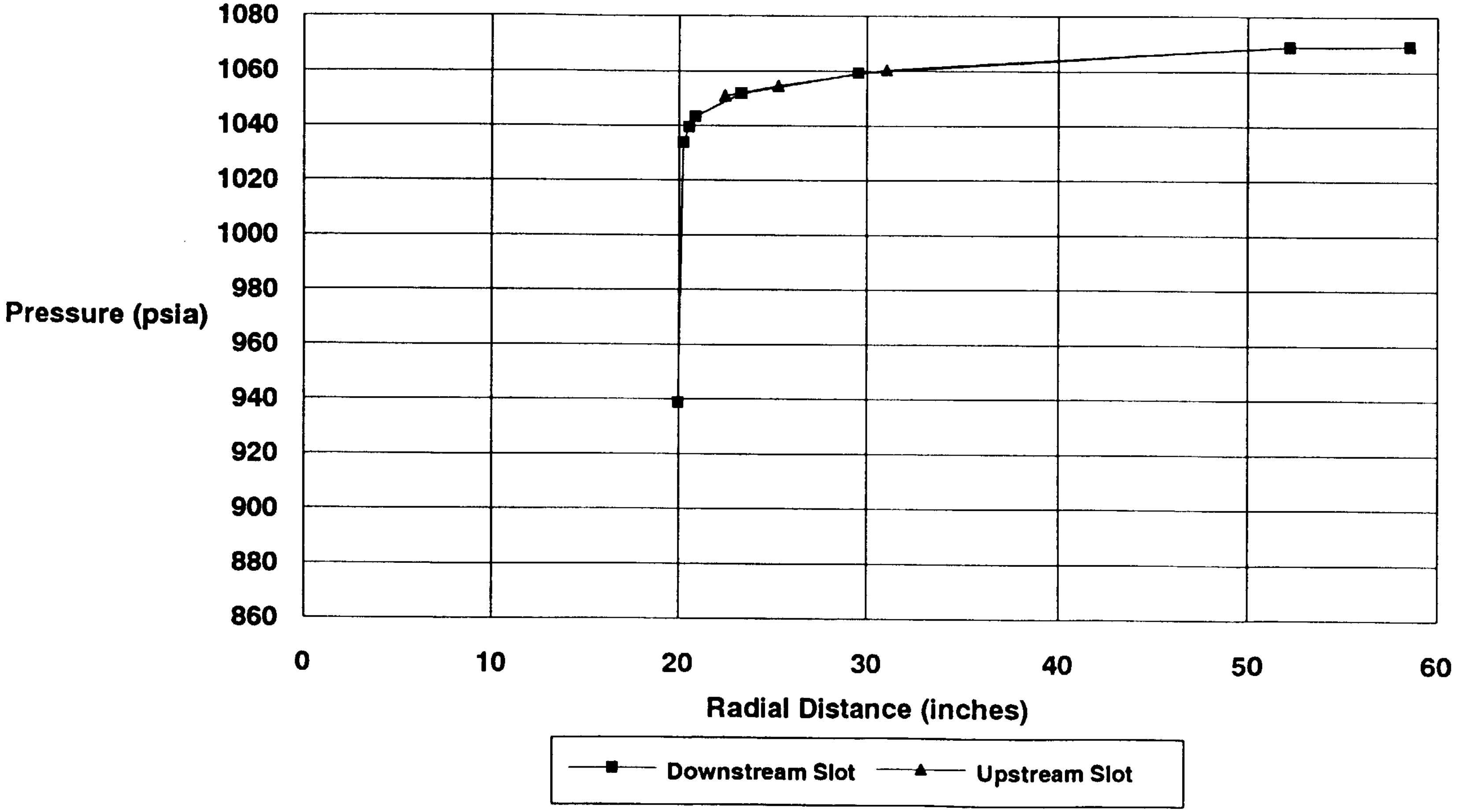

Figure 11. Flow Field Mach Number Contours For Configuation 1.

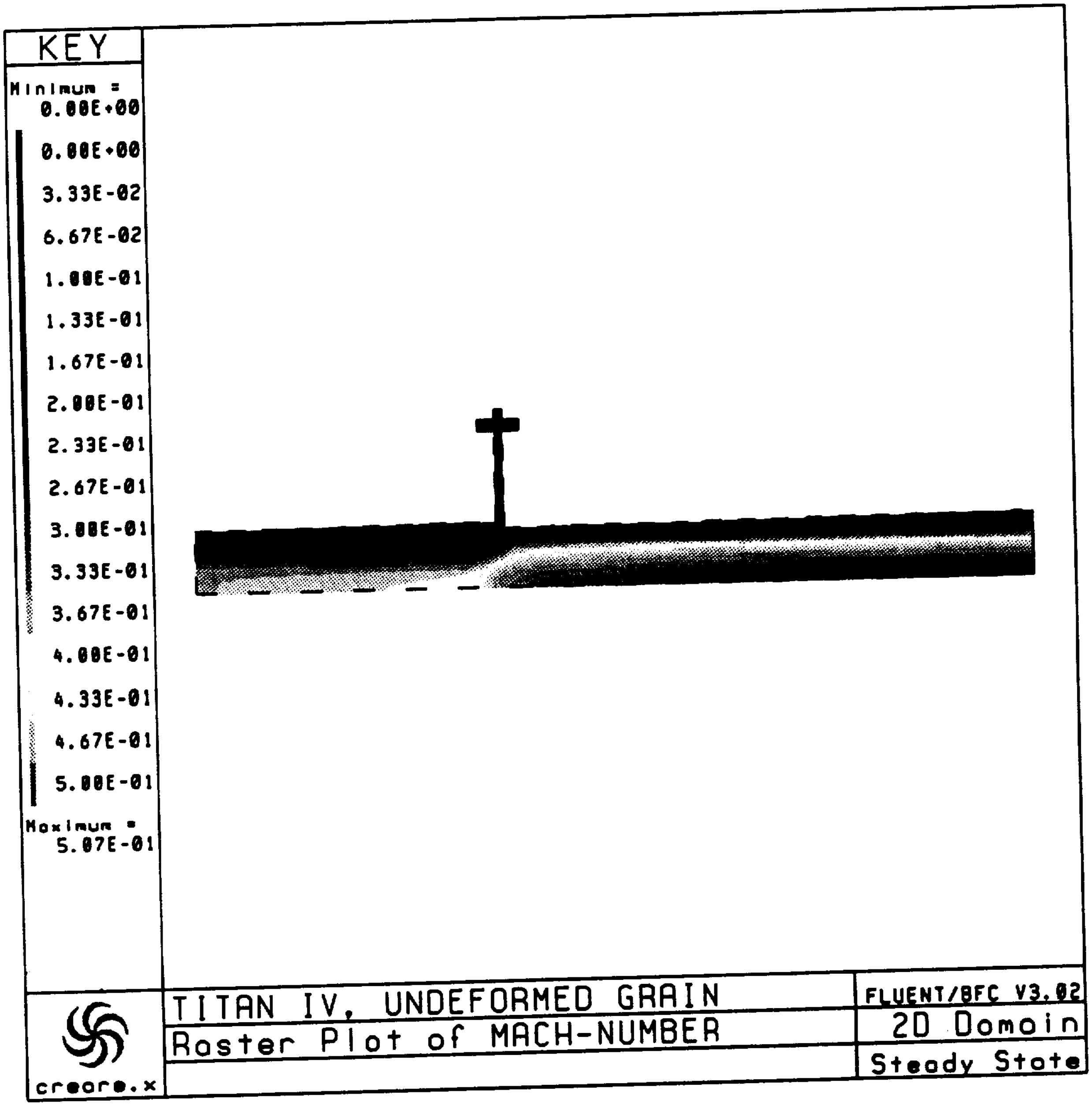

Figure 10. Velocity Vector Flow Field In The Aft Slot Region Of The Motor For Configuration 1.

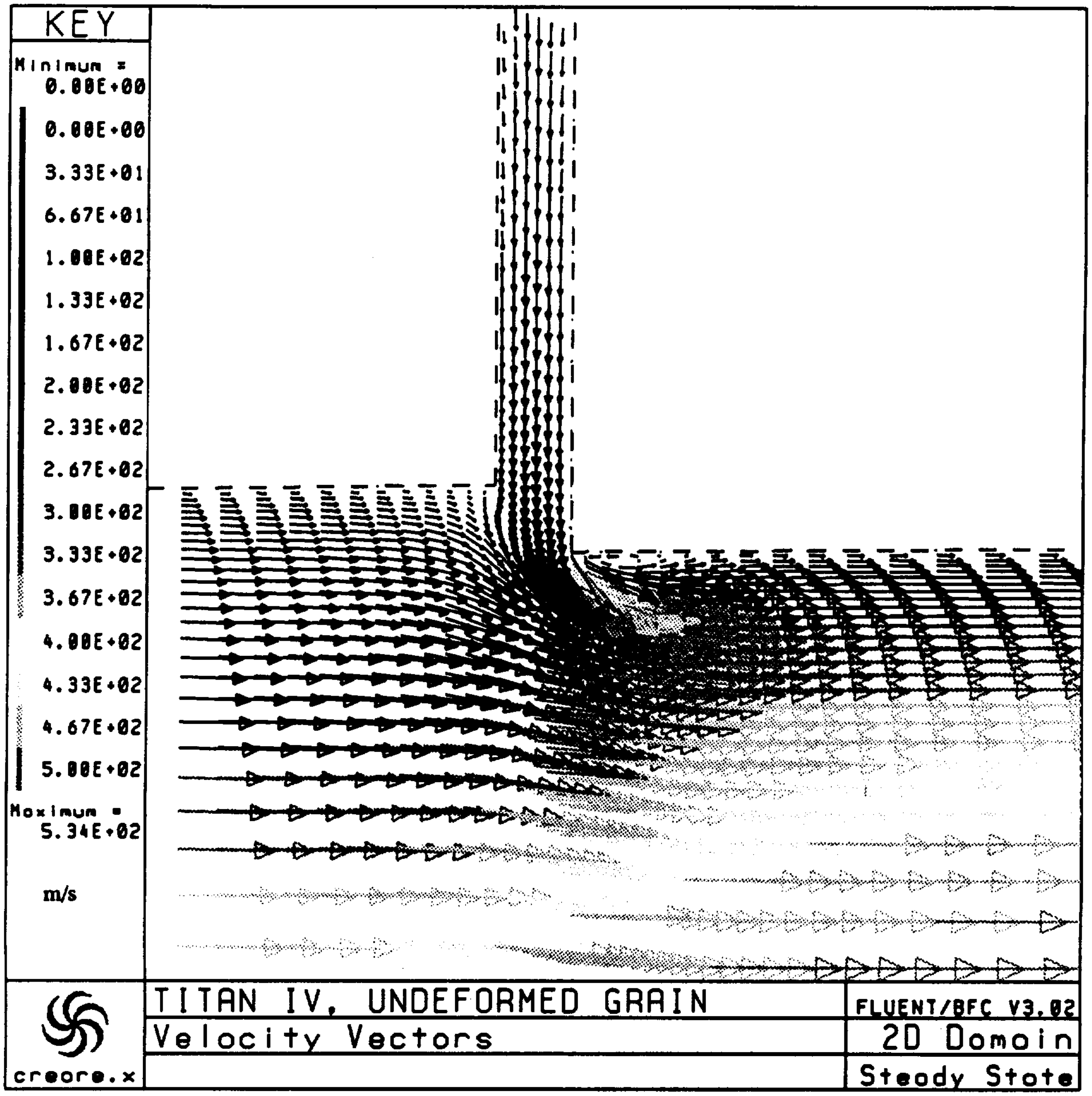

Figure 9. Configuration 1 Port Pressures On the Surface and at the Motor Centerline

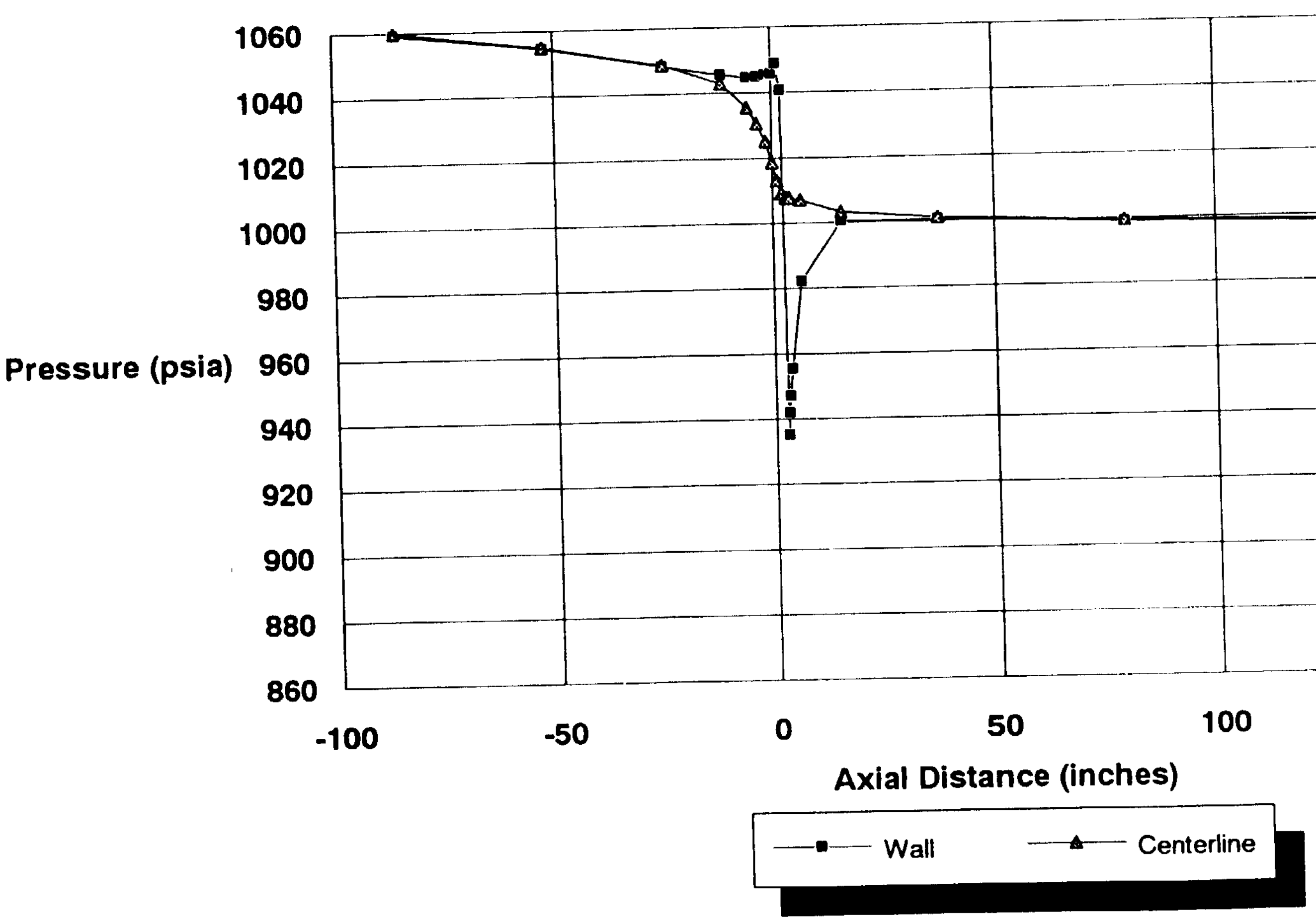

Figure 8. Culick Velocity Profile Used at the Inlet Boundary

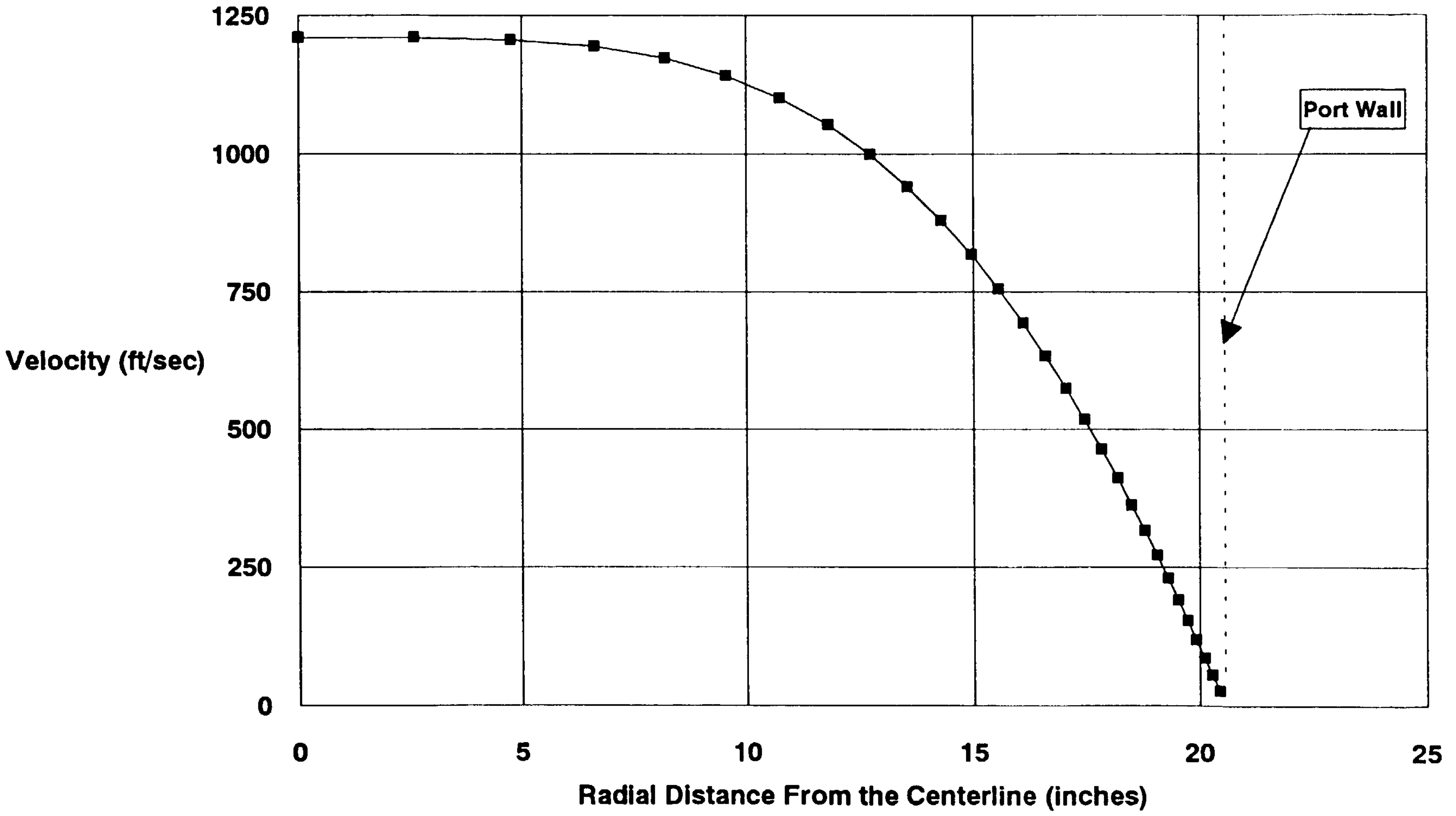

Figure 7. Illustration Of The Flow Field Thermochemical Properties and Boundary Conditions.

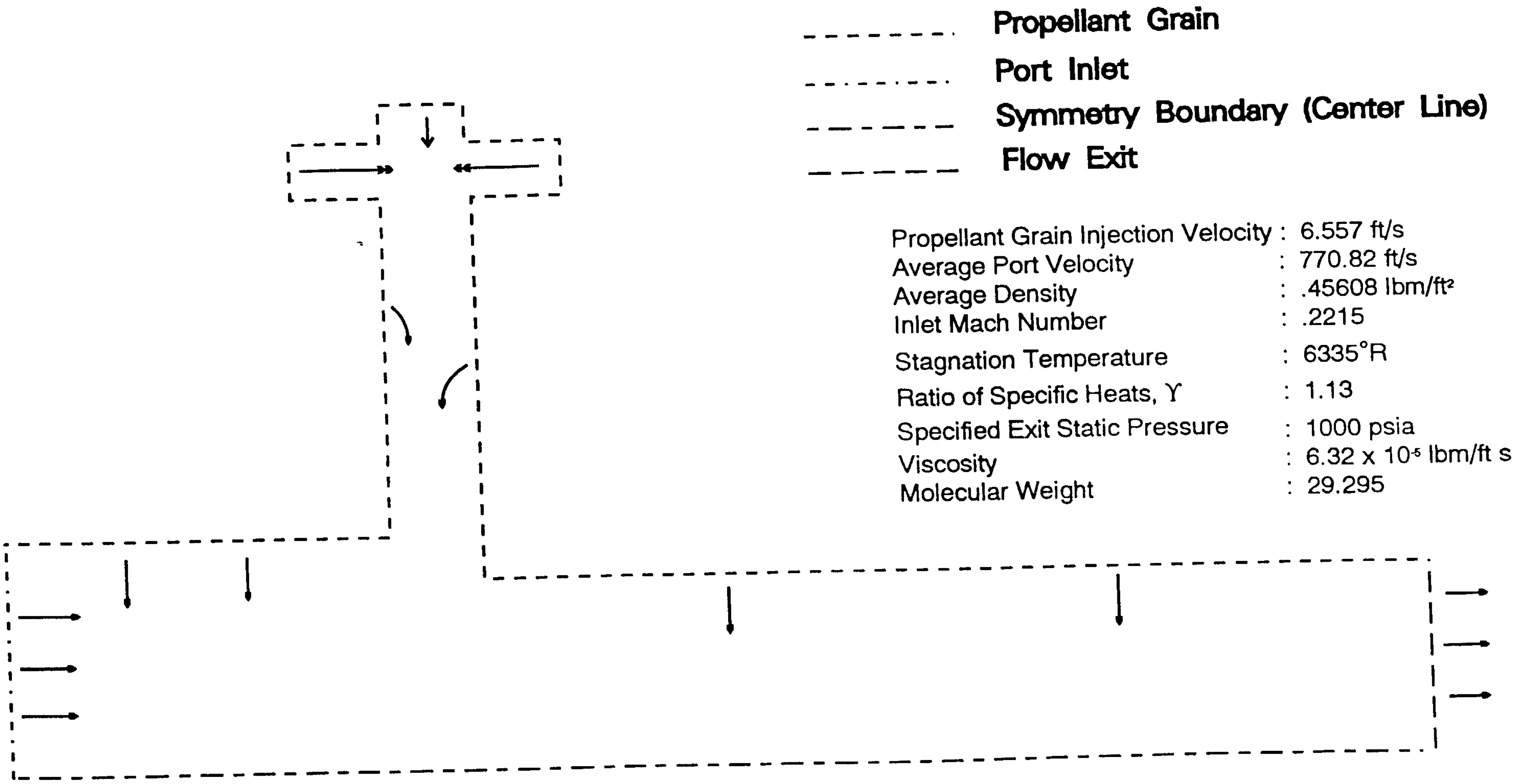

Propellant Grain Injection Velocity	: 6.557 ft/s
Average Port Velocity	: 770.82 ft/s
Average Density	: .45608 lbm/ft²
Inlet Mach Number	: .2215
Stagnation Temperature	: 6335°R
Ratio of Specific Heats, γ	: 1.13
Specified Exit Static Pressure	: 1000 psia
Viscosity	: 6.32×10^{-5} lbm/ft s
Molecular Weight	: 29.295

Figure 6. Titan IV SRMU Aft Slot, Deformed Grain Dimensions With Cure Shrinkage, Gravity And Flow Field Pressure Load Effects Included, Configuration 4.

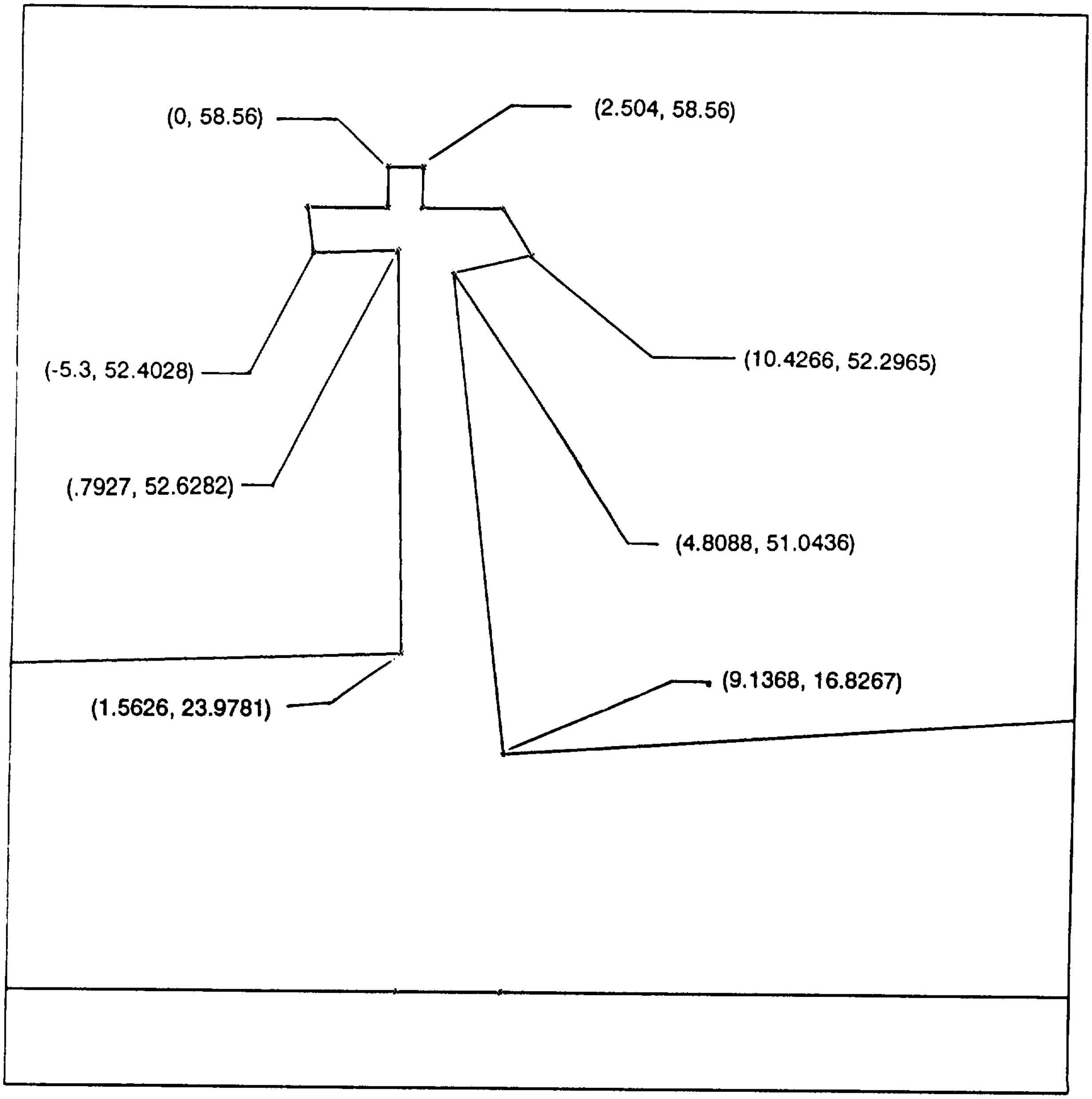

Dimensions in inches

Figure 5. Titan IV SRMU Aft Slot, Deformed Grain Dimensions With Cure Shrinkage, Gravity And Flow Field Pressure Load Effects Included, Configuration 3.

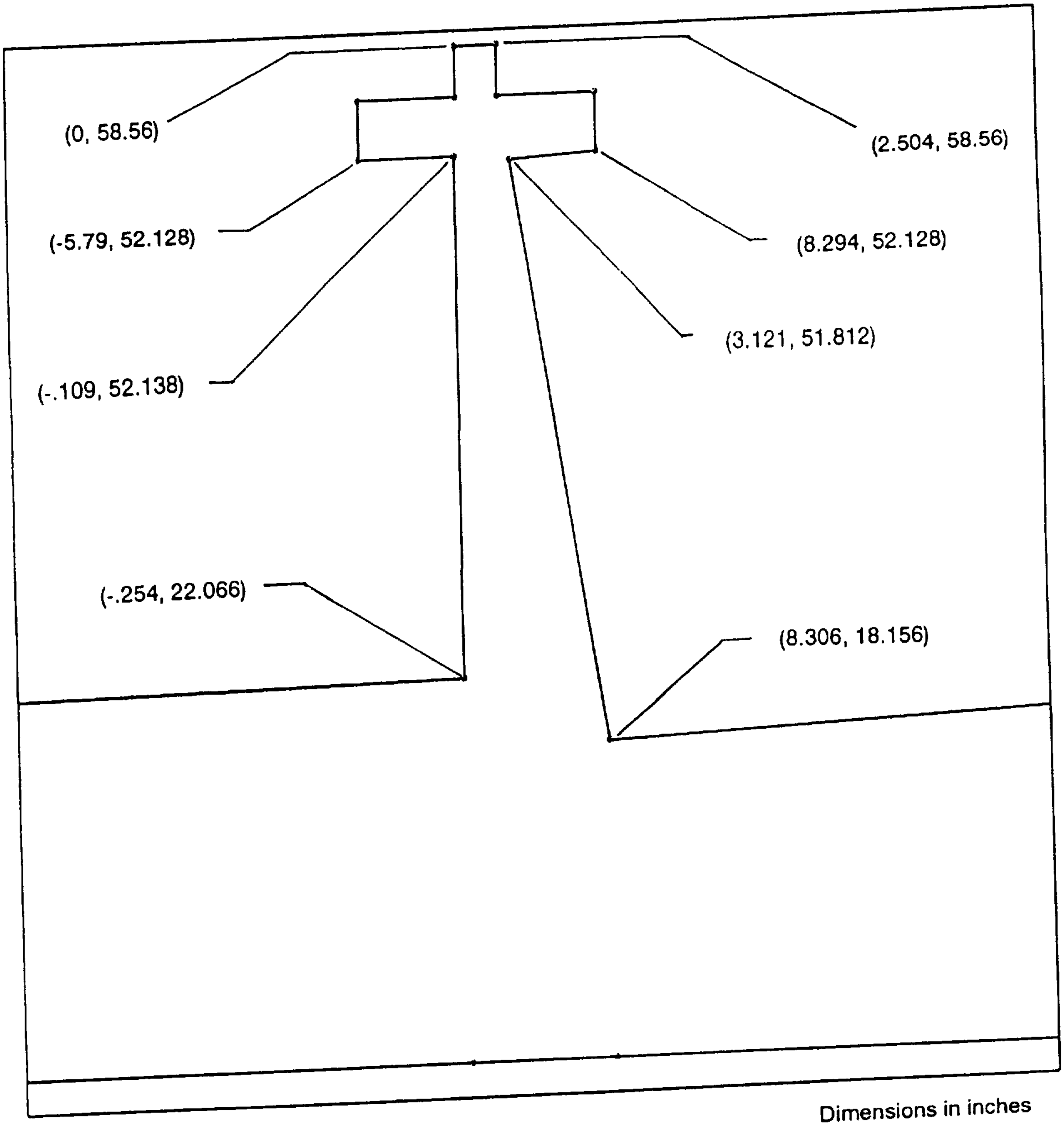

Figure 4. Titan IV SRMU Aft Slot, Deformed Grain Dimensions With Cure Shrinkage And Gravity Effects Included, Configuration 2.

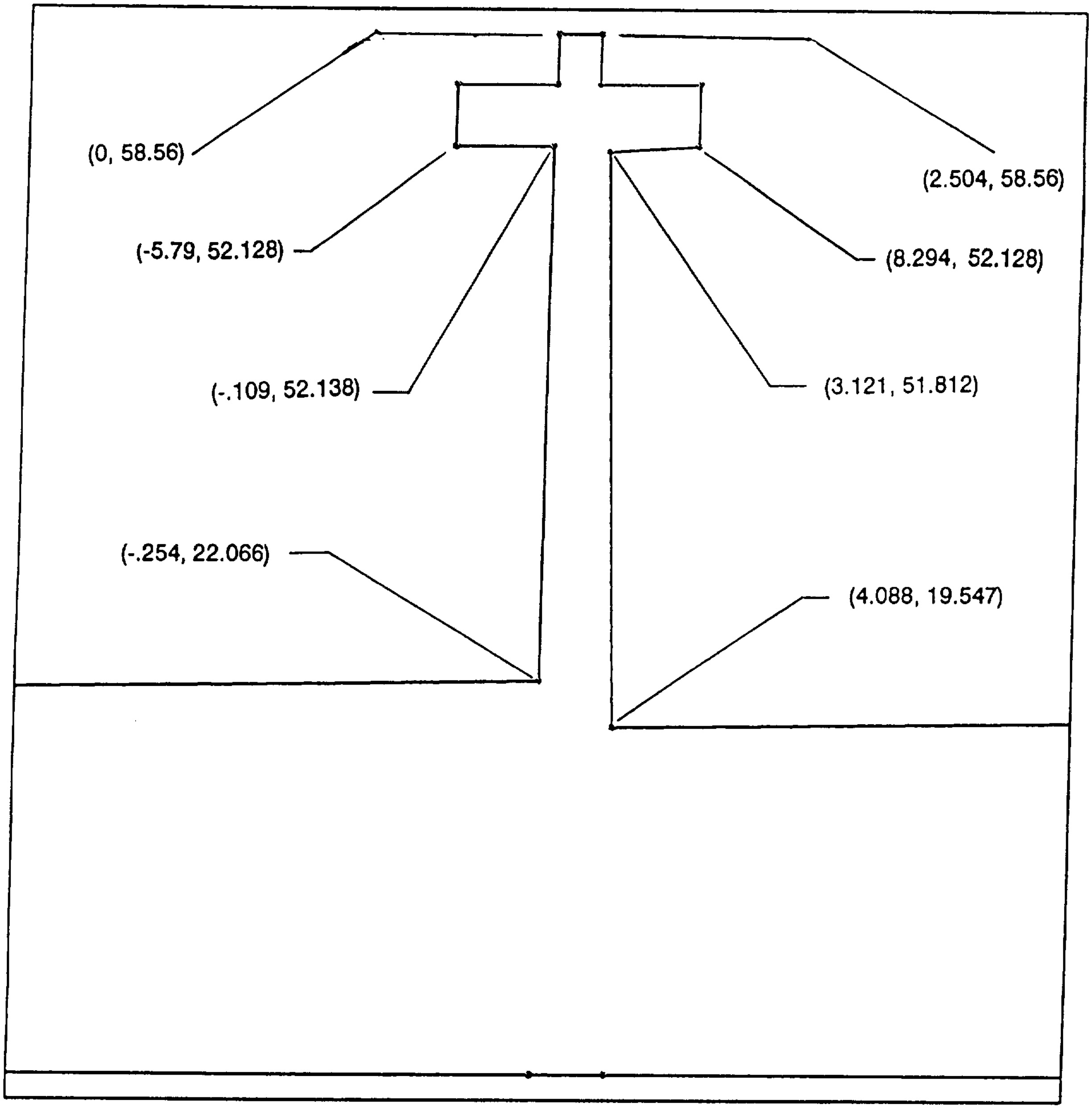

(Dimensions in inches)

Figure 3. Titan IV SRMU Aft Slot, Nominal Undeformed Propellant Grain Design Dimensions, Configuration 1.

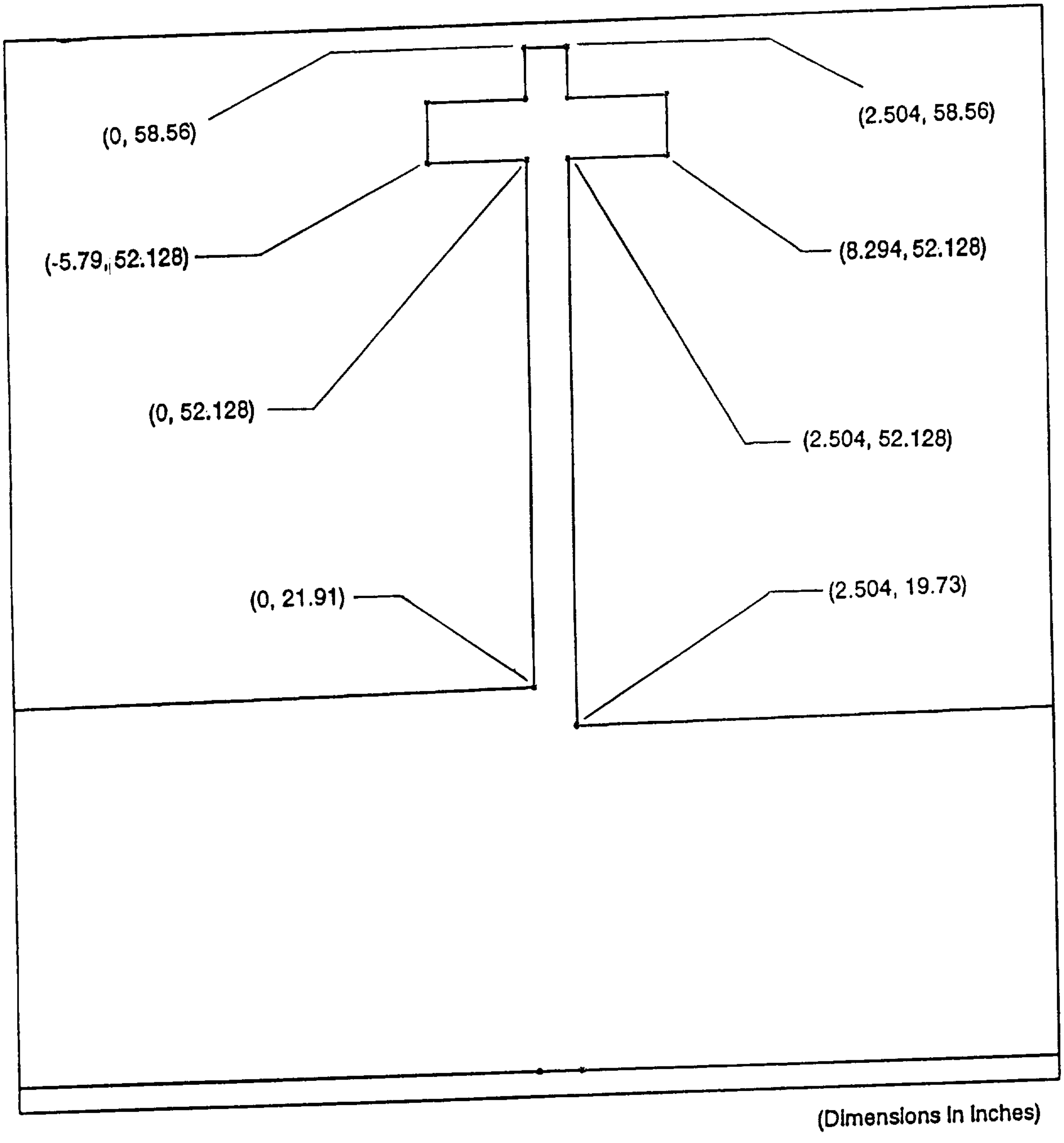

Figure 2. Nominal Propellant Grain Geometry, Configuration 1.

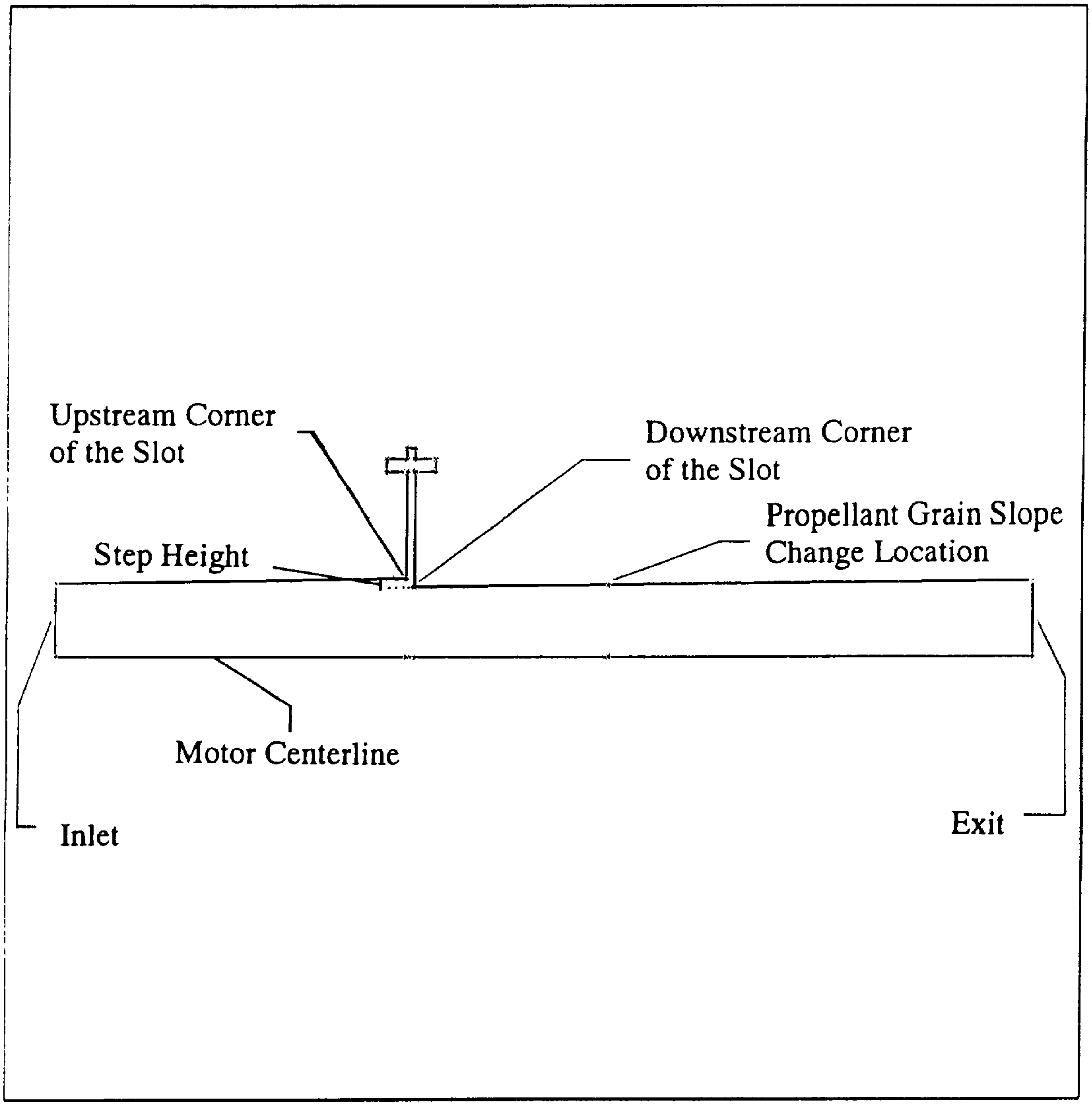

Figure 1. Full Titan IV SRMU Configuration

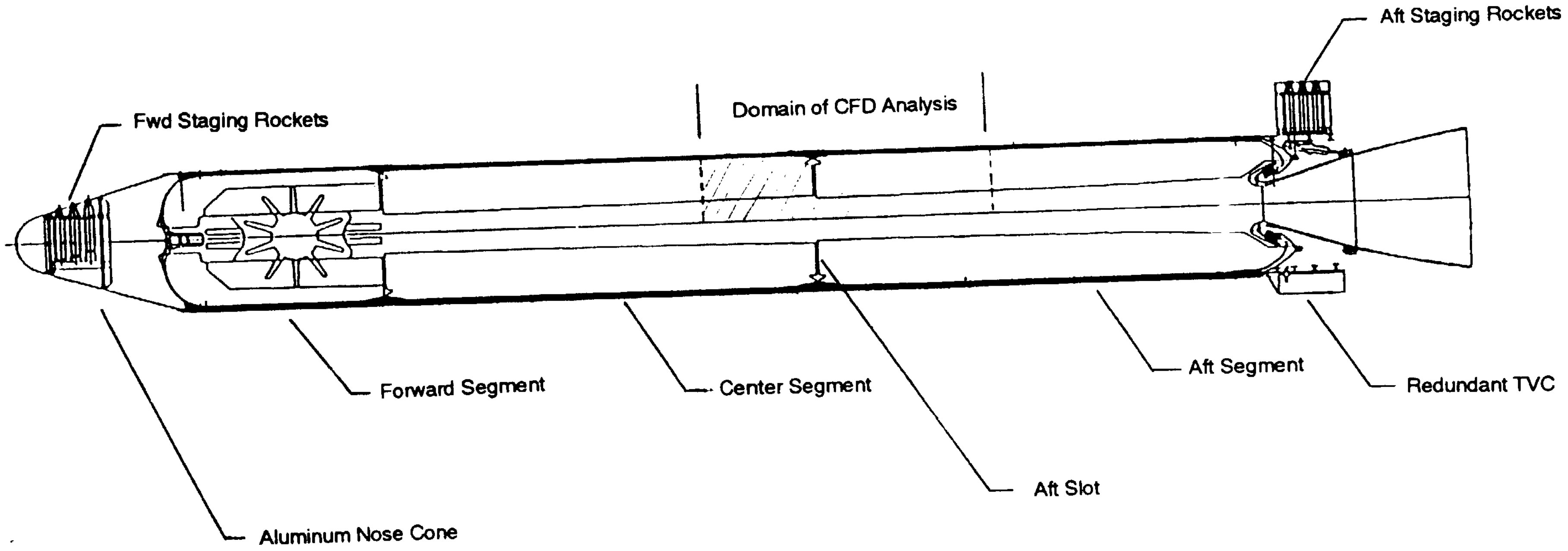

(labeled in Figure 2) to the downstream corner of the slot due the deformation of the downstream corner of the slot.

Figure 4 shows the altered slot region for configuration 2, from Step 2a. This deformed grain configuration included the effects of cure shrinkage and 1-g axial gravity acceleration on the propellant grain. As shown in the figure, the slot opening has increased by a factor of 1.6 over the nominal grain configuration and the step height has increased by a factor of 1.16. The aft propellant grain segment has rotated into the flow field toward the motor centerline by less than 0.2 inches and therefore has a small effect on the flow field. The corner point of the aft propellant grain segment shown in Figure 4, (4.088" , 19.547"), is faired back into the remainder of the unaltered propellant grain by connecting this altered geometry point by a straight line with a point 58 inches downstream of the aft slot. This point on the propellant grain can be seen in Figure 2 as the point where the aft propellant grain segment changes slope.

Figure 5 shows the third deformed grain configuration analyzed, configuration 3. The deformations shown in this configuration include the effects of cure shrinkage, 1-g axial gravity acceleration and alterations in the propellant geometry due to the initial flow field pressure loads. This configuration shows significant differences in all the geometric dimensions which affect the flow field. The slot width is a factor of 2 wider than the deformed grain configuration including only the effects of cure shrinkage and axial acceleration and the step height is a factor of 1.55 times larger. The aft propellant grain also moved radially toward the centerline of the motor a significant amount, 1.4 inches more than for the second configuration analyzed. This movement will act as a constriction to the flow field and has a significant effect on the propellant grain pressure loads observed.

Figure 6 shows the final deformed grain configuration analyzed, configuration 4, which resulted from the Step 3(b) stress analysis. The step height for this configuration, 3.24 inches, is significantly greater than the step height for configuration 3. The slot width has also decreased by .99 inches which increases the jet effect of the slot mass injection. But the most significant difference in this final deformed grain configuration is the increased rotation of the aft segment radially into the port flow. The aft segment in this final configuration has rotated radially 1.33 more inches into the port flow. This will be shown to have a significant effect on the pressure distribution on the aft propellant grain.

All CFD runs except for the final deformed grain configuration were made using the boundary conditions and thermochemical properties shown in Figure 7. The final deformed grain configuration, configuration 4, differed only in using an exit pressure boundary condition of 950 psia instead of 1000 psia. This was due to numerical instabilities which developed in the solution using an exit pressure of 1000 psia. The boundary conditions and properties were taken from a 1-D SPP ballistic performance prediction for the SRMU. This data was furnished by the MSFC Solid

Propulsion Branch, EP54, as it was received from Aerospace Corporation. The static pressure was fixed at the exit for all runs. A velocity boundary condition was used for the port flow at the inlet. The Culick velocity profile, shown in Figure 8, was patched at inlet location as a reasonable representation of the upstream port flow. A velocity boundary condition was imposed on all the propellant surfaces with the specified injection velocity normal to the propellant grain shown in Figure 7.

Coupled interacting fluid dynamic effects exist in the aft slot flow field. There is a strong port flow in comparison to the mass injected from the propellant surfaces. A forward facing step of specified step height also exists for all geometry configurations. This acts to alter the direction of the port flow in the slot region and rapidly increase the port Mach number in the slot region. The step height determines the magnitude of this effect. The port flow as well as the interaction of the flow with the step is also affected by the jet action of the mass flow emanating from the burning propellant in the slot. This jet effect tends to alter and constrict the port flow as the extra mass flow from the slot mixes with the port flow. The flow separates at the downstream corner of the slot in each geometric configuration. The size of the recirculation region at the rear corner of the slot is greatly affected by the strength of the slot flow as will be supported by the plots shown in this report.

The CFD runs representing the four configurations of the Titan IV aft slot were each run for more than 4000 iterations and the level of global mass conservation for each of the runs was 0.5 % or less. This mass conservation measure of convergence means that the summation of the mass flux error over all finite volume elements was less than 0.5 %. Local checks at the inlet, exit and various locations down the port were made and showed mass conservation error levels less than 0.1 %.

Figure 9 shows a good overview of the total flow field for configuration 1. The forward edge of the undeformed slot is located at the zero axial distance point in the plot. The plot shows the motor static pressures at the wall and the motor centerline. The first noticeable flow field feature created by the slot is the development of a radial pressure gradient about 25 inches upstream of the slot (as noted by the separation of the wall and centerline pressures) as the flow is turned toward the motor centerline. This is caused by the additional mass flux from the slot (a type of jet effect) and the step height existing between the center and aft propellant segments. This effect is further illustrated by observing the velocity field shown in Figure 10. Notice the strong jet effect as the flow exits from the slot into the port flow. The flow from the upstream port decelerates and is turned sharply toward the motor centerline. This effect can also be observed in the wall pressure plotted in Figure 9 in the pressure increase on the surface of the center propellant segment just upstream of the slot. There is then a rapid drop in the pressure across the slot due to the strong slot flow and accelerating port flow. The centerline pressure drops more slowly since the reaction of the centerline port flow to the slot flow and step height change is much more gradual (since the centerline is radially much further away from the slot). Aft of the slot the pressure gradient across the radial flow field decreases rapidly as the effects of the slot flow interaction die out. Also note the size of the recirculation region at the aft edge of the slot. The size of this recirculation region will decrease for configurations 2 and 3 due to the weaker jet effects associated with a wider slot and the decrease in the slot wall angle from 90 degrees at the aft corner of the slot.

Figure 11 shows a Mach number raster plot for the entire configuration 1 flow field. The rapid increase in the flow field velocities are clearly seen in the immediate slot region. A high velocity jet of fluid is also evident as flow emanates from the slot. Figure 12 shows the pressure drop on the upstream and downstream faces of the slot. The overall pressure drop on the downstream face of the slot is 131 psi. In order to perform the stress analysis on the center and aft propellant segments of the motor, the CFD calculated pressure distribution was faired into the Aerospace ballistic motor data obtained from NASA/MSFC. Figure 13 and Figure 14 show the overall pressure distributions on the center and aft propellant segments, respectively. These were provided to the NASA stress analyst.

The propellant surface and motor centerline pressure distributions for configuration 2 are shown in Figure 15. This pressure plot looks very similar to Figure 9 for configuration 1 with a few noted exceptions. The upstream port pressure has been reduced by more than 10 psia and the pressure on the surface aft of the slot is slightly depressed from that of configuration 1. This upstream port pressure decrease will be discussed more at the end of the report. Due to the fact that the slot opening is larger in configuration 2 than in configuration 1, there is a weaker jet effect in the slot region. Notice that the pressure rise just upstream of the slot is not as great as in configuration 1. Also observe that the flow field velocity vectors in Figure 16 just upstream of the slot are slightly less affected by the flow out of the slot. This is due to reduced velocity of the flow emanating from the slot.

Figure 17 shows the Mach number raster plot for the entire flow field region of configuration 2. The pressure distributions across the upstream and downstream faces of the slot are plotted in Figure 18. The total radial pressure drop across the downstream face of the slot is 126 psi. As shown for configuration 1, Figure 19 and Figure 20 show the port propellant surface pressures faired into the ballistic data for configuration 2. Figure 19 shows the center segment surface pressure and Figure 20 shows the aft segment surface pressure. As a final note in discussing configuration 2, the radial step height increase and the distance the aft propellant segment moves toward the motor centerline are not enough to cause a drastic change in the propellant surface pressure distributions. Configuration 3, however will show a drastic change in the pressure distributions.

The propellant surface and motor centerline pressure distributions for configuration 3 are shown in Figure 21. The upstream maximum pressure has decreased from configuration 2 and there are several important noticeable differences in the pressure distribution of configuration 3 as compared to the other configurations.

Because the slot width has increased by a factor of 2, the jet effect of the flow exiting the slot which was prominent in configuration 1 and 2 has been greatly reduced. As the surface pressure curve in Figure 21 approaches the slot opening there is no increase in the pressure as was present in configuration 1 and 2. Figure 22 provides clear graphical evidence of what is shown in Figure 21. Figure 22 shows the velocity field in the slot region for configuration 3. The port flow is much less affected by the flow emanating from the slot. Observe that the direction and magnitude of the port flow velocity vectors are not stagnated at the slot upstream edge. In this configuration the step height of the downstream slot face is the factor which is driving the port flow to change direction and magnitude. Both the step height and the distance the downstream face of the slot has moved toward the motor centerline are important factors for this configuration. These quantities are significantly greater in this run, and the added resistance to the port flow is evidenced by noting the increased drop in the pressure across the downstream face of the slot, 167 psi. The pressure also remains significantly reduced on the propellant grain downstream of the constricted slot region.

Figure 23 is a raster plot of the Mach number in the port and slot for the entire configuration 3 geometry. The figure shows the increased Mach number in the vicinity of the slot and the deceleration of the flow downstream of the slot as the flow returns to the original port radius downstream of the slot. The slot pressure distributions on the upstream and downstream faces of the slot are shown in Figure 24. Notice that the upstream slot face shows little pressure drop down the slot since the velocities in the slot have been greatly reduced by the increased slot width. As previously noted, the radial pressure drop across the downstream face of the slot has increased to 167 psi. The flow is separated at the corner of the downstream face of the slot but there is no discernable recirculation region in Figure 22. The recirculation area is much smaller than in configuration 1. Figures 25 and 26 show the pressure distributions on the center and aft propellant segments for configuration 3. These distributions were given to the NASA stress analyst in order to assess how the increased pressure load distribution affects the propellant grain.

Figure 27 shows a plot of the wall pressure and the motor centerline pressure down the motor port for configuration 4, the final deformed grain configuration analyzed. The pressure drop on the propellant grain at the downstream corner of the slot has drastically increased for configuration 4. The extremely large pressure drop shown as a spike just downstream of zero axial distance in Figure 27 is much greater than the pressure drop seen in any of the other configurations analyzed. Figure 28 shows the pressure drop across the upstream and downstream face of the slot. The pressure drop from the bottom of the slot to the port wall has increased to 385 psi for this configuration. Figure 29 shows the velocity field in the slot region. A recirculation region has developed on the downstream radial slot face due the combined effects of mass injection from the slot and the large step height of this deformed configuration. This recirculation is responsible for the pressure increase seen in Figure 28 just before the large drop in pressure at the intersecting corner for the slot and the port.

Figure 30 shows a raster plot of the Mach number in the port and slot for the entire configuration 4. The figure shows a marked increase in the port Mach number just downstream of the slot due to the fact that the aft propellant grain has rotated radially toward the centerline much more than in the previous configurations analyzed. Figures 31 and 32 show the port propellant surface pressures faired into the ballistic data. Figure 31 shows the center segment surface pressure and Figure 32 shows the aft segment surface pressure. These pressure distributions for the final deformed grain configuration were given to NASA stress analysts for further investigation.

In order to get a comparison of the four configurations in the slot region, color raster plots were made of the static pressure. These are shown in Figure 33, Figure 34, Figure 35 and Figure 36 which show configurations 1, 2, 3 and 4 respectively. The first three plots are made on a scale using the same minimum and maximum pressures so that the color levels between the minimum and maximum colors have the same meaning. Configuration 4 could not be plotted on the same scale due to the extremely large pressure variation in the slot region. However, the magnitude of the pressure drop in the slot region will be apparent for this configuration. The relative pressure drop across the downstream face of the slot is much greater in configuration 3 than in configurations 1 or 2. Likewise, there is a tremendous increase in the pressure drop for configuration 4. Also, the area of lower pressure downstream of the slot covers a much greater propellant surface area for configuration 3 and 4. The progressive increase in the pressure loads on the propellant grain from configuration 1 to configuration 4 illustrate that there indeed exists a "boot-strapping" effect on the aft propellant grain which tends to rotate the aft propellant grain radially inward toward the port centerline.

A brief explanation of the absolute pressures observed in the runs discussed will be given at this point to fully understand the results. The boundary conditions which had to be used to solve this problem involved a specified pressure at the downstream exit and a velocity boundary condition at the upstream port inlet. This means that as the flow resistance is increased (due to the slot downstream face moving toward the motor centerline) an adjustment must be made to the flow field. Since the velocity is specified at the inlet and the pressure is specified at the exit the CFD code responds to the increased flow resistance by decreasing the pressure upstream of the slot and thus reducing the flow rate. The port inlet flow rate for configurations 1, 2 and 3 are 3358 lbm/s, 3301 lbm/s and 3233 lbm/s, respectively. This occurrence could be eliminated by adjusting the specified exit pressure to give the same port inlet mass flow rate. In the case of configuration 4, the exit pressure was readjusted to 950 psia after numerical instabilities occurred in the solution process. The results for all configurations as they stand do show the correct relative pressure drops in the motor which is the important factor in this problem.

Thus the absolute value of pressures may not be always realistic for every configuration but the pressure gradients and therefore the loads on the propellant grain should be realistic.

Conclusions

The forward facing step in the wall geometry at the aft field joint where the port velocity is high causes a pressure differential to develop between the forward face and the bore surface of the aft segment grain. This pressure differential causes the forward end of the aft segment propellant grain to rotate radially inward which further increases the forward facing step height and consequently, the pressure differential. Thus it appears that as the aft segment grain rotates radially inward, the increased flow resistance generates an increasingly adverse pressure load on the aft propellant grain. This radially inward rotation is facilitated by the stress relief groove at the bottom of the slot. The radial pressure gradient in the slot is not a prime contributor to the final pressure loading and deformation of the propellant. This is due to the actual width of the slot being much greater than the drawing value when the effects of cure shrinkage, thermal cooldown, 1g vertical loading, and pressure loading are included.

The results of configuration 4 were transmitted to the NASA/MSFC stress analyst to determine how this increased pressure load finally affects the propellant grain.